

AFRL-IF-RS-TR-2003-161
Final Technical Report
July 2003



MICROFABRICATION TECHNIQUES FOR PLASTIC MICROELECTROMECHANICAL SYSTEMS (MEMS)

University of Michigan

APPROVED FOR PUBLIC RELEASE; DISTRIBUTION UNLIMITED.

The views and conclusions contained in this document are those of the authors and should not be interpreted as necessarily representing the official policies, either expressed or implied, of the Defense Advanced Research Projects Agency or the U.S. Government.

**AIR FORCE RESEARCH LABORATORY
INFORMATION DIRECTORATE
ROME RESEARCH SITE
ROME, NEW YORK**

This report has been reviewed by the Air Force Research Laboratory, Information Directorate, Public Affairs Office (IFOIPA) and is releasable to the National Technical Information Service (NTIS). At NTIS it will be releasable to the general public, including foreign nations.

AFRL-IF-RS-TR-2003-161 has been reviewed and is approved for publication.

APPROVED:



DUANE GILMOUR
Project Engineer

FOR THE DIRECTOR:



JAMES A. COLLINS, Acting Chief
Information Technology Division
Information Directorate

| | | | | |
|---|---|--|---|-----------------------------------|
| REPORT DOCUMENTATION PAGE | | | <i>Form Approved</i> <i>OMB No. 074-0188</i> | |
| Public reporting burden for this collection of information is estimated to average 1 hour per response, including the time for reviewing instructions, searching existing data sources, gathering and maintaining the data needed, and completing and reviewing this collection of information. Send comments regarding this burden estimate or any other aspect of this collection of information, including suggestions for reducing this burden to Washington Headquarters Services, Directorate for Information Operations and Reports, 1215 Jefferson Davis Highway, Suite 1204, Arlington, VA 22202-4302, and to the Office of Management and Budget, Paperwork Reduction Project (0704-0188), Washington, DC 20503 | | | | |
| 1. AGENCY USE ONLY (Leave blank) | | 2. REPORT DATE JULY 2003 | 3. REPORT TYPE AND DATES COVERED Final Jun 98 – Sep 02 | |
| 4. TITLE AND SUBTITLE MICROFABRICATION TECHNIQUES FOR PLASTIC MICROELECTROMECHANICAL SYSTEMS (MEMS) | | | 5. FUNDING NUMBERS C - F30602-98-2-0197 PE - 63739E PR - E117 TA - 00 WU - 44 | |
| 6. AUTHOR(S) C. H. Mastrangelo | | | | |
| 7. PERFORMING ORGANIZATION NAME(S) AND ADDRESS(ES) University of Michigan Center for Integrated Microsystems Department of Electrical Engineering and Computer Science 1301 Beal Avenue Ann Arbor Michigan 48109-2122 | | | 8. PERFORMING ORGANIZATION REPORT NUMBER N/A | |
| 9. SPONSORING / MONITORING AGENCY NAME(S) AND ADDRESS(ES) Defense Advanced Research Projects Agency AFRL/IFTC 3701 North Fairfax Drive 26 Electronic Parkway Arlington Virginia 22203-1714 Rome New York 13441-4514 | | | 10. SPONSORING / MONITORING AGENCY REPORT NUMBER AFRL-IF-RS-TR-2003-161 | |
| 11. SUPPLEMENTARY NOTES AFRL Project Engineer: Duane Gilmour/IFTC/(315) 330-3550/ Duane.Gilmour@rl.af.mil | | | | |
| 12a. DISTRIBUTION / AVAILABILITY STATEMENT APPROVED FOR PUBLIC RELEASE; DISTRIBUTION UNLIMITED. | | | | 12b. DISTRIBUTION CODE |
| 13. ABSTRACT (Maximum 200 Words) This report presents research and development of new micromachining techniques and fabrication technologies for the construction of plastic MEMS devices. Plastic MEMS are of major importance in the implementation of miniature chemical reaction systems, such as DNA diagnostic, bacteriophage, and other bio-assays chips. Further, because of their low temperature construction, plastic MEMS devices can be integrated with conventional electronic circuits easily and inexpensively. Three main technology directions were conducted. First, technology developments for implementing plastic microsystems using both surface and bulk micromachining techniques were investigated. Surface micromachining techniques include deposition of thin and thick polymer films using vacuum and spin-casting techniques. Bulk micromachining of plastics is used for creating a viable technology for system substrates. Bulk micromachining techniques include injection molding, embossing, casting, bonding and lamination. Secondly, the integration of surface and bulk micromachining technologies leads to a robust technology for creating complete plastic microsystems. The third development direction was in the implementation of the aforementioned developed plastic micromachining technologies as several demonstration devices including microactuators, microvalves, a micropump, a microdevice for polymerase chain reactions (PCR), a capillary electrophoresis (CE) microdevice for DNA separations, and devices for patterning protein doped conductive polymers using laminar flows. | | | | |
| 14. SUBJECT TERMS Plastic MEMS, Plastic Packaging, Plastic Micromachining, Microactuator, Microvalve, Microfluidics, Micropump, Microchannel, Injection Molding, Microcasting, Embossing | | | | 15. NUMBER OF PAGES 146 |
| | | | | 16. PRICE CODE |
| 17. SECURITY CLASSIFICATION OF REPORT UNCLASSIFIED | 18. SECURITY CLASSIFICATION OF THIS PAGE UNCLASSIFIED | 19. SECURITY CLASSIFICATION OF ABSTRACT UNCLASSIFIED | 20. LIMITATION OF ABSTRACT UL | |

Table of Contents

| | |
|--|-----------|
| 1.0 Summary | 1 |
| 2.0 Introduction | 3 |
| 3.0 Technology Development | 4 |
| 3.1 Surface Micromachining | 4 |
| 3.1.1 Materials | 4 |
| 3.1.1.1 Paraffin | 4 |
| 3.1.1.1.1 Thermophysical Properties | 6 |
| 3.1.1.2 Parylenes | 11 |
| 3.1.2 Process Technology | 12 |
| 3.1.2.1 Deposition of Thin Polymer Films | 13 |
| 3.1.2.1.1 Paraffin Deposition | 13 |
| 3.1.2.1.2 Parylene Deposition | 14 |
| 3.1.2.1.3 Nickel Electrodeposition | 15 |
| 3.1.2.1.4 Electrochemical Deposition of Conductive Polymers | 16 |
| 3.1.2.2 Etching of Thin Polymer Films | 19 |
| 3.1.2.2.1 Paraffin Etching | 20 |
| 3.1.2.2.2 Parylene Etching | 20 |
| 3.1.3 Cell Attachment | 21 |
| 3.1.3.1 Micropatterning Proteins for Cell Attachment | 21 |
| 3.1.3.2 Lithography and Stencil Patterning | 22 |
| 3.1.3.3 Micro-contact Printing | 22 |
| 3.1.3.4 Patterning using Laminar Flows | 22 |
| 3.1.3.5 Deposition of PPy/PSS and PPy/Collagen | 23 |
| 3.2 Bulk Micromachining | 24 |
| 3.2.1 Materials | 24 |
| 3.2.1.1 Epoxy | 24 |
| 3.2.1.1.1 Types of Epoxy resins | 24 |
| 3.2.1.1.2 Curing Agents (Hardeners) | 25 |
| 3.2.1.1.3 Amine Based Curing Agents | 25 |
| 3.2.1.1.4 Phenolic Hardener | 25 |
| 3.2.1.1.5 Toughening of Epoxy Resins | 26 |
| 3.2.1.1.6 Toughening Agents | 26 |
| 3.2.1.2 EPOTEK Casting Epoxies | 26 |
| 3.2.2 Process Technology | 28 |
| 3.2.2.1 Substrate Etching | 28 |
| 3.2.2.1.1 Photodefinable Glass Substrates | 28 |
| 3.2.2.1.2 Deep Reactive Ion Etching Silicon | 29 |
| 3.2.2.2 Microcasting | 29 |
| 3.2.2.2.1 Stamper Fabrication | 29 |
| 3.2.2.2.2 Fabrication Process | 31 |
| 3.2.2.3 Lamination and Bonding | 34 |
| 3.2.2.3.1 Lamination | 35 |
| 3.2.2.3.2 Bonding | 37 |
| 3.2.2.4 Feed-throughs on Plastic Substrates | 38 |
| 3.2.2.5 Injection Molding | 39 |
| 3.2.2.5.1 Molding Results | 40 |
| 3.2.2.6 Flip-Chip Bonding | 41 |
| 3.2.2.6.1 Solder Joining | 43 |
| 3.2.2.6.2 Conductive and Non-conductive Adhesives | 43 |
| 3.2.2.6.3 Polymer Flip-Chip Process | 44 |
| 3.2.2.6.3.1 Chip on Flex | 44 |
| 3.2.2.6.3.2 Polymer Flip-Chip Process for Embedded Detectors | 45 |

| | |
|---|------------|
| 3.2.2.7 Micro Screen Printing (μ -Screen)..... | 47 |
| 3.2.2.7.1 Electrically Conductive Epoxy | 48 |
| 3.2.2.8 Precision Die Placement..... | 49 |
| 3.2.2.8.1 Embedding Silicon Chips with Heaters on Plastic | 51 |
| 4.0 Demonstration Devices..... | 53 |
| 4.1 Paraffin Microactuators..... | 53 |
| 4.1.1 Microactuation..... | 53 |
| 4.1.2 Polymer Phase Change Microactuators | 54 |
| 4.1.3 Piston-Type Microactuator | 55 |
| 4.1.3.1 Device Structure | 56 |
| 4.1.3.2 Diaphragm Deflection | 56 |
| 4.1.3.3 Heater Structure..... | 57 |
| 4.1.3.4 Fabrication..... | 57 |
| 4.1.3.5 Experiments..... | 59 |
| 4.1.3.5.1 Diaphragm Deflection | 59 |
| 4.1.3.5.2 Heater Resistance | 60 |
| 4.1.3.5.3 Electrothermal Models | 60 |
| 4.1.3.5.3.1 One Dimensional Steady State Model | 61 |
| 4.1.3.5.4 Electrical Characteristics | 64 |
| 4.1.3.5.5 Three Dimensional Finite Difference Models | 66 |
| 4.1.3.5.5.1 Steady State Model | 66 |
| 4.1.3.5.5.2 Transient Response Model | 68 |
| 4.1.4 Hydraulic Advantage Structure | 70 |
| 4.1.4.1 Device Structure | 71 |
| 4.1.4.2 Diaphragm Deflection | 71 |
| 4.1.4.3 Fabrication..... | 72 |
| 4.1.4.4 Experiments..... | 72 |
| 4.1.4.4.1 Diaphragm Deflection | 72 |
| 4.2 Microvalves | 74 |
| 4.2.1 Active Blocking Microvalve..... | 75 |
| 4.2.1.1 Device Structure | 75 |
| 4.2.1.2 Steady State Gas Flow Model..... | 76 |
| 4.2.1.3 Microvalve Flow Model..... | 79 |
| 4.2.1.4 Fabrication..... | 81 |
| 4.2.1.4.1 Nickel Electroplated Microvalves | 82 |
| 4.2.1.4.2 Parylene Microvalves | 83 |
| 4.2.1.5 Experiments..... | 84 |
| 4.2.2 Mass Flow Control Valve..... | 88 |
| 4.2.2.1 Device Structure | 89 |
| 4.2.2.2 Fabrication..... | 90 |
| 4.2.2.3 Experiments..... | 92 |
| 4.2.2.3.1 Flow Rate Measurements | 92 |
| 4.2.3 Inline Microvalve | 94 |
| 4.2.3.1 Device Structure | 95 |
| 4.2.3.2 Fabrication..... | 97 |
| 4.2.3.3 Experiments..... | 99 |
| 4.3 Microfluidic Pump..... | 100 |
| 4.3.1 Nozzle-diffuser pumps theory | 100 |
| 4.3.2 Fabrication..... | 101 |
| 4.3.3 Thermal Modeling | 104 |
| 4.3.4 Measured Results..... | 107 |
| 4.4 PCR Device | 109 |
| 4.4.1 Device Fabrication..... | 109 |
| 4.4.2 Thermal Modelling | 111 |
| 4.4.3 Device Characterization | 111 |
| 4.4.4 On-Chip Thermal Lysis and PCR..... | 112 |

| | |
|---|------------|
| 4.5 Capillary Electrophoresis Device | 113 |
| 4.5.1 Device Fabrication..... | 113 |
| 4.5.2 Separation Results (HEC)..... | 115 |
| 4.5.3 Separations results (UV gels) | 115 |
| 4.6 Laminar Flow Patterning of Protein Doped Conductive Polymers | 116 |
| 4.6.1 Electrode Fabrication..... | 116 |
| 4.6.2 Channels for Laminar Flow Patterning..... | 117 |
| 5.0 Conclusion..... | 118 |
| 6.0 List of Publications | 119 |
| 6.1 Theses | 119 |
| 6.2 Refereed Journal Publications..... | 119 |
| 6.3 Conferences | 119 |
| 7.0 List of Inventions | 120 |
| 8.0 References | 121 |

List of Figures

| | |
|---|----|
| Figure 1: Organization and scope of work. | 1 |
| Figure 2: Planar zigzag representation of normal paraffins..... | 5 |
| Figure 3: Variation of paraffin melting temperature with numbers of carbon atoms | 6 |
| Figure 4: High pressure dilatometry measurements showing volumetric expansion characteristics of Logitech paraffin | 7 |
| Figure 5: High pressure dilatometry measurements showing volumetric expansion characteristics for tetratetracontane 98% (Alfa Products) | 8 |
| Figure 6: Measured heat capacity as a function of temperature for Logitech paraffin using Perkin Elmer DSC-7 differential scanning calorimeter (a) heating (b) cooling scans..... | 9 |
| Figure 7: Measured heat capacity of hexatriacontane as a function of temperature | 10 |
| Figure 8: Calculated (solid line) and measured thermal conductivity as a function of temperature for Logitech paraffin | 11 |
| Figure 9: Parylene-C chemical structure | 12 |
| Figure 10: Infrared absorption spectra of an 18 μm thick Parylene-C film..... | 12 |
| Figure 11: a) Thermal evaporator constructed for this research (b) modified crucible holder eliminating polymer splashing..... | 13 |
| Figure 12: 100 x 100 μm^2 tapping mode AFM scan (a) example of scanned surface (b) example of average surface roughness measurement | 14 |
| Figure 13: Vacuum deposition process of parylene..... | 14 |
| Figure 14: Electrochemical polymerization reaction..... | 18 |
| Figure 15: Cyclic Voltammetry of PPY/PSS and PPY/BSA, PPY/Collagen swept between 0.5 and – 0.9V | 19 |
| Figure 16: Etching rate behavior for $\text{CF}_4\text{-O}_2$ plasma for RF planar diode etching system..... | 20 |
| Figure 17: Patterned ECD of protein doped conductive polymers using laminar flow patterning | 23 |
| Figure 18: ECD of PPY/PSS and PPY/Collagen on fabricated device | 24 |
| Figure 19: The structure of an epoxide group. | 24 |
| Figure 20: The structure of Diglycidyl ether of bisphenol-A. | 25 |
| Figure 21: Plot showing the spectral transmittance of epoxies at various wavelengths of light..... | 27 |
| Figure 22: Glass transition temperatures of the EPOTEK epoxies used. | 28 |
| Figure 23: Foturan glass heat treatment schedule..... | 28 |
| Figure 24: Fabricated through wafer holes in Foturan substrates (a) circle (b) square..... | 29 |
| Figure 25: SEMs of silicon wafer with DRIE negative replicas of desired features. | 30 |
| Figure 26: Shown are aluminum mold plates for open and closed mold casting. | 31 |
| Figure 27: Schematic of the open casting process. | 32 |
| Figure 28: Shown is a microscope picture of a cast epoxy channel obtained by open casting | 32 |
| Figure 29: Schematic of the closed mold casting process. | 33 |
| Figure 30: Microscope and SEM pictures of channels fabricated using the closed mold casting process. .. | 34 |
| Figure 31: Surface roughness of a cast epoxy channel obtained by casting. | 35 |
| Figure 32: Process flow for lamination. | 36 |
| Figure 33: Kepro desktop roll type laminator..... | 36 |
| Figure 34: Cross section of a laminated channel. | 37 |
| Figure 35: Process flow for the bonding technique. | 37 |
| Figure 36: Pictures of channels bonded using bonding wax..... | 38 |
| Figure 37: Stainless steel mold for fabrication of through vias and a fabricated epoxy channel with through vias. | 39 |
| Figure 38: The molds plates used for Injection molding | 40 |
| Figure 39: Injection molded polycarbonate substrate..... | 40 |
| Figure 40: SEMs of injection molded low aspect ratio structures. | 41 |
| Figure 41: Cross sections of different flip-chip processes..... | 42 |
| Figure 42: Basic flip-chip joints using solder and metal. | 42 |
| Figure 43: Flip-chip joints using conductive and non conductive adhesive. | 43 |
| Figure 44: Flip chip bonding for electrical contacts. | 44 |
| Figure 45: Comparison of the detector area to the total die area [114]. | 45 |
| Figure 46: Shown are silicon chips embedded in a cast epoxy substrate with fluidic circuits. | 45 |
| Figure 47: Process flow for embedding silicon chips in plastic. | 46 |

| | |
|--|----|
| Figure 48: Alternative process flow for embedding chips in plastic. | 46 |
| Figure 49: A typical stencil type micro-screen for micro-screen printing applications. | 47 |
| Figure 50: Typical screen printing machine for printing on flat surfaces. | 48 |
| Figure 51: Screen printed conductive epoxy bumps. | 49 |
| Figure 52: The Royce 110 die pick and place system. | 50 |
| Figure 53: Close up view a silicon chip held by the vacuum tip just before placement. | 51 |
| Figure 54: Microscope pictures of the back and front side of a precision placed silicon chip on a plastic substrate. | 52 |
| Figure 55: Embedded active silicon micromachined devices on plastic. | 52 |
| Figure 56: Cross-section of thermally activated paraffin microactuator. | 56 |
| Figure 57: Serpentine heating structure shown with circular pattern representing the patterned paraffin actuating layer. | 57 |
| Figure 58: Simplified paraffin microactuator process flow. | 58 |
| Figure 59: Top view of sealed actuator with heater clearly visible (Cr/Au physical mask has been removed). | 59 |
| Figure 60: Deflection height measurements (using Wyko NT-2000 non contact surface profilometer) for a 200 μm diaphragm device for three different heater voltages. | 59 |
| Figure 61: Deflection height measurements (using Wyko NT-2000 non contact surface profilometer) as a function of input power. | 60 |
| Figure 62: One dimensional schematic of actuator cross-section. | 61 |
| Figure 63: Differential element of actuator used for electrothermal analysis. | 62 |
| Figure 64: Infrared absorption spectra of an 18 μm thick parylene film for estimating surface emissivity in the 3.4 - 5.0 μm spectral band. | 63 |
| Figure 65: Measured parylene diaphragm surface temperature as a function of heater power. | 64 |
| Figure 66: Example of the steady state temperature profile for an aluminum heater on a Foturan glass substrate for different currents. | 64 |
| Figure 67: Measured steady state heater resistance as a function of temperature (a) 400 μm diameter actuator (b) 600 μm diameter actuator. | 65 |
| Figure 68: Measured aluminum heater voltage-current characteristics for electrothermally actuated paraffin microactuator. | 66 |
| Figure 69: Three dimensional steady state heater simulation results for different heater electrical input power values. | 68 |
| Figure 70: Three dimensional transient simulation results. | 69 |
| Figure 71: Test circuit used to measure actuator response time. | 69 |
| Figure 72: Measured response time for a 200 μm radius diaphragm Logitech actuator on a glass substrate. | 70 |
| Figure 73: Measured heater phase response for the 200 μm radius diaphragm showing 30 Hz cutoff. | 70 |
| Figure 74: Top view of microactuator diaphragm with posts. | 71 |
| Figure 75: Top view of the constrained diaphragm microactuator with and an evaporated paraffin thickness of 3 μm and 600 μm diameter diaphragm. | 72 |
| Figure 76: Measured diaphragm deflection of a 400 μm radius pinned diaphragm device with a 3 μm thick paraffin layer as a function of input power. | 73 |
| Figure 77: Measured deflection height as a function of input power for the 400 μm radius pinned diaphragm device with a 3 μm thick paraffin layer. | 73 |
| Figure 78: Measured deflection vs. input power for the partially constrained diaphragm actuator (a) 1:4 Logitech $\text{C}_{36}\text{H}_{74}$ layer (b) 2:3 Logitech: $\text{C}_{36}\text{H}_{74}$ layer. | 74 |
| Figure 79: Cross-section of blocking microvalve. | 75 |
| Figure 80: Channel dimensions labels used for all channel sections (a) rectangular sections (b) circular section. | 77 |
| Figure 81: Lumped gas flow model showing four dominant channel conductances. | 79 |
| Figure 82: Accuracy of a piecewise linear approximation. | 80 |
| Figure 83: Saber gas flow simulation model. | 81 |
| Figure 84: Simplified nickel electroplated blocking microvalve fabrication process flow. | 81 |
| Figure 85: Photograph of paraffin actuator with 9 μm thick paraffin layer and a 4 μm thick, patterned parylene diaphragm layer. | 82 |

| | |
|---|-----|
| Figure 86: SEM photograph of device (a) circular reservoir with outlet orifice over the paraffin actuator (b) square reservoir covering the inlet hole..... | 83 |
| Figure 87: Microscope photograph of nickel electroplated valve backside showing (a) actuator (b) inlet hole through substrate | 83 |
| Figure 88: Microscope photograph of parylene microvalve (a) Top side of circular reservoir clearly showing outlet hole and actuator (b) bottom of circular reservoir clearly showing the heater, electrodes, reservoir and channel..... | 84 |
| Figure 89: Photograph of (a) die containing ten microvalves (three test actuators) bonded to test circuit board (b) circuit board mounted in the top vacuum test chamber | 84 |
| Figure 90: Measured actuator center deflection through the outlet hole with a Zygo NewView 5000 non contact surface profilometer (a) 400 μm diameter actuator (b) 800 μm diameter actuator | 85 |
| Figure 91: Experimental flow rate measurement apparatus | 86 |
| Figure 92: Measured (circles) and simulated (line) flow rate through a 400 μm diameter actuator device as a function of input power (linear-log scale) | 87 |
| Figure 93: Measured (circles) and simulated (line) flow rate through a 600 μm diameter actuator device as a function of input power (linear-log scale) | 88 |
| Figure 94: Measured (circles) and simulated (line) flow rate through an 800 μm diameter actuator device as a function of input power (linear-log scale) | 88 |
| Figure 95: Typical pressure based sensing mass flow controller..... | 89 |
| Figure 96: Top view and cross-section of the micro flow control valve | 90 |
| Figure 97: Simplified nickel electroplated micro flow controller fabrication | 91 |
| Figure 98: Microscope photograph of paraffin microactuator..... | 91 |
| Figure 99: Microscope photograph of the nickel electroplated micro flow controller valve system..... | 92 |
| Figure 100: Photograph of (a) die containing a flow controller valve unit bonded to test circuit board (b) circuit board mounted in top pressure chamber..... | 93 |
| Figure 101: Measured actuator center deflection through the outlet hole with a Zygo NewView 5000 non contact surface profilometer (a) 400 μm diameter actuator (b) Measured flow rate through a single microvalve (2.2 μm gap) as a function of input power | 93 |
| Figure 102: Measured flow rate through the four-valve microvalve system (2.2 μm gap heights) as a function of input power | 94 |
| Figure 103: Three dimensional view of inline microvalve showing the paraffin actuation layer..... | 95 |
| Figure 104: Cross-section of inline microvalve (a) normally-open state (b) actuated-closed state | 95 |
| Figure 105: Top view of inline microvalve (a) without paraffin actuation layer showing the heater structure (b) with paraffin actuation layer showing the paraffin reservoirs, funnel structure and reduced channel region | 96 |
| Figure 106: Simplified inline microvalve fabrication process flow | 97 |
| Figure 107: Microscope photograph of a 7.5 x 7.5 mm ² die showing many independently operating valves | 98 |
| Figure 108: Microscope photograph of a single fabricated inline valve..... | 99 |
| Figure 109: Microscope photographs of the inline microvalve opening and closing the capillary to deionized water flow | 100 |
| Figure 110: Principle of operation of nozzle-diffuser pumps and fluid flow with increasing and decreasing chamber volume. | 101 |
| Figure 111 (a) and (b). Shown is the process flow for fabrication of the channel structure and wax actuator respectively..... | 103 |
| Figure 112: (a) Pictures show SEM of EPOTEK 301-2 FL substrate with chamber, channel and nozzle-diffuser geometry, (b) wax actuator on EPOTEK 314 substrate and (c) bonded nozzle-diffuser pump respectively..... | 104 |
| Figure 113. The graph shows the calculated change in heater temperature with increasing current..... | 105 |
| Figure 114: Layer by layer representation of the actuator..... | 105 |
| Figure 115: The graph shows the change in fluid temperature with increasing current. The pump usually operates below 30 milliamps (2.5V DC). | 106 |
| Figure 116: Optical profiles of the deflection heights of the wax actuator surface obtained at different voltages using a ZYGO optical interferometer..... | 107 |

| | |
|---|-----|
| Figure 117: Channel design for calculation of (a) flow rate with zero back pressure and (b) pumping pressure..... | 108 |
| Figure 118: Volume flow rates obtained at different pulse frequencies for different applied voltages..... | 108 |
| Figure 119: Pumping pressure generated at 5V, plotted for different pulse frequencies..... | 109 |
| Figure 120: Device design and fabricated PCR device. | 110 |
| Figure 121: Process flow for fabrication of the PCR device. | 111 |
| Figure 122: Meshing and Heat Distribution around the PCR chamber. | 112 |
| Figure 123: Profiles of heating and cooling cycles using on-chip heaters and coolers. | 112 |
| Figure 124: PCR product compared with control reaction through gel electrophoresis..... | 113 |
| Figure 125: Process flow for fabricating the CE device. | 114 |
| Figure 126: Fabricated CE device. | 114 |
| Figure 127: DNA plug and separated bands (HEC). | 115 |
| Figure 128: DNA plug and separated bands (UV gels). | 116 |
| Figure 129: Fabricated electrodes..... | 117 |
| Figure 130: Fabricated device for laminar flow patterning of protein doped conductive polymers..... | 118 |
| Figure 131: Laminar flow demonstration in fabricated channel structure..... | 118 |

List of Tables

| | |
|--|-----|
| Table 1: Chemical formulas for several normal paraffins | 5 |
| Table 2: Calculated latent heat fusion for various paraffins | 10 |
| Table 3: Physical properties and curing schedule for the different epoxies used | 27 |
| Table 4: Physical properties of H-20E..... | 49 |
| Table 5: Actuation power P_a for several low voltage microactuators. Dimensions used to calculate P_a for the paraffin microactuator: $P_a=100$ MPa, $A_a=4\pi \cdot 10^{-8}$ m ² , $\epsilon_a=10 \times 10^{-6}$ m, and $V_a=4\pi \times 10^{-13}$ m ³ | 54 |
| Table 6: Thermally induced volumetric changes due to solid to liquid phase change of several polymers. | 55 |
| Table 7: Calculated Grashof numbers as a function of heater input power. | 67 |
| Table 8: Flow Regimes..... | 77 |
| Table 9: Simulated microvalve pressure distribution and comparison between calculated and measured open flow..... | 88 |
| Table 10: Simulated microvalve pressure distribution and comparison of calculated Q_{calc} and measured Q_{meas} open flowrate..... | 93 |
| Table 11: Simulated and measured flow ranges | 94 |
| Table 12: Thermal conductivity of materials used in fabricating the PEG 8000 actuator | 106 |

1.0 Summary

This report summarizes research in the development of new micromachining techniques and fabrication technologies for the construction of plastic MEMS devices. Plastic MEMS are of major importance in the implementation of miniature chemical reaction systems, such as DNA diagnostic, bacteriophage, and other bio-assays chips. For example, they can play an increasingly important role as soft, deformable, distributed, and artificial muscle actuators used as active elements in microfluidic valves. Further, because of their low temperature construction, plastic MEMS devices can be integrated with conventional electronic circuits easily and inexpensively.

Despite the potentially wide applicability of plastic materials in MEMS to date, there are no, in general, micromachining techniques specific for plastic or organic MEMS. Unlike silicon and other inorganic materials, plastic materials require special surface and bulk micromachining techniques because of their intrinsic low temperature constraints, high susceptibility to swelling and deformation, and low resistance to etchants. The work presented in this report covers these important missing processing techniques.

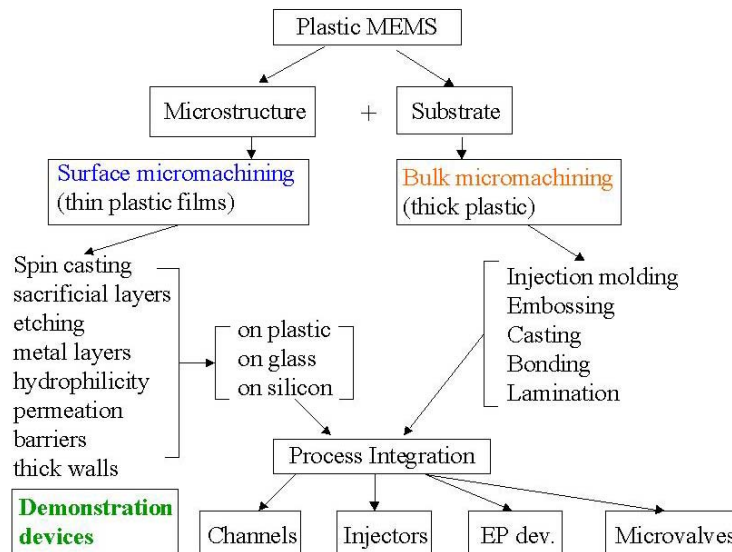


Figure 1: Organization and scope of work.

Under this work, we have developed two types of complementary plastic microfabrication technologies based on (a) surface micromachining (lithographic) and (b) microcasting methods. These two technologies are complementary since lithographic methods are required for plastic devices with multiple layers (hence requiring precise alignment) and molding techniques are needed for definition of large features on substrates and thicker layers.

The application of these fabrication technologies has been implemented in both passive and active plastic MEMS. Passive and active systems are constructed on glass or plastic substrates while active systems can also be integrated with electronic substrates. Figure 1 shows the organization and scope of the work. Using the fabrication techniques that were developed during the research effort, we have adopted microfluidic systems and actuators as technology demonstrations, because of the large number of military and

commercial applications. Several plastic microfluidic devices, including polymer activated microactuators, microvalves, a micropump, a polymerase chain reaction system, and an electrophoresis stage for DNA separation are presented for the first time in this final research report.

2.0 Introduction

This report presents research and development of new micromachining techniques and fabrication technologies for the construction of plastic MEMS devices. Three main technology directions were conducted. First, technology developments for implementing plastic microsystems using both surface and bulk micromachining techniques were investigated. Surface micromachining techniques include deposition of thin and thick polymer films using vacuum and spin-casting techniques. Bulk micromachining of plastics is used for creating a viable technology for system substrates. Bulk micromachining techniques include injection molding, embossing, casting, bonding and lamination. Secondly, the integration of surface and bulk micromachining technologies leads to a robust technology for creating complete plastic microsystems. The third development direction is in the implementation of the aforementioned developed plastic micromachining technologies as several demonstration devices including microactuators, microvalves, a micropump, a microdevice for polymerase chain reactions (PCR), a capillary electrophoresis (CE) microdevice for DNA separations, and devices for patterning protein doped conductive polymers using laminar flows.

Plastic micromachining, both surface and bulk, are presented sections 3.1 and 3.2, respectively. Surface micromachined devices were constructed by the successive deposition and patterning of thin solid films 0.1-10 μm thick. Typically, polymers are temperature sensitive; therefore, special consideration must be given to heat generating processes, such as plasma related processes. The thermal expansion of paraffin is used as the actuating medium for microactuators, microvalves, and a micropump presented in this report. Bulk micromachining is used to fabricate microfluidic systems on polycarbonate substrates. Techniques to form microchannels, reactors, and input and output fluidic ports are discussed.

The implementation of the developed surface and bulk micromachining technologies within demonstration devices are presented in section 4. Presented are techniques for fabrication of high quality, cheap, disposable polymers used to implement a variety of microanalytical systems, including a micro PCR system and a CE system for amplifying and separating DNA, respectively. Demonstrations on how to integrate complexity into plastic based systems is shown using two techniques, sub-die embedding and surface micromachining. A technique for cellular micropatterning is also shown, using electrochemical deposition of conductive polymers doped with extracellular matrix proteins.

3.0 Technology Development

The technology development for plastic micromachining is presented in two major areas: surface and bulk micromachining. All fabrication steps used in this research are performed with temperatures less than or equal to 110°C, with the exception of photodefinable glass substrate processing, described in a later section.

3.1 Surface Micromachining

Surface micromachined devices are constructed by the successive deposition and patterning of thin solid films 0.1-10 μm thick. Typically, polymers are temperature sensitive; therefore, special consideration must be given to heat generating processes such as plasma related processes. Since plasma related processes (i.e. RIE, and sputter coating) can expose the polymeric sample to the hot plasma for extended periods of time, the sample substrate temperatures must be controlled at or below room temperature. In addition, in most cases plasma power levels must be reduced which in turn increase deposition and etch times.

3.1.1 Materials

Thin polymer films were used in the development of the novel electrothermal microactuators for active microfluidic applications presented in this research. Thin, thermally evaporated paraffin films, have also been used as actuating layers for microactuators. Thin films of vapor deposited para-xylylene (parylene-C or parylene) serve as a sealing layer and microactuator diaphragms.

Thermophysical properties of Logitech paraffin have been measured and are presented in this research. Thermophysical properties of hexatriacontane and tetratetracontane have been taken from literature [35] and are used as comparison for measurements performed in this research. Specific volume as a function of temperature and pressure has been measured using high pressure dilatometry. Heat capacity and thermal conductivity have also been measured and used to model the electrothermal behavior of the piston microactuator structure.

Thermophysical properties of parylene have been provided by the manufacturer of the vapor deposition system [36]. Infrared absorption spectra have been used to estimate the average spectral emissivity of the thin parylene films. The emissivity of the parylene films is used to accurately measure the diaphragm surface temperature of the thermally activated microactuators.

3.1.1.1 Paraffin

Thin films of pure and mixtures of simple straight chain paraffins were used as the actuation layer for microactuators developed in this research due to their large actuating power capability. Paraffins are saturated hydrocarbon mixtures, consisting of mixtures of numerous alkanes or purified alkanes of different chain lengths. Hydrocarbon components of paraffin can exist in gas, liquid or solid states depending on their temperature and pressure. These saturated hydrocarbons occur in the form of simple straight chains called normal paraffinic hydrocarbons or branched chains which are called iso-paraffinic hydrocarbons. The general term *paraffin* will be used to describe normal alkanes throughout the remainder of this work.

The general chemical formula for paraffin is C_nH_{2n+2} because there are two hydrogen atoms bonded to each carbon atom of the chain plus one additional hydrogen atom bonded to each end of the chain. In saturated hydrocarbons, there are only single bonds. Figure 2 shows the general chemical *zigzag* structure of normal paraffins.

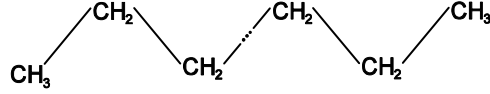


Figure 2: Planar zigzag representation of normal paraffins

Normal paraffins are named according to the number of carbon atoms in the chain. Table 1 shows the names and chemical formulas for several normal paraffins. The large selection of paraffins with different chain lengths; hence different melting temperatures; makes them very attractive for different microactuator applications.

Table 1: Chemical formulas for several normal paraffins

| N | Name | Formula |
|----|-------------------|-------------------------|
| 1 | methane | CH_4 |
| 2 | ethane | $CH_3 CH_3$ |
| 3 | propane | $CH_3 CH_2 CH_3$ |
| 4 | butane | $CH_3 (CH_2)_2 CH_3$ |
| 5 | pentane | $CH_3 (CH_2)_3 CH_3$ |
| 10 | decane | $CH_3 (CH_2)_8 CH_3$ |
| 14 | tetradecane | $CH_3 (CH_2)_{12} CH_3$ |
| 20 | eicosane | $CH_3 (CH_2)_{18} CH_3$ |
| 30 | triacontane | $CH_3 (CH_2)_{28} CH_3$ |
| 36 | hexatriacontane | $CH_3 (CH_2)_{34} CH_3$ |
| 40 | tetracontane | $CH_3 (CH_2)_{38} CH_3$ |
| 44 | tetratetracontane | $CH_3 (CH_2)_{42} CH_3$ |

The increased length of the carbon atom chains increases the molar weight resulting in higher melting temperatures of the material. Figure 3 shows the range of melting temperatures for paraffins with different numbers of carbon atoms. For applications which are sensitive to elevated temperatures, such as polymerase chain reaction (PCR) systems with thermally reactive enzymes, paraffin actuated valves with low temperature actuation is required. Alternatively, applications requiring actuation control in high temperature environments, actuators utilizing long chain paraffins can be used.

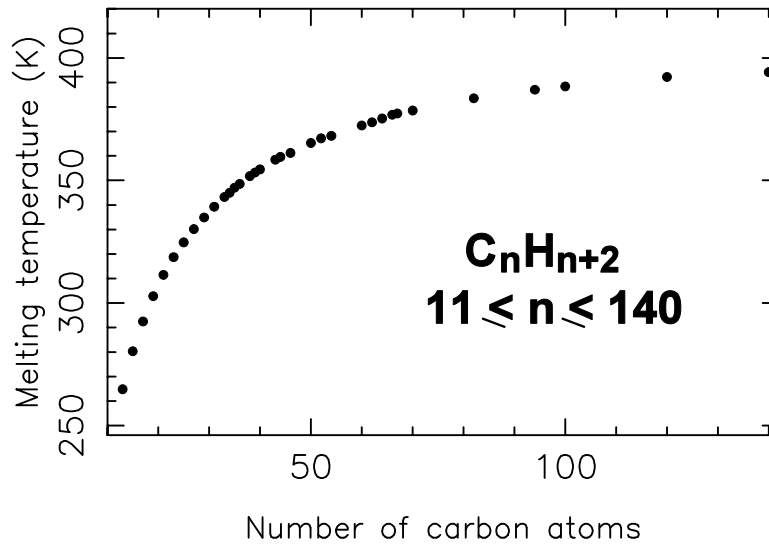


Figure 3: Variation of paraffin melting temperature with numbers of carbon atoms

Like most other organic materials, paraffins have a low thermal conductivity. In addition, they also have low electric conductivity, which accounts for their excellent insulating properties. Paraffins have very low chemical reactivity with nearly all materials which is the origin of the name paraffin, derived from the latin expression *parum affinis* meaning chemically inactive. In fact, paraffins are widely used as corrosion prevention materials, for example in photocathodes [37]. Paraffins are stable up to approximately 250°C; therefore no boiling of the molten will result even at high operating temperatures. The viscosity is low in the liquid phase, which means low pressure loss in the flow process. Liquid paraffin is a non-polar liquid and therefore does not mix with polar liquids such as water or alcohol.

Unlike many other polymeric materials, paraffin materials are long-lasting and stable throughout phase change cycles, since there is no chemical reaction during the thermal energy storage process. Melting and solidification are purely physical processes which is why the paraffin actuation properties remain nearly constant throughout the actuator's working life. This section presents thermophysical properties of paraffin for use as an actuation material for microactuators.

3.1.1.1.1 Thermophysical Properties

Thermophysical properties of linear paraffin macromolecules have been studied by many researchers [38, 39, 40] and are essential to predict the thermal behavior of the microactuators developed in this research. Since the operation of the paraffin microactuators is based on melting and solidification of a sealed paraffin actuation layer, thermal characteristics in both solid and liquid states must be known. The kinetics of melting for crystalline structures has been well developed; however, far less information is available for linear macromolecules.

Specific Volume

The specific volume of paraffin, as with many polymers, is strongly temperature dependent. As paraffin is heated near its glass transition temperature, the material experiences a very small volumetric increase. When the material is heated beyond the

melting temperature a large volumetric increase occurs. This thermal expansion is due to the phase transition from the solid to liquid phase or melting of the material. Differences in volume between solid and liquid phases vary widely from negative values to as much as 40% when heated to temperatures ranging from 65 - 150°C depending on the length of the chain. For certain macromolecules with the planar zigzag conformation, a 15% volume change is typical.

Temperature and pressure dependent specific volume, sometimes referred as pressure-volume-temperature or PVT measurements, of the Logitech paraffin has been measured in an essentially isothermal mode of operation using high pressure dilatometry, a specialized measurement technique [41]. For certain temperatures below the melting temperature, the specific volume is not an equilibrium property. Thus requiring high pressure dilatometry to measure the change in specific volume as a function of pressure and temperature. The equilibrium specific volume of the liquid phase above the melting temperature can be easily measured by standard density measuring techniques. In the high pressure dilatometric measurements the temperature of the paraffin was fixed and starting from atmospheric pressure, pressures were increased to 200 MPa.

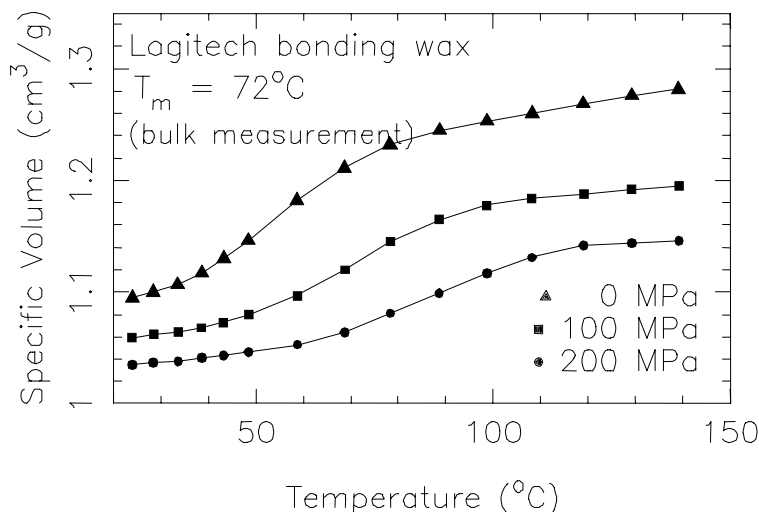


Figure 4: High pressure dilatometry measurements showing volumetric expansion characteristics of Logitech paraffin

Figure 4 shows the specific volume as a function of temperature and pressure for samples of the Logitech material. As the temperature is increased beyond the melting temperature, the material melts causing the volume to increase (density decreases). In the liquid state, the paraffin volume increases nearly linearly. Figure 5 shows the specific volume plot for a sample of pure tetratetracontane (Alfa Products, 98%) [41].

At the melting temperature T_m , the samples undergo a melting transition where the loss of crystal structure of the material leads to an equilibrium melt condition. At high temperatures the data pertain to an equilibrium melt. One of the major difficulties in PVT measurements of polymers is that the volume of a polymer does not, in general, depend only on the current temperature and pressure, but on previous history as well. Typically, hysteresis in the PVT measurements ranging from 1-6°C has been reported [39], but has not been measured in this work.

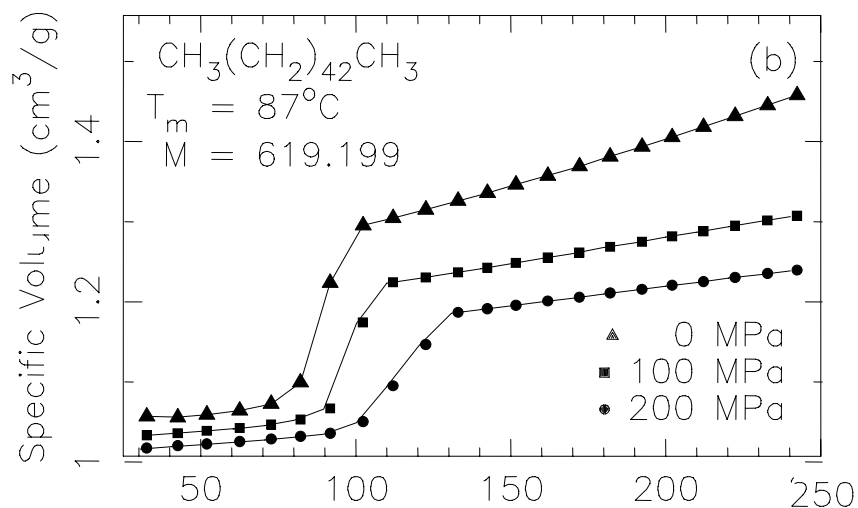


Figure 5: High pressure dilatometry measurements showing volumetric expansion characteristics for tetratetracontane 98% (Alfa Products)

Heat Capacity

The heat capacity of linear macromolecules has been studied by many researchers [35, 42, 43] and can be used to estimate nearly all other important thermophysical material properties. In general, the change in heat capacity on melting of paraffins is small. A large contribution to the heat capacity comes from the group vibrations, which are slightly affected by the phase change. A decrease in vibrational contributions on melting can result from changes to rotational and translational motion. This decrease is often compensated by contributions arising from potential energy increase and chain conformation changes.

Heat capacity has been measured for the Logitech paraffin using a Perkin Elmer DSC-7 Differential Scanning Calorimeter (DSC). Figure 6 shows the experimentally measured heat capacity of the Logitech paraffin for both heating and cooling scans. The DSC heating scan reveals two peaks. The first peak is very broad with maximum of 6.473 kJ/kg°C at 338.15K. The second peak maximum of 8.478 kJ/kg°C occurs at 352.15K. The first peak is very broad, at least 35°C, indicating a composition of materials with varying melting temperatures. This data corroborates the *smooth* volume increase as the material is heated beyond the melting temperature, as shown in Figure 4.

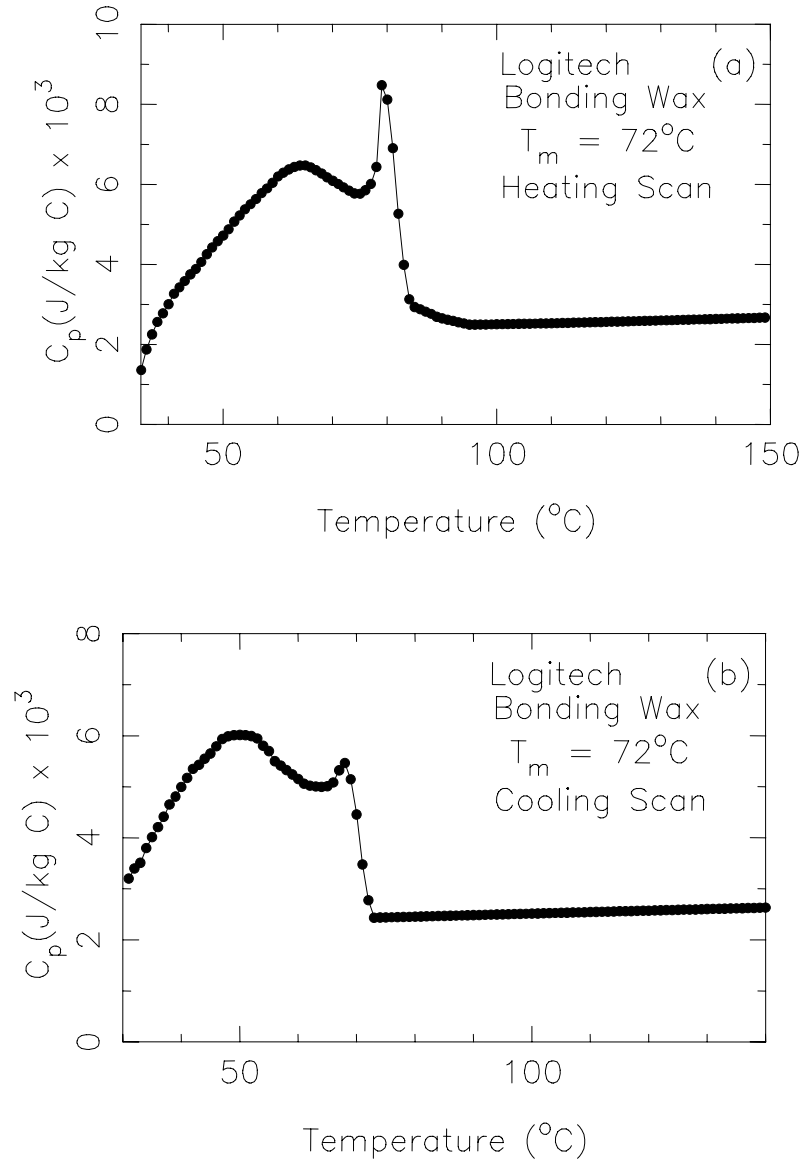


Figure 6: Measured heat capacity as a function of temperature for Logitech paraffin using Perkin Elmer DSC-7 differential scanning calorimeter (a) heating (b) cooling scans

The second peak is very narrow indicating a single paraffin-like material. The center temperature of the second peak is slightly higher than the measured transition temperature of 345.15K. This type of discrepancy is not uncommon in polymers. The melting temperature of paraffins, as with most polymers, can vary depending on many factors, including heating rate. The DSC cooling scan also reveals two peaks. The first peak is also very broad with maximum of 6.016 kJ/kg°C at 323.15K. The second peak maximum of 5.464 kJ/kg°C occurs at 342.15K. The difference in the center temperatures of 10°C between the heating and cooling scans is an approximation of the hysteresis in the Logitech material. This hysteresis is larger than reported values of 1°C for pure paraffin materials [39].

In contrast, the volume increase of pure paraffins heated beyond the melting temperature is very sharp at atmospheric pressure. Heat capacity measurements further support this as reported by [35] on high purity samples of hexatriacontane, tetratetracontane and polyethylene. Figure 7 shows heat capacity measurements for hexatriacontane in solid and liquid states as a function of temperature. The pure paraffin materials have a very narrow transition region, consequently, the measurements near the transition temperature are typically difficult to obtain.

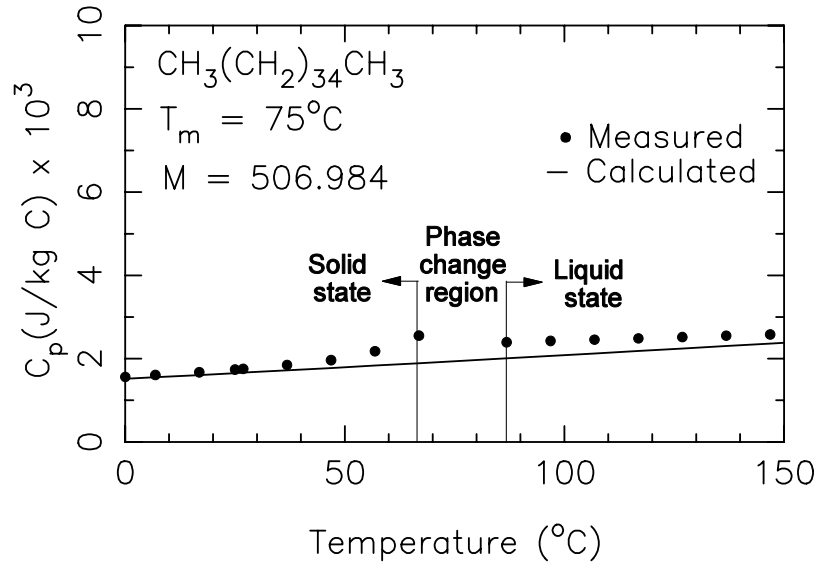


Figure 7: Measured heat capacity of hexatriacontane as a function of temperature

Latent Heat of Fusion

The change from one phase to another is accompanied by the evolution or absorption of a certain amount of heat, called the latent heat of transition. According to the conditions of equilibrium, such a transition occurs at constant pressure and temperature. The heat of fusion is the measure of heat content required to induce the phase transition from solid to liquid phase without increase in temperature. The heat of fusion can be calculated from heat flow measurements using differential scanning calorimetry. Table 2 lists calculated latent heat of fusion for paraffins [35] used in this research.

Table 2: Calculated latent heat fusion for various paraffins

| Paraffin | ΔH_f (kJ/kg) |
|-------------------|----------------------|
| Hexatriacontane | 175.21 |
| Tetratetracontane | 226.70 |

Thermal Conductivity

Most polymers are insulating systems, therefore, any electron effects are negligible and heat conduction occurs as a result of lattice vibrations. The simplified thermal conductivity for semicrystalline and amorphous polymers is proportional to the heat capacity [40], given by

$$\kappa(T) = 1/3 C(T) v(T) l \quad (1)$$

where $C(T)$ is the heat capacity per unit volume, $v(T)$ is average phonon velocity and l is the phonon mean free path. The velocity of sound can be estimated as

$$v(T) = \sqrt{E/\rho(T)} \quad (2)$$

where, E is Young's modulus and $\rho(T)$ is the paraffin density. Using a value of $v(T)$ equal to 19×10^5 cm/sec, and $C(T)$ and $\rho(T)$ from previous measurements and $l = 140 \text{ \AA}$ [40], the thermal conductivity of the Logitech paraffin can be estimated.

Thermal conductivity has been measured on samples of the Logitech paraffin using the ASTM-D 5930, standard transient line-source measurement technique. The AC Technology K-System-II was used for all measurements (system specifications: probe constant = 0.793, length = 50 mm, settling time = 45 seconds, equilibrium time = 1 minute, data acquisition time = 45 seconds and probe voltage = 3 volts). Prior to testing, the samples were dried at 70°C for 3 hours in a vacuum oven. The temperature was scanned from 28°C to 150°C . Figure 8 compares calculated and measured values of the thermal conductivity. The thermal conductivity increases monotonically to a value of about 0.203 W/mK at 137°C where it decreases and becomes approximately constant to a temperature of 150°C .

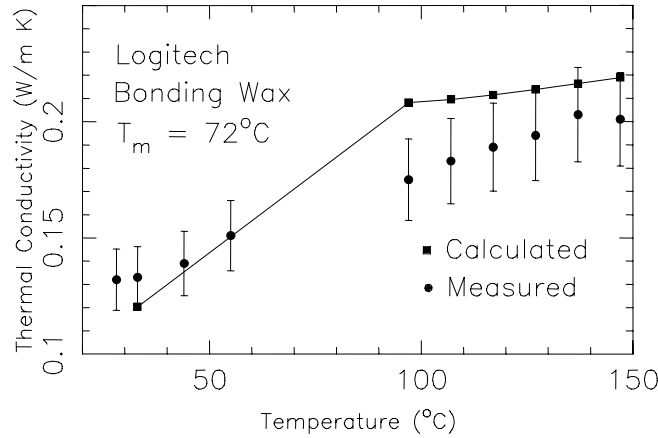


Figure 8: Calculated (solid line) and measured thermal conductivity as a function of temperature for Logitech paraffin

3.1.1.2 Parylenes

Parylene is a common name for a class of polymers called para-xylylene. Four forms of parylene are currently available. Each form represents the basic polymer backbone of xylylene with a replacement of 1-4 atoms in the ring. Parylenes have been used for many applications, such as intermetal dielectrics [40], and as an encapsulation method for microelectronic circuits [45]. The conformal deposition technique of parylene has facilitated its countless uses.

Parylene has made its way into micromachining in the last few years. The properties of parylene have been exploited in microfluidics [46, 47], microvalves [48, 49, 50], membrane filters [4], and many other micromachining applications. The chemical formula for parylene-C is shown in Figure 9. Parylene-C is produced from a basic linear molecule with the addition of a chlorine atom.

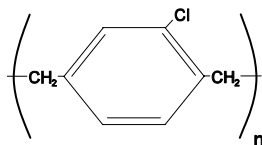


Figure 9: Parylene-C chemical structure

Thin vapor deposited parylene films have been used extensively as sealing and diaphragm layers for the all paraffin microactuators developed in this research. Prediction of the electrothermal behavior of the new microactuators requires the measurement of the device thermal boundary conditions. Since the sealed paraffin devices are electrothermally actuated, the measurable boundary parameters are the substrate and parylene diaphragm surface temperatures. Surface temperatures have been measured with a medium magnification infrared camera requiring absorption spectra for glass and thin parylene materials.

Optical Properties

Parylene-C (parylene) exhibits very little absorption in the visible region (400 - 800 nm) and is therefore transparent and colorless. The infrared absorption spectrum of parylene is shown in Figure 10. The spectra shown in Figure 10 were taken from an

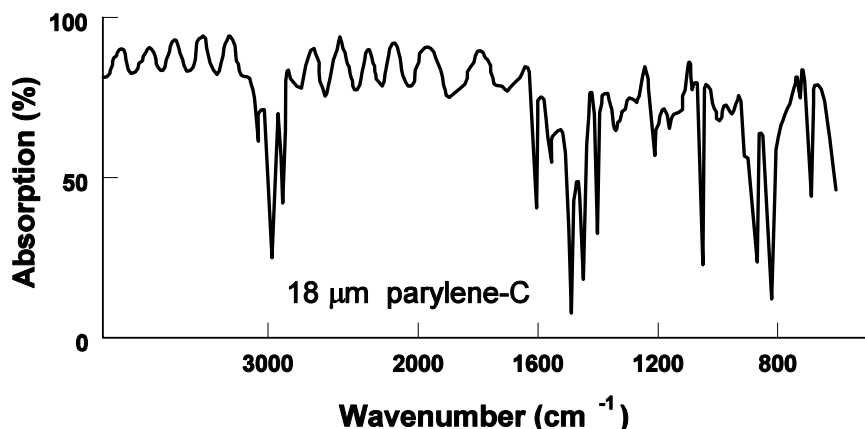


Figure 10: Infrared absorption spectra of an 18 μm thick Parylene-C film

18 μm thick parylene film. Although the energy absorption is dependent on film thickness, these measurements are useful for roughly predicting the optical properties of the films. The surface temperature of the parylene diaphragm of the paraffin microactuator was measured with an infrared camera, requiring emissivity of the parylene film. Kirchoff's law, which equates the spectral absorption and emissivity, was utilized.

3.1.2 Process Technology

The process technologies used to fabricate surface micromachined polymer microdevices are presented in this section. First, processing techniques for depositing thin polymer films are discussed. Thin paraffin films, which are used for the actuation layers, are thermally evaporated in high vacuum. Thin parylene films are used as the sealing and diaphragm layers for the paraffin microactuators, and as the structural layers of some of the microchannels used for microvalve testing. Parylene films have been deposited in a

commercial vacuum pyrolysis system. Techniques for etching both polymer films in conventional reactive ion etching (RIE) systems are discussed. Both polymer films have been etched in oxygen and oxygen:tetrafluoromethane plasmas and will be discussed in later sections.

Microchannels have also been fabricated using thick deposits of nickel from a nickel sulfamate electrolytic solution. Techniques for electrodepositing thick nickel layers and appropriate deposition seed layers are discussed. The blocking microvalves fabricated in this research require access holes through the substrate (both glass and silicon). Through substrate access holes in glass have been fabricated using photodefinable glass substrates (Foturan, Schott Glass, Inc.). Access holes in silicon have been made using deep reactive ion etching (DRIE). Finally, general techniques for low temperature processing are discussed.

3.1.2.1 Deposition of Thin Polymer Films

The deposition of thin films from polymers can be carried out using a number of techniques which include polymerization of a monomer from a glow discharge, deposition from solution, deposition from bulk polymer by thermal evaporation, deposition from bulk polymer by radio frequency sputtering, or deposition and polymerization of monomers from vacuum pyrolysis of a suitable dimer material.

3.1.2.1.1 Paraffin Deposition

Thin paraffin films have been deposited by thermal evaporation. Paraffin materials can easily be evaporated due primarily to their high vapor pressures. The chamber pressure was maintained at $< 5 \times 10^{-6}$ Torr as measured with an ionization gauge. The paraffin samples were evaporated from quartz mounted in a tungsten crucible holder. Figure 11(a) shows the thermal evaporator constructed for this research.

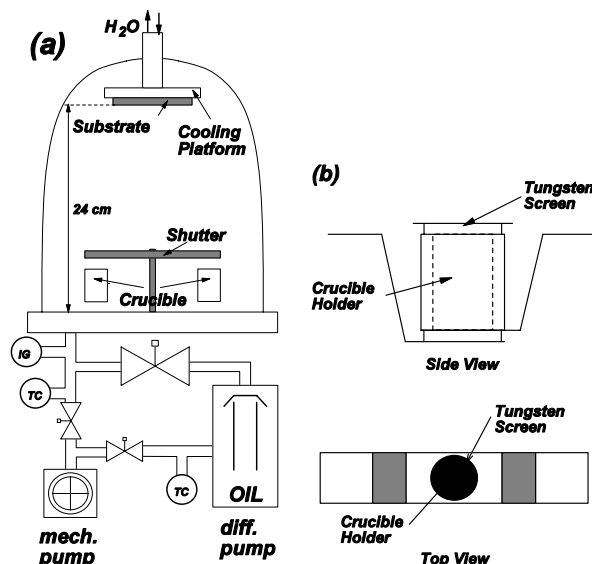


Figure 11: a) Thermal evaporator constructed for this research (b) modified crucible holder eliminating polymer splashing

Contamination of the thin deposited film, by large solid spheres, when evaporating paraffin is due to the boiling action of the molten paraffin. Smooth, contamination free,

thin paraffin films have been obtained by choosing a low evaporation temperature and consequently a low deposition rate. Figure 11(b) shows the modified crucible holder which eliminates splashing of the polymer onto the substrate. All paraffin evaporations were done in a custom built deposition system with 5×10^{-6} Torr chamber pressure, 150°C material temperature with a deposition rate of about 1000 Å/min. Figure 12 shows images of a 4 µm thick logitech film scanned with a Digital Instruments Nanoscope IIIa atomic force microscope (AFM) in tapping mode. The surface roughness (R_a) measurements were without plane fitting the scanned surface. Typical surface roughness of the evaporated paraffin of 420 Å and less has been measured.

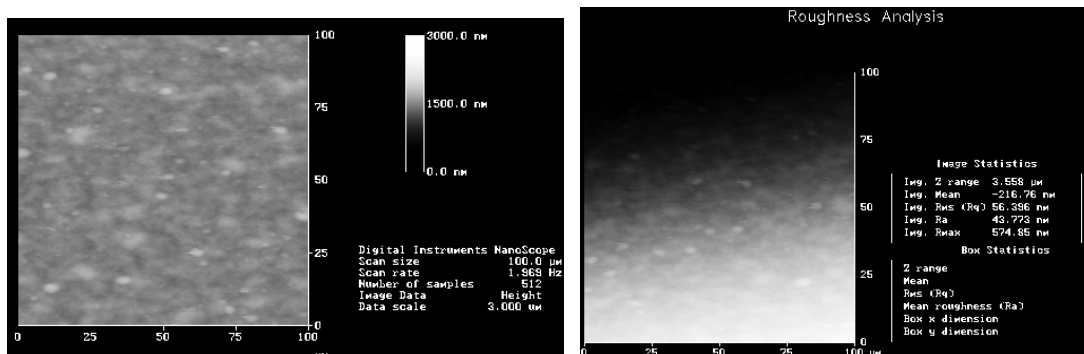


Figure 12: 100 x 100 µm² tapping mode AFM scan (a) example of scanned surface (b) example of average surface roughness measurement

3.1.2.1.2 Parylene Deposition

Parylene polymers are vapor deposited at room temperature in a commercial pyrolysis deposition system. Figure 13 shows a diagram of the deposition process. The solid parylene dimer is first sublimated at 120-150°C. The dimer is subsequently split into two monomers in a pyrolysis furnace at 680-720°C. The monomers will then polymerize on surfaces below room temperature. Since the deposition chamber pressure is maintained around 100 mTorr, the deposition is conformal.

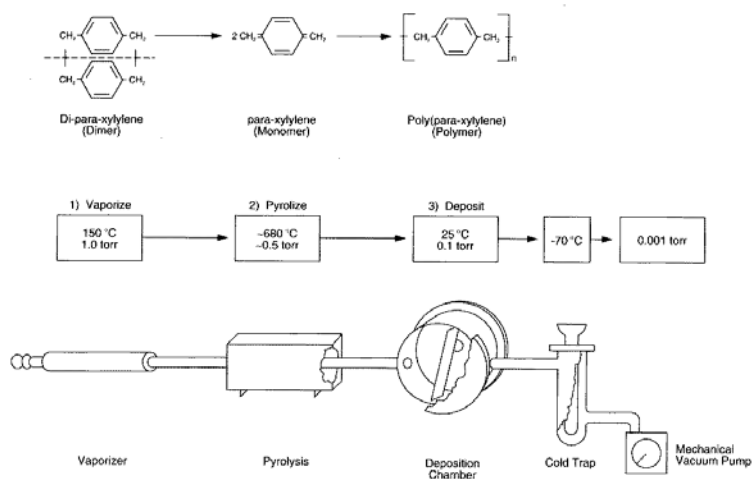


Figure 13: Vacuum deposition process of parylene

Adhesion

Adhesion of parylene is greatly improved by the silanation of silicon dioxide and silicon nitride surfaces. While the silanation of silicon itself will improve parylene adhesion, parylene adheres better to the silicon dioxide and silicon nitride films. Silanation can be performed by different methods, but the following method is preferred. First, a small bottle of 50 ml DI, 50 ml IPA, and 5 ml A174 silane is prepared. The solution is allowed to mix overnight. Wafers are cleaned in IPA for 10 minutes, spin dried and baked at 100°C for 5 minutes. A towel is attached to the baffle of the parylene deposition system. The towel is soaked with one pipette full of mixed silane solution (10 ml). Wafers are loaded into the parylene machine and the deposition cycle is initiated. The wafers are coated with the adhesion promoter solution as the chamber evacuates.

Adhesion of parylene to most polymers is improved by exposing the polymer surface to a short oxygen plasma. This plasma treatment etches the surface of the polymer and exposes active polymer sites for parylene to bond to. For parylene to adhere well to other parylene layers this plasma treatment is necessary. The plasma treatment parameters typically used are a 200 mTorr O₂ plasma at 100 W for 1 minute.

Stripping photoresist layers on top of parylene can be problematic. Resist strippers like PRS2000 (Microposit, Inc.) tend to soften the parylene films. Delamination of parylene and other films deposited on top can result. Therefore resist must be removed with acetone only. This restriction limits resists to be softbaked only. Softbaked resists (90°C) can easily be removed with acetone. However, hardbaked (110°C) photoresists may not be completely removed with acetone and could leave a thin residue film upon removal. Likewise, RIE etching times of parylene films with photoresist masks may be limited due to heating of the substrates.

3.1.2.1.3 Nickel Electrodeposition

Microchannels in this research are formed from thick deposits of nickel from a nickel sulfamate electrolytic solution (Barrett SN, MacDermid, Inc.). Electrodeposition of metal films on conducting surfaces occurs due to an oxidation-reduction process in metal ionic solutions. The nickel sulfamate solution contains nickel ions Ni²⁺ in addition to a constant metal ion supply from a solid nickel anode ($\text{Ni} \rightarrow \text{Ni}^{2+} + 2\text{e}^-$). The cathode is the deposition surface. The nickel sulfamate electrolytic solution has been used to electrodeposit films for the structural layers of microvalves developed in this research. An additional 15 g/L of boric acid is used to adjust the pH of the solution at the deposition temperature of 50°C. A sulfur depolarized nickel anode was used to ensure maximum corrosion of the anode.

Electrodeposition Seed Layers

The electrodeposition seed layer is a thin metallic film providing conduction for the metal ions to the deposition surface. For high quality electrodeposited films, the seed layer surface must be free from contamination. The seed layers are chosen based on material properties which closely match with the deposited films. The seed layer must have a higher standard electrode potential than the deposited layer. Since the nickel has a standard electrode potential of -0.25 volts, the seed layer electrode potential must be greater than this value. Additionally, the seed metal lattice constant should match reasonably well to that of the electrodeposited layer. Nickel has a face centered cubic (FCC) structure and lattice constant $a = 3.524 \text{ \AA}$. Electrodeposited nickel films in this

research use a 3000 Å thick gold seed layer and a 500 Å thick titanium adhesion layer to improve the adhesion of gold to either glass or silicon substrates.

Electroforming Micromold

Electrodeposition molds are fabricated using thick patterned photoresist. The gold seed layer is first cleaned in acetone and deionized (DI) water rinse followed by spin drying. The substrates are then baked in a convection oven for 15 minutes to remove moisture from the surface. First, a hexamethyldisilazane (HMDS) adhesion layer is spin coated in the seed layer. A 20 µm photoresist (AZ 9260, Clariant, Inc.) layer is spin coated on the substrate. The photoresist is then softbaked, exposed and developed. The entire substrate is then descummed in an O₂ plasma. The nickel film is then deposited onto the seed layer.

Seed Layer Removal

The seed layer is removed using an iodide based wet etchant (GE 8148, Transene, Inc.) which minimally affects the electrodeposited nickel film. The titanium adhesion layer is removed with a dilute hydrofluoric acid (HF) solution.

3.1.2.1.4 Electrochemical Deposition of Conductive Polymers

The abbreviation ECD applies to both electrochemical and chemical plating processes. Although in chemical plating (usually referred to as electroless plating) an external supply of "electrons" is not necessary, it is still an electrochemical process. For all types of ECD batch processing, the electrolytes are usually operated at temperatures from room temperature to about 90°C, which helps to reduce equipment needs as well as costs in general. Operating temperatures close to room temperature will reduce the problems originating from differences in thermal expansion (between Si and most metals), that are known from other deposition techniques.

Basic Electrochemistry

An electrochemical reaction is a chemical reaction in which transfer of electrons from one species (called Red for reduced) generates another (called Ox for oxidized). If the number of electrons involved in the reaction is called z, this can be expressed as:



Such a reaction is called a half-cell reaction, because the electron "donor" reaction must have an "acceptor" counterpart - since free electrons can not exist in the electrolyte. Consider an electrochemical cell consisting of two electrodes submerged in an electrolyte. If z electrons are transferred, the two half-cell reactions would be:



As indicated by the double arrows used in all the equations, the electrochemical reactions can move in both directions depending on the activity (concentration) of the species involved, the temperature and the standard electrode potentials. When an external

potential is applied (outside power supply or battery) the "concentration" of electrons will increase. If we look at the right half-cell reaction above, it will move towards B^0 (to the right) as the number of available electrons is increased. When no external potential is applied to the cell, the electromotive force, E , depends on the activity of the different species as expressed in the Nernst equation:

$$E = E_{right} - E_{left} = E^0 + \frac{RT}{zF} \ln \left[\frac{ox}{red} \right] \quad (6)$$

The electromotive force will tell us the direction of spontaneous reaction. When E is greater than 0 the reaction will move to the left (B will dissolve) and when E is less than 0 the reaction will move to the right (A will dissolve). E^0 is the standard electromotive force for the entire system (two half-cells). E_{left} and E_{right} are the electromotive forces for each of the two half-cells.

In order to calculate the electromotive force of a cell, it is usually more convenient to focus on the difference between the half-cells, that is:

$$E = E_{right} - E_{left} = E_{right}^0 + \frac{RT}{zF} \ln \left[\frac{ox_{right}}{red_{right}} \right] - E_{left}^0 + \frac{RT}{zF} \ln \left[\frac{ox_{left}}{red_{left}} \right] \quad (7)$$

Applying the general reactions from the two half-cells above we get:

$$E = E_{right} - E_{left} = E_{right}^0 + \frac{RT}{zF} \ln \left[\frac{B^{z+}}{B^0} \right] - E_{left}^0 + \frac{RT}{zF} \ln \left[\frac{A^{z+}}{A^0} \right] \quad (8)$$

The activity of solid metals and other pure compounds (like water, etc.) is 1 by definition. When R is 8.3144 J/mole·K, T is 298 K (room temperature), F is 96487 C/mole and we use that $\ln(x) = \ln(10) \cdot \log(x) = 2.3026 \cdot \log(x)$ we get:

$$E = E_{right} - E_{left} = E_{right}^0 + \frac{0.0592}{z} \ln \left[\frac{B^{z+}}{A^{z+}} \right] \quad (9)$$

In most diluted solutions the activity of an ion is equal to the concentration. The two standard electrode potentials, E_{right}^0 and E_{left}^0 , can be found in the literature for most half-cell reactions. They have been measured experimentally at standard conditions versus the Standard Hydrogen Electrode (SHE). By definition, the standard electrode potential of this half-cell reaction:



is set to zero. Using this electrode (and a rather complicated set-up) as the left electrode, it is possible to measure a relative potential of any electrode on the right versus the SHE.

Polypyrrole Deposition

Polypyrrole (PPy) is an electrically conductive polymer that can be polymerized electrochemically and deposited onto electrodes. The ease of preparation, inherent electrical conductivity, controllability of surface properties, and compatibility with mammalian cells make polypyrrole an attractive candidate for biomedical applications. Additionally, when polypyrrole is in its oxidized state, it exists as a polycation with delocalized positive charges along its conjugated backbone. In order to neutralize this charge, counter ions in the solution are incorporated into the polypyrrole film during electrochemical deposition. The conductivity, morphology, and stability of polypyrrole vary significantly when the counter ions are changed. When a polyelectrolyte having negative charges serves as the counter ion, it is incorporated into the polymer through the reaction shown in Figure 14, where PE^- stands for polyelectrolyte. Based on this mechanism, bioactive species, such as DNA, heparin, poly (hyaluronic acid), proteins, nerve growth factors, and even red blood cells have been patterned onto electrode sites together with the electrically conductive polypyrrole.

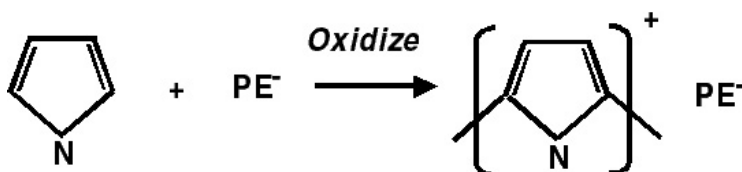


Figure 14: Electrochemical polymerization reaction

Electrochemical polymerization has many advantages over other methods in the surface modification for biomedical applications. The method can be used on many different electrically conductive surfaces, whereas chemical attachment techniques are usually limited to a few substrate choices. The coating can be precisely patterned specifically onto the active site of the electrode without covering the nonfunctional areas of the device. The deposition of organic and biologic species does not compromise the electrical functionality of the electrode since the coating material is electrically conductive. Actually the signal transport can be enhanced because of the unique surface morphology of the coatings.

ECD of Polypyrrole doped with proteins

Any polyelectrolyte with negative charge can serve as a counter ion and will be incorporated into polypyrrole by the reaction shown earlier. Bioactive species like proteins serve as excellent polyelectrolytes. However the conductivity, morphology and stability of the polypyrrole varies significantly with the counter ion. Most ECM proteins are good polyelectrolytes and can be incorporated into polypyrrole. In this section we discuss the incorporation of ECM proteins, like collagen, by electrochemically polymerizing polypyrrole on gold electrodes in microfluidic channels. Laminar flows can be used to pattern only specific sections of the electrode. This technique will be particularly useful in cell culture applications where precise patterning of proteins is essential for cell attachment. Proteins can be specifically patterned and then the top channel structure, which is made of a soft elastomeric epoxy, is lifted off and the bottom substrate with the patterned protein can be used for applications like cell culture.

Cyclic Voltammetry

During deposition there is a reversible redox reaction in the polypyrrole film. The redox reaction involves the charging and discharging of polypyrrole and is also accompanied by movement of ions. Because the oxidized state and reduced state have very different electrical properties, this redox reaction provides a switching ability to the doped polypyrrole films. Cyclic voltammetry shows the intrinsic redox reaction of the electrode material as the potential of the electrode is swept in a cyclic manner. No redox reactions occur at the gold electrode, but the switching ability of polypyrrole was demonstrated. Within a cycle of voltage sweeping, there are two peaks (one anodic and one cathodic) at potentials of -0.14 and -0.56 V, which are indications of oxidation and a reduction reaction of PPy/PSS respectively. The redox reaction was accompanied by the movement of small cations in and out of the film. Additionally, the interaction between the polypyrrole and the large dopant molecules were changed upon each reaction, as were the electronic properties of the film. CV was also performed to determine if PPy/Collagen and PPy/BSA were electrochemically active. PPy/BSA did not show redox peaks which are an indication that PPy/BSA is not electrochemically active. On the other hand, PPy/Collagen is electrochemically active and shows two redox peaks at -0.2 and 0.1 V. The electrodes were swept between 0.5 to -0.9 V, the electrode area was 0.002 mm² and the scan rate was 100 mV/sec. The results are detailed in Figure 15.

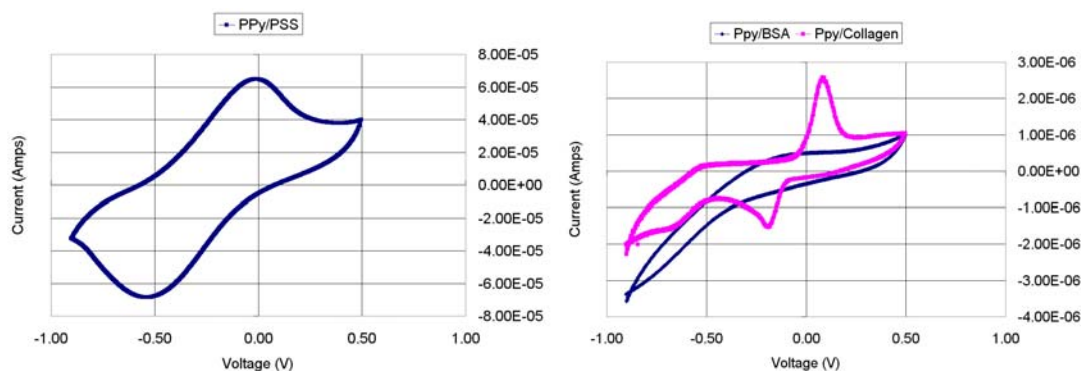


Figure 15: Cyclic Voltammetry of PPY/PSS and PPY/BSA, PPY/Collagen swept between 0.5 and - 0.9V

3.1.2.2 Etching of Thin Polymer Films

The literature contains many examples comparing etching behaviors for different polymers. These comparisons have been made for etching polymers in pure oxygen plasmas and for plasmas using pure tetrafluoromethane (CF₄) or methane (CH₄) with the addition of molecular oxygen (O₂).

The addition of fluorine containing gases, such as CF₄ is known to increase the oxygen atom concentration relative to that obtained in pure O₂ plasmas. The observed increase in fluorine atom concentration in gas feed mixtures rich in CF₄ has been proposed to be the result of either the reaction between oxygen and the dissociated products of CF₄ or the reaction between electronically excited metastable oxygen molecules and CF₄ [52, 53]. The authors [54] reported a model to explain the products which are observed downstream from a CF₄-O₂ plasma.

Etching rate dependence on $\text{CF}_4\text{-O}_2$ gas feed composition for several different polymers in several different systems have been reported [52] from several researchers. Figure 16 shows etching rate behavior for three polymer films in various $\text{CF}_4\text{-O}_2$ gas compositions [55].

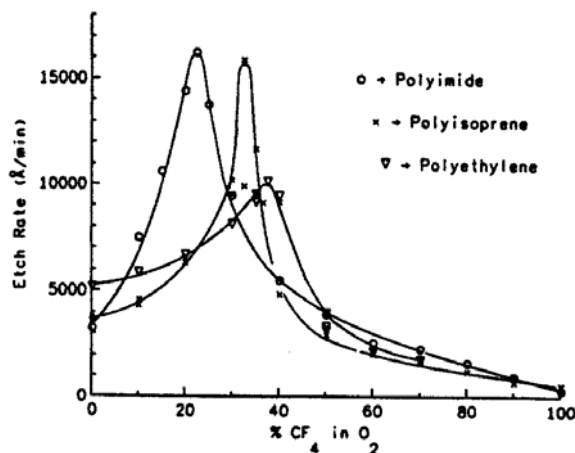


Figure 16: Etching rate behavior for $\text{CF}_4\text{-O}_2$ plasma for RF planar diode etching system

The etch rate for polyethylene is of importance in this research. Polyethylene has essentially the same chemical make up as paraffins with an ultra long chain length. A peak etch rate of about 1 $\mu\text{m}/\text{min}$ was reported for a 37.5% composition of CF_4 in O_2 with 350 mTorr chamber pressure, 72 sccm total flow and 37.5% CF_4 in O_2 gas ratio, and 700 Watt electrode power.

3.1.2.2.1 Paraffin Etching

Two different RIE systems have been used to etch paraffin. Two paraffin films, Logitech and n-hexatriacontane, have been characterized. An Applied Materials 8300 RIE system has been used to etch thin paraffin films using a 260 mTorr chamber pressure, 20:80 sccm ($\text{CF}_4\text{:O}_2$) gas feed, and 1100 W (RF) electrode power level (hexode system). An average etch rate of 1000 $\text{\AA}/\text{min}$ has been measured. In addition, a Semi-Group 1000 TC/CC RIE planar electrode system, has been used to etch the paraffin films using a 300 mTorr chamber pressure, 27:45 sccm ($\text{CF}_4\text{:O}_2$) gas feed composition, and 70 W (RF) electrode power. Significantly lower power levels are necessary such that the paraffin does not melt during etching. Etch rates between 2500-3000 $\text{\AA}/\text{min}$ have been measured. The single most important aspect of the RIE system is that the bottom electrode, where the substrate is mounted, must be maintained at or below room temperature preventing the paraffin from melting during processing.

3.1.2.2.2 Parylene Etching

Two different RIE systems have been used to etch thin parylene films. An Applied Materials 8300 RIE system has been used to etch the parylene films using a 260 mTorr chamber pressure, 100 sccm O_2 gas feed, and 1100 W (RF) electrode power level (hexode system). An average etch rate of 2000 $\text{\AA}/\text{min}$ has been measured. In addition, a Semi-Group 1000 TC/CC RIE planar electrode system, has been used to etch the parylene films using a 100 mTorr chamber pressure, 100 sccm O_2 gas feed composition,

and 200 W (RF) electrode power. Etch rates between 2500-3000 Å/min have been measured.

3.1.3 Cell Attachment

Mechanisms by which cells recognize certain substrates as suitable for attachment and growth has been an important topic of study to understand cell proliferation and differentiation. Cell adhesion is mediated by cell membrane bound receptors. In particular, integrins, a family of heterodimeric transmembrane proteins that are linked to the cytoskeleton on the cytoplasmic side of the membrane, recognize specific peptide sequences present in the fibrillar protein meshwork found in vivo and known as the ECM. Integrins establish mechanical links between the membrane and the ECM substrate and also between the ECM and the cytoskeleton. Integrins aggregate in organized structures termed focal contacts. In most cell types, biochemical signals essential for cell growth, function, and survival are initiated by integrins upon attachment. Failure of integrins to attach causes the cell cycle to end resulting in apoptosis [249]. Since many cell types secrete ECM, an artificial substrate is capable of supporting cell adhesion even if it is not initially coated with an ECM protein. Success in creating cellular micropatterns depends on the ability to control the size, geometry, and chemical nature of the adherent layer. Cells are sensitive to other physical parameters of the substrate, such as local temperature, which may be used for selective attachment of cells to surfaces. Materials other than physiological biomolecules were the first to be explored owing to the constraints imposed by early micropatterning techniques. Initially, micropatterning techniques involved micro patterns of metals and polymers. With the emergence of more flexible microfabrication techniques, ECM proteins, peptides with RGD sequences for cell attachment and bioactive molecules have been micropatterned. The following section is a detailed review about the existing techniques for micropatterning proteins.

3.1.3.1 Micropatterning Proteins for Cell Attachment

Many researchers have tried a variety of different techniques to create protein micro patterns for cell culture. Physisorbed protein layers are not stable in aqueous solutions. Also, proteins present in the medium or secreted by the cells after attachment may displace an underlying protein layer. Many researchers have focused on the chemical immobilization of proteins via cross-linkers or photoreaction schemes. Even though chemical (or physical) immobilization of proteins is likely to induce partial denaturation of the protein structure, which can affect cell function, the peptide sequences necessary for attachment seem to remain largely exposed. Denaturation is to be expected when the micropattern is exposed to solvents during the micropatterning step. It is still found that cells attach, spread, grow, and function on denatured ECM proteins, either physisorbed or chemisorbed, because denaturation does not affect integrin binding. It is believed that protein adhesiveness correlates with the hydrophobicity of the surface. But, neither very hydrophilic surfaces, such as agarose gels, nor very hydrophobic surfaces, such as Teflon, support protein adhesion. Even though physisorbed protein layers may elute from the surface as a function of time, physisorption procedures promoting cell attachment are simple and have been used in cell culture on a variety of materials. Protein physisorption onto polymers may be enhanced by plasma polymerization or plasma glow discharge (e.g. the tissue culture-grade polystyrene petri dishes) of the polymer surface.

These treatments introduce a rich variety of chemical functionalities that attract proteins through electrostatic or dipolar interactions.

3.1.3.2 Lithography and Stencil Patterning

Letourneau and colleagues created the first biomolecular micropatterns based on the fact that cell adhesiveness of laminin could be inactivated by selective UV irradiation through a metal stencil. Most existing microfabrication and micropatterning techniques use photolithography. Photoresist is first patterned by exposure to light and then developed leaving patterned areas. Metals like gold, which are excellent for protein attachment, are then evaporated on the substrate followed by dissolving the photoresist which results in a liftoff to create islands or features with metals. The whole process involves several steps; however, treatment with an alkaline or organic solution to dissolve the photoresist is incompatible with patterning proteins or cells. Photolithography involves the use of solvents. Elastomeric stencils may be used to mask the physisorption of protein or the direct attachment of cells on a surface. The elastomeric membranes can be used to provide patterned access to the surface. After patterning, the membranes can be physically lifted off the substrate. Stencils are convenient for patterning cell types, such as fibroblasts, which feature poor adhesiveness and selectivity, and for patterning cells on homogeneous surfaces. Multiple materials can be patterned using multiple, stacked membranes.

3.1.3.3 Micro-contact Printing

Another way to eliminate the problems associated with photoresist removal is to use metal and elastomeric microstamps for micropatterning ECM proteins followed by cell attachment and culture. The general procedure for micro-contact printing involves inking the stamp with a solution of the substance to be printed. As the solvent (ethanol) evaporates, the protein is deposited on the relief structure. The stamp is then brought into conformal contact with the surface for a predetermined period of time. On removing the stamp from the surface, a pattern is left that is defined by the features on the stamp. Rudolph [264] fabricated microtextured surfaces with deep trenches in a variety of biomedical polymers and selectively physisorbed proteins onto the mesas by carefully dipping the microstructures in a protein solution. As a result, only the mesas, and not the trenches, were coated with protein solution. With this method, cells with fibronectin coated PDMS mesas were created.

3.1.3.4 Patterning using Laminar Flows

In microfluidic systems with micrometer sized channels it is almost impossible avoid laminar flows. Reynolds number is a dimensionless parameter that determines the type of flow of the liquid. Laminar conditions in a fluid are obtained at low values of velocity, diameter of the capillary, and density of the liquid; and high values of viscosity. Fluids are said to flow in the laminar regime if the Reynolds number is < 2000 . Because the diameter of the channels is small for microfluidic systems, Reynolds numbers are typically 0.1–1 for the commonly used flow rates. Channel systems, in combination with laminar flow, can be used to pattern material onto a surface from solution. Delamarche [265, 266] used multiple, adjacent channels to pattern proteins onto a surface and to direct chemical reactions on surfaces. The system uses small volumes of reagents and

may be useful in immunoassays. Laminar flow of liquids can be used to generate simple patterns of proteins and cells inside a channel.

Precise patterning of the area of deposition can be achieved using multiple streams, which flow in the laminar flow regime. As explained earlier, the streams do not mix and are well defined. The first experiment done was to achieve precise deposition of PPy/Collagen by supplying the second of the three inlet reservoirs with the polyelectrolyte and supplying the other two reservoirs with PPy/BSA (electrochemically inactive). This results in three streams in the main channel, BSA/Collagen/BSA. Deposition occurs only on parts of the electrode which is in contact with the PSS stream. Deposition was done at 2 mA/cm^2 and Figure 17a shows the precisely patterned ECD of PPy/Collagen. The experiment was done again but the order of the streams was modified to be Collagen/BSA/Collagen and deposition was achieved at the two ends of the electrode. Figure 17b shows the results obtained.

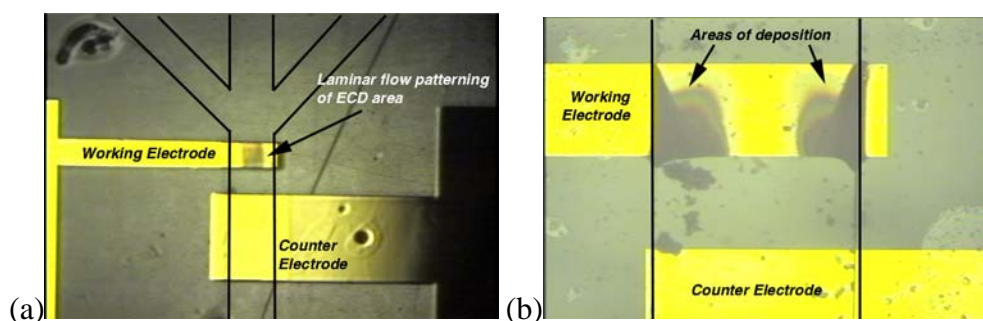


Figure 17: Patterned ECD of protein doped conductive polymers using laminar flow patterning

3.1.3.5 Deposition of PPy/PSS and PPy/Collagen

Initial experiments were performed to characterize the deposition of PPy/PSS (0.3 mg/ml, 0.3 mg/ml, pH 7 buffer), PPy/BSA (0.3 mg/ml, 0.3 mg/ml, pH 7 buffer) and PPy/Collagen (0.3 mg/ml, 0.3 mg/ml, pH 7 buffer), which were supplied to the electrodes through microchannels. The reservoirs were filled with the polyelectrolyte, which then completely filled the channel structure. A pump was used to ensure continuous flow over the electrodes and avoid bubble formation due to the electrochemical reaction. From the cyclic voltammetry plots, the minimum deposition current was determined. The area of the working electrode is 0.0045 cm^2 . For PPy/PSS the minimum deposition current is 0.5 mA/cm^2 and for PPy/Collagen the minimum deposition current is 1.5 mA/cm^2 . A femtostat setup was then used to maintain a constant current supply of 0.9 mA/cm^2 for PPy/PSS and 2 mA/cm^2 for PPy/Collagen, respectively. Deposition on the working electrode is observed. Figure 18 shows deposited PPy/PSS and PPy/Collagen layers using the fabricated device. The channel was continuously flowed with the polyelectrolyte at $20 \text{ } \mu\text{l/min}$ to avoid bubble formation. The flow was controlled by the use of a syringe pump.

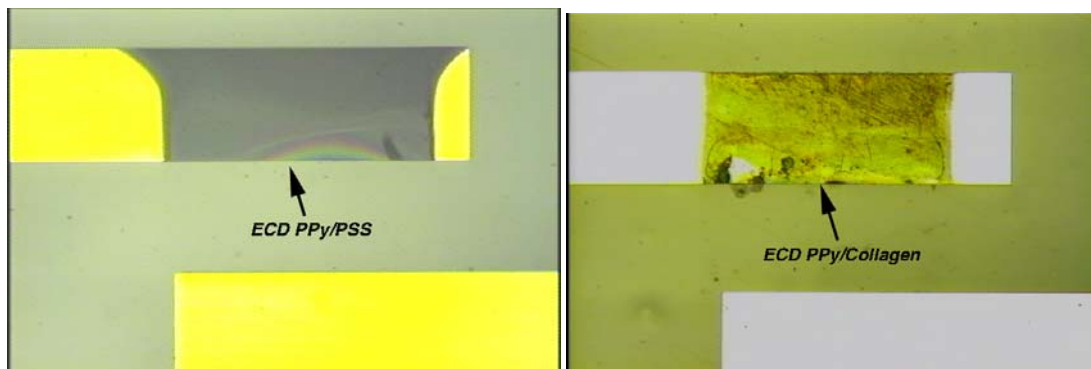


Figure 18: ECD of PPy/PSS and PPy/Collagen on fabricated device

3.2 Bulk Micromachining

3.2.1 Materials

3.2.1.1 Epoxy

Epoxy resin is defined as a molecule containing more than one epoxide group. The epoxide group also termed as, oxirane or ethoxyline group, is shown in Figure 19.

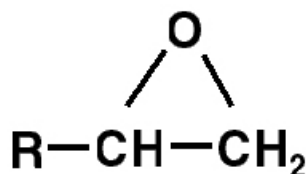


Figure 19: The structure of an epoxide group.

These resins are thermosetting polymers and are used as adhesives, high performance coatings, and potting and encapsulating materials. These resins have excellent electrical isolation properties, low shrinkage, good adhesion to many metals, good resistance to moisture, and both thermal and mechanical shock. Viscosity, epoxide equivalent weight and molecular weight are the important properties of epoxy resins.

3.2.1.1.1 Types of Epoxy resins

There are two main categories of epoxy resins, namely the glycidyl epoxies and non-glycidyl epoxies. The glycidyl epoxies are further classified as glycidyl-ether, glycidyl-ester and glycidyl-amine. The non-glycidyl epoxies are either aliphatic or cycloaliphatic resins. Glycidyl epoxies are prepared via a condensation reaction of appropriate dihydroxy compound, dibasic acid or a diamine and epichlorohydrin. While, non-glycidyl epoxies are formed by peroxidation of olefinic double bond. Glycidyl-ether epoxies such as, diglycidyl ether of bisphenol-A (DGEBA) are most commonly used.

Diglycidyl Ether of Bisphenol-A (DGEBA)

Diglycidyl ether of bisphenol-A (DGEBA) is a typical commercial epoxy resin and is synthesized by reacting bisphenol-A with epichlorohydrin in presence of a basic catalyst.

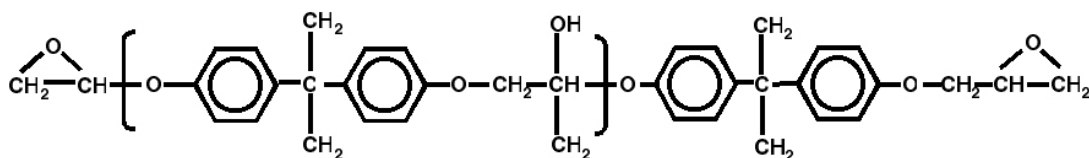


Figure 20: The structure of Diglycidyl ether of bisphenol-A.

Casting epoxy resins are glycidyl ethers of phenolic epoxy resins. Phenols are reacted in excess, with formaldehyde in presence of acidic catalyst to produce phenolic novolac resin. Casting epoxy resins are synthesized by reacting phenolic novolac resin with epichlorohydrin in the presence of sodium hydroxide as a catalyst. Casting epoxy resins generally contain multiple epoxide groups. The number of epoxide groups per molecule depends upon the number of phenolic hydroxyl groups in the starting phenolic epoxy resin, the extent to which they reacted and the degree of low molecular species being polymerized during synthesis. The multiple epoxide groups allow these resins to achieve high cross-link density resulting in excellent temperature, chemical and solvent resistance. Casting epoxy resins are widely used to formulate the molding compounds for microelectronics packaging because of their superior performance at elevated temperature, excellent moldability and mechanical properties, superior electrical properties, and heat and humidity resistance.

3.2.1.1.2 Curing Agents (Hardeners)

A wide variety of curing agents for epoxy resins is available depending on the process and properties required. The commonly used curing agents for epoxies include amines, polyamides, phenolic resins, anhydrides, isocyanates and polymercaptans. The cure kinetics and the T_g of cured system are dependent on the molecular structure of the hardener. The choice of resin and hardeners depends on the application, the process selected, and the properties desired. The stoichiometry of the epoxy-hardener system also affects the properties of the cured material. Employing different types and amounts of hardener control the cross-link density and the structure. The amine and phenolic resin based curing agents, described below, are widely used for curing of epoxy resins.

3.2.1.1.3 Amine Based Curing Agents

Amines are the most commonly used curing agents for epoxy cure. Primary and secondary amines are highly reactive with epoxy. Tertiary amines are generally used as catalysts, commonly known as accelerators for cure reactions. Use of excessive amounts of catalyst achieves faster curing, but usually at the expense of working life, and thermal stability. The catalytic activity of the catalysts affects the physical properties of the final cured polymer.

3.2.1.1.4 Phenolic Hardener

Epoxy resins when cured with a phenolic hardener, give excellent adhesion, strength, and chemical and flame resistance. Phenolic cured epoxy systems are mainly used for encapsulation because of their low water absorption, excellent heat and electrical resistance. An accelerator is necessary for the complete cure to occur.

3.2.1.1.5 Toughening of Epoxy Resins

The usefulness of epoxy resins in many engineering applications is often limited by their brittle nature and poor thermal conductivity. The term toughness is a measure of material's resistance to failure i.e. the total amount of energy required to cause failure. There are several approaches to enhance the toughness of epoxy resins which includes: chemical modification of the epoxy backbone to make it a more flexible structure, increasing the molecular weight of epoxy, lowering the cross-link density of matrix, incorporation of dispersed toughener phase in the cured polymer matrix, and incorporation of inorganic fillers into the neat resin. Amongst these approaches, toughening via dispersed toughener (flexibiliser) phase has been shown to be most effective. The flexibilisers can be reactive or non-reactive rubber.

3.2.1.1.6 Toughening Agents

Various types of thermoplastic polymers as well as reactive rubbers are employed to enhance the toughness of epoxy resin. Thermoplastic polymers, such as polyetherimide, polysulphone, polyethersulphone, and polycarbonate have been studied to modify epoxy resins. These studies show significant improvement in the toughness of epoxy resins. The reactive rubbers used for toughening epoxy resins include, liquid acrylonitrile-butadiene copolymers with various terminal groups, polysiloxanes, polyepichlorohydrin, and polyurethanes.

Although liquid acrylonitrile-butadiene copolymers with carboxyl- (CTBN) and amine- (ATBN) terminated groups have been widely used for epoxy toughening, the relatively high glass transition temperature of the copolymer limits their low-temperature applications. In addition, these copolymers also increase the CTE value of the molding compound. Also the presence of unsaturated structure of butadiene system is prone to thermal instability and thus unsuitable for long-term use at higher temperatures. Polysiloxanes have excellent thermal stability, moisture resistance, good electrical properties, low stress and lower T_g values. However polysiloxanes are not compatible with epoxy resins. Addition of compatibilisers such as, methylphenylsiloxane enhances the compatibility but at the same time raises the T_g of polysiloxane modifier restricting its low temperature applications.

3.2.1.2 EPOTEK Casting Epoxies

Epoxy technologies (EPOTEK) are commercial suppliers, who supply optical grade epoxies for casting applications. The physical and chemical properties of the epoxies can vary significantly based on their formulation. Generally the optical grade epoxies are glycidyl ether based epoxy resins, which are cured using phenolic hardeners. They have excellent transparency, low auto fluorescence, and good barrier properties. They can be cured to form rigid substrates by mixing portions of the resin and hardener in the correct ratio. They cure at atmospheric pressure and room temperature but the curing time is in the order of 20-30 hours. The curing time can be decreased significantly by raising the resin-hardener mixture to elevated temperatures. Care must be taken to find the optimal curing temperature, since curing at high temperatures can compromise the quality of the cured resin and can result in rough surface finish and poor physical and chemical properties. Four epoxies with excellent optical and barrier properties but with varying physical properties were chosen. Table 3 shows a list of epoxies used and their

physical properties. The spectral transmittance at different wavelength is illustrated in Figure 21 and the glass transition temperatures are shown in Figure 22.

Table 3: Physical properties and curing schedule for the different epoxies used

| <i>Epoxy</i> | <i>301-2</i> | <i>301-2 FL</i> | <i>310</i> | <i>314</i> |
|---------------------------------|------------------|-----------------|------------------|------------------|
| <i># of components</i> | 2 | 2 | 2 | 2 |
| <i>Mix ratio</i> | 10 : 3.5 | 10 : 3.5 | 10 : 5.5 | 10 : 0.6 |
| <i>Cure temperature</i> | 80 °C (3 hrs) | 80 °C (3 hrs) | 80 °C (3 hrs) | 80 °C (3 hrs) |
| <i>Viscosity</i> | 300-600 cPs | 125 cPs | 450-850 cPs | 400-800 cPs |
| <i>Refraction Index</i> | 1.564 | 1.514 | 1.507 | 1.494 |
| <i>Spectral Transmittance</i> | > 97% 300-900 nm | 100% 300-900 nm | > 96% 340-900 nm | > 93% 480-900 nm |
| <i>Color before/after cure</i> | Clear/dear | Clear/dear | Clear/dear | Clear/dear |
| <i>Lap shear strength (psi)</i> | 2000 | 2600 | 570 | 800 |
| <i>Shore D hardness</i> | 82 | 75 | --- | 80 |
| <i>Tg</i> | > 65 °C | > 60 °C | ambient | > 150 °C |
| <i>Shelf life</i> | 1 year | 1 year | 1 year | 1 year |
| <i>Pot life</i> | 8 hours | 12 hours | 2 hours | 4 days |

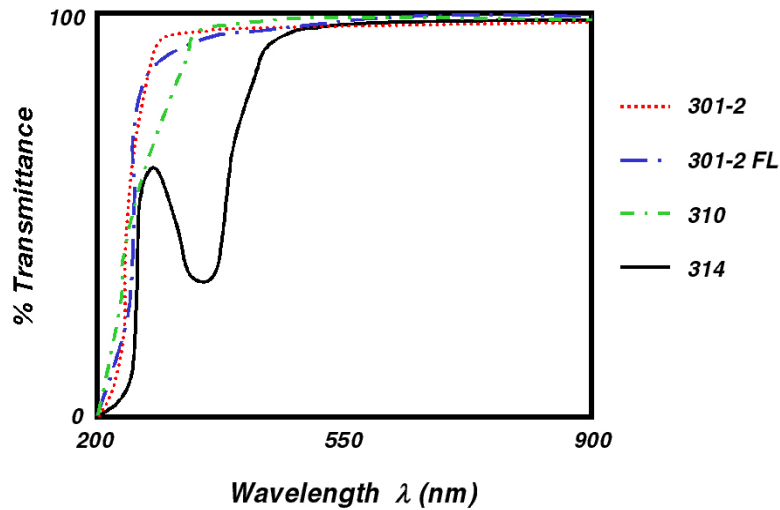


Figure 21: Plot showing the spectral transmittance of epoxies at various wavelengths of light.

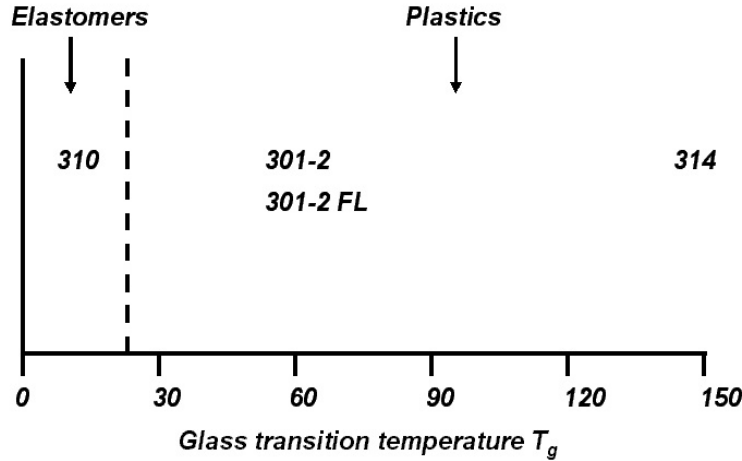


Figure 22: Glass transition temperatures of the EPOTEK epoxies used.

3.2.2 Process Technology

3.2.2.1 Substrate Etching

Inlet holes through the substrate are needed for the blocking microvalve and microflow control valve devices. Through wafer holes in both glass and silicon substrates are fabricated using two different methods. Holes in glass substrates are fabricated using photodefinable substrates. Holes in silicon substrates are fabricated using deep reactive ion etching (DRIE).

3.2.2.1.1 Photodefinable Glass Substrates

Photodefinable glass substrates (Foturan, Schott, Inc.) have been used to fabricate the through wafer inlet holes. The Foturan substrates have been impregnated with Ce_2O_3 and Ag_2O . During exposure to UV light at about 310 nm Ce_2O_3 gives up an electron. The Ce_3 ions in the glass absorb photons stripping one electron to go into the stable state.

The extra electrons are absorbed by the silver ions which are reduced to silver atoms. This creates an invisible image on the substrate. Approximately 2 J/cm^2 of energy density is required to sufficiently structurize a 1 mm thick substrate [56]. A heat treatment cycle is then required to form large lithium metasilicate (Li_2SiO_3) nuclei which etch nearly 20 times faster than the unprocessed glass in dilute HF acid. Figure 23 shows the suggested heat cycle for processing the Foturan substrates.

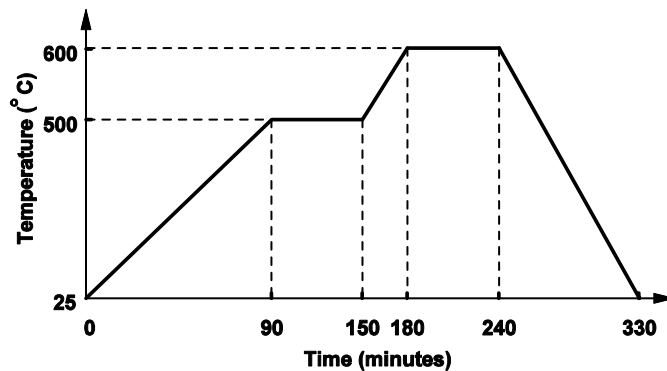


Figure 23: Foturan glass heat treatment schedule

Substrates are heated slowly to 500°C and held for 60 minutes where nucleation of the silver atoms occurs forming larger nuclei. The temperature is then increased to 600°C and held for 60 minutes. At 600°C, the glass crystallizes around the silver nuclei forming Li_2Si_3 . These crystals have diameters ranging between 1-10 μm . During the heat treatment cycle, the glass substrates reflow typically leaving the surface extremely rough. After heat treatment the substrates are planarized and polished using conventional chemical mechanical polishing equipment. Figure 24 shows fabricated through wafer holes etched in Foturan glass substrates.

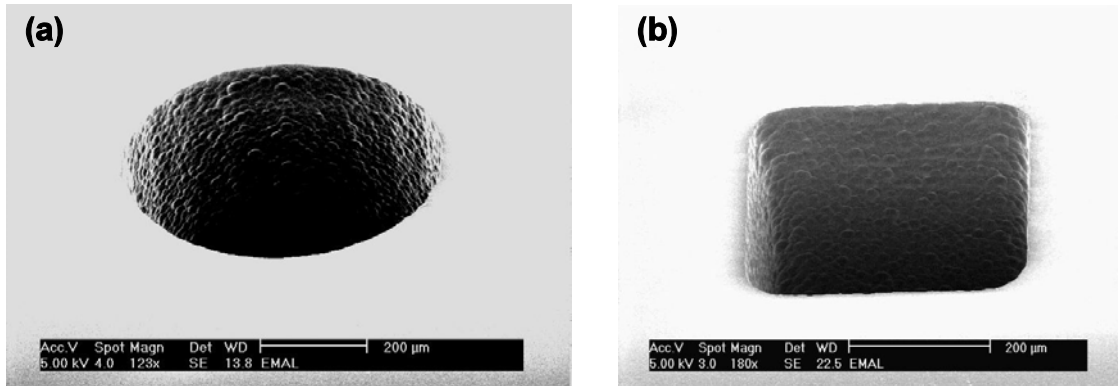


Figure 24: Fabricated through wafer holes in Foturan substrates (a) circle (b) square

3.2.2.1.2 Deep Reactive Ion Etching Silicon

High aspect ratio silicon etching of the access or inlet holes have been formed using an inductively couple plasma (ICP), deep reactive ion etching (DRIE) system from Surface Technology Systems, Ltd. (STS). The STS ICP (high density) plasma source uses an alternating process of etching and polymer deposition achieving aspect ratios as high as 30:1. The alternating process uses SF_6 for etching silicon and C_4F_8 for polymer deposition. Etch rates as high as 4.8 $\mu\text{m}/\text{min}$ have been measured for etching silicon which occupy about 1% of the wafer surface.

3.2.2.2 Microcasting

3.2.2.2.1 Stamper Fabrication

The first step involved in any replication based plastic fabrication technique is to fabricate a stamper. Replication methods, like casting, require the use of a stamper or master from which the required part is molded or replicated. The master contains a negative replica of the required part and most of the replication techniques faithfully replicate the master. The fabrication of the master may be expensive since care has to be taken to assure quality of the part. This can then be used to create multiple replications. In our process we use a silicon master, which contains deep etched negative replicas of the desired features.

A blank silicon wafer is first taken and a 2.7 μm thick layer of photoresist (Microposit SC 1827) is spun on at 4000 rpm. The photoresist is then soft baked at 90°C for 30 minutes. Then a photo mask with 2-D replica of the desired features is used to pattern the photoresist. The patterned photoresist is then hard baked at 110°C for 10 minutes. The silicon wafer with the hard baked photoresist mask is then etched using a

deep silicon reactive ion etcher (DRIE). Silicon is etched at the rate of 2.5 $\mu\text{m}/\text{min}$ using a high aspect ratio etch recipe (SF_6 120 sscm, O_2 13 sscm, Coil power 800 W, Platen power 200 W). The process is performed using alternating etch and passivation cycles to ensure straight side wall profiles. The substrate is etched for 12 seconds and passivated for 6 seconds, and this is repeated throughout the process. The passivation cycle (C_4F_8 85 sscm, Coil power 600 W) is performed using C_4F_8 , a polymer which coats itself on the sidewalls, thus preventing undercuts due to etching of sidewalls during the etching cycle, thereby ensuring straight sidewalls. Channel heights of up to 300 μm with surface roughness in the order of hundreds of angstroms can easily be obtained using this process. Once the features have been etched to the required depths, the substrate is stripped of the photoresist and the resulting silicon substrate is used as the stamper or master. Figure 25 shows a DRIE silicon stamper for replication methods.

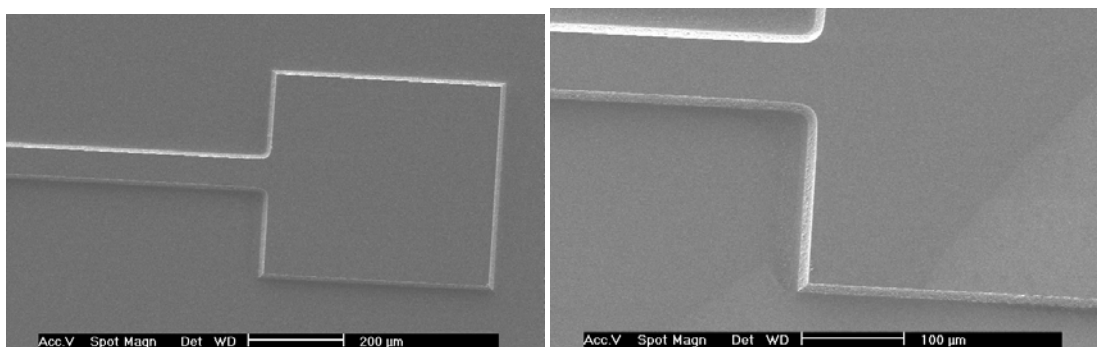


Figure 25: SEMs of silicon wafer with DRIE negative replicas of desired features.

Release Layer

It is important to treat the surface of the master/stamper to aid release of the molded or cast part from the stamper. Molding polymers usually undergo shrinkage on curing into rigid substrates and it is important that the interaction between the molded part and the stamper surface be limited to a minimum. There are commercially available mold release agents both in solution and aerosol form which can be coated on the stamper to make the surface of the stamper inert which limits interaction with the liquid polymer but the thickness of the coat is usually in the order of 10's of microns which is close to the dimensions of the features on the molded part. The only solution to this problem is to coat the surface with an extremely thin layer of an inert polymer like Teflon, parylene [122] or even some types of silanes to make the surface of the stamper inert.

Parylene-C is a chemically inert polymer, which can be deposited as extremely thin (sub micron) layers using a chemical vapor deposition process. To improve the adhesion of parylene-C to the silicon stamper the silicon stamper is treated with a silane (AZ 174). Parylene is available as a dimer, which can be vaporized at 170°C and split into monomers in a furnace which is at 700°C, as described earlier in this document.

Mold fabrication

Mold plates are required to hold the stamper and to aid in heat transfer from the outside to the liquid polymer resin. The only requirements are that the material be cheap, strong enough to withstand working conditions and have high thermal conductivity. Aluminum satisfies all these conditions and can be easily machined into any required

geometry to hold the stamper. Two aluminum blocks were cut and machined to make the surfaces smooth (roughness in the order of a few microns). A groove the shape of a silicon wafer was cut in one of the aluminum blocks to hold the stamper in place. The molds were also provided with clamping screws to clamp both the plates together tightly. Figure 26 shows the fabricated aluminum mold plates for both open and closed mold casting.

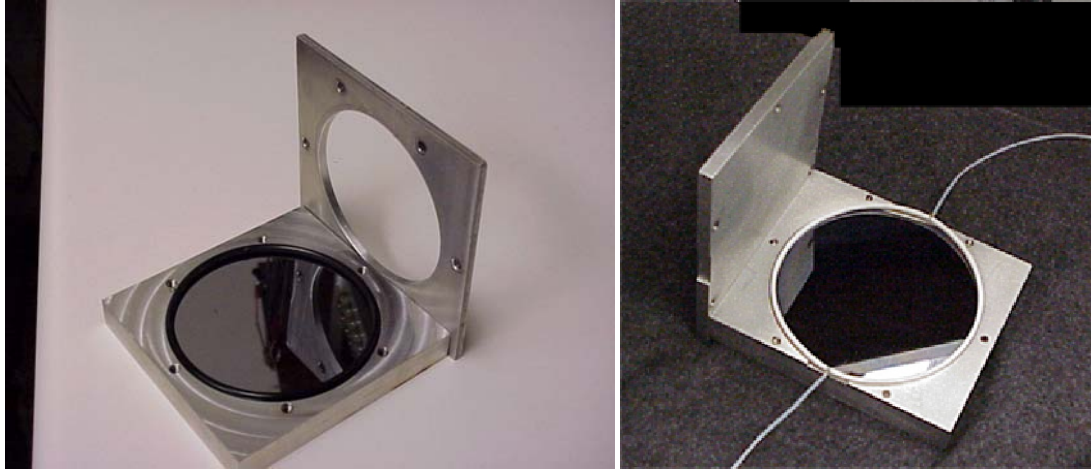


Figure 26: Shown are aluminum mold plates for open and closed mold casting.

Backing wafer and O-rings

In most cases smooth surfaces are desired on both sides of the substrate. One side usually has microfeatures, like channels, and the other side is smooth and flat. In order to obtain a flat surface on the other side a smooth flat backing wafer made of an inert material like teflon or polypropylene is used. The wafer is also cut the shape of a silicon wafer and sandwiched with the stamper. There is an O-ring between the stamper and the backing wafer, which determines the thickness of the cast part. The O-ring is also made of a material like teflon. There are cases where two stampers are sandwiched to produce substrates with features on both sides eliminating the need for a backing wafer.

3.2.2.2.2 Fabrication Process

Epoxy casting is an extremely simple replication process. A silicon stamper is used to produce substrates with cast microfeatures. Based on the assembly of the molding setup, the casting process can be classified into two types (1) open casting and (2) closed mold casting.

Open casting

Figure 27 details the open casting process. A silicon stamper with the parylene C release layer is first placed on the bottom aluminum mold plate and a Teflon O-ring is placed on top of it. A second aluminum plate with an opening cut on top is placed on top of the O-ring and clamped using clamping screws to the bottom mold plate. The epoxy resin is then poured into the recess with the stamper and cured at 80°C for 3 hours. Then the mold plates are disassembled and the molded substrate is removed. One side of the substrate faithfully replicates the stamper but the other side is not guaranteed to be perfectly flat. Figure 28 shows a picture of a channel cast using the open casting process.

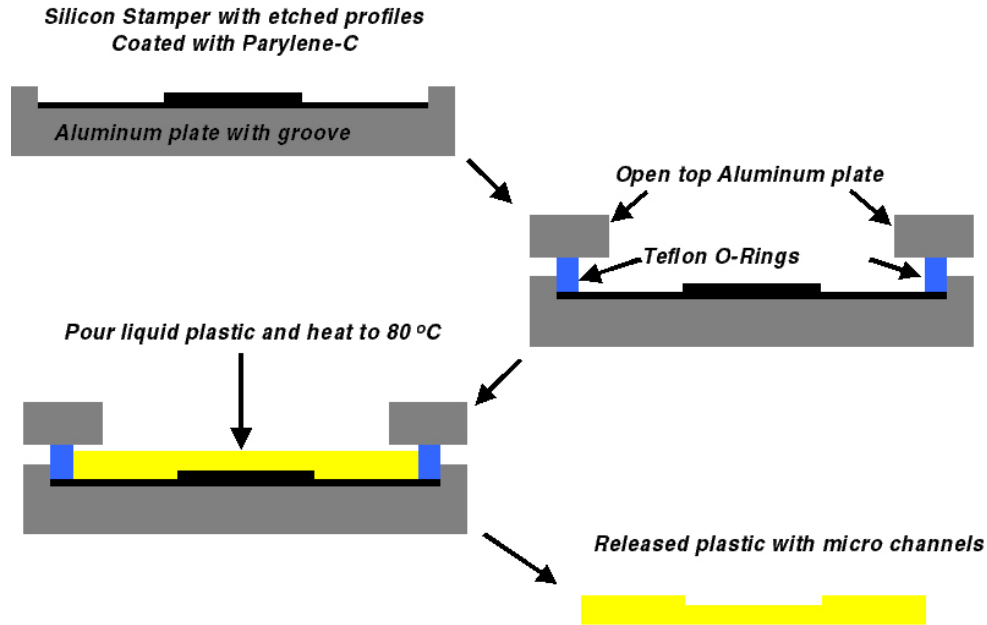


Figure 27: Schematic of the open casting process.

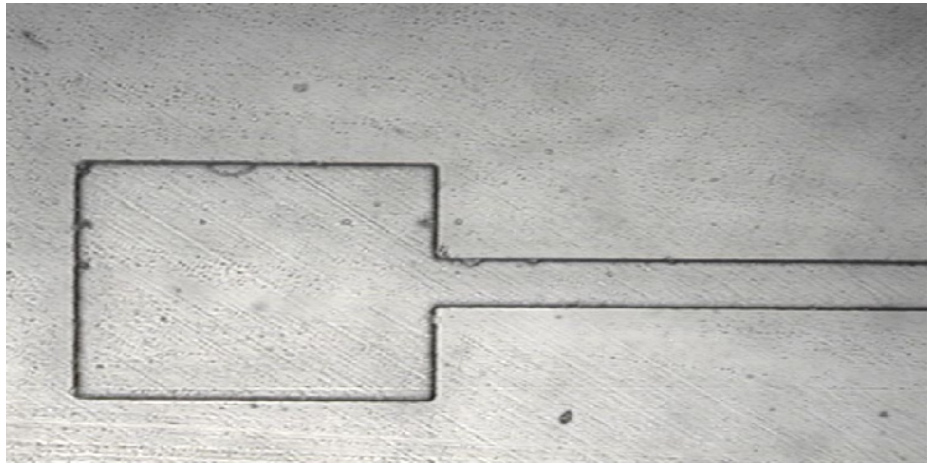


Figure 28: Shown is a microscope picture of a cast epoxy channel obtained by open casting.

Closed mold casting

This process is similar to the open casting process with the only difference being that a backing wafer made of polypropylene is placed on top of the O-ring to ensure a smooth surface on the back side of the substrate. A small access hole is cut in the Teflon O-ring to facilitate injection of liquid resin into the closed mold. Once the mold is filled with the resin, the setup is heated to 80°C and cured for 3 hours. The mold is then disassembled and the cured substrate is released. Figure 29 shows a schematic of the closed mold casting process and Figure 30 shows microscope and SEM pictures of microfeatures produced using the closed mold casting process.

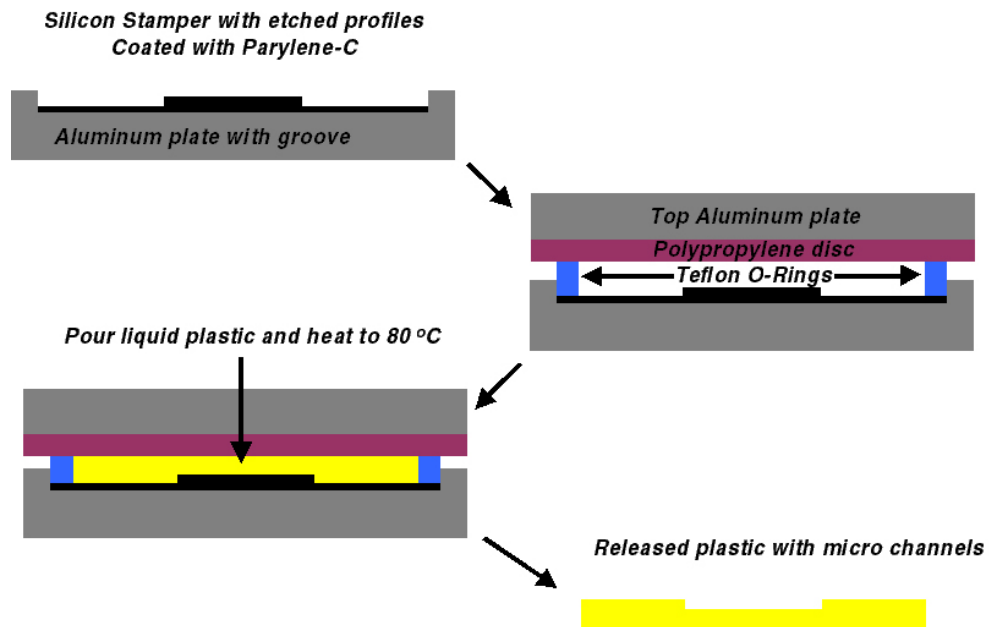


Figure 29: Schematic of the closed mold casting process.

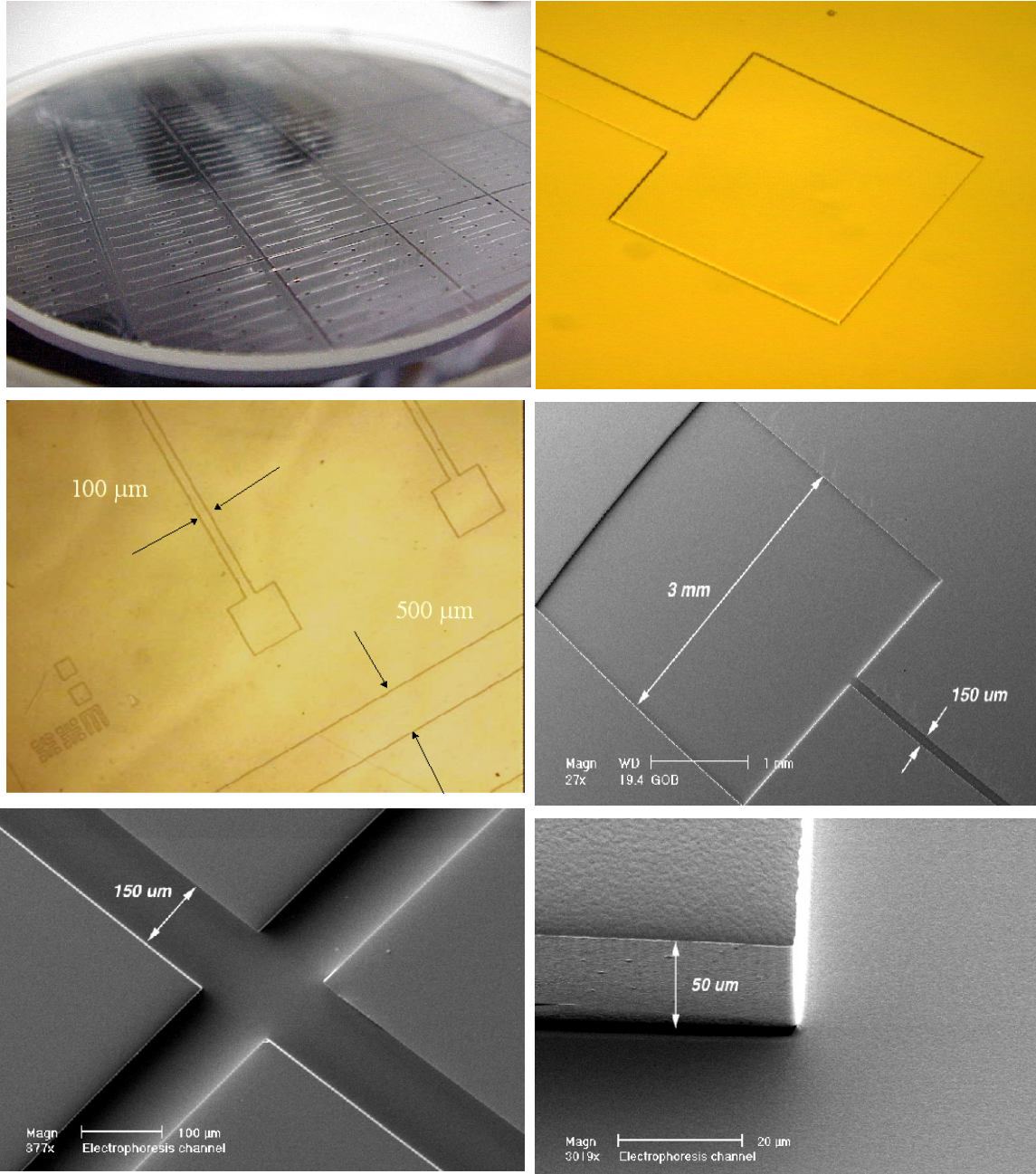


Figure 30: Microscope and SEM pictures of channels fabricated using the closed mold casting process.

3.2.2.3 Lamination and Bonding

Channels and reservoirs fabricated using replication technologies have to be sealed in order to provide a closed circuit for transport and handling of fluids. Two techniques, lamination and bonding have been extensively used for these purposes. Channels on the cast substrate can be sealed by laminating adhesive coated thin films using a laminator under controlled temperature and pressure. Alternatively, the channels can also be sealed by bonding to another substrate.

There are a large number of bonding techniques which have been demonstrated which can be used based on this type of application to produce hermetically sealed

channels. Both lamination and bonding use adhesives to achieve attachment. Care must be taken to ensure that the adhesives have excellent optical and barrier properties and suitable physical and chemical properties to withstand normal working conditions. This process is capable of achieving sub micron resolution features. The surface roughnesses obtained were of the order of 20 nm. This is an exact replication of the roughness of the sidewalls of the silicon wafer used as a stamper. Figure 31 shows the sidewall of a cast epoxy channel, which is an exact replication of the rough silicon stamper, obtained after DRIE.

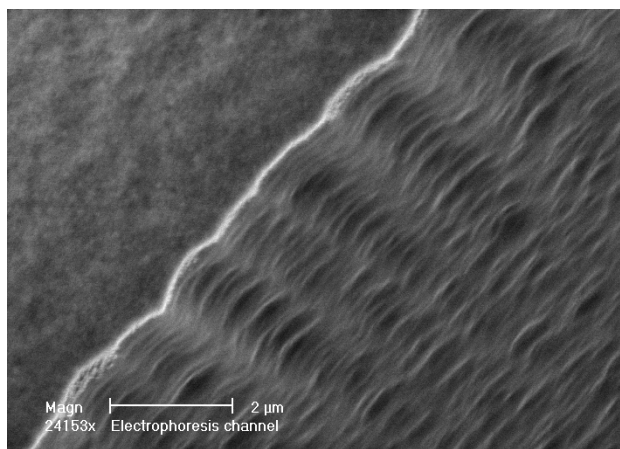
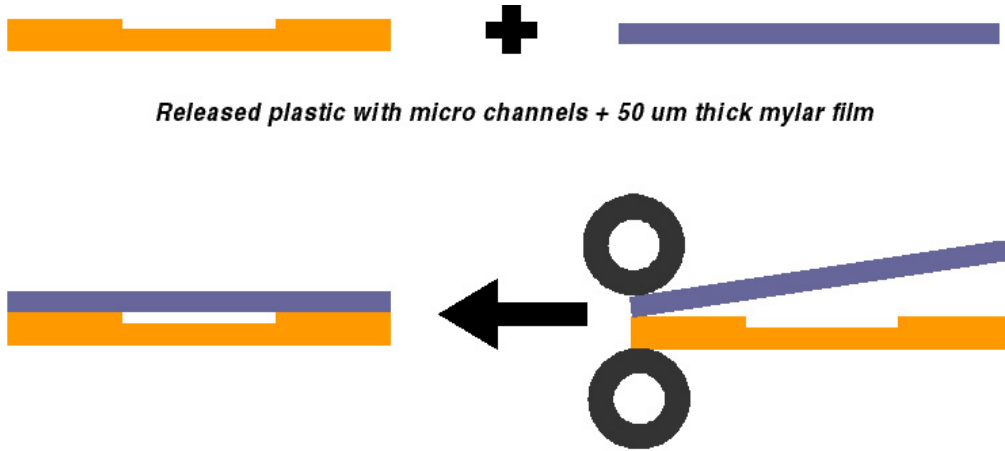


Figure 31: Surface roughness of a cast epoxy channel obtained by casting.

3.2.2.3.1 Lamination

In order to seal channels and reservoirs, a flexible transparent film is laminated [123] on top of the epoxy substrates. The lamination process uses a desktop roll type laminator (Kepro Circuit Systems, Inc. BLT 121-A, Figure 33) and a thin mylar film (2 mil, Monokote, Top-Flite, Inc.) is used to laminate the plastic substrates. The substrate is first treated with acetone, and then the film is laminated onto the substrate by passing it between two rollers, Figure 32. The process is carried out at room temperature and at a feed rate of 2 ft/min. Figure 34 shows the cross section of a laminated channel. These structures show excellent permeation barrier characteristics with water permeability $P < 1.7 \mu\text{l}/\text{cm}^2/\text{day}$ at room temperature. When these capillaries are filled with a sample, there is no seeping present at the bond interface.



Released plastic with micro channels + 50 µm thick mylar film

Lamination is achieved by sending the plastic + lamination film between two hot rollers at 80 °C at 2 ft/min and a gauge thickness of 2 mm.

Figure 32: Process flow for lamination.



Figure 33: Kepro desktop roll type laminator.

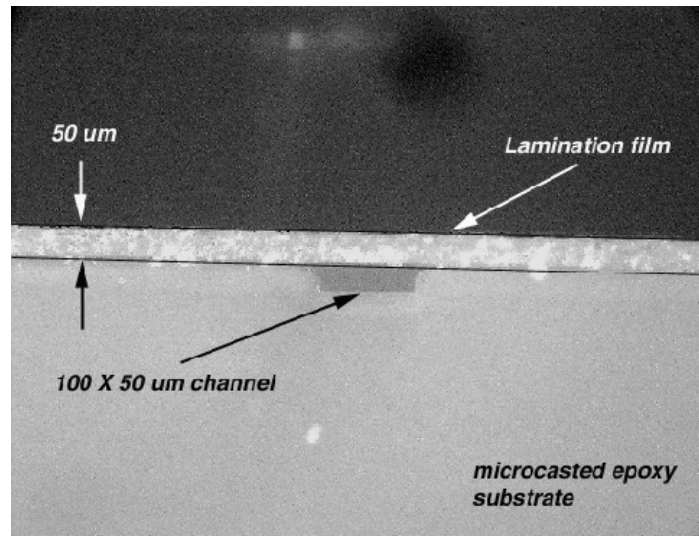


Figure 34: Cross section of a laminated channel.

3.2.2.3.2 Bonding

Another technique to seal cast epoxy channels is bonding. A flat cast epoxy substrate is bonded to the epoxy substrate with microchannels using a thin adhesive layer. The adhesive used is a Blanchard wax solution. Blanchard wax is a commercially available bonding wax for bonding dies to PC boards. It is soluble in acetone and can be dissolved completely into a bonding wax solution. Depending on the mix ratio, we can get low viscosity solutions which when spun on the wafer yield sub micron thick layers. Blanchard wax is dissolved in acetone (25:100, blanchard wax: acetone by weight) for 30 minutes and stirred continuously to ensure complete dissolution of the wax in acetone. Figure 35 shows the schematic for the wax bonding technique. First a thin layer of the bonding wax solution is spun on the substrate with channels then the other flat substrate is aligned with a flat substrate under a microscope.

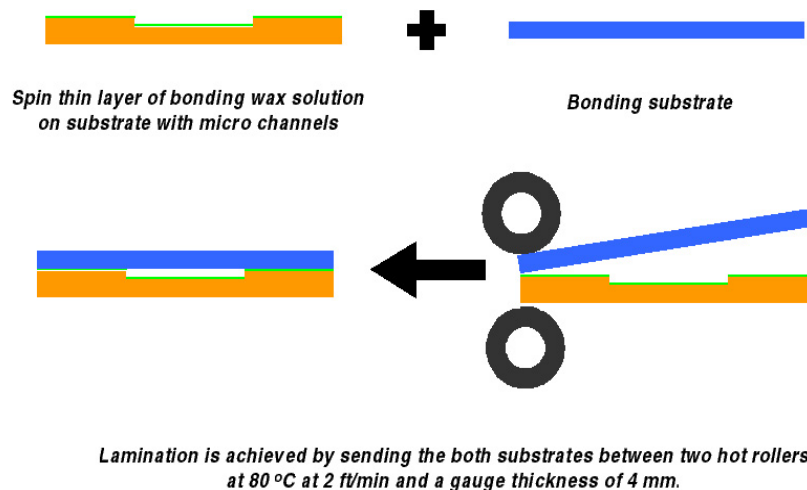


Figure 35: Process flow for the bonding technique.

The microscope has an x-y stage for alignment and a z stage for vertical movement and to apply bonding pressure. Once the two substrates are aligned then the z stage vertical lift is used to bring the substrates together and apply bonding pressure. The substrates are held together for 2 minutes to ensure proper bonding. Figure 36 shows pictures of fluids in the cast epoxy channels bonded using bonding wax.

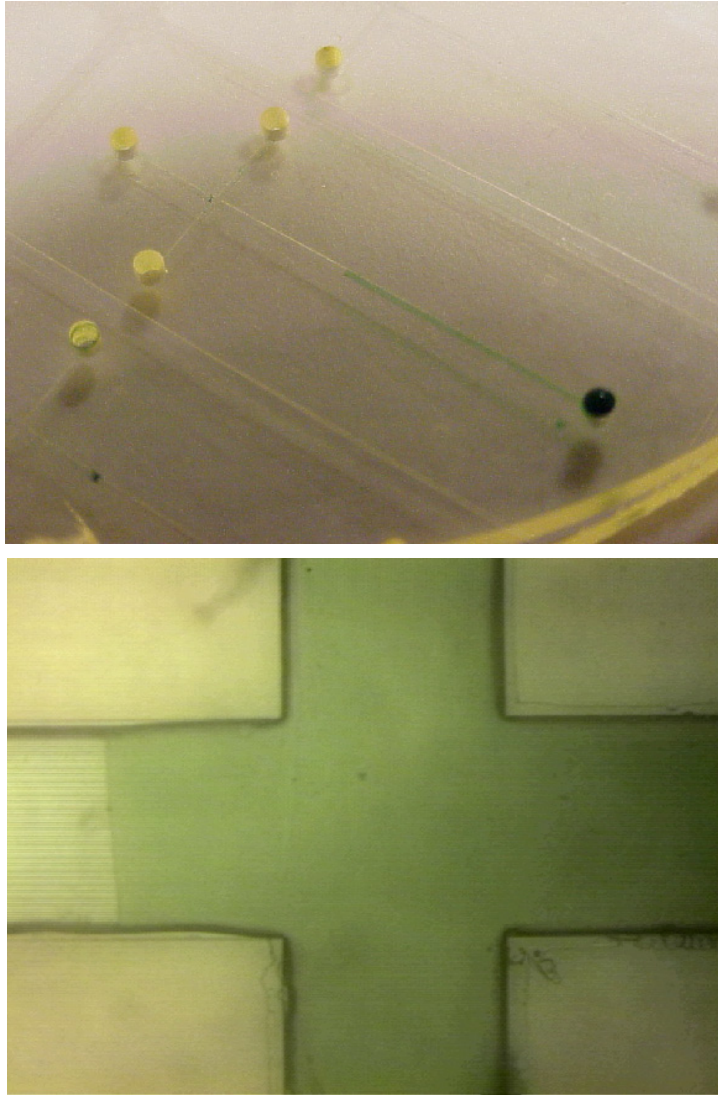


Figure 36: Pictures of channels bonded using bonding wax.

3.2.2.4 Feed-throughs on Plastic Substrates

On-chip chemical analysis also requires reservoirs on the plastic substrate to store gels and other reagents. Currently this is done by mechanically drilling holes for this purpose. We have demonstrated a two mold single cast process that created the channels and reservoirs simultaneously, Figure 37. A stainless steel plate, the size of a 100 mm diameter silicon wafer was made and pins of height 1.5 mm and diameter 1.5mm were press fitted in the stainless steel plate. This plate was then coated with a release layer and used on one side of the mold to form feed throughs on the plastic substrate. The plate was uniformly coated with an aerosol based commercially available mold release.

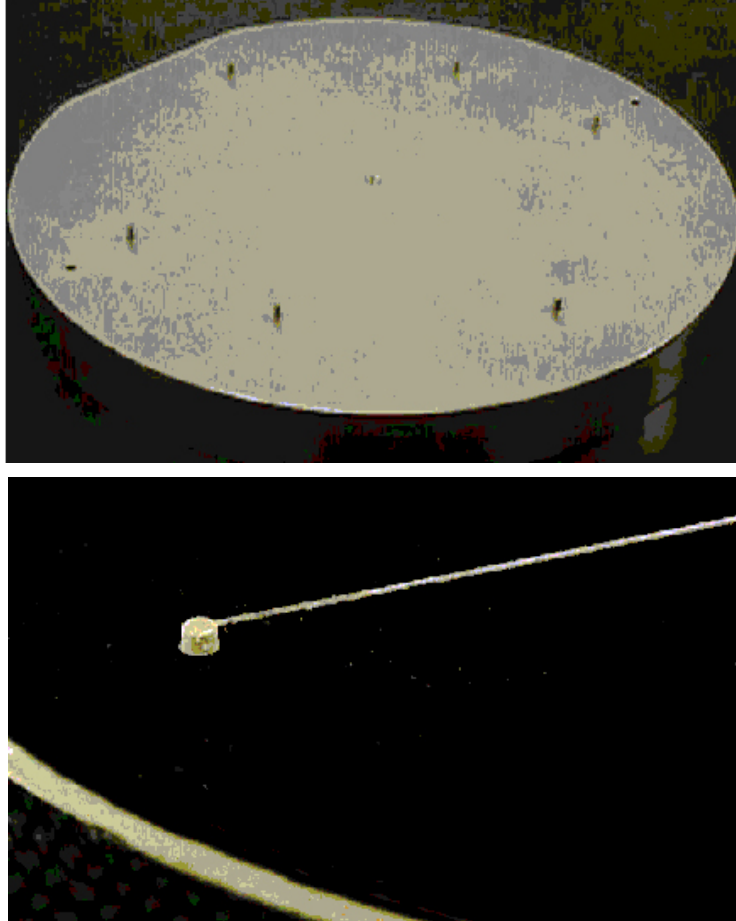


Figure 37: Stainless steel mold for fabrication of through vias and a fabricated epoxy channel with through vias.

3.2.2.5 Injection Molding

We have also fabricated plastic substrates for microfluidic applications by injection molding. We fabricated mold inserts by the silicon etching micromachining bulk technique. These molds are then used as stampers in molding inserts for the fabrication of plastic substrates. The molds are designed to fabricate 1 mm flat structures with one side that is micromachined by introducing a silicon or glass high-resolution stamp.

We fabricated the mold plates at a commercial machine shop. A two-piece fixture with injection port, cavity insert, heater, cooling channels, and release mechanism was designed and manufactured in aluminum because of its machining ease and thermal properties. Figure 38 shows the manufactured mold. The complete mold system was used in several mold trials with the following: (a) material: polycarbonate (excellent optical, chemical, and mechanical properties) (b) geometry: 4" circular plate with microstructures on one surface (batch fabrication) (c) machine: Arburg Allrounder 221M 350-75, 40 tons (clamping force), 30 mm (screw diameter) conventional injection molding machine. The process parameters include injection pressure, injection velocity, melt temperature, mold temperature, and plate thickness.

Figure 39 shows a typical injection molded polycarbonate substrate (100 mm diameter, 2 mm thick) with channels fabricated by this method. The width of the channel

is 200 μm and its depth is 5 μm . It can be seen from the pictures that the sidewalls are not very sharp.



Figure 38: The molds plates used for Injection molding.

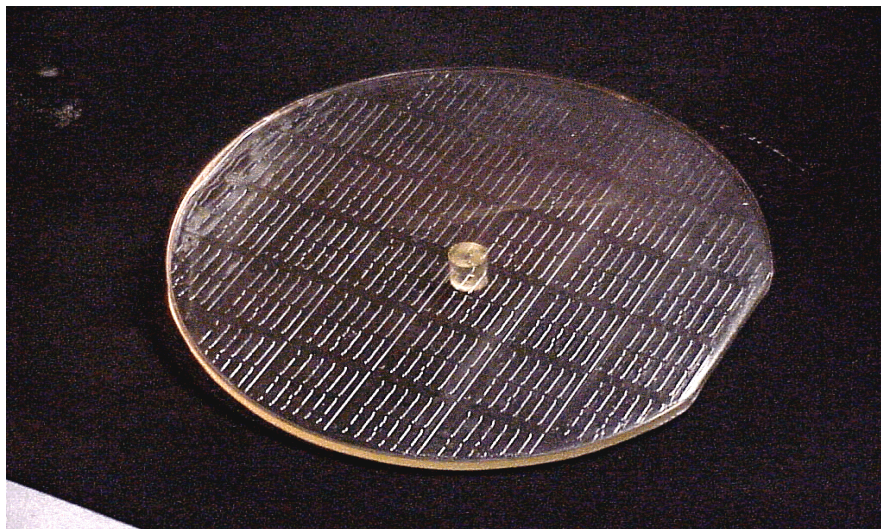


Figure 39: Injection molded polycarbonate substrate.

3.2.2.5.1 Molding Results

Results indicate that only low resolution replication of microstructures on polymer surfaces is possible. In addition the polymer melt cannot fill micro cavities completely. All of the current structures have a low aspect ratio. Finally, a flow mark is observed on the polymer surface. Figure 40 shows SEM photographs of low aspect ratio, injection molded structures.

Based on the results obtained and consideration of the equipment and tool making costs, it was decided that casting was a more suitable alternative. Another problem with injection molding was that the features obtained were not completely formed. The pyramid or dome shaped features in Figure 40 are a result of incomplete material flow into the cavities. Complete material flow would have resulted in rectangular shaped features with completely flat top surface. In order to obtain a flat top surface, the mold

plates have to be fit with heaters to maintain the temperature of the mold at the melting temperature of the material. In addition, high pressures have to be applied. Casting on the other hand, is a simpler process with much greater flexibility.

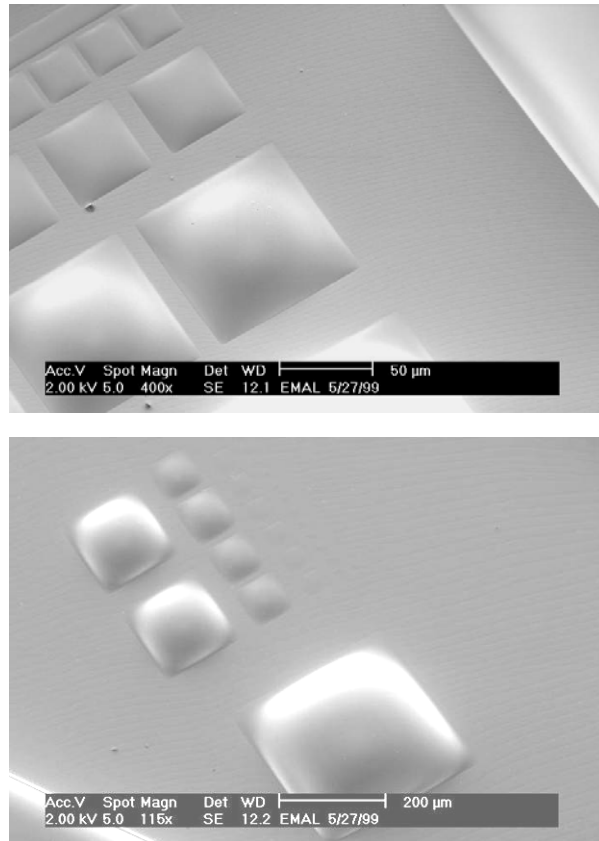


Figure 40: SEMs of injection molded low aspect ratio structures.

3.2.2.6 Flip-Chip Bonding

In the development of packaging of electronics, the aim is to lower cost, increase the packaging density and improve the performance while still maintaining or even improving the reliability of the circuits. The concept of flip-chip process where the semiconductor chip is assembled face down onto circuit board is ideal for size considerations, because there is no extra area needed for contacting on the sides of the component. The performance in high frequency applications is superior to other interconnection methods, because the length of the connection path is minimized. Also, reliability is better than with packaged components due to decreased number of connections. In flip-chip joining there is only one level of connections between the chip and the circuit board.

There are many different alternative processes used for flip-chip joining. A common feature of the joined structures is that the chip is placed face down to the substrate and the connections between the chip and the substrate are made using bumps of electrically conducting material. Cross sections of flip-chip joints with and without underfill material are shown in Figure 41. Examples of the different types of flip-chip joints are schematically shown in Figures 42 and 43. The two most commonly used

techniques, however, are solder bumping and the use of conductive and non-conductive adhesives.

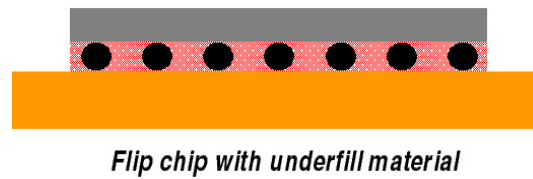
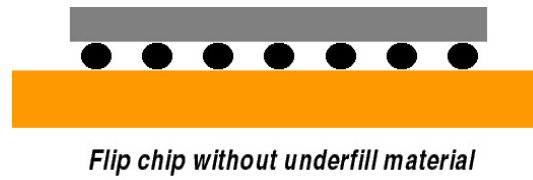


Figure 41: Cross sections of different flip-chip processes.

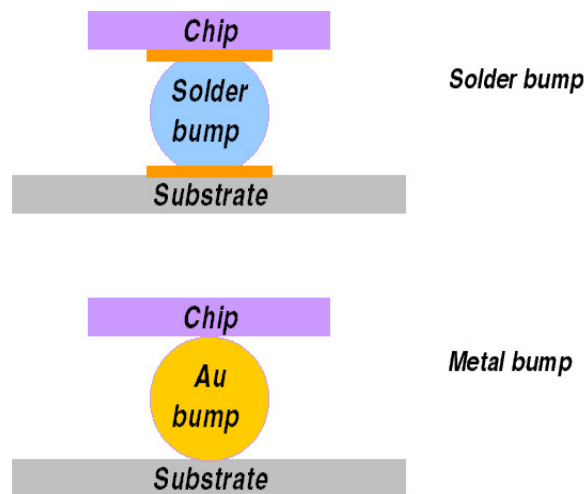


Figure 42: Basic flip-chip joints using solder and metal.

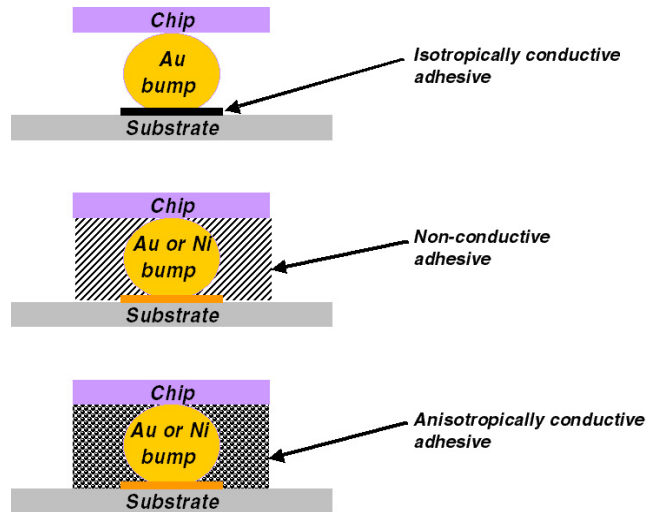


Figure 43: Flip-chip joints using conductive and non conductive adhesive.

3.2.2.6.1 Solder Joining

In flip-chip soldering processes, solder bumped chips are soldered onto the circuit board. Solder is also, but not always, deposited onto the substrate pad areas. For fine pitch applications, solder can be deposited by electroplating, solder ink jet or solid solder deposition. Tacky flux is applied to the solder contact areas either by dipping the chip into a flux reservoir or by dispensing flux onto the substrate. For coarse pitch applications (>0.4 mm) solder paste is deposited on the substrate by stencil printing. The bumps of chips are placed into the tacky paste and they are reflowed in an oven. After the reflow process, cleaning of the flux is preferred. The underfill material is applied by dispensing along one or two sides of the chip, from where the low viscosity epoxy is drawn by capillary forces into the space between the chip and substrate. Finally the underfill is cured by heat. Repairing of the flip-chip joint is usually impossible after the underfill process. Therefore testing must be done after reflow but before the underfill application.

3.2.2.6.2 Conductive and Non-conductive Adhesives

Conductive adhesives have become a viable alternative to tin-lead solders used in flip-chip joining. Adhesively bonded flip-chip joining combines the advantages of thin structures and cost efficiency. The advantages of conductive adhesives include ease of processing, low curing temperatures, and elimination of the need to clean after the bonding process. Anisotropically conductive adhesives also have the ability to connect fine pitch devices. Figure 44 shows a schematic drawing of flip-chip bonding with isotropically and anisotropically conductive adhesives (ICAs and ACAs). Also, nonconductive adhesives can be used for flip chip bonding; in this case the joint surfaces are forced into intimate contact by the adhesive between the component and substrate.

Isotropically conductive adhesives are pastes of polymer resin that are filled with conducting particles to a content that assures conductivity in all directions. Generally, the polymer resin is epoxy and conducting particles are silver. Anisotropically conductive adhesives are pastes or films of thermoplastics or b-stage epoxies. They are filled with metal particles or metal-coated polymer spheres to a content that assures electrical insulation in all directions before bonding. After bonding the adhesive becomes

electrically conductive in z-direction. The metal particles are typically nickel or gold and these metals are also used to coat polymer spheres.

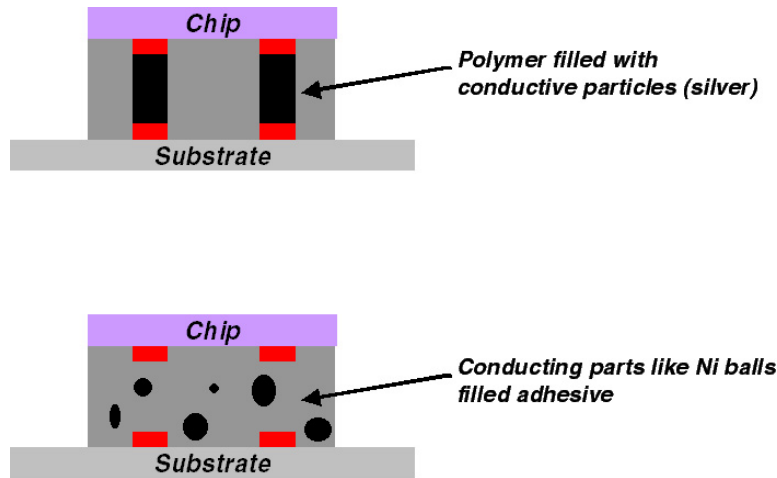


Figure 44: Flip chip bonding for electrical contacts.

3.2.2.6.3 Polymer Flip-Chip Process

The polymer flip-chip process developed is a modification of commonly available conductive adhesive based flip chip processes. Two key techniques - micro-screen printing and precision die placement - along with basic microfabrication and casting techniques are used. The only major difference is thin film metal contact pads are photolithographically patterned on the plastic substrate instead of the metal bumps.

3.2.2.6.3.1 Chip on Flex

Plastic based microfluidic systems are being increasingly used because they offer high quality devices, which are a low cost alternative, and the turnaround time for fabricating these devices is extremely small. However due to the material properties of plastics, fabrication of detectors and sensors on plastics is not feasible. Silicon on the other hand has excellent material properties but is significantly more expensive and fabrication process is more complex. Attempts have been made to perform on chip detection using optical, electrochemical and chemiluminescence techniques. In all these devices, the detectors are built on a silicon substrate and the channel structures are either built on top of the detectors or separately fabricated on another substrate and bonded to the substrate with the detectors. The die space required to support the channel structure is significantly larger than the area of the detectors, as shown in Figure 45, and much of the area on the expensive silicon wafer is wasted in supporting the channel structure. Polymer flip-chip technology offers a cheaper solution by integrating detector die which can be mass fabricated on a complete silicon wafer, and then embedded in an extremely low cost plastic microfluidic system. Figure 46 shows pictures of some embedded silicon chips in cast epoxy substrates.

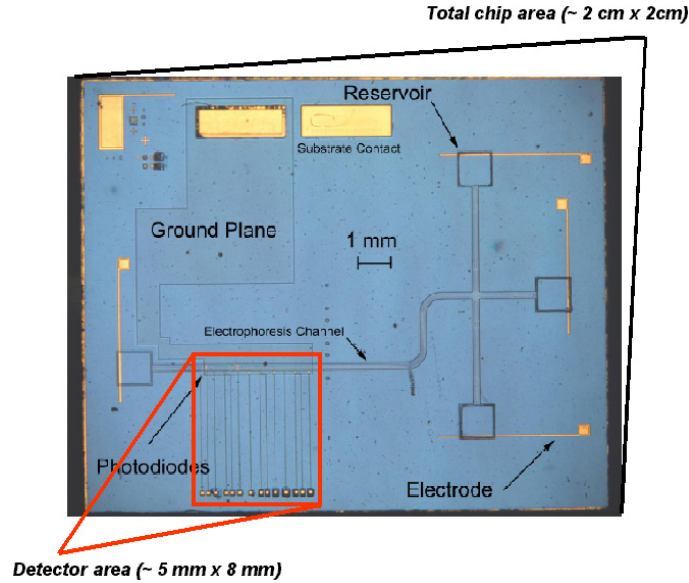


Figure 45: Comparison of the detector area to the total die area [114].

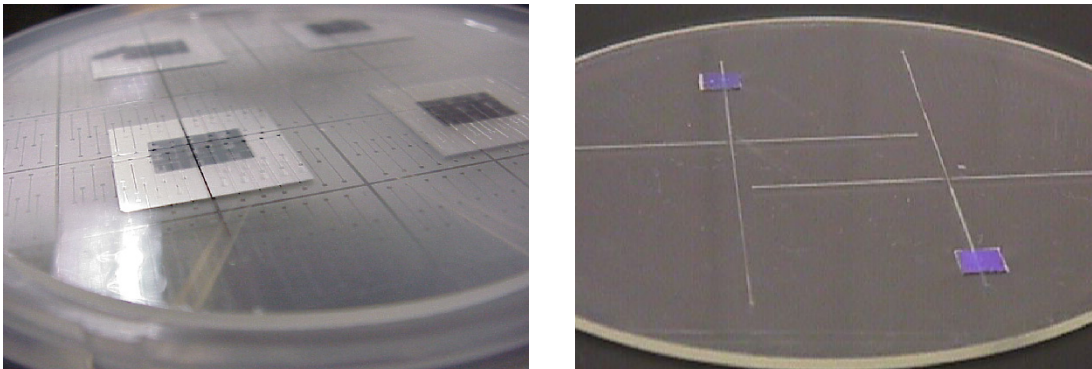


Figure 46: Shown are silicon chips embedded in a cast epoxy substrate with fluidic circuits.

3.2.2.6.3.2 Polymer Flip-Chip Process for Embedded Detectors

The polymer flip-chip process involves integration of silicon micromachined chips with plastic based systems. It is important to ensure that the functions of the chip after integration are not affected by the process and continue to perform like they did before embedding. The key techniques include precise chip location on the plastic substrate to ensure that the chip is at the right position with respect to the fluidic circuit on the plastic substrate, attachment of the die to the plastic substrate, ensuring perfect electrical contact to the chip and access to the chip contacts from the outside.

Figure 47 illustrates the process flow for integrating a silicon chip with a plastic wafer using the polymer flip chip process. A plastic substrate with channels is first laminated to seal the channels. Then a thin layer of metal is evaporated and lithographically patterned to form the contacts and alignment marks on the plastic wafer. Electrically conductive epoxy, which serves as both an electrical contact and glue, is micro-screen printed on the contact pads on the plastic substrate. The silicon die is patterned with backside alignment marks corresponding to the alignment marks on the plastic. A precision pick and place machine is used to precisely locate the die on the

plastic wafer such that the die is aligned and the contact pads on the die are bonded to the conductive epoxy on the plastic wafer. The electrically conductive epoxy sets over a period of 12 hours but the process can be accelerated by heating. To enclose the device, the plastic substrate with the attached chip is set in an aluminum mold with an O-ring and a backing wafer and liquid epoxy resin is used to embed the chips. Contact holes to the electrodes can be drilled using a drill press.

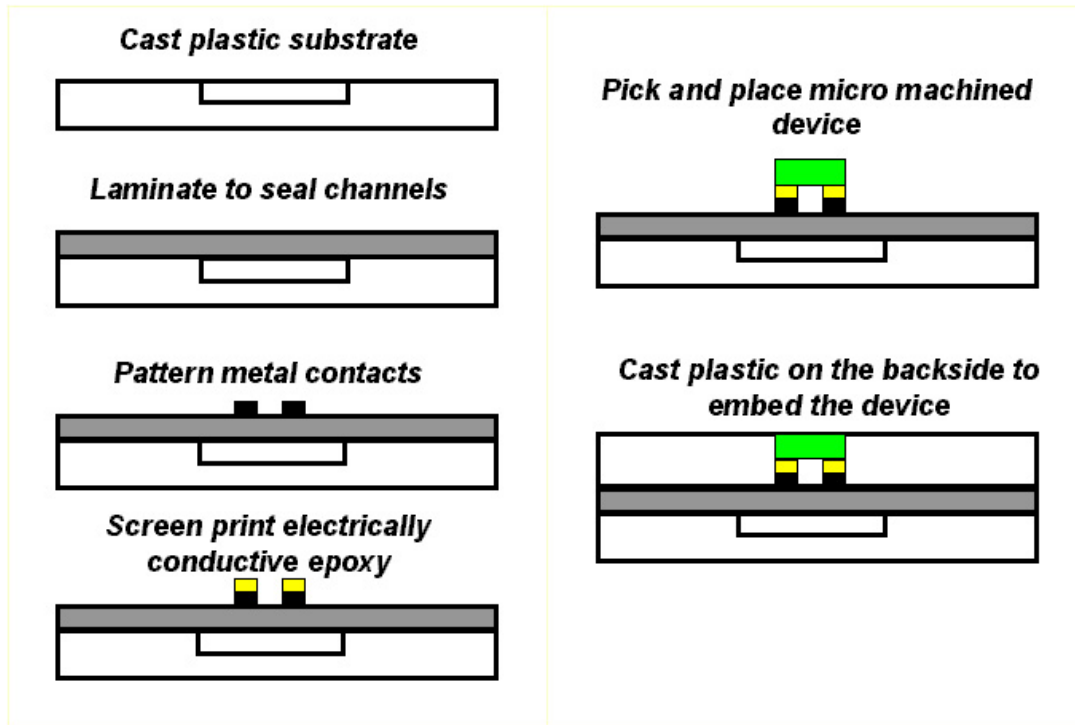


Figure 47: Process flow for embedding silicon chips in plastic.

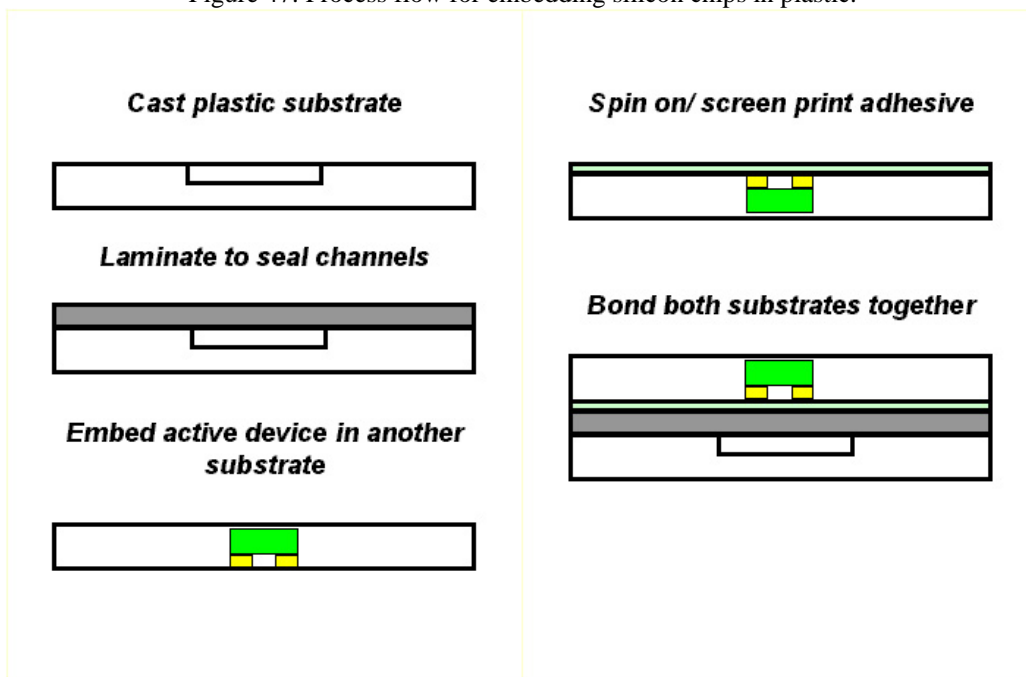


Figure 48: Alternative process flow for embedding chips in plastic.

An alternative approach using the same techniques like precision die placement and μ -screen printing can also be employed to embed chips in a separate substrate and then bond that substrate to another substrate with the channels. Figure 48 illustrates this process flow.

3.2.2.7 Micro Screen Printing (μ -Screen)

Micro-screen printing is a development of screen printing technology aimed at the production of very fine features for electronic or other applications. It is a simpler alternative to other more complex patterning techniques like lithography, liftoff and etching. It is particularly useful in cases where the feature sizes are fairly big ($> 50 \mu\text{m}$) and the feature definition is not very critical. Another advantage is the flexibility of the process; by controlling the printing parameters any liquid or gel can be screen printed on any substrate.

The μ -screen shown in Figure 49 can be used on a standard thick film-printing machine in the same way as a standard mesh screen. However, because of its unique construction, it is capable of much greater resolution down to $50 \mu\text{m}$ line and space. Wider lines can also be printed. The μ -screen is made from a stainless steel foil, which is micro-etched with a series of ink feeder holes. The etched feeder hole pattern is computer generated from a customer's own CAD layout file. Hence, each μ -screen effectively has a custom mesh which exactly matches the print pattern. This avoids the interference and poor print edge definition produced by the random alignment of a pattern to a standard wire mesh. An organic gasketing layer is applied to the underside of the foil, which allows the ink to flow beneath the metal 'bridges' between the holes and defines the sides of the printed lines and areas. The μ -screen is mounted in a conventional screen frame and is used in a normal off-contact mode on a standard printing machine.

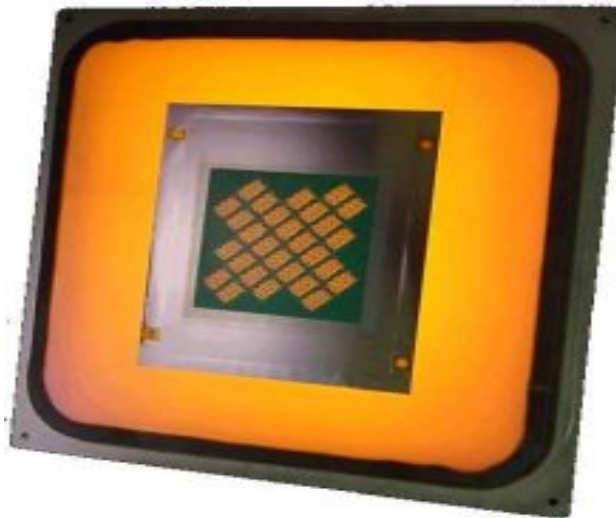


Figure 49: A typical stencil type micro-screen for micro-screen printing applications.

The design is made as a CAD layout showing the features to be printed. Specially developed software is then used to produce artwork for etching ink feeder holes and for patterning the gasketing (emulsion) layer. Ink feeder holes are produced in the metal foil by electro-chemical etching. A gasketing layer (emulsion) is applied to the underside of

the etched foil, and patterned to form channels that control the spread of the printing solution. The foil is then mounted onto a carrier mesh in a conventional printing frame.

Figure 50 shows a typical screen printing machine. The machine contains a holder onto which the screen is mounted and locked into position. There is an x-y stage capable of angular motion which also contains a vacuum chuck to hold the substrate on which the printing is done. There is also a Teflon squeegee that is mounted in a holder located right above the screen. The squeegee is capable of x (downward) and y (along the plane of the screen) movement. The pressure applied by the squeegee on the screen (printing pressure) and the speed at which it moves across the screen can be controlled or automated. There is a microscope with alignment cross hairs located right above the chuck that holds the wafer. The process is simple. A blank substrate is loaded on the chuck and the chuck is moved underneath the screen. The screen is brought down and the material (solution) to be screen printed is applied at one end of the screen. The squeegee presses down on the screen applying printing pressure and then sweeps across the screen thus evenly coating the material through the openings on the screen. The squeegee is then withdrawn and the chuck is brought back to the original position under the microscope. The cross hairs are aligned to the printed features and the blank substrate is removed. The substrate on which printing is to be done is then placed on the chuck and the chuck is moved using the x-y stage to align areas to be screen printed to the cross hairs (alignment process). Once the alignment is complete the chuck is again moved under the screen and the squeegee is used to print the material evenly through the holes in the screen onto the substrate. The substrate is then removed with the printed features.



Figure 50: Typical screen printing machine for printing on flat surfaces.

3.2.2.7.1 Electrically Conductive Epoxy

The H-20E compound is a commercially available electrically conductive epoxy recommended for screen printing on plastic substrates. This silver filled epoxy resin adhesive is ideal for creating strong, highly conductive solderless connections and

repairs. It is used for circuit board repair, surface mount connections, static discharge, shielding and grounding. This epoxy is excellent for bonding heat sensitive components. The physical properties of H-20E are shown in the table 4.

Table 4: Physical properties of H-20E.

| Epoxy | H-20E |
|----------------------------|------------------------|
| # of components | 2 |
| Mix ratio | 1:1 |
| Cure temperature | 60°C |
| Viscosity | 2200-3200 cPs |
| Volume resistivity | < 0.00004 Ω -cm |
| Thermal conductivity | 29 W/mK |
| Max. operating temperature | 200°C |
| Lap shear strength | 3400 psi |
| Degradation temperature | 400°C |
| Shelf life | 4 days |

The H-20E provides quick, solderless electronic connections, which are excellent for bonding surface mount components. These epoxies offer excellent electrical conductivity while also providing high strength conductive bonds. They can be quickly cured at low temperatures or no heat cure (air-dries) in a few hours (cold solder). They are also flexible enough that even after curing the epoxy can be reworked or removed using a hot soldering iron. Figure 51 shows micro screen printed H-20E bumps on a plastic substrate.

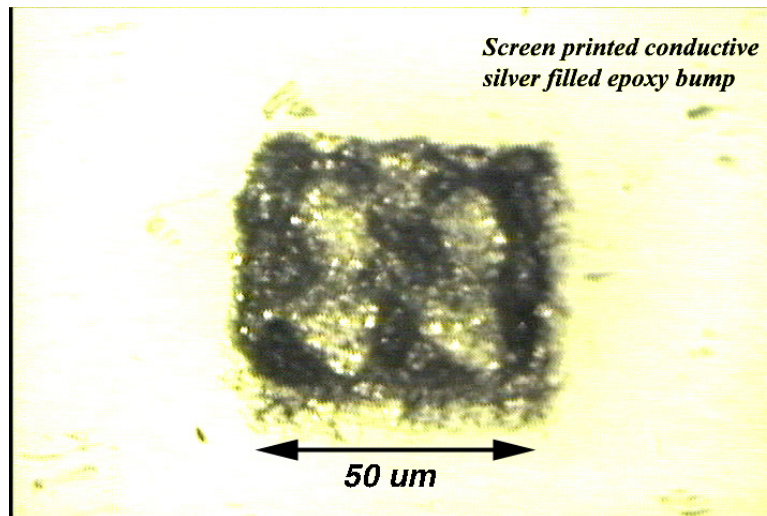


Figure 51: Screen printed conductive epoxy bumps.

3.2.2.8 Precision Die Placement

To enable integration of silicon chips with plastics, a second key technique is required. This technique involves die placement at precise locations on the plastic substrate. A die pick and place instrument (Royce instruments) is used to accomplish this. The semi-automatic die pick and place system is an elegantly simple, low cost machine

for picking die from sawn wafers mounted on adhesive film or waffle packs and placing them on plastic wafers. The die pick-and-place system is designed for die handling where flexibility and rapid setup are of great importance. Capabilities include picking and testing laser diodes, handling die as small as 0.008 in^2 , picking pressure sensitive die and CCD imager chips with non-surface contact option. The instrument, shown in Figure 52, was modified to improve accuracy. The microscope setup was removed and replaced by two microscopes with CCD cameras connected to TV screens. The cameras are at right angles to each other to help minimize alignment error. The alignment marks on the plastic wafer are accomplished by using metal lines, which can be patterned along with the electrical contacts. The silicon wafer, with the chips for embedding, is patterned on the backside to provide alignment marks which are necessary since the silicon chips have to be flipped before being placed on the plastic substrate. The plastic wafer is placed on a vacuum chuck, which is placed on a moving table. The table is capable of movement along the x and y directions. The die is picked up using a vacuum tip, shown in Figure 53, which is capable of movement along the z direction and rotational movement. The die is picked up and then the table moves bringing the plastic substrate under the tip. The table movement can be programmed since the system is provided with a computer. Once the die is approximately above the given location, precise alignment can be done using a puck which controls the fine motion of the table. The puck moves the table both in the x and y directions and also controls the rotation of the tip. The die is brought in close proximity with the plastic substrate and the alignment is completed. Then the tip is brought down and the chip is released. The chip bonds to the conductive epoxy on the bonding pads. Entire wafers can easily be processed using this machine. Die placement locations can be programmed which improves the process speed and offers a degree of automation.



Figure 52: The Royce 110 die pick and place system.

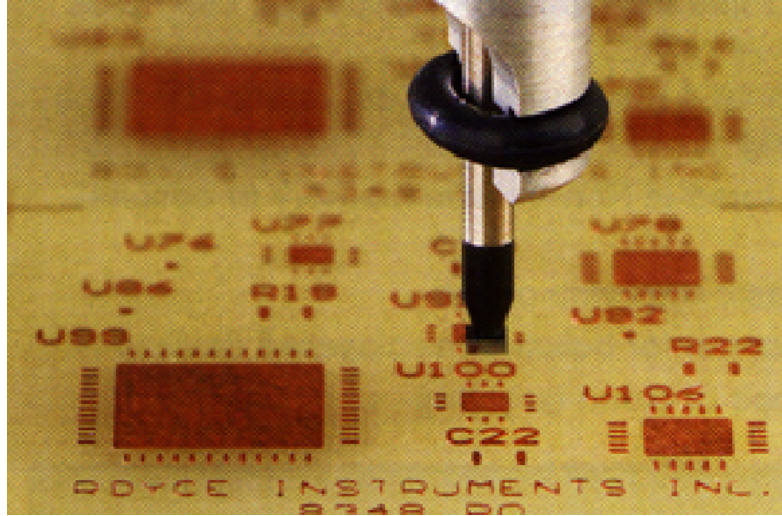


Figure 53: Close up view a silicon chip held by the vacuum tip just before placement.

3.2.2.8.1 Embedding Silicon Chips with Heaters on Plastic

After developing the techniques for precision silicon die placement onto plastic substrates we decided to pick and place chips with simple devices to establish proof of concept. First, metal heaters were mass fabricated on silicon wafers. A blank silicon wafer was taken and a 1 μm layer of thermal oxide isolation layer was grown. Then a layer of aluminum (200 nm) was deposited using an evaporation process. The aluminum was photolithographically patterned into resistive heaters with 20 μm wide heater lines. The substrate was then flipped over and backside alignment marks were patterned photolithographically using photoresist. The wafer was diced and individual dies were transferred to wafer packs.

A cast epoxy wafer with channels was sealed using the lamination process. Then, metal layers of chrome (adhesion layer) and aluminum were evaporated on the laminated surface (Cr/Al, 50/200 nm). The metal layers were then photolithographically patterned to form the metal contacts, interconnects and alignment marks. The contact pads on the plastic wafer were screen printed with silver filled electrically conductive epoxy bumps using the μ -screen printing process. A stainless steel emulsion mask with 50 μm square openings was used. The height of the features obtained was approximately 30 μm . The plastic wafer with the contacts printed with silver epoxy is transferred to the pick and place system and the dies are picked and precisely placed by aligning the alignment marks on the back side of the silicon chip to the alignment metal lines on the plastic substrate. Figure 54 shows pictures of the back side and front side of a chip with a heater which has been placed using the above process. Figure 55 shows a plastic substrate with embedded silicon chips with heaters.

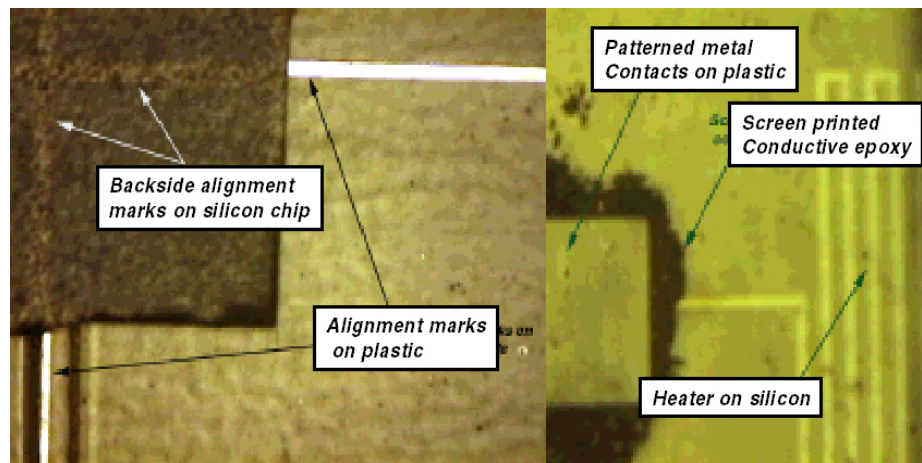


Figure 54: Microscope pictures of the back and front side of a precision placed silicon chip on a plastic substrate.

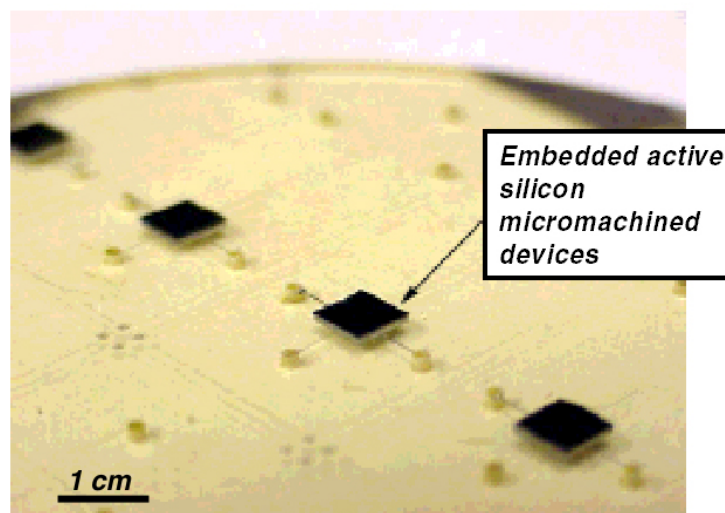


Figure 55: Embedded active silicon micromachined devices on plastic.

4.0 Demonstration Devices

The integration of multiple analysis functions on a single device, and the integration of off-chip device control elements, will provide advantages in miniaturization, system portability, and operational automation. Microfabricated devices with multi-analytical functions for molecular and biochemical analysis have been reported on glass, silicon-glass and silicon-plastic. The use of plastics as substrates for these kinds of devices is becoming a feasible alternative approach as a result of the versatile material properties and the ease of batch fabrication through molding and embossing processes. However, function or active component integration is difficult to achieve with these fabrication technologies. Plastic casting as an alternative technology presents unique advantages. While high-resolution microfluidic features can be fabricated by curing casting material against a microfabricated mold, this technique also allows complex devices with integrated functional components is cast formed through embedding. In this section of the report we discuss numerous demonstration devices, including the first cast formed miniature plastic micro thermal reactor with integrated heating, cooling and temperature sensing elements. These demonstration devices leverage the work that was performed on surface and bulk micromachining techniques, as discussed in section 3 of this final report.

4.1 Paraffin Microactuators

This section describes a new, yet simple, family of microactuators that provide both large displacements and high forces, are simple to fabricate, and are easily integrated with a large variety of microelectronic and microfluidic components. The actuators use the high volumetric expansion of a sealed, surface micromachined patch of paraffin heated near its melting point to deform a sealing diaphragm. Two types of actuators have been fabricated using a simple three mask process. A piston-type structure consisting of a circularly patterned patch of paraffin sealed with a thin metallized parylene diaphragm, on top of a metallic heater element used to melt the paraffin. The second microactuator uses a constrained volume reservoir structure providing hydraulic advantage thus magnifying the center deflection height of the diaphragm.

Steady state diaphragm deflection measurements as a function of heater power have been measured using Wyko NT-2000 and Zygo NewView 5000, non contact, optical surface profilometers. All center deflection measurements correlate to calculated values, within 5% relative error.

Response time of the actuators has also been measured for devices on both glass and SiO₂/Si substrates. Two methods are used to measure the response time. First, a gain-phase analyzer (Hewlett Packard 4194) is used to measure the frequency response of the phase shift of the heater impedance. The frequency at which the phase shift is a minimum is the cutoff frequency of the device. The second measurement technique measures the response with a test circuit [57] which uses an operational amplifier whose time dependent output voltage is proportional to the time dependent resistance of the actuator heater. Both measurement techniques produce similar results.

4.1.1 Microactuation

Currently, many low voltage electromechanical microactuators based on electrostatic, magnetic, bimorph, thermopneumatic, and shape-memory forces have been

fabricated. A parameter that characterizes the ability of an electromechanical actuator to exert work on a load is the actuation energy [24] $F_a \epsilon_a$, where F_a is actuator force and ϵ_a its maximum displacement. Actuators can be scaled and operate under various conditions. Therefore a more suitable parameter is the actuation energy divided by the total actuator volume,

$$P_a = F_a \epsilon_a / V_a \quad (11)$$

when the actuator is operated under low voltages. P_a has units of pressure (or J m^{-3}) and approximately *normalizes* these differences. Table 5 shows P_a extracted for several low voltage microactuators [25, 26, 27, 28]. The majority of these devices can provide either a large deflection but not a large force or vice-versa. It is clear that the electrostatic actuators hold the lowest density and the thermal actuators have the highest [27]. Among these thermopneumatic and shape memory alloy (SMA) microactuators pack the largest density. This is not surprising since they convert electrical to mechanical work through a high density *working substance*. SMA actuators provide very large forces, but their linear

Table 5: Actuation power P_a for several low voltage microactuators. Dimensions used to calculate P_a for the paraffin microactuator: $P_a=100 \text{ MPa}$, $A_a=4\pi \cdot 10^{-8} \text{ m}^2$, $\epsilon_a=10 \times 10^{-6} \text{ m}$, and $V_a=4\pi \times 10^{-13} \text{ m}^3$.

| Actuation Type | $P_a \text{ (J m}^{-3}\text{)}$ |
|---|---|
| Piezoelectric (PZT) | 10^5 |
| Electrostatic (comb-drive) | 10^3 |
| Electromagnetic Thermal Expansion (Ni/Si) | 10^5 |
| Thermo-pneumatic | 10^5 |
| Solid-Liquid Phase Change (acetimide) | 10^6 |
| Shape Memory Alloy (Ni-Ti) | 10^7 |
| Solid-Liquid Phase Change (paraffin) | 10^7 |

deformation strain is limited to about 8% [27]. Therefore SMA often use mechanical advantage schemes to increase displacement. In addition, SMA actuators are typically difficult to fabricate due to film stoichiometry or inherent stress problems. Thermopneumatic actuators provide both large displacements and forces, but their fabrication and integration in large microsystems is often cumbersome [29] due to the necessity of loading the working substance, typically a liquid, into a sealed cavity. The last *bold* entry of Table 5 shows the actuation power of a paraffin solid-liquid phase change microactuator, a new type of microactuation device developed in this research.

4.1.2 Polymer Phase Change Microactuators

Volume dilatation can be induced by phase transformation by varying the temperature of the polymer, thus providing an actuation function for most polymers.

Thermal expansion is related to the internal structure of the material. Intermolecular forces play a more significant role than the intramolecular bonds primarily because the bond lengths between atoms and those between segments of the chain are essentially independent of temperature [30].

Typically, a large increase in molar volume accompanies the solid-liquid phase change (melting) process. Table 6, adapted from [30], lists the measured volume change of several polymers indicating that many polymers experience a large volumetric change, as large as 40%, upon melting. These large changes in volume may be used to provide a large actuation power, as shown previously in Table 5. Hexatriacontane and tetratetracontane are alkanes which provide a large volumetric expansion with relatively low melting temperatures. The Logitech material (0CON-195) is a paraffin wax mixture, used for bonding applications and has a lower volumetric expansion than the pure paraffins but the same melting temperature as hexatriacontane.

Table 6: Thermally induced volumetric changes due to solid to liquid phase change of several polymers.

| Polymer | T _m (K) | Volume change (%) |
|------------------------------|--------------------|-------------------|
| Polyethylene | 410 | 14.8 |
| Polypropylene | 456 | 20.9 |
| Polybutene | 400 | 13.9 |
| Poly(4-methyl pentane) | 510 | 10.4 |
| Polyisobutylene | 320 | 11.3 |
| Polystyrene | 513 | 11.8 |
| Poly(tetra fluoroethylene) | 600 | 21.7 |
| Polyformaldehyde | 460 | 20.5 |
| Poly(ethylene oxide) | 340 | 15.1 |
| Poly(ethylene terephthalate) | 540 | 7.9 |
| Nylon 6,6 | 538 | 11.6 |
| Tetratetracontane | 360 | 38.1 (513K) |
| Hexatriacontane | 348 | 40.9 (513K) |
| Logitech | 345 | 17.7 (423K) |

Mechanical work in the new polymer microactuators is created through the volumetric expansion of the paraffin actuation layer during the melting process as the paraffin is electrothermally heated. As the polymer is heated beyond its melting temperature it expands creating hydrostatic pressure. This pressure, typically in the 6.9 - 69 MPa range [31], is translated to the output of the actuator. Macroscale paraffin actuators have been used for many years with the earliest reported applications in automotive thermostats [32]. Recently, paraffin actuators have been used in other applications [31] and in satellite antenna positioning systems [33]. More recently, endoscopic surgical instruments based on a paraffin actuation mechanism resulting with a stroke of 8 mm against a load of 1 kg have been reported [34]. In general, paraffin actuating films are attractive for microactuator applications for the following reasons: 1) low temperatures can generate large forces 2) paraffins are cheap and plentiful with varying chain lengths 3) expansion characteristics can be *smoothed* for specific applications and 4) paraffins can easily be surface micromachined.

4.1.3 Piston-Type Microactuator

A piston-type microactuator structure has been designed and fabricated using a thin paraffin actuation layer which is sealed with a thin parylene layer. The parylene layer

also serves as the actuator diaphragm. Mechanical work is created through the volumetric expansion of paraffin occurring during the solid to liquid phase change when the paraffin is heated. As the actuator is heated through the melting temperature range of the paraffin, the paraffin expands thus creating hydrostatic pressure translated directly to the diaphragm.

4.1.3.1 Device Structure

Figure 56 shows the piston-type microactuator structure which is based upon the thermal expansion upon melting of a thin layer (typically 5-20 μm) of paraffin. The paraffin layer is deposited over a metallic heater on either glass or SiO_2 /silicon substrates. The paraffin layer is then patterned and sealed with a flexible parylene layer which also serves as the diaphragm.

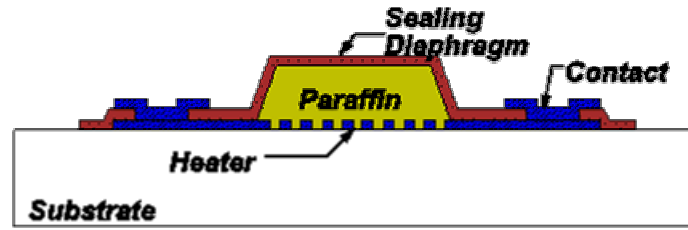


Figure 56: Cross-section of thermally activated paraffin microactuator.

4.1.3.2 Diaphragm Deflection

For the case of a circular plate of radius r_a under a uniformly distributed load p_0 , the lateral displacement is

$$u = c_1 \ln r + c_2 r^2 \ln r + c_3 r^2 + c_4 + p_0 r^4 / 64D \quad (12)$$

where the c 's are constants of integration. For a plate with clamped edge the boundary conditions are

$$u = 0, du/dr = 0 \quad (r = r_a), \quad (13)$$

$$c_1 = c_2 = 0, c_3 = -p_0 r_a^2 / 32D, c_4 = p_0 r_a^4 / 64D \quad (14)$$

The deflection is then

$$u(r) = p_0 / 64D (r_a^2 - r^2)^2 = p_0 r_a^4 / 64D (1 - r^2 / r_a^2)^2 \quad (15)$$

Therefore

$$u(\eta) = u_{\max} (1 - \eta^2)^2 \quad (16)$$

where $\eta = r/r_a$ and u_{\max} is the maximum center deflection of the diaphragm. Equation (16) depends somewhat on the boundary conditions chosen at the rim. The volume underneath the deflected diaphragm is then calculated

$$V_d \approx u_{\max} \int_0^{r_a} 2\pi u(r) r dr = (1/3) \pi u_{\max} r_a^2. \quad (17)$$

This volume must be occupied by the expanding paraffin. Therefore

$$u_{\max} = 3mt_p, \quad (18)$$

where t_p is the thickness of the paraffin layer and m is the percent volume expansion coefficient of the material. For the Logitech material with $m = 0.1$ and film thickness $t_p = 9 \mu\text{m}$ then

$$u_{\max} = 2.7 \mu\text{m} \quad (19)$$

4.1.3.3 Heater Structure

The heating elements used in this research are made of either aluminum (Al) or gold (Au), both E-beam evaporated with a thin chrome (Cr) layer to improve adhesion to the substrate. A serpentine structure was chosen such that a nearly uniform area can be heated. Figure 57 shows the serpentine heater structure for a $200 \mu\text{m}$ diameter circular paraffin layer.

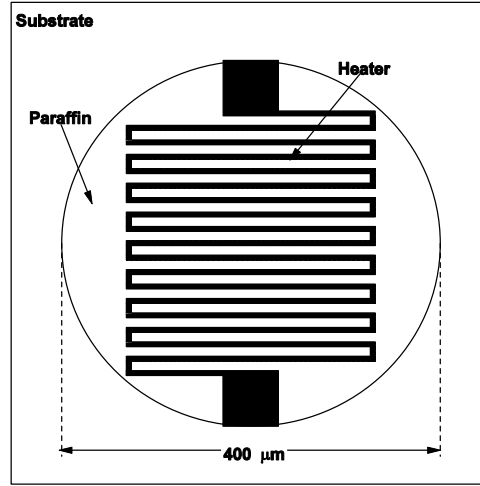


Figure 57: Serpentine heating structure shown with circular pattern representing the patterned paraffin actuating layer.

The heating element generates the energy required to heat the paraffin layer due to electrical resistance (Joule) heating. The heater resistance is defined as

$$R = (\rho_e/t)(L/W) = R_{\square}N, \quad (20)$$

where ρ_e is the electrical resistivity, t is the heater thickness, L the length, W the width, $R_{\square} = \rho_e/t$ is the sheet resistance, and $N = L/W$ is the number of squares. The corners of the heating element have a larger resistance than a straight heater section and have been taken into consideration. For a corner with a ratio of 1 the resistance is 2.5 times larger than a straight section of equal length.

4.1.3.4 Fabrication

The microactuators presented in the previous section have been fabricated using surface micromachining steps at temperatures below 110°C using three lithography steps. Figure 58 shows a simplified process flow. The actuators are fabricated by first patterning

metallic heaters on the substrate followed by the thermal evaporation of the paraffin actuation layer.

Following the deposition of the thin paraffin actuating layer, all processing temperatures must be less than the melting temperature of the paraffin material, which in this research is between 75-87°C. Lithography dehydration and soft bake temperatures are reduced to a value of 65°C for 1.5 hours. Since all feature sizes, patterned with these low temperatures, are large ($< 50 \mu\text{m}$), the low curing temperatures did not significantly affect the performance of the lithography. Standard exposure energy density values (as suggested by photoresist suppliers) for a power density of $5 \text{ mW}/\text{cm}^2$ and subsequent development times have been used for all low temperature lithography steps.

Next, a 5000 \AA thick layer of parylene is vapor deposited on the paraffin film. A Cr/Au ($500/3000 \text{ \AA}$) RIE etch mask layer is next evaporated on top of the parylene film. A $2.7 \mu\text{m}$ thick layer of photoresist (Microposit SC1827) is next spin casted and softbaked at 65°C for 1.5 hours until it is no longer tacky. The resist is then exposed and developed but not hardbaked. Next the Cr/Au layer is wet etched to form the physical etch mask. The parylene and paraffin beneath are then selectively patterned in an $\text{O}_2:\text{CF}_4$ plasma in an Applied Materials 8300 RIE with a water cooled electrode (maintained between $10\text{-}17^\circ\text{C}$). A $2\text{-}4 \mu\text{m}$ thick layer of parylene is next deposited on the paraffin to form the sealing diaphragm. Finally, after etching the contact holes, aluminum contact pads are evaporated and patterned. Figure 59 shows a microscope photograph of a piston-type microactuator with a $9 \mu\text{m}$ thick layer of thermally evaporated paraffin with the Cr/Au etch mask removed clearly showing the heater underneath the transparent paraffin film.

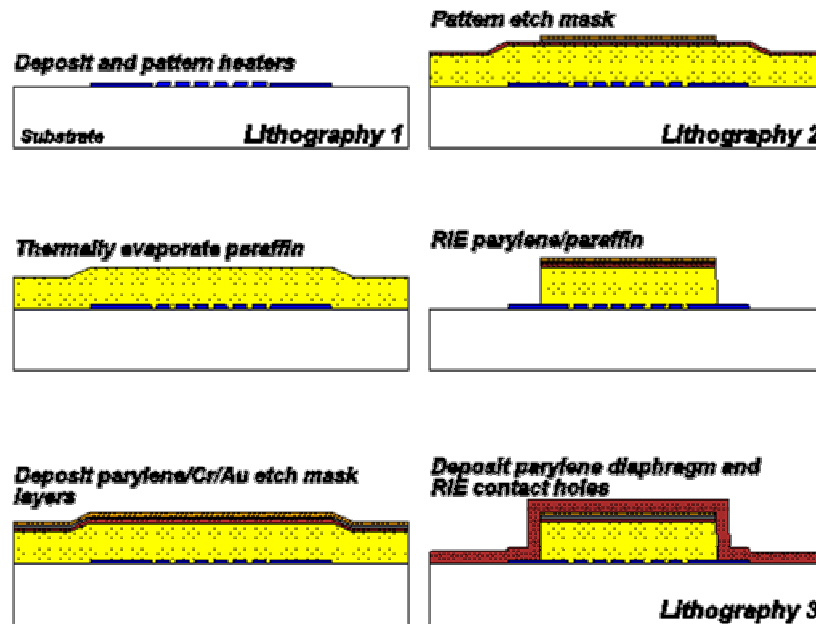


Figure 58: Simplified paraffin microactuator process flow.

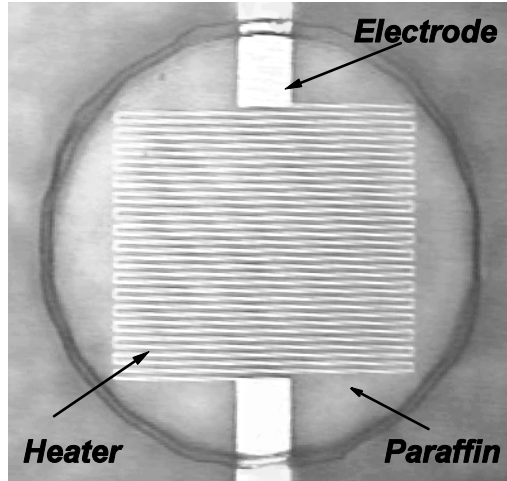


Figure 59: Top view of sealed actuator with heater clearly visible (Cr/Au physical mask has been removed).

4.1.3.5 Experiments

Fabricated actuators have been packaged and wire bonded. The deflection heights for all actuators have been measured optically using a non contact surface profilometer (Wyko NT 2000). The deflection height as a function of electrical input power has also been measured.

4.1.3.5.1 Diaphragm Deflection

The actuator parylene diaphragm profile has been measured for different input powers. Figure 60 shows the diaphragm deflection profile for the piston-type device, with a 9 μm thick Logitech paraffin layer, for different heater voltages. The deflection for the 300 and 400 μm devices was also 2.7 μm . The measured deflection was very close to the calculated value verifying an expansion coefficient of about $m = 0.1$ for thermally evaporated Logitech paraffin films.

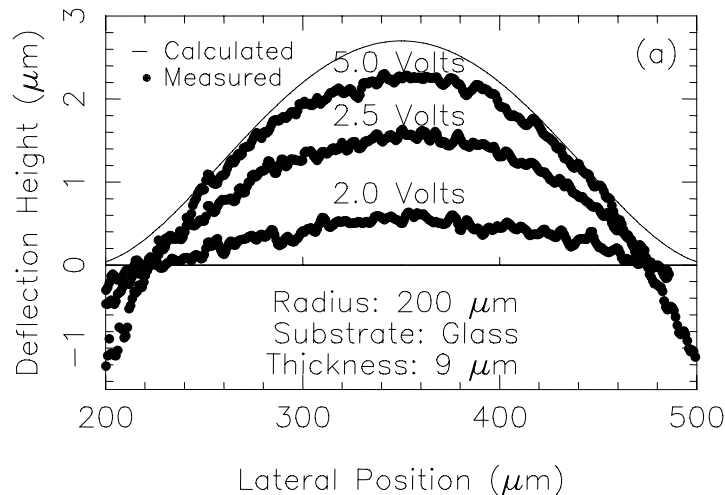


Figure 60: Deflection height measurements (using Wyko NT-2000 non contact surface profilometer) for a 200 μm diaphragm device for three different heater voltages.

Figure 61 shows the measured peak deflection as a function of power for a 200 μm radius diaphragm on a glass substrate. To achieve the 2.7 μm deflection height requires approximately 100 mW input power for the 200 μm radius actuator and about 150 mW input power for the larger 400 μm device.

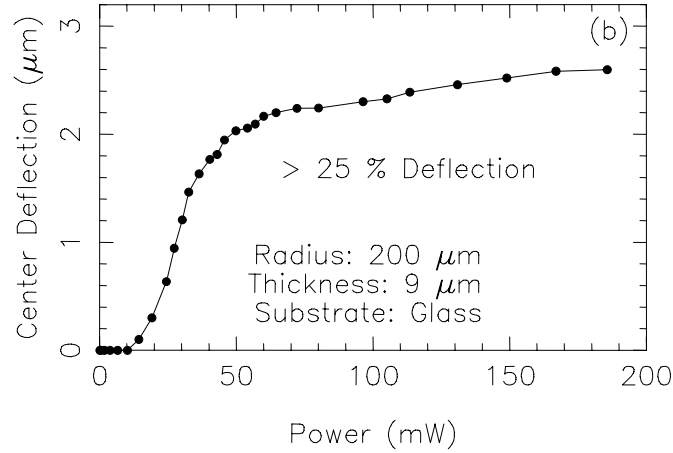


Figure 61: Deflection height measurements (using Wyko NT-2000 non contact surface profilometer) as a function of input power.

4.1.3.5.2 Heater Resistance

The measured resistances deviated from the calculated values mainly due to processing related issues. Since the metal heaters were patterned using wet, isotropic etchants, the geometry of the metal lines is far from ideal. When the width of the heater legs are increased, the effect of patterning is less significant. The actuator heaters for the mass flow control valve were designed to be at least 8 μm wide. The wider heater legs resulted in only 5% deviation between designed and measured resistance values at room temperature.

The metal heaters, in these devices, are operated at relatively large current densities and therefore are susceptible to an electromigration effect. Electromigration is caused by the movement of atoms in a thin metal film due to momentum transfer from the electrons carrying the current. During operation at large current densities, the metal atom movement can induce voids ultimately resulting in an open circuit heater failure. The most common solution is to add a small amount of a heavier metal. Aluminum heaters were found to perform better than gold heaters. Gold heaters were susceptible to open circuit failures with relatively low current densities.

4.1.3.5.3 Electrothermal Models

Electrothermal models of the paraffin microactuator have been developed to predict both steady state and transient behavior of the actuator heater. A simple one dimensional model has been developed to predict the steady behavior of the actuator heater. A three dimensional finite difference electrothermal model of the device has also been constructed and simulated using the *Heating 7.2* software package [59].

Many material parameters are required for evaluating both electrothermal models. For steady state thermal models, thermal conductivity is required for all materials. Figure 8 showed the measured thermal conductivity of the Logitech paraffin. For the one

dimensional model, an average thermal conductivity of the paraffin has been used. For the three dimensional finite difference based model, the temperature dependent thermal conductivity has been used. For transient models the heat capacity of all materials is required. Figure 6 showed the measured heat capacity of the Logitech paraffin used in the three dimensional transient simulations. Emissivity of the parylene diaphragm layer has been calculated using infrared absorption spectra from [36] and used for surface temperature measurements as boundary conditions for the electrothermal model of the paraffin microactuator.

4.1.3.5.3.1 One Dimensional Steady State Model

Figure 62 shows the one dimensional cross-sectional slice of one of the heating elements of the actuator structure. A one dimensional electrothermal model of this slice has been developed and used to estimate the temperature profile of the device. Since the paraffin overlaps the heater onto the substrate, excess heat will be lost from the paraffin to the substrate. This extra heat loss has been accounted for in the model using a shape factor coefficient η . The value of η can be estimated from measured data from the microactuator. The temperature profile of the one dimensional structure can be estimated by solving the one dimensional heat equation.

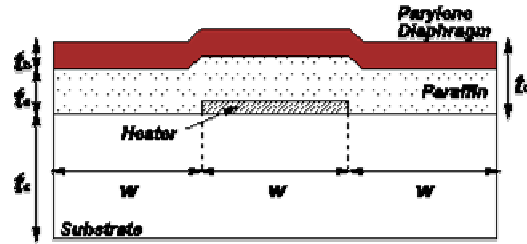


Figure 62: One dimensional schematic of actuator cross-section.

Figure 63 shows the differential element of the microactuator slice of the cross-sectional area. Formulation of the electrothermal model of the actuator begins by first performing a heat balance of the differential element. The actuator heat balance is estimated by

$$q_{\text{total}} = P_g + q_{\text{cond}} + q_{\text{conv}} + q_{\text{rad}}, \quad (21)$$

where q_{total} is the net rate of change of the internal energy of the heater element, P_g is the heat generation term, q_{cond} is conductive heat flow, q_{conv} is convective heat flow, and q_{rad} is radiated heat flow. The total heat flow can be expressed as

$$q_{\text{total}} = c_h \rho_h w z \Delta x [\partial v / \partial t], \quad (22)$$

where c_h is the specific heat of the heater, ρ_h the heater density, w is the heater width, z is the heater thickness and Δx is the length of the differential element.

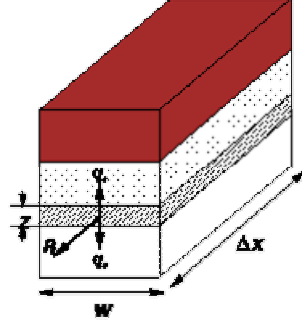


Figure 63: Differential element of actuator used for electrothermal analysis.

The power generation term is given by

$$P_g = J^2 \rho_0(v) w z \Delta x = J^2 \rho_0 w z \Delta x (1 + \chi(v - T_0)). \quad (23)$$

The conductive heat flow in a single element primarily consists of heat flow into the paraffin/parylene layer, q_c , and the heat lost to the substrate, q_s . Combining all terms, taking the limit and neglecting the effect of the convective and radiative heat loss leads to the one dimensional heat equation

$$\partial^2 v / \partial x^2 + \varepsilon v = (1/\alpha_h) \partial v / \partial t - \varphi \quad (24)$$

where

$$\varepsilon = \beta + \gamma \Delta \chi \varphi = \Delta \chi T_0 - T_{sp} - \gamma T_{sg} - \delta \quad (25)$$

$$\alpha_h = \kappa_h / c_h \rho_h, \quad (26)$$

$$\beta = v z t_p (\kappa_p / \kappa_h), \quad (27)$$

$$\gamma = (1/z t_p) (\kappa_g / \kappa_h) a \quad (28)$$

$$\delta = J^2 \rho_0 / \kappa_h, \quad (29)$$

where $v = T(x) - T_0$ ($T_0 = 300$ K), χ is the linear temperature coefficient of resistance, α_h is the thermal diffusivity of the heater material, J is the current density, ρ_0 is the electrical resistivity at temperature T_0 , κ_h is the thermal conductivity of the heater material, η is the shape factor coefficient to compensate for the heat loss from the paraffin film to the substrate, T_{sp} is the top surface temperature of the parylene diaphragm layer and T_{sg} is the bottom surface temperature of the glass substrate layer. Thermal conductivity, κ_c , is the composite thermal conductivity of the paraffin and parylene regions

$$\kappa_c = (\kappa_{pa} t_a + \kappa_{pb} t_b) / (t_a + t_b), \quad (30)$$

where κ_{pa} and κ_{pb} are the thermal conductivities of the paraffin and parylene layers, respectively. Equation (24) is solved subject to the boundary conditions $v(x=0, t) = v(x=L, t) = v(x, t=0) = T_0$, $T_{sg} = T_{sp}$ as a function of input power. Using the method of separation of variables, we get

$$v(x, t) = v_{ss} + v_{tr}, \quad (31)$$

where v_{ss} is the steady state solution and v_{tr} is the transient temperature solution which is not applicable for this model. The average steady state temperature of the heater can be calculated

$$\underline{v}_{ss} = 1/L \int_0^L v_{ss} dx, \quad (32)$$

which after integration becomes

$$\underline{v}_{ss} = \phi/\varepsilon - (\phi/\varepsilon - T_0) \tanh(\sqrt{\varepsilon} L/2) / \sqrt{\varepsilon} L/2. \quad (33)$$

Evaluation of Eq. (25) requires material parameters as well surface temperatures of the parylene diaphragm layer (T_{sp}) and the bottom surface of the glass substrate (T_{sg}). For all operating conditions, it is assumed that T_{sg} does not significantly increase above ambient temperature because the glass substrate is 1 mm thick. The parylene diaphragm, however, is expected to increase above ambient temperature depending on the heater input power. The parylene surface temperature has been measured under steady state conditions using an infrared detector (Inframetrics, Inc. SC 1000 with close-up lens adaptor) with 100 μm spot size with a 3.4 - 5.0 μm spectral band. Variables important for surface temperature measurements are distance between sample and detector and surface emissivity. The sample was measured to be 10 cm from the detector for all temperature measurements. The average emissivity is calculated numerically in the 3.4 - 5.0 μm spectral band, determined by the infrared detector using the infrared absorption characteristics of an 18 μm thick parylene film, as shown in Figure 64. An emissivity of $\varepsilon = 0.7$ has been used for all infrared measurements. Figure 65 shows measured diaphragm surface measurements as a function of heater input power.

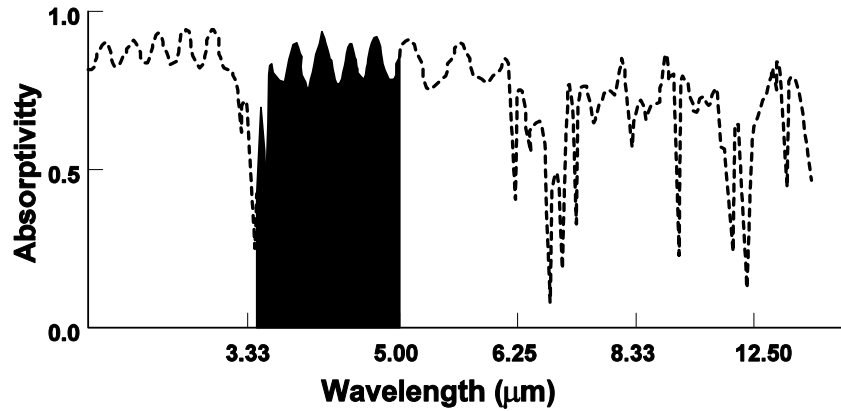


Figure 64: Infrared absorption spectra of an 18 μm thick parylene film for estimating surface emissivity in the 3.4 - 5.0 μm spectral band.

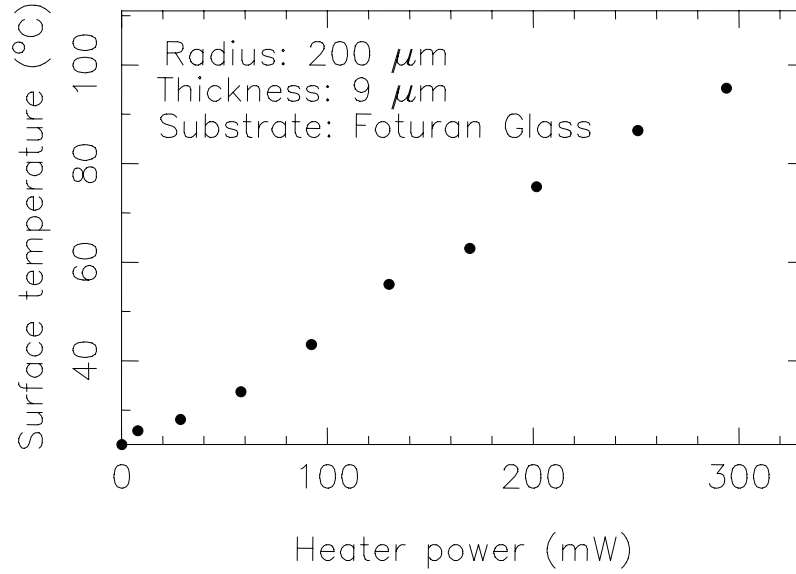


Figure 65: Measured parylene diaphragm surface temperature as a function of heater power.

Assuming the paraffin actuation material occupies a circular region, with a radius of 200 μm and thicknesses: $t_a = 10 \mu\text{m}$, $t_b = 4 \mu\text{m}$, $t_s = 1 \text{ mm}$, $L = 5.22 \text{ mm}$, $z = 0.5 \mu\text{m}$ and $\eta = 3.52$ together with the appropriate thermophysical constants, the temperature profiles have been calculated. Figure 66 shows the calculated steady state temperature profile of the heater. A required power generation P_g of about 92.1 mW is required to raise the temperature of the paraffin to about 100°C on glass substrates.

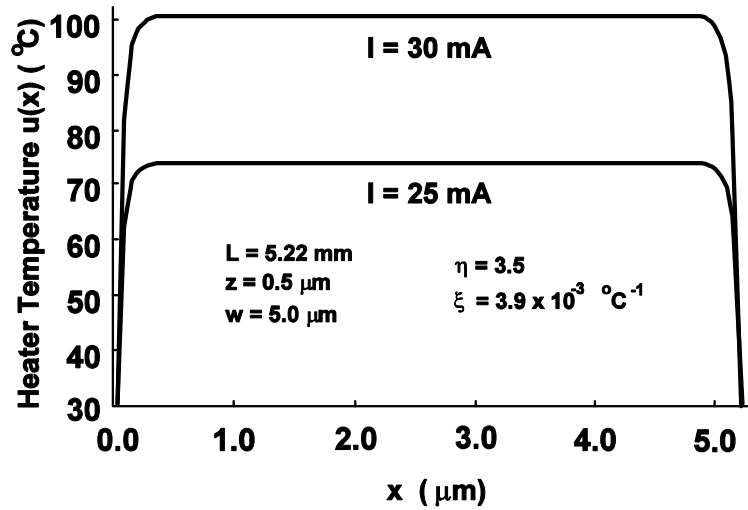


Figure 66: Example of the steady state temperature profile for an aluminum heater on a Foturan glass substrate for different currents.

4.1.3.5.4 Electrical Characteristics

The steady state electrical characteristics of the actuator can be derived from the heater temperature characteristics

$$R_h = R_0(1 + \chi(\underline{y} - T_0)). \quad (34)$$

Steady state resistance as a function of temperature has been measured. Paraffin microactuators were mounted on laminated circuit boards and wire bonded. The devices were placed in a Thermolyne 48000 laboratory furnace with electrical feed-throughs connected to an Hewlett Packard 34401A digital multimeter with 8 digit accuracy to measure heater resistance. The furnace was increased from room temperature (23°C) to 150°C in increments of 5°C. The devices were soaked at each temperature for 2 hours before a resistance value was recorded. Figures 67(a) and (b) show the temperature dependence of the actuator heaters for the 400 and 600 μm diameter actuators, respectively.

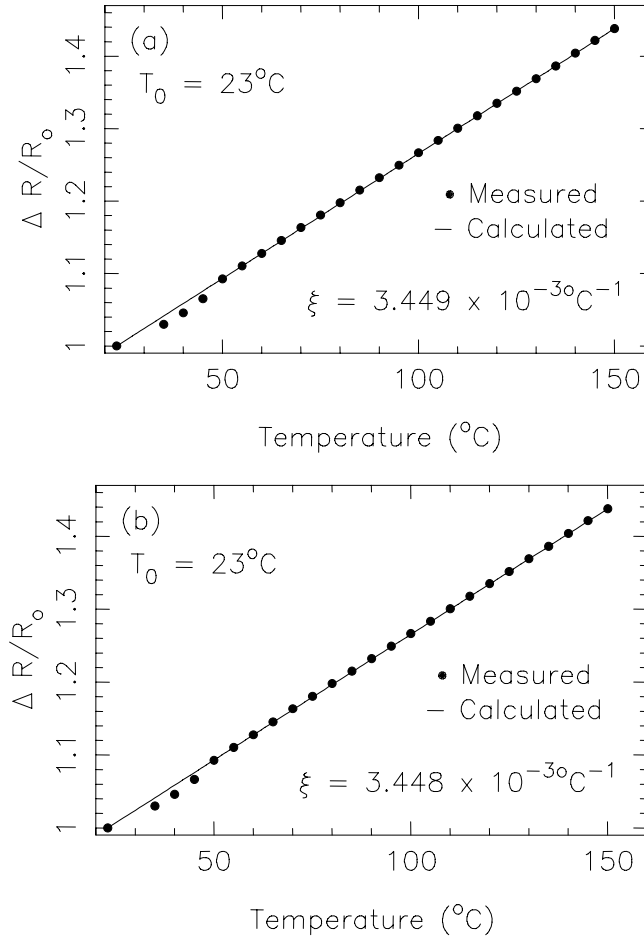


Figure 67: Measured steady state heater resistance as a function of temperature (a) 400 μm diameter actuator (b) 600 μm diameter actuator.

The heater voltage as a function of current and average steady state temperature can be expressed as

$$V_h = IR_h = (I\rho_0 L/wz)(1 + \chi(\underline{v} - T_0)) = V_{hss} + V_{htr} \quad (35)$$

Equation (35) accurately predicts the voltage-current relationship of common materials for low current densities. However, for larger current densities, the heating effect

dominates resulting in a nonlinear voltage-current relationship. Figure 68 shows the measured voltage-current characteristics for a circular 200 μm radius paraffin microactuator with a 5000Å thick aluminum heater.

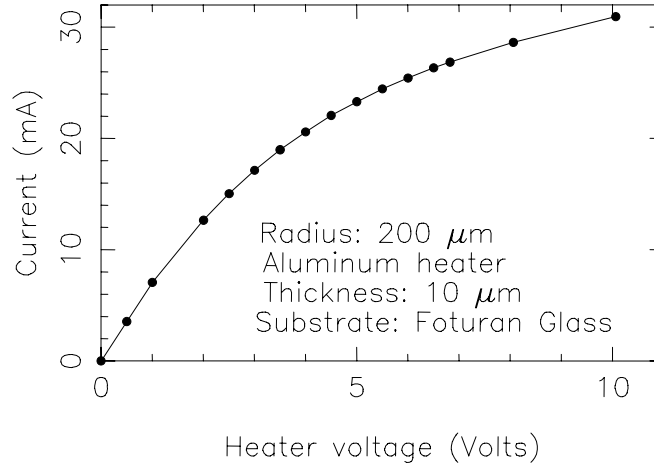


Figure 68: Measured aluminum heater voltage-current characteristics for electrothermally actuated paraffin microactuator.

4.1.3.5.5 Three Dimensional Finite Difference Models

For the three dimensional steady state and transient heat conduction model of the paraffin microactuator with heat generation, Eq. (36) can be solved numerically using the finite difference technique with all relevant boundary conditions.

$$\nabla^2 v(r,t) = 1/\alpha \partial v(r,t)/\partial t + 1/k P(r,t). \quad (36)$$

The *Heating 7.2* [59] finite difference code has been used to simulate the three dimensional thermal behavior of the paraffin microactuators. The microactuator structure was discretized for input into the *Heating 7.2* software.

4.1.3.5.5.1 Steady State Model

For steady state solutions, the thermal conductivity and density of all materials are required. Thermal conductivity and density of the glass substrate, evaporated aluminum heater and parylene diaphragm are assumed to be temperature independent. Figure 8 showed the measured thermal conductivity of the Logitech paraffin which is highly temperature dependent. Figure 4 showed the measured specific volume (inverse of density) of the Logitech paraffin which is highly temperature dependent. The bottom substrate and top diaphragm surface temperatures are the model boundary conditions. The bottom surface of the glass substrate is assumed to remain near room temperature for all thermal modeling of the device. The top diaphragm surface has been measured in a previous section of this report.

The effects of convective heat transfer have been considered for the three dimensional model. Forced convection is assumed negligible as no detectable airflow was induced across the microactuator surface. The effect of free convection (or natural convection) was estimated by calculating the Grashof number for the actuator structure. The Grashof number plays the same role in free convection as the Reynolds number plays

in forced convection. The Grashof number (G_{RL}) is a ratio of the buoyancy force to the viscous force acting on the field

$$G_{RL} = g\beta(T_s - T_\infty)L^3/\nu^2 \quad (37)$$

where, g is the gravitational acceleration, β is the expansion T_∞ ambient temperature, ν is the kinematic viscosity and L is the characteristic length of the surface. All fluid properties are used at the average temperature $T_f = \beta(T_s - T_\infty)/2$. The Grashof number has been calculated for three different heater conditions with air as the surrounding fluid. All fluid properties were taken from tabulated data [60]. For a horizontal surface the characteristic length is

$$L = A_s P, \quad (38)$$

where, A_s is the actuator diaphragm surface temperature and P its perimeter. Table 7 shows the calculated Grashof numbers for different heater input power levels.

Table 7: Calculated Grashof numbers as a function of heater input power.

| Power (mW) | T_s (°C) | Grashof number |
|------------|------------|-----------------------|
| 58.00 | 33.70 | 6.98×10^{-5} |
| 169.12 | 62.80 | 2.31×10^{-4} |
| 293.79 | 95.30 | 3.28×10^{-4} |

Due to the low Grashof numbers, the free convection effects are assumed Negligible [61]. The heat losses due to radiation, although small, have been included in the three dimensional model

$$q_{rad} = \varepsilon A \sigma (T_s^4 - T_\infty^4), \quad (39)$$

where, ε is the surface emissivity, A the area of the actuator diaphragm and σ is the Stefan-Boltzmann constant. The surface emissivity of the parylene diaphragm in the spectral range of the infrared measuring instrument was calculated earlier in this section and the value of $\varepsilon = 0.7$ is used for modeling the radiative heat loss term in the three dimensional model. The steady state model was input to *Heating 7.2* for the three different heater input power values using the boundary conditions and material parameters discussed earlier. The steady state problem was solved using the steady state overrelaxation (SOR) technique [59] with a steady state convergence of 10^{-4} and overrelaxation factor $\beta = 1.9$. Computation time on a Sun SPARC10 workstation was 14 minutes and 4 seconds. Figure 69 shows steady state simulation results for three different heater power levels. The diagrams show the temperature profiles across the surface of heater structure.

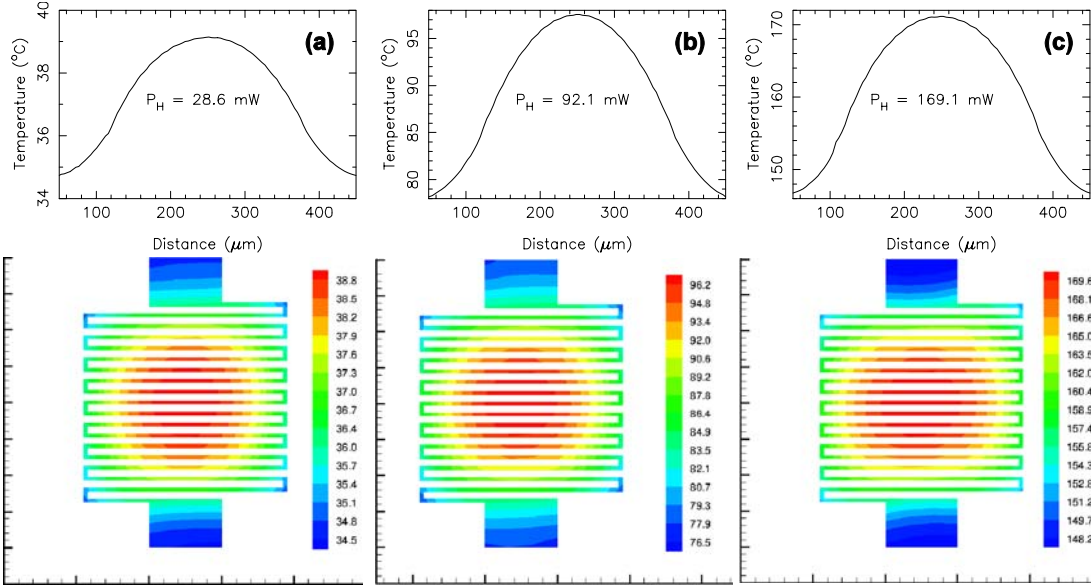


Figure 69: Three dimensional steady state heater simulation results for different heater electrical input power values.

4.1.3.5.2 Transient Response Model

The transient response of the paraffin microactuator has been modeled using the three dimensional finite difference model developed in the previous section with the inclusion of the measured thermally dependent heat capacity material parameters and the latent heat of transition material parameter for the paraffin actuating layer. The heat capacity for the glass substrate, aluminum heater and parylene diaphragm are assumed to be independent of temperature. Figure 6 showed the measured heat capacity as a function of temperature for the Logitech paraffin. Transient models were constructed for simulation with *Heating 7.2* using the steady state results for heater input electrical powers of 169 and 92 mW with diaphragm temperatures of 62.8 and 43.3°C, respectively, as the initial conditions for the transient calculations. Since the actuator model has been constructed on a glass substrate, the frequency response of this device is determined by the cooling rate of the actuation layer. The transient solution was found using Levy's explicit method with a 10^{-7} time step. The transient solution for an initial heater temperature of 171°C was found in 208 minutes using a Sun SPARC10 workstation. Figure 70 shows the calculated cool down time of the actuator heater for the two initial temperatures. For the 171°C initial heater temperature, the heater cools down in about 40 ms (25 Hz), roughly consistent with measurements on devices with the same dimensions.

The transient responses of the actuator heaters have been measured. First, the time response of the microactuator has been measured indirectly. Figure 71 shows the test circuit [57] used to measure the time response of the microactuator. The circuit driving voltage $V_i(t)$ with a period 2Δ is used to alternate heating and cooling cycles of the actuator with switching diodes D_1 and D_2 . The amplifier output is proportional to the thermal response time of the actuator as the input source is cycled from positive to negative.

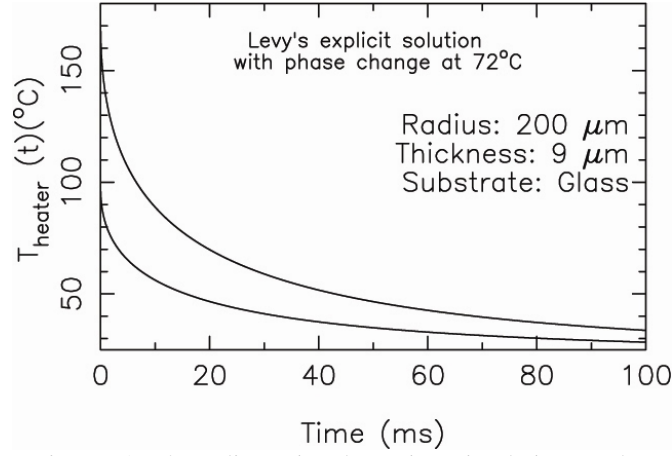


Figure 70: Three dimensional transient simulation results.

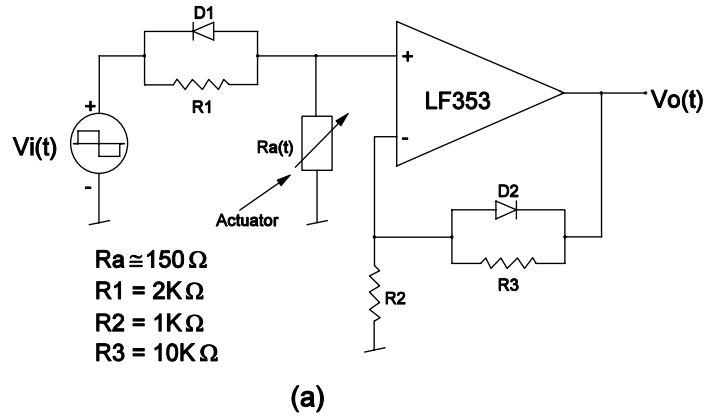


Figure 71: Test circuit used to measure actuator response time.

When D_1 and D_2 are forward biased (negative cycle), the driving voltage is applied across the terminals of the actuator heating element for time Δ and the current through the heating element in this cycle is

$$I_{a1}(t) \approx V_i(t)/R_a. \quad (40)$$

In the positive cycle, D_1 and D_2 are reversed biased and therefore

$$I_{a2} \approx V_i(t)/R_1 \text{ since } R_1 \gg R_a(t). \quad (41)$$

Since $I_{a1} \gg I_{a2}$, this is the *cooling* cycle and $R_a(t)$ decays to a lower value. The output of the amplifier is [57]

$$V_o(t) \approx R_a(t) V_g/R_1(1 + R_3/R_2) \propto R_a(t). \quad (42)$$

Figure 72 shows that during the cooling cycle the output voltage reaches a minimum in about 35 ms, which is consistent with the previous measurement for devices on glass

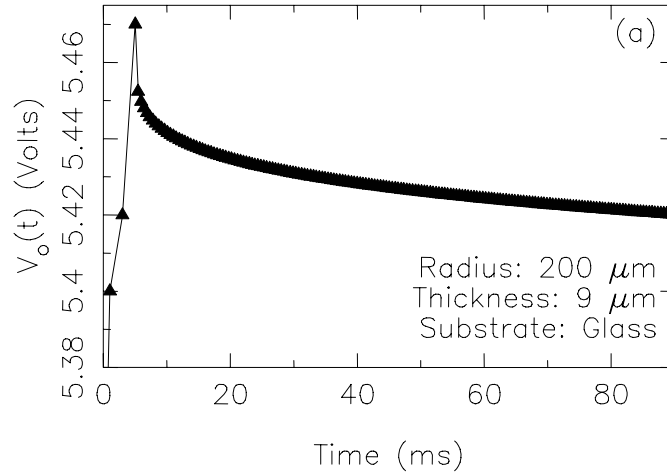


Figure 72: Measured response time for a 200 μm radius diaphragm Logitech actuator on a glass substrate.

substrates. Response times for silicon devices of about 3 ms (333 Hz) have been measured. Measured response times ranged from 30 to 50 ms for 400 to 200 μm radius devices which is consistent with the high thermal storage of the latent heat of fusion for paraffin equal to about 175 kJ/kg. For the SiO_2 /silicon substrate devices, the time constant is reduced by a factor of 10 (3-5 ms) at the expense of much larger power dissipation. Phase measurements of the heater impedance were also measured with a Hewlett Packard 4194 Gain Phase Analyzer (HP4194). The minimum in the phase response indicates a maximum response time of the device. Figure 73 shows the results for an actuator with 400 μm diameter, 9 μm thick actuating film on a 1 mm thick glass substrate. The minimum phase response indicates the upper cutoff frequency of about 30 Hz for this device.

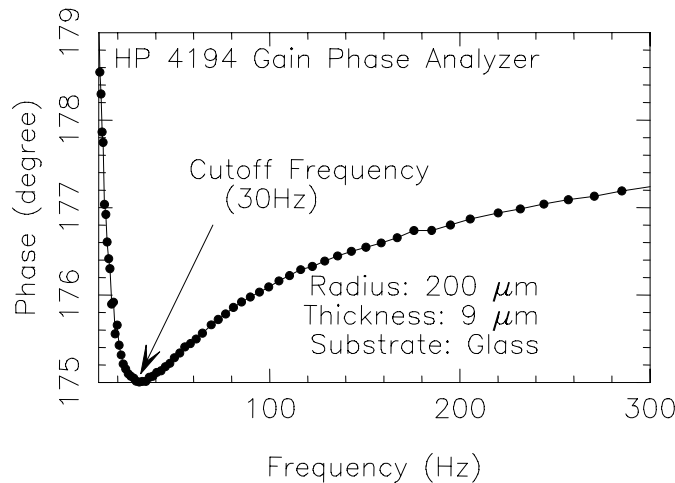


Figure 73: Measured heater phase response for the 200 μm radius diaphragm showing 30 Hz cutoff.

4.1.4 Hydraulic Advantage Structure

The center diaphragm deflection can be further increased by rigidly confining a portion of the diaphragm, thus allowing a smaller surface area of the diaphragm to deflect an increased distance. A much larger deflection is achieved from the microactuator

because the volume is constrained on the edges by a diaphragm, reaching a deflection between 100 - 125% of its thickness at its peak.

4.1.4.1 Device Structure

Figure 74 shows that this is practically achieved by introducing etched support posts for the sealing diaphragm such that $r_o > r_a$. When the paraffin is electrothermally heated beyond its melting point it expands. Since the paraffin must expand, and the outer ring of the diaphragm is constrained with posts, the molten paraffin will flow towards the center of the device thus deflecting the unconstrained region of the diaphragm. The posted regions essentially form a reservoir of expanding wax that must flow and expand in the central region only. Since this structure introduces an increased deflection height, then less material is required, thus improving the response of the microactuator.

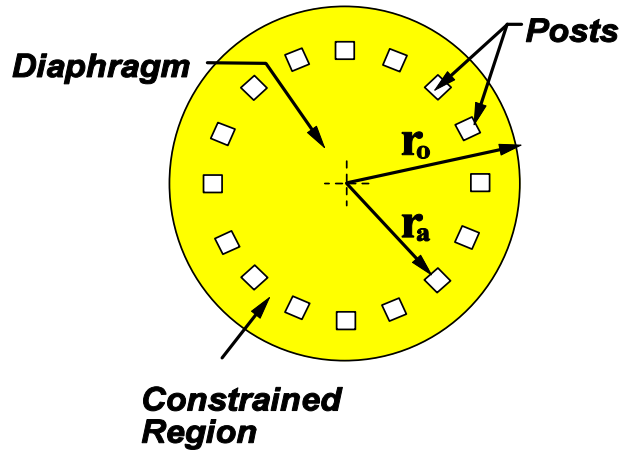


Figure 74: Top view of microactuator diaphragm with posts.

Based on experiments, the dimensions of the etched posts were chosen such that the posts were large enough to withstand the pressure of the expanded paraffin while small enough not to hinder the inward flow of the molten paraffin. The designed posts are square and 10 μm on a side.

4.1.4.2 Diaphragm Deflection

The deflection of the hydraulic advantage diaphragm when actuated is easily calculated and shows that the deflection height is magnified by factor which is the square of the ratio of the radii.

$$u_{\max} = 3mt_p(r_o/r_a)^2 \quad (43)$$

For this design, radius dimensions are chosen such that $r_o = 2r_a$ resulting in an ideal central diaphragm deflection magnification factor of four. For a film thickness of 3 μm , the central deflection is

$$u_{\max} = 3.6 \mu\text{m} \quad (44)$$

4.1.4.3 Fabrication

Actuators with hydraulic advantage have been fabricated using the same process steps described previously, however, the third lithography mask was changed defining etch holes in the physical mask for the posts. Figure 75 shows microscope photographs of an actuator with support posts.

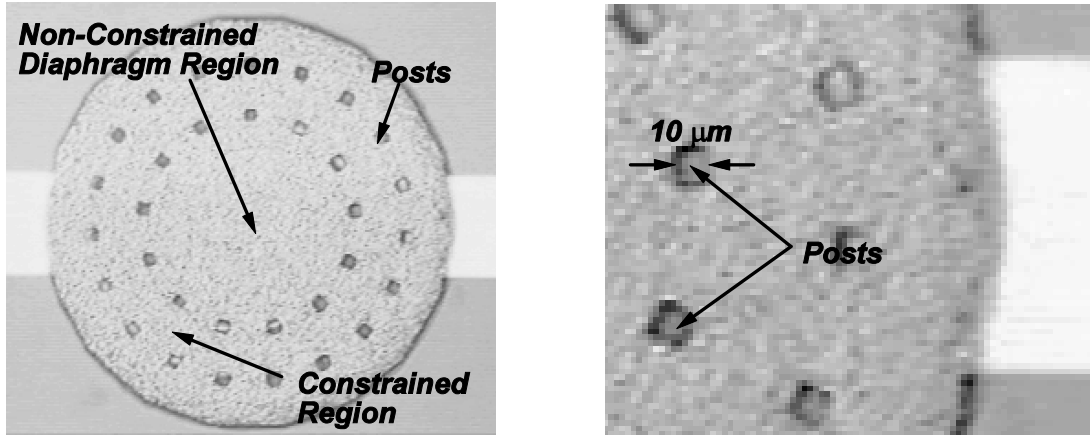


Figure 75: Top view of the constrained diaphragm microactuator with and an evaporated paraffin thickness of 3 μm and 600 μm diameter diaphragm.

4.1.4.4 Experiments

Fabricated actuators have been packaged and wire bonded. The deflection height for all of the actuators has been measured optically using a non contact surface profilometer (Wyko NT 2000). The deflection height as a function of electrical input power has also been measured.

4.1.4.4.1 Diaphragm Deflection

Figure 76 shows the measured diaphragm deflection profile for a 400 μm partially constrained diaphragm device. The center diaphragm deflection was about 3.1 μm , which is very close to the calculated value of 3.6 μm , assuming an expansion coefficient of $m = 0.1$. The constrained regions were not completely restrained from moving, shown in Figure 76, accounting for the discrepancy between the measured and calculated center diaphragm deflection distances. At higher input voltages, the diaphragm in the constrained regions expanded indicating a post failure or failure of the flexible parylene layer to withstand bending between the support posts. Although the measured deflection height deviated from the ideal estimation, the device presented demonstrates the concept of using the hydraulic advantage principle to improve the performance of the paraffin microactuators. Figure 77 also shows the measured deflection as a function of input power. Note the reduction in power consumption in the pinned diaphragm device due to the volume reduction and thinner film.

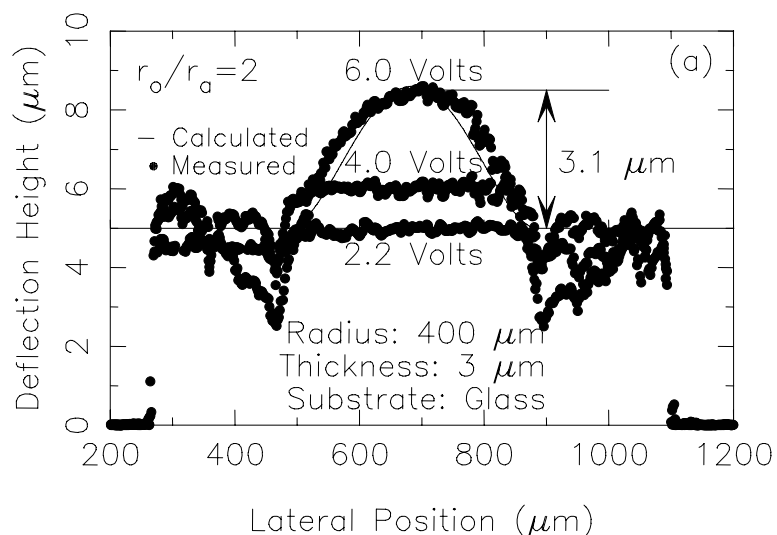


Figure 76: Measured diaphragm deflection of a 400 μm radius pinned diaphragm device with a 3 μm thick paraffin layer as a function of input power.

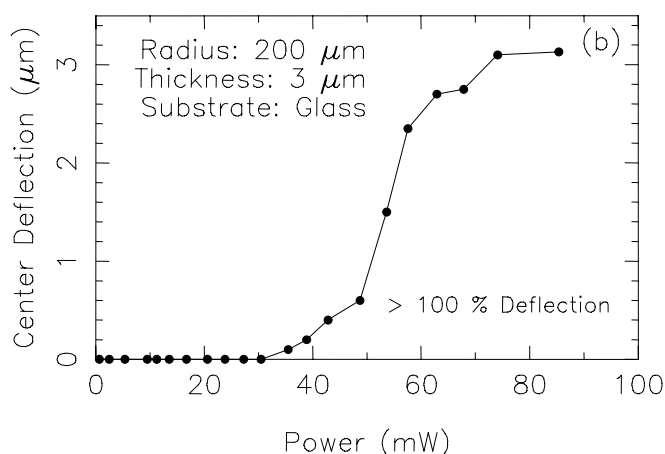


Figure 77: Measured deflection height as a function of input power for the 400 μm radius pinned diaphragm device with a 3 μm thick paraffin layer.

Microactuators with the hydraulic advantage structure have been fabricated using 1:4 and 2:3 OCON-195 $\text{C}_{36}\text{H}_{74}$ compound paraffin mixtures resulting in volumetric expansions of 22% and 19%, respectively. Figure 78(a) shows the measured deflection height versus input power for devices on silicon substrates with 1:4 compound actuating films. The power dissipation was approximately 10 times for the same deflection previously. Figure 78(b) shows measured results for a pinned diaphragm device with a 2:3 Logitech $\text{C}_{36}\text{H}_{74}$ compound actuation layer which produced peak center deflection heights ranging from 2.1 - 3.1 μm with a paraffin thickness of 3 μm . Actuators were constructed on both glass and silicon substrates. The glass devices required between 50 - 200 mW of power and had response times between 30 - 50 ms. The response times for silicon devices were much faster (3 - 5 ms) at the expense of a larger actuation power ranging between 0.5 - 2 W. The large volume expansion materials are much more

efficient in terms of power dissipation and response time because thinner films can be used to obtain the same deflection.

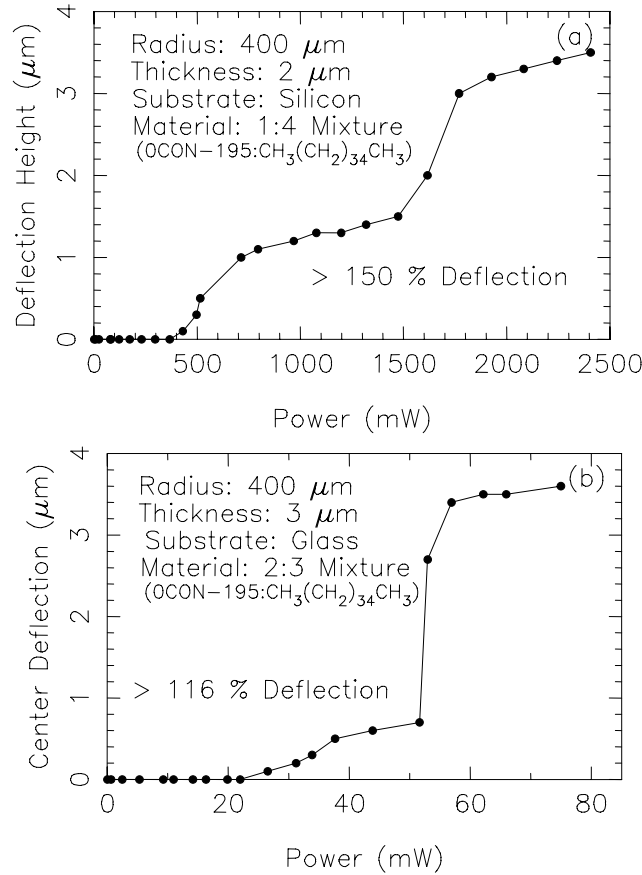


Figure 78: Measured deflection vs. input power for the partially constrained diaphragm actuator (a) 1:4 LogitechC₃₆H₇₄ layer (b) 2:3 Logitech:C₃₆H₇₄ layer.

4.2 Microvalves

Microvalves can be divided into two groups: active and passive. Active valves use an actuator to control the valving action, while passive valves do not contain the active actuator element. In general, active microvalve performance can be characterized by a set of measurable quantities. The important valve characteristics are ease of fabrication, low power consumption, flow range, leak rate, size, scalability and potential for batch fabrication.

Passive microvalves are typically used as check valves [14] or flow control components for micropumps [15]. Passive valves can also be used as rectifiers to regulate gas or liquid flow [16]. The relationship between the flow rate and pressure is analogous to electrical current and voltage relationship in a semiconductor diode. Typically, a small reverse gas or liquid leakage, a high breakdown pressure and fast response time are the most important device characteristics.

Active microvalves are devices which use a mechanical actuator as the flow control mechanism. The mechanical actuator is the physical mechanism which can precisely control the flow of gas or liquids. A key advantage of active versus passive

valves is that the active devices can be operated despite the differential pressure across the device.

Over the past decade elaborate microfluidic valves have been constructed based on electrostatic, magnetic, piezoelectric, bimorph and thermopneumatic actuation methods [15, 5, 1]. Because of their complexity, the majority of these devices are made by bonding many thick glass or silicon substrates together; some even requiring external cavity fills. This bulk micromachining construction technique makes the valves large and difficult to integrate with other components in microfluidic systems.

Key to the successful fabrication of these active microvalves is a reliable actuation mechanism which provides reasonably fast response times, low power requirements, low leak rates, simple fabrication process and can be easily integrated with the microvalve structure and other microfluidic components.

Active microvalves developed in this research use a microactuator based on the thermal expansion of a sealed, surface micromachined patch of high actuating power paraffin film. The working substance is in solid state throughout the fabrication process permitting the fabrication of many actuators on the same die without the need for working fluid filling or post-process sealing operations.

4.2.1 Active Blocking Microvalve

This section presents the design, fabrication and testing of a new, active, normally-open blocking microvalve that uses the piston-type paraffin microactuator. The entire structure is batch-fabricated by surface micromachining the actuator and channel materials on top of a single substrate. The paraffin actuated microvalves are suitable for applications requiring many devices on a single die, low processing temperatures, and simple, non-bonded process technology. Gas flow rates in the 0.01 - 0.1 sccm range have been measured for several devices with actuation powers ranging from 50 - 150 mW on glass substrates. Leak rates as low as 5×10^{-4} sccm have been measured. Both nickel electroplated and parylene valves have been fabricated and differ only in the reservoir and channel structural materials.

4.2.1.1 Device Structure

Figure 79 shows the cross-section of the blocking microvalve which has a 500 μm diameter inlet hole through the 1 mm thick substrate leading to a reservoir. The reservoir is connected to a 3 mm long capillary channel with a $200 \times 10 \mu\text{m}^2$ cross-sectional area.

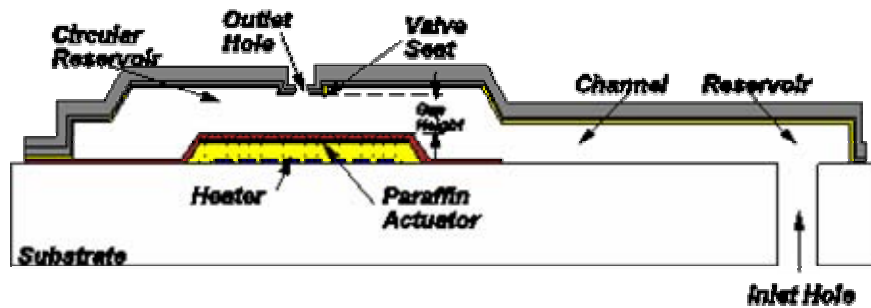


Figure 79: Cross-section of blocking microvalve.

The channel leads to a circular reservoir where the actuator and outlet hole are located. Directly above the actuator is the 100 μm diameter outlet hole. When the actuator is activated, the diaphragm is deflected vertically pressing the diaphragm layer against the valve seat thus sealing the outlet hole. Since paraffin can provide very large actuation forces, a very good seal is easily attained with low actuation power.

The distance between the diaphragm and the valve seat is the gap height, which is determined by the deflection height on the actuator. For this design, the deflection distance was about 3 μm , therefore a 1.3 μm gap height was used, ensuring a good seal between the diaphragm and valve seat. Larger deflection distances are possible using thicker paraffin films, alternative paraffin materials (larger volumetric expansion), or mechanical advantage schemes [62]. In addition, the gap height can be easily increased using a thicker *gap setting* sacrificial photoresist layer as will be shown in the next chapter.

4.2.1.2 Steady State Gas Flow Model

The steady state gas flow in the gas valves developed in this research can be described by flow models developed for the vacuum industry [63, 64, 65, 66].

Flow Regimes

The gas flow in the microvalve can be in a *viscous state*, a *molecular state* or in a state which is intermediate between these called the *transition state*. The mean free path is very small at atmospheric pressure so the flow of gas is limited by its viscosity. At low pressures when the mean free path of the molecules is similar to the channel, the flow is governed by viscosity as well as by molecular phenomena; that is intermediate flow. At very low pressures where the mean free path is much larger than the channel dimensions, the flow is molecular.

In the range where the state of the gas is viscous, the flow can be turbulent or laminar. Thus the flow can be turbulent, laminar, intermediate, or molecular. The limit between the turbulent and laminar flow regimes is defined by the value of the Reynolds number. The Reynolds number is a dimensionless quantity expressed for round channels by

$$R_e = \rho v D_h / \eta, \quad (45)$$

where ρ is the gas density, v the velocity, η the viscosity, and D_h the hydraulic diameter of the channel. For Reynolds numbers larger than 2100, the flow is entirely turbulent whereas when $R_e < 1100$ the flow is entirely laminar. The exact value of R_e for which the flow changes from turbulent to laminar is dependent on the surface roughness of the channel among many other factors, but is valid for most cases [64]. All viscous state flows in this research are assumed to be in the laminar flow regime.

The limit between laminar, intermediate, and molecular flow are described by the value of the Knudsen number K_n a dimensionless quantity defined as

$$K_n = D_h / \lambda, \quad (46)$$

where D_h is the hydraulic diameter of the channel and λ is the mean free path calculated using the average pressure in that section of channel. For circular channels, the hydraulic parameter is simply the channel diameter. For rectangular channels, different hydraulic diameter expressions have been defined [67]. In this work, the hydraulic diameter for rectangular channels is

$$D_h = 4A/P, \quad (47)$$

where A is the area of the cross-section and P is the perimeter of the channel cross-section. The Knudsen number range is

$$\begin{aligned} K_n > 110 &: \text{Laminar flow regime} \\ 1 < K_n < 110 &: \text{Transition flow regime} \\ K_n < 1 &: \text{Molecular flow regime} \end{aligned}$$

Figure 80(a) shows the channel dimension labels used for all rectangular channel sections. Figure 80(b) depicts the cross-section of the circular region of the valve structure. The effective width of the channel is the circumference of the aperture hole (outlet hole). The length of the channel is $L = r_2 - r_1$.

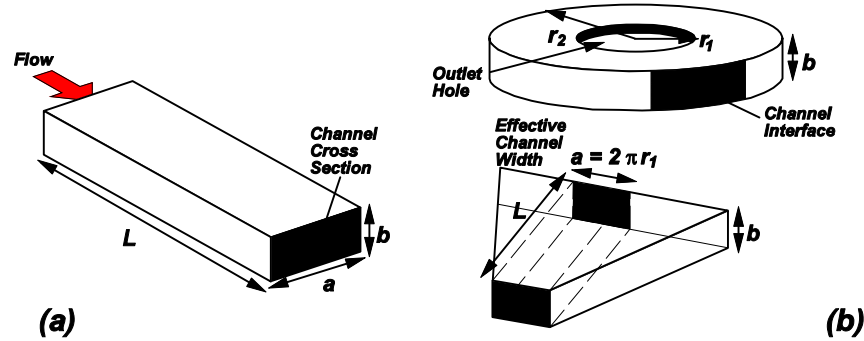


Figure 80: Channel dimensions labels used for all channel sections (a) rectangular sections (b) circular section.

Table 8 summarizes the flow regimes discussed in this section.

Table 8: Flow Regimes.

| State of Gas | Flow Regime | Condition |
|--------------|--------------|-----------------|
| viscous | Turbulent | $Re > 2100$ |
| | Laminar | $Re < 1100$ |
| transition | Intermediate | $1 < K_n < 110$ |
| rarified | Molecular | $K_n < 1$ |

Conductance Models

Flow conductance in the laminar flow regime for a circular aperture and rectangular channel are needed for this device. The laminar flow model predicts the flow of gaseous fluids when the average pressure in the channel is large. Flow conductance in

the laminar flow regime through the rectangular channel, for nitrogen gas is modeled as [67, 68]

$$C_v = 634Y(a^2b^2)/L \underline{P}, \quad (48)$$

Where

$$Y = (b/a)[1 - (192/\pi^5)(b/a)\tanh((\pi/2)(a/b)) + 0.0045] \quad (49)$$

The flow conductance in the intermediate flow regime is modeled using the Knudsen relationship, an empirical expression

$$C_t = C_v + Z C_m, \quad (50)$$

where the factor Z is [66]

$$Z = (1 + 2.507K_n)/(1 + 3.095K_n) \quad (51)$$

The flow conductance in the molecular flow regime is modeled as

$$C_m = U_o W, \quad (52)$$

where the entrance conductance U_o is expressed by

$$U_o = Av_m/4, \quad (53)$$

where A is the channel cross-sectional area v_m is the mean velocity of the gas

$$v_m = \sqrt{(8k_B T)/(\pi m)}, \quad (54)$$

where k_B is the *Boltzmann constant*, T is temperature, and m the mass of the gas molecule. The term W is the transmission probability and depends on the geometry of the channel. All channels used in this work can be modeled as either rectangular channels or parallel plates depending on the ratio a/b. The transmission probability for molecular flow in rectangular channels such that $b \geq a$ is well known [69], and is defined as

$$W_R = (R_{eff}/L)\sqrt{\pi}\delta(m_1 + m_2 + m_3 + m_4) \quad (55)$$

where

$$A = ab, \delta = b/a, R_{eff} = \sqrt{ab}/\pi. \quad (56)$$

When $a \gg b$, the transmission probability for molecular flow in the rectangular channel is modeled as flow between parallel plates, which is also well known [69]

$$W_P = w_1 - w_2, \quad (57)$$

where $x = L/b$ and

$$w_1 = (1/2)[1 + \sqrt{(1 + x^2)} - x] \quad (58)$$

$$w_2 = ((3/2)(x - \ln[x + \sqrt{(x^2 + 1)}])^2)/(x^3 + 3x^2 - 4 - (x^2 + 4\sqrt{(1 + x^2)})) \quad (59)$$

The transition conductance C_t gives the conductance in any flow regime, assuming that over the whole length of the channel L , the flow regime remains constant. For molecular flow the term ZC_m is more dominant than C_v and becomes the more dominant term for flow in the viscous regime. The transition conductance expression inherently introduces 5% error into the estimations of laminar and molecular flow [64].

4.2.1.3 Microvalve Flow Model

The flow conductances presented in the previous section are used to model the gas flow through the valve structure. Figure 81 shows the conductance model of the channel structure. Four different conductances are shown each representing a portion of the channel with different dimensions. The effects of the inlet and outlet apertures were found to be negligible for the device structures in this research.

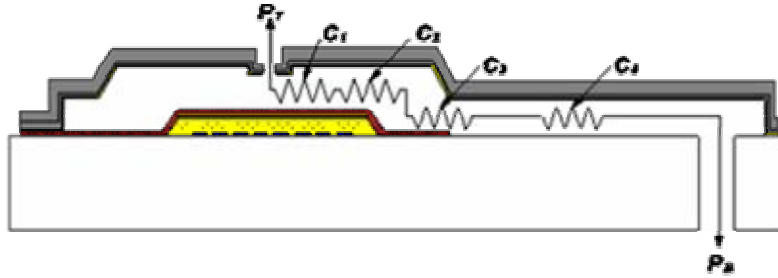


Figure 81: Lumped gas flow model showing four dominant channel conductances.

Conductance C_1 represents the flow in the valve seat region. Conductances C_2 and C_3 represent the flow conductance from the valve seat region to the channel formed by the sacrificial layer. Finally, conductance C_4 represents the flow conductance through the channel. The flow rate through the device is

$$Q = \Delta P C, \quad (60)$$

where,

$$\Delta P = P_T - P_B. \quad (61)$$

and since the conductances are in series they can be combined as

$$1/C = 1/C_1 + 1/C_2 + 1/C_3 + 1/C_4 \quad (62)$$

Saber Model

Saber (Avant!, Inc.) has a model independent simulation environment with a built-in analog modeling language (MAST). It also has the capability to interface with foreign routines written in the C or Fortran languages. This means the new expanded

models can easily be added. These developed models are therefore portable to newer versions of Saber. Furthermore, Saber accepts state variables with different units as required in MEMS modeling. In addition, Saber has extensive capabilities for selection of solution methods and iterative schemes. These features enhance the abilities in solving the nonlinear dynamics of the system encountered in MEMS device simulation.

Most iterative numerical solvers experience convergence difficulties. In order to obtain the solution, it is essential to select an appropriate number of steps in numerical iterations. For example, if a device characteristic has a sharp transition at a particular point, many sample points and small steps near this region are required, while for smooth regions of operation, fewer sample points and large steps are needed.

Figure 82 shows the accuracy of the piecewise linear approximation of a nonlinear function $y = f(x)$ where the linear approximation intersects the function at x_1 and x_2 [70]. That is, x_1 and x_2 are sample points of $y = f(x)$. Further, y_1 and y_2 are the

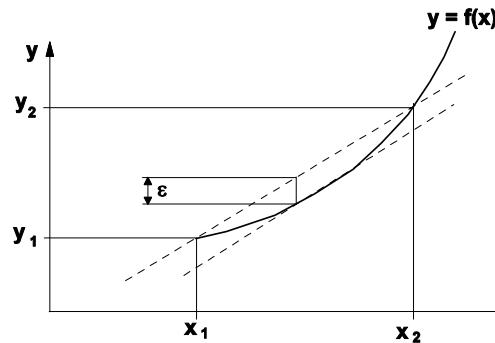


Figure 82: Accuracy of a piecewise linear approximation.

function values at x_1 and x_2 , respectively, and ϵ is the maximum error of the linear approximation of $f(x)$ between x_1 and x_2 . In order to find approximate sample points for x , we need to express ϵ as a function of $\Delta x = x_2 - x_1$. For a given ϵ , the spacing between x_1 and x_2 depends on the error bounds. Smaller Δx can yield less ϵ at the expense of more computation points and CPU time. However, larger Δx can speed up the analysis with the problem of much error.

One of the nice features of Saber is that it permits a direct control of the number of sample points over a specific region which other simulators do not permit. Therefore, direct adjustment of the density of sample points with the model is feasible to achieve. The best convergence is achieved by using piecewise linear approximation with predefined sample point densities.

Saber uses the Newton-Raphson algorithm to find the DC operating point and transient solutions (Katzenelson algorithm is also available for transient solution) to the system of nonlinear equations. The Newton-Raphson algorithm used in Saber is an iterative procedure which linearizes the nonlinearities as one of the steps in the iteration loop. Saber provides two control settings that improve the solution-finding ability of the Newton Raphson algorithm. The first setting specifies sample points in the model that define the corners of a piecewise linear approximation of nonlinear continuous device characteristics. Therefore, by increasing the sample point density at selected regions the piecewise linear approximation used in Saber can model critical parts of the nonlinear characteristics with adequate accuracy.

A flow model for the blocking valve has been written for simulation with Saber. The conductance models from the previous section have been programmed in MAST. Figure 83 shows the schematic of the flow simulation model. Symbols P_T and P_B represent steady state pressure sources. Symbols $C_1 - C_4$ are referenced to the flow conductance model templates. Intermediate pressures $P_{C1} - P_{C3}$ and flow rate are system variables which are solved by the simulator. Steady state simulation results are compared with measured results in a later section.

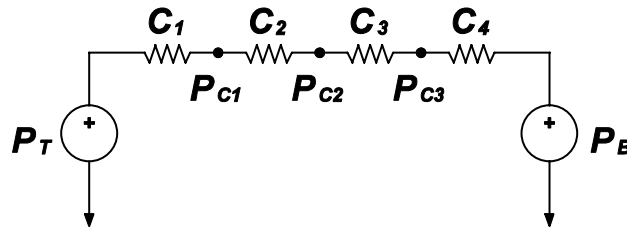


Figure 83: Saber gas flow simulation model.

4.2.1.4 Fabrication

The entire blocking microvalve is fabricated using a low temperature process ($< 110^\circ\text{C}$ with the exception of processing the photodefinable glass substrates) and eight lithography steps. Figure 84 shows the simplified process flow for a nickel electroplated microvalve. The fabrication begins by patterning the inlet hole in photodefinable glass substrates (Foturan, Schott Corp.). Patterning the Foturan substrates requires UV (312nm) exposure followed by a heat treatment schedule which reaches 600°C for 1 hour. During the heat treatment, the substrate surfaces become very rough requiring surface refinishing. The substrates are then planarized with a $20\ \mu\text{m}$ calcined aluminum oxide slurry (Logitech, Ltd., 0CON-012) for 5 minutes (using the appropriate grinding

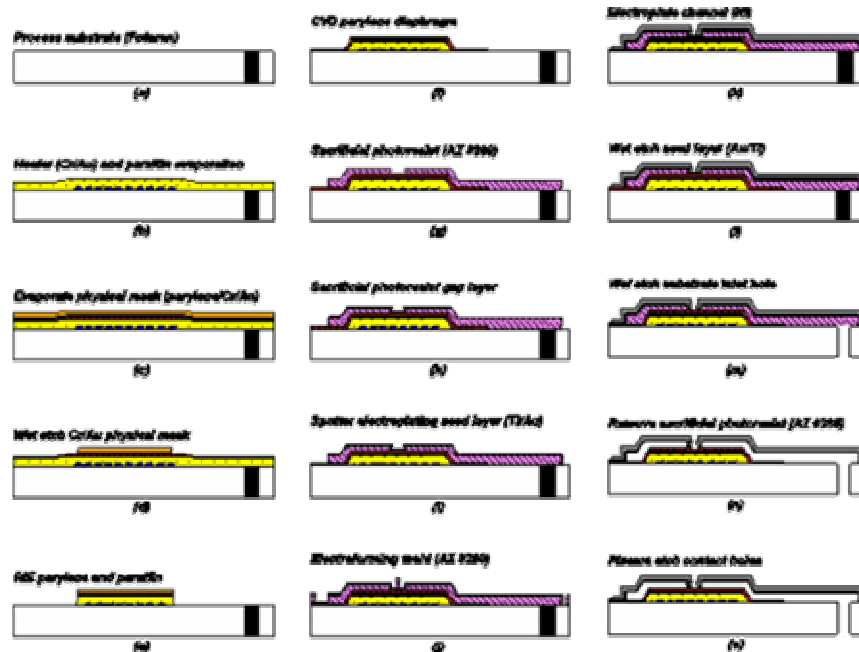


Figure 84: Simplified nickel electroplated blocking microvalve fabrication process flow.

pad) and later polished with an alkaline colloidal silica slurry (Logitech, Ltd., SF1 0CON-140) for 60 minutes. Next, Cr/Au (500/5000Å) heaters are evaporated and patterned on the substrate followed by the thermal evaporation of the paraffin. The paraffin is then selectively patterned using RIE (pressure=260 mT, CF₄:O₂ 20:80 sccm, power = 1100W) with a parylene/Cr/Au (5000/500/3000Å) etch mask. The patterned paraffin patches are then sealed with a 3 µm thick parylene layer. Adhesion to the gold and substrate layers is assisted by a silanation procedure. The parylene layer is then etched in an O₂ plasma using a 20 µm thick photoresist mask (Clariant AZ 9260). A fabricated actuator is shown in figure 85.

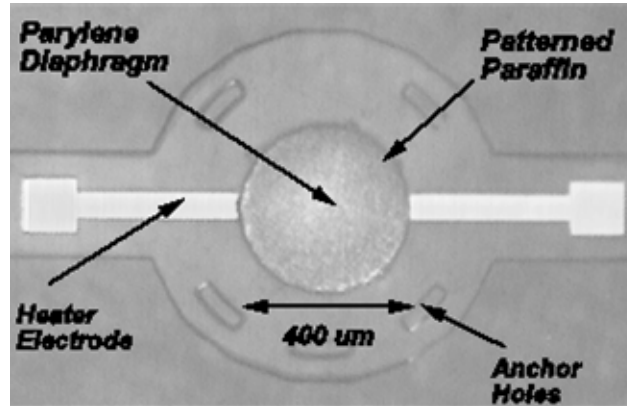


Figure 85: Photograph of paraffin actuator with 9 µm thick paraffin layer and a 4 µm thick, patterned parylene diaphragm layer.

4.2.1.4.1 Nickel Electroplated Microvalves

Following the completion of the actuator fabrication, the channel and reservoir structures are constructed on top of the actuator. First, the sacrificial channel and reservoir areas are formed by spin casting a 20 µm thick photoresist (AZ 9260) layer followed by softbake (65°C for 1.5 hour), exposure (5mW/cm² for 400 sec.), and development (1:4 AZ400K (Clariant):DI H₂O for 5 mins.). Next, a thin photoresist layer is spin cast on the substrate defining the gap height. The entire substrate is then sputter coated with a Ti/Au (300/3000Å) electroplating seed layer. This is followed by spin casting, exposure, and development of a thick photoresist (AZ 9260) layer (> 20 µm) forming the channel and reservoir mold for nickel electroplating. Next, the 20 µm thick channel structures are electroplated (Barrett-SN nickel sulfamate solution, MacDermid Inc.). Following plating, the photoresist mold is removed in acetone and the Ti/Au seed layer is then wet etched using a commercial Au etchant (GE-8148, Transene Co., Inc. which does not significantly attack the Ni films) and dilute HF solution (10:1 DI H₂O:HF(49%)) to remove the Ti layer. The front side of the substrate is then spin cast with a thick photoresist (AZ9260) and softbaked at 65°C for 1 hour. The parylene on the backside of the substrate (from prior depositions) is removed using an O₂ plasma. The Foturan glass substrates are then wet etched (10:1 DI H₂O: HF(49%)) forming the inlet holes while at the same time dicing the wafer. Finally, the sacrificial photoresist is removed from the channels of each device in an acetone bath for at least 60 minutes. Figure 86(a) shows an SEM photograph of the valve reservoir surrounding the paraffin

actuator where the outlet hole is directly above the actuator. Figure 86(b) shows the reservoir surrounding the inlet hole.

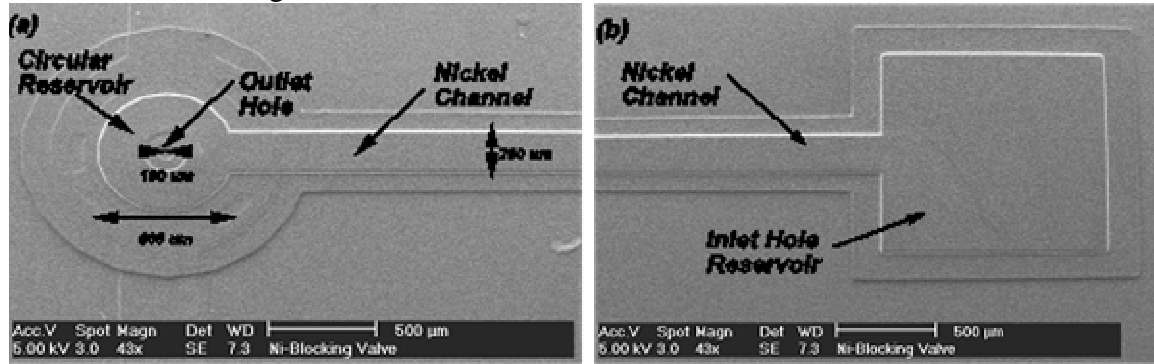


Figure 86: SEM photograph of device (a) circular reservoir with outlet orifice over the paraffin actuator (b) square reservoir covering the inlet hole

Figure 87 is a microscope photograph showing the backside of the fabricated device. Figure 87(a) clearly shows the actuator. Figure 87(b) shows the etched inlet hole through the substrate.

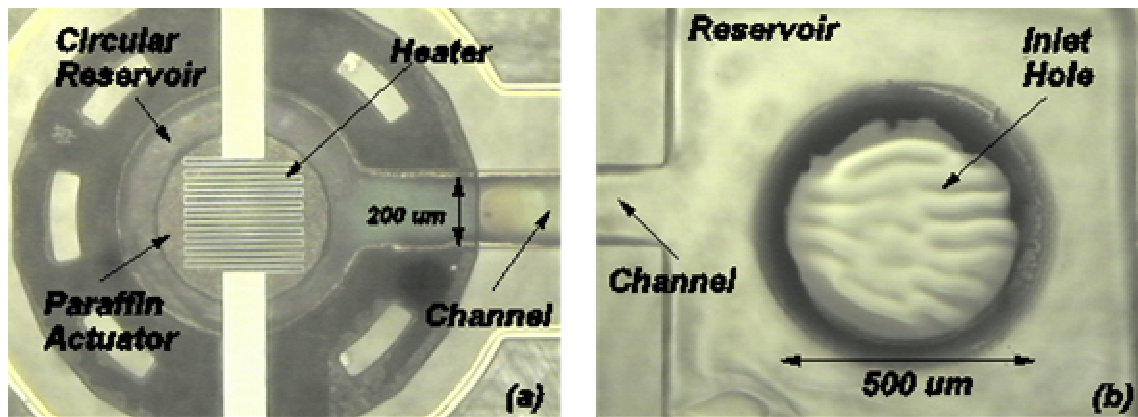


Figure 87: Microscope photograph of nickel electroplated valve backside showing (a) actuator (b) inlet hole through substrate

4.2.1.4.2 Parylene Microvalves

The microactuators for the parylene valves are fabricated using the same process as the nickel plated valves as well as the sacrificial channel and gap regions. Next, a 15 μm thick layer of parylene is vapor deposited. A Ti/Au (500/5000 \AA) mask layer is sputter coated on the entire substrate. The Ti/Au mask is patterned and the parylene layer is etched in an O_2 plasma. Figure 88 shows a fabricated parylene channel valve.

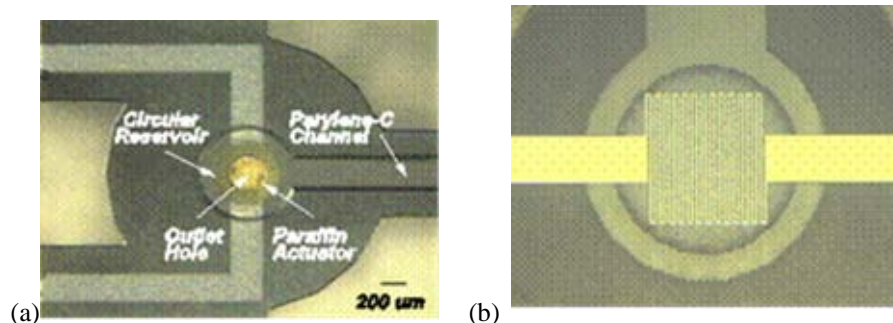


Figure 88: Microscope photograph of parylene microvalve (a) Top side of circular reservoir clearly showing outlet hole and actuator (b) bottom of circular reservoir clearly showing the heater, electrodes, reservoir and channel

4.2.1.5 Experiments

The fabricated microvalves were mounted on custom made circuit boards and mounted in a custom made flow rate measurement system. Flow rates were measured indirectly by monitoring the change in pressure of a fixed volume vessel for a fixed amount of time. Using the ideal gas law, the flow rates were calculated. Since measurements were performed in vacuum, the ideal gas law assumption holds with adequate precision.

Gas Flow Measurements

The die were mounted on custom made circuit boards (copper clad laminate, kepro circuit systems) with 1 mm diameter access holes concentric with the inlet holes of the test devices. The dice ($1.5 \times 1.5 \text{ cm}^2$) were bonded to the circuit boards with a vacuum epoxy (Kurt J. Lesker Co.). Figures 89 (a) and (b) show a die mounted on the circuit board and the circuit board mounted in the top pressure chamber of the flow rate measurement system, respectively.

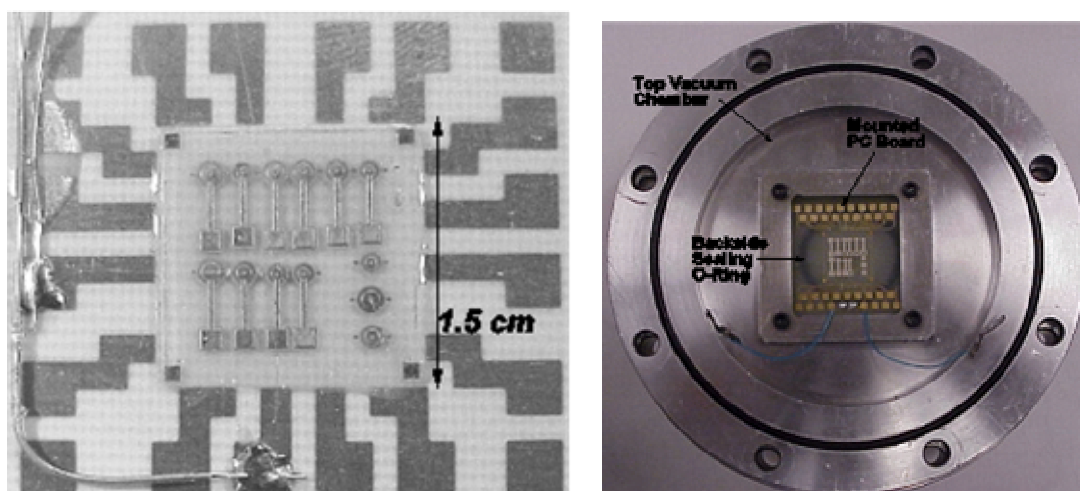


Figure 89: Photograph of (a) die containing ten microvalves (three test actuators) bonded to test circuit board (b) circuit board mounted in the top vacuum test chamber

The center diaphragm deflection was measured through the outlet hole for various input voltages using a Zygo NewView 5000 non contact surface profilometer with 100X

magnification and a 5 μm , high resolution scan length. Figure 90 shows the center deflection characteristics for the 9 μm thick paraffin actuators at 2 different diameters, 400 and 800 μm .

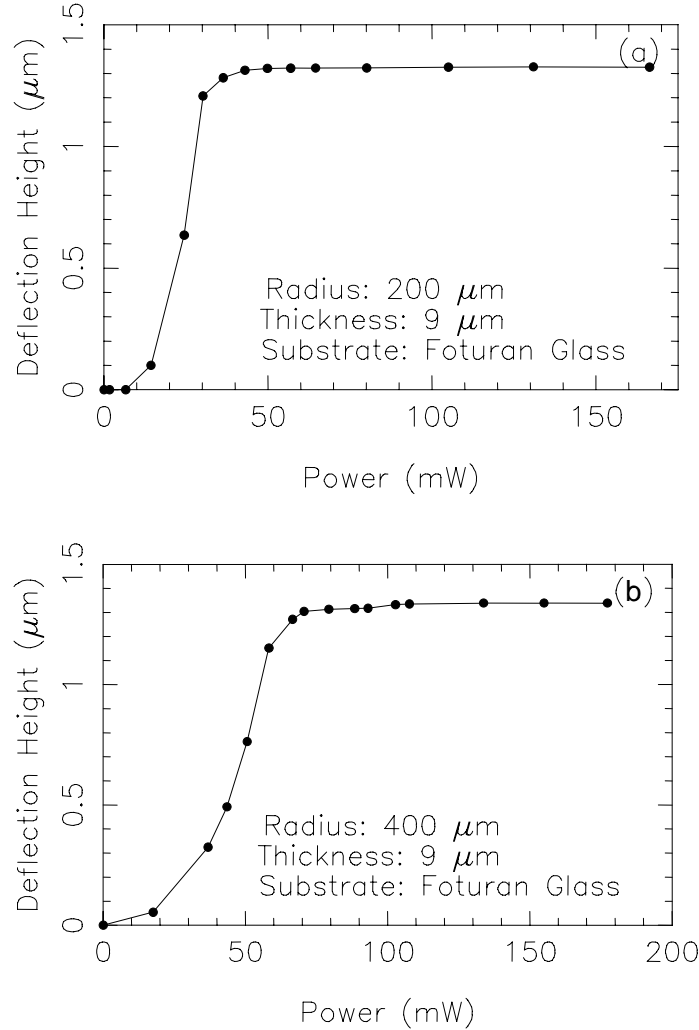


Figure 90: Measured actuator center deflection through the outlet hole with a Zygo NewView 5000 non contact surface profilometer (a) 400 μm diameter actuator (b) 800 μm diameter actuator

The valve with a 200 μm radius diaphragm deflected the entire gap height with less than 50 mW. However, the larger valve required about 100 mW input power to deflect the entire gap region. The slight deflection beyond the gap height is due to the soft parylene diaphragm pushing into the outlet hole by the molten paraffin.

Since flow and leak rates are expected to be very small, no commercially available flow meters exist in these small ranges. Therefore, an indirect approach has been used where pressure change ΔP for a known period of time Δt are measured in a known volume V at the outlet of the device [71, 49]. Figure 91 shows a schematic and photograph of the test apparatus.

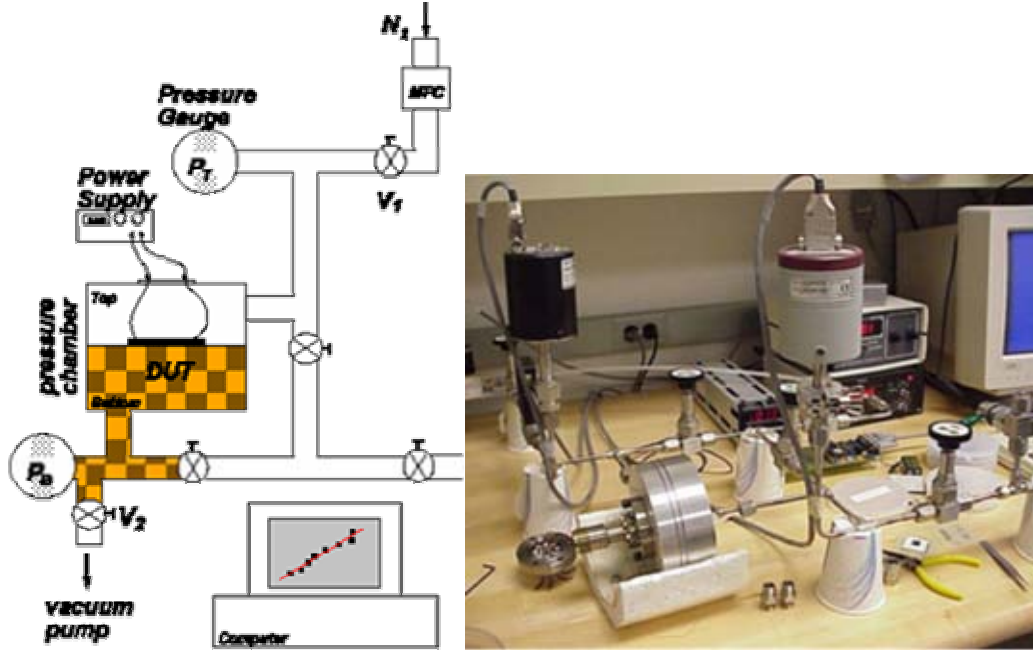


Figure 91: Experimental flow rate measurement apparatus

The measurement procedure is as follows, initially valves V_1 and V_2 are open and nitrogen is passed through the entire system. The mass flow controller (MFC) is adjusted such that the pressure in the top chamber P_T is 800 Torr (V_1 remains open). To perform a measurement, valve V_2 is closed. The pressure increase in the bottom chamber (shaded portion in Figure 91) is due to the flow through the device under test (DUT) and a small background system leak. The pressure change P_B is measured with a capacitive manometer pressure sensor connected to the bottom chamber for a period of time Δt . The system leak was measured periodically throughout testing and typically was about 2.5×10^{-4} sccm. Since the volume of the bottom chamber V is known, fixed, and assuming the gas is ideal, the volumetric flow rate Q (Torr-L/s) can be determined from the relationship

$$Q = d(PV)/dt \quad (63)$$

which expands to

$$Q = P dV/dt + V dP/dt \quad (64)$$

and since V is constant, then $dV/dt \approx 0$ and the flow rate can be expressed as

$$Q = (\Delta P/\Delta t) V. \quad (65)$$

From the ideal gas law, the molar flow rate (moles/s) can be determined

$$\Delta N/\Delta t = (\Delta P/\Delta t)(V/RT) \quad (66)$$

where N is the number of moles, R is the universal gas constant and T the gas temperature.

Flow rates were measured for different applied voltages for valves with $1.3\text{ }\mu\text{m}$ gap heights. When the diaphragm is fully deflected the flow rate through the device is the leak rate of the valve. For all measurements, the top side pressure P_T of the device was maintained at 800 Torr, while the bottom pressure P_B was maintained in vacuum. Figures 92 - 94 show the measured flow rate through $400\text{ }\mu\text{m}$, $600\text{ }\mu\text{m}$ and $800\text{ }\mu\text{m}$ diameter devices as a function of input voltage and power.

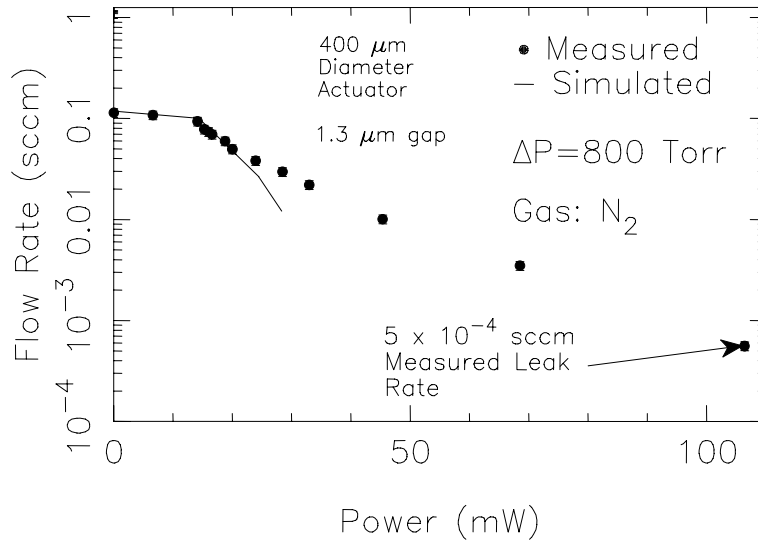


Figure 92: Measured (circles) and simulated (line) flow rate through a $400\text{ }\mu\text{m}$ diameter actuator device as a function of input power (linear-log scale)

The calculated flow rate matches well to the measured flow rate from 0.1 to about 0.01 sccm. The flow model was evaluated only to 0.01 sccm because it fails to predict the flow rate accurately for very small gaps. This deviation probably occurs because the flexible diaphragm is pushing against the valve seat creating a complex, non-linear situation. Measurements indicate flow rates in the 0.1 - 0.01 sccm range, depending on the gap height, for actuation voltages less than 10 volts while consuming between 50 - 150 mW. The flow rate for this device is determined primarily by the gap height. Leak rates as low as 5×10^{-4} sccm have been measured for the smallest devices. The leak rate for these devices could possibly be reduced through refinements in the device design. The leak rates could be reduced by coating the final device with a thin conformal parylene layer [49]. The final coating layer can enhance the sealing properties of the diaphragm and seat layer because they are the same material. In addition, silicone rubber material can also be used to improve the sealing properties of microvalves. Silicone rubber materials, such as poly-methylsiloxane (PDMS) which can be spin coated and later patterned are promising microvalve gasket or O-ring materials. Thin plasma polymerized rubber films from a hexamethyldisiloxane (HMDSO) source offer interesting alternatives for fabricating microvalve gaskets. Table 9 lists the simulated pressure distributions for the three devices as well as a comparison between the simulated and measured open flow rates.

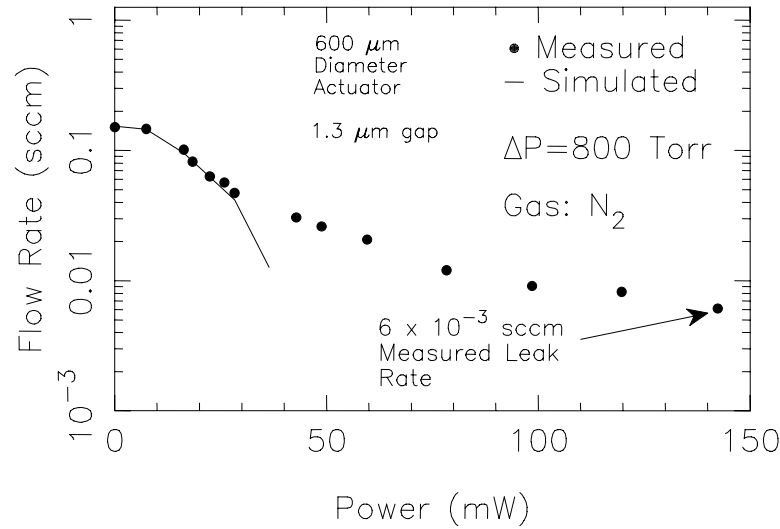


Figure 93: Measured (circles) and simulated (line) flow rate through a 600 μm diameter actuator device as a function of input power (linear-log scale)

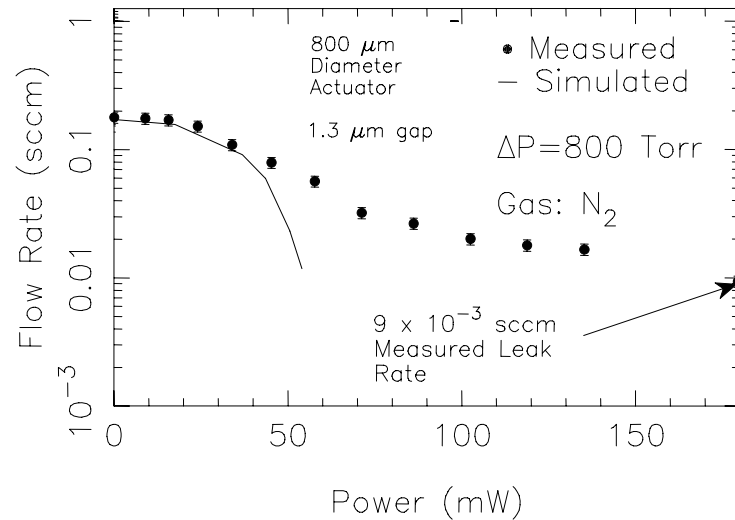


Figure 94: Measured (circles) and simulated (line) flow rate through an 800 μm diameter actuator device as a function of input power (linear-log scale)

Table 9: Simulated microvalve pressure distribution and comparison between calculated and measured open flow

| Radius (μm) | P_T (Torr) | P_{C1} (Torr) | P_{C2} (Torr) | P_{C3} (Torr) | P_B (Torr) | Q_{calc} (sccm) | Q_{meas} (sccm) | Error (%) |
|-----------------------------|-----------------|--------------------|--------------------|--------------------|-----------------|-----------------------------|-----------------------------|--------------|
| 200 | 800 | 266.6 | 265.6 | 264.8 | 0.1 | 0.123 | 0.114 | 7.8 |
| 300 | 800 | 302.4 | 299.2 | 298.5 | 0.1 | 0.153 | 0.151 | 1.6 |
| 400 | 800 | 320.3 | 317.9 | 317.4 | 0.1 | 0.172 | 0.179 | 3.7 |

4.2.2 Mass Flow Control Valve

A system of microvalves, which use the normally-open blocking valve structure, as the control valve for a precision mass flow control system was designed. The control valve is designed to operate over a 0.01 - 5.0 sccm flow range (dynamic range: 500 or 10-bit resolution) at a pressure of 800 Torr and analog control. The flow range for this type of control valve can easily be increased by adding more valve units and/or

increasing the gap height. System leak rates as low as 3.2×10^{-3} sccm (N_2) have been measured.

Mass flow controllers (MFCs) are used in applications requiring accurate gas flow measurement and control. In the semiconductor industry, MFCs are essential to most thermal and dry etching processes where etch uniformity and reproducibility are influenced, in large part, by gas flow rates. If the etch rate is limited by the supply of reactants, small variations in flow rate or gas distribution may lead to large etch rate non uniformities [72].

Typical MFCs can be separated into two main components: a mass flow meter (MFM) and proportioning (PID) controller [73]. The MFM either separates the flow between the sensing element and a bypass where most of the flow passes in the case of heated based sensing or passes the flow through a restrictor with known conductance to accurately measure the pressure drop and corresponding flow rate. The proportioning controller typically consists of a control valve and electronics. The electronic controller drives the valve to the correct position so that the measured flow equals the desired flow setpoint. Figure 95 shows a block diagram of a pressure based mass flow controller [74].

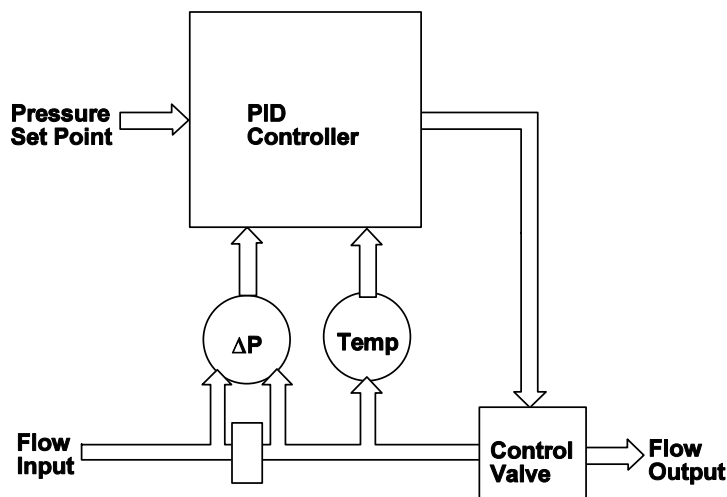


Figure 95: Typical pressure based sensing mass flow controller

Conventional control valves for pressure and flow control typically use magnetically actuated solenoids or motor drives. Although the majority of commercial mass flow controllers provide a very low leak rate (typically less than 10^{-7} sccm (N_2)), they are not able to reliably control very small mass flow rates below about 0.1 sccm. Commercially available, electrically actuated flow control microvalves have been reported, however, suffer from relatively large leak rates.

4.2.2.1 Device Structure

The normally open blocking microvalve has been used to fabricate the precision flow control valve. Four microvalves have been connected to a single reservoir. The gap height of the valves has been increased for this device resulting in an increased open flow. The simulated open flow of a single valve is 1.265 sccm, therefore the four valve flow controller is designed to have an open flow of about 5 sccm at 800 Torr. Using the measured results from the previous section, the minimum controlled flow occurs at about

0.01 sccm. Since the paraffin actuated microvalves have a fairly linear and predictable behavior from open flow to a minimum flow value of around 0.01 sccm, the flow controller is operated in an analog mode. Figure 96(a) shows a schematic of the top view of the flow control microvalve system. Figure 96(b) shows the cross-section A-A' of the device with design dimensions. The gas flows through the 500 μm diameter inlet hole through the silicon substrate (≈ 535 μm thick) leading to the inlet hole reservoir. The reservoir is connected to four 900 μm long channels leading to the circular reservoirs. All channels have a 200×20 μm^2 cross-sectional area. The open flow condition occurs when all valves are open (non-actuated state) and the leak rate is measured with all valves closed (actuated state).

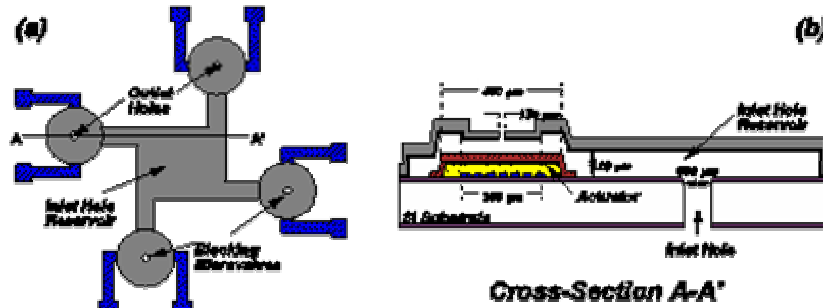


Figure 96: Top view and cross-section of the micro flow control valve

4.2.2.2 Fabrication

The entire blocking microvalve is fabricated using a low temperature process ($< 110^\circ\text{C}$ with the exception of the deposition of the silicon dioxide isolation layer) and seven lithography steps. Process steps (a)-(q) in Figure 97 show the simplified process flow for the nickel electroplated flow control valve. A 2 μm thick thermal SiO_2 layer is first grown on the blank silicon wafers. The inlet holes are then patterned in the SiO_2 layer on the back side of the substrate. The inlet hole is then partially etched (450 μm deep) in the wafer back side (not completely through the substrate) using the Surface Technology Systems (STS) Multiplex Inductively Coupled Plasma (ICP) deep reactive ion etching (DRIE) system. The Cr/Al (500/5000 \AA) heaters are then E-beam evaporated and patterned (requires back side alignment). Logitech paraffin, 10 μm thick, is then thermally evaporated followed by the deposition of the parylene/Cr/Au (5000/500/3000 \AA) film stack. The Cr/Au layer is then patterned forming the parylene/paraffin etch mask. The exposed parylene/paraffin areas are removed using a $\text{CF}_4:\text{O}_2$ RIE step. The parylene diaphragm layer is then vapor deposited and patterned. Figure 98 shows a fabricated actuator before the channel is formed. The first sacrificial photoresist layer is then spin casted and patterned forming the reservoirs and channel regions. The second sacrificial photoresist layer is then spin casted on top of the first layer and patterned forming the gap height above the actuator. A Ti/Au (500/5000 \AA) seed layer for the electrodeposited nickel layer is sputter coated on the sample. The thick photoresist electroforming mold is then spin casted and patterned. The thick nickel structure is then electroplated (20 μm) forming the reservoir and channel regions. After the nickel deposition is complete, the photoresist mold is removed with acetone and the exposed Au/Ti areas are wet etched. The inlet holes are then completely etched through the silicon substrate (50-100 μm) using the STS DRIE. The SiO_2 layer is removed from

the inlet hole area and finally the sacrificial photoresist is removed from the reservoir and channel regions in acetone. Figure 99 is a microscope photograph showing the fabricated device.

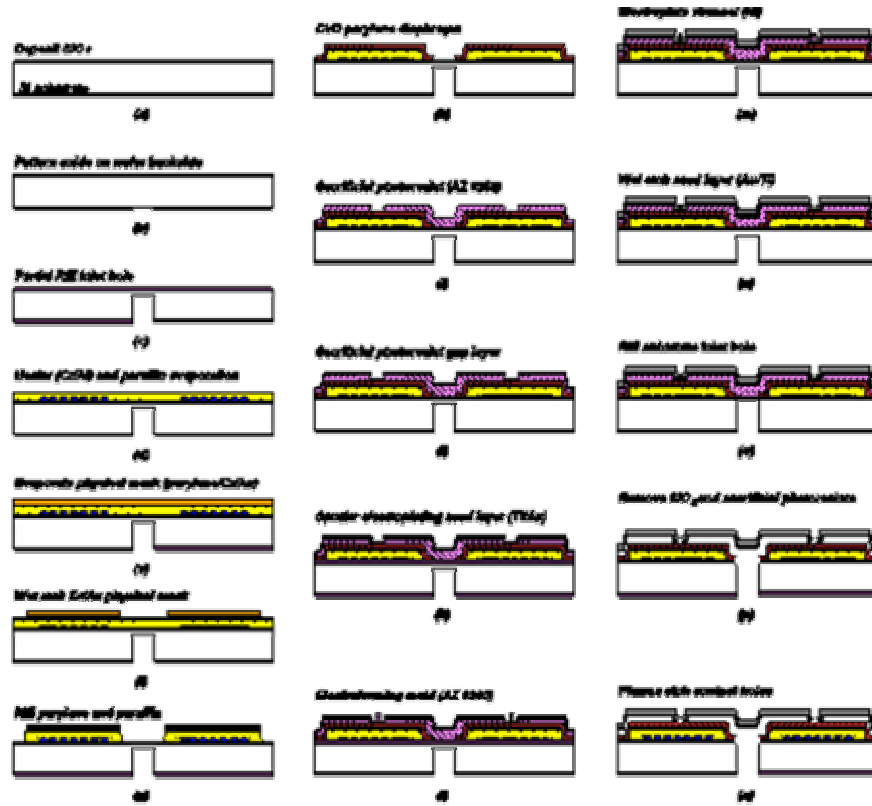


Figure 97: Simplified nickel electroplated micro flow controller fabrication

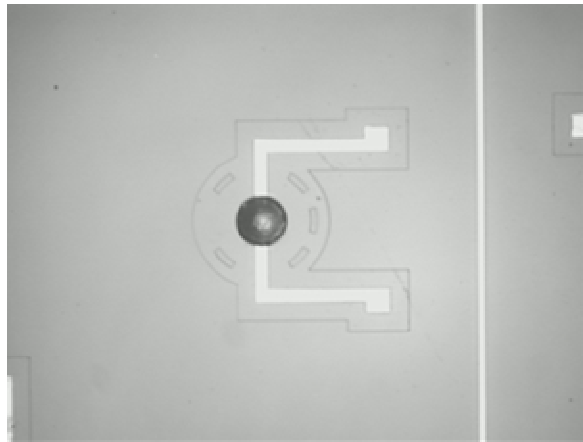


Figure 98: Microscope photograph of paraffin microactuator

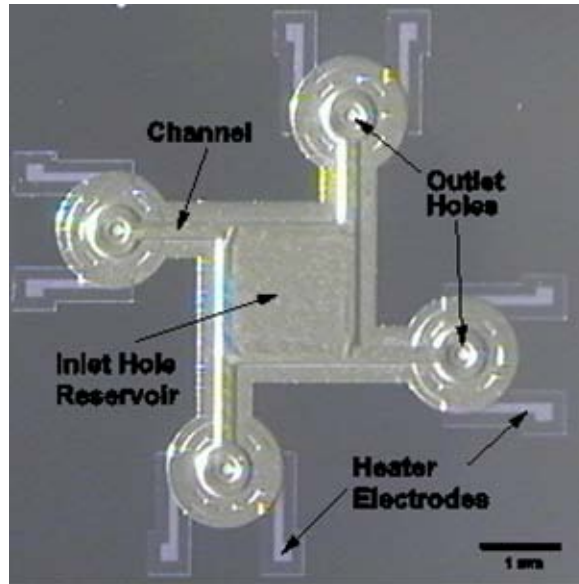


Figure 99: Microscope photograph of the nickel electroplated micro flow controller valve system

4.2.2.3 Experiments

The fabricated devices were again mounted on custom made circuit boards and mounted in a custom made flow rate measurement system. Flow rates were measured indirectly by monitoring the change in pressure of a fixed volume vessel for a fixed amount of time. Using the ideal gas law, the flow rates were calculated. Since measurements were performed in vacuum, the ideal gas law assumption holds with adequate precision.

4.2.2.3.1 Flow Rate Measurements

The microvalve system die were mounted on custom made circuit boards (copper clad laminate, kepro circuit systems) with 1 mm diameter access holes concentric with the inlet hole of the test device. The die ($7.5 \times 7.5 \text{ mm}^2$) were bonded to the circuit boards with a vacuum epoxy (Kurt J. Lesker Co.) ensuring a leak tight seal. Figures 100 (a) and (b) show a die mounted on the circuit board and the circuit board mounted in the top pressure chamber of the flow rate measurement system, respectively.

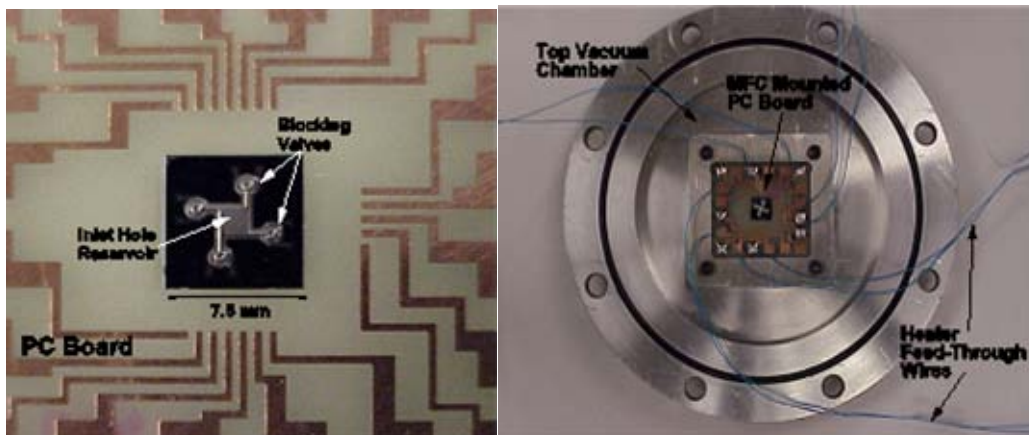


Figure 100: Photograph of (a) die containing a flow controller valve unit bonded to test circuit board
(b) circuit board mounted in top pressure chamber

Single Microvalve Measurements

Flow rates were measured for different applied voltages for single valves with 2.2 μm gap heights. When the actuator diaphragm is fully deflected the flow rate through the device is the leak rate of the valve. For all measurements, the top side pressure P_T of the device was maintained at 800 Torr, while the bottom pressure P_B was maintained in a vacuum. Figure 101 shows a measured flow rate through the 400 μm diameter actuator as a function of input voltage and power.

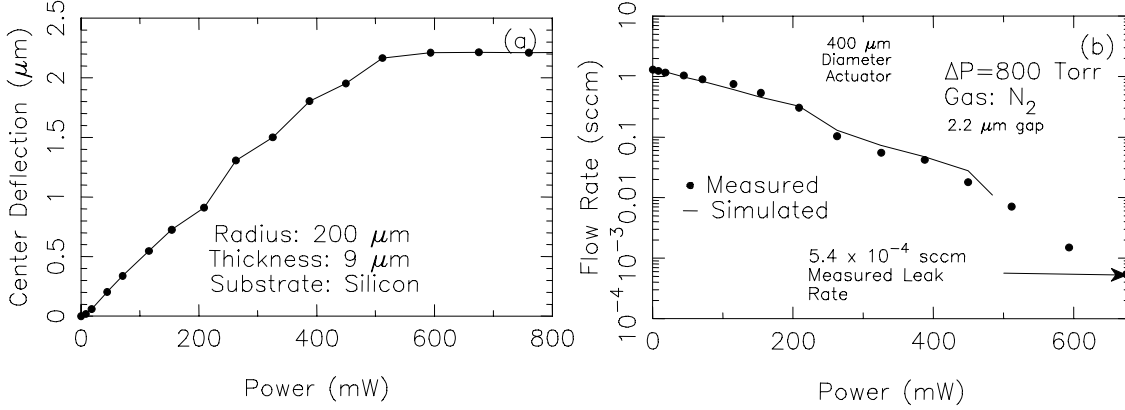


Figure 101: Measured actuator center deflection through the outlet hole with a Zygo NewView 5000 non contact surface profilometer (a) 400 μm diameter actuator (b) Measured flow rate through a single microvalve (2.2 μm gap) as a function of input power

Measurements indicate flow rates for a single valve ranges from 0.02 - 1.305 sccm range for actuation voltages less than 7 volts while consuming about 680 mW of power (SiO_2 silicon substrates). Figure 101 shows an example of a measured leak rate of 5.4×10^{-4} sccm for single microvalve (average measured system leak rate 2.8×10^{-4} sccm). The flow rate for this device, as in the blocking microvalve device, is determined primarily by the gap height, as discussed earlier. Table 10 lists the simulated pressure distributions for one of the valves as well as a comparison between the calculated and measured open flow rates.

Table 10: Simulated microvalve pressure distribution and comparison of calculated Q_{calc} and measured

| Q_{meas} open flowrate | | | | | Q_{calc} (sccm) | Q_{meas} (sccm) | Error (%) |
|---------------------------------|--------------------|--------------------|--------------------|-----------------|-----------------------------|-----------------------------|--------------|
| P_T (Torr) | P_{C1} (Torr) | P_{C2} (Torr) | P_{C3} (Torr) | P_B (Torr) | | | |
| 800 | 175.6 | 173.6 | 172.1 | 0.65 | 1.25 | 1.36 | 8.16 |

Flow Control Microvalve Measurements

The microvalve system flow rate was measured for different states of the four microvalves all with 2.2 μm gap heights. For all measurements, the top side pressure P_T of the device was maintained at 800 Torr, while the bottom pressure P_B was maintained in vacuum (1.382 Torr). Table 11 shows the simulated and measured flow ranges for the flow controller. Figure 102 shows the measured flow rate through the four flow control valves as a function of input power. First, the open flow rate was recorded with all valves

in the open (not actuated state) position. Flow rates were then recorded for one valve

Table 11: Simulated and measured flow ranges

| Valve 1 | Valve 2 | Valve 3 | Valve 4 | Q_{calc} | Q_{meas} |
|----------|----------|----------|----------|------------|------------|
| open | open | Open | Open | 5.00 | 4.96 |
| variable | open | Open | open | 3.75–5.00 | 3.67–4.96 |
| closed | variable | Open | open | 2.50–3.75 | 2.26–3.67 |
| closed | closed | Variable | open | 1.25–2.50 | 1.17–2.26 |
| closed | closed | Closed | variable | 0.01–1.25 | 0.021–1.17 |

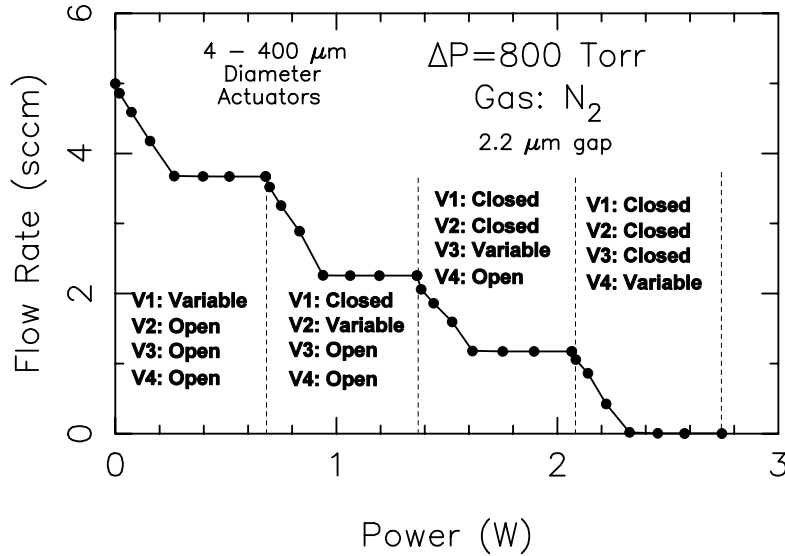


Figure 102: Measured flow rate through the four-valve microvalve system (2.2 μm gap heights) as a function of input power

actuated from 0.0 to 7.0 Volts, while the other three valves were in the open flow condition. Next, the flow rate was measured for one valve in the closed position, one valve actuated from 0.0 to 7.0 Volts and the other two valves in the open position. The flow rate was then measured for two valves in the closed position, one valve actuated from 0.0 to 7.0 Volts and one valve in the open flow position. Finally, the flow rate was measured for three valves in the closed position and one valve actuated from 0.0 to 7.0 Volts. Measurements indicate a system flow rate ranging from 0.02 - 4.996 sccm for actuation voltages less than 7 volts while consuming between 0.675 - 2.73 Watts of power (silicon substrates), depending on how many devices are operating at the same time. The flow rate for this device, as in the blocking microvalve device, is determined primarily by the gap layer because its height is an order of magnitude less. Leak rates as low as 3.2×10^{-3} sccm have been measured for the system corresponding to measured leak rates of previous devices.

4.2.3 Inline Microvalve

This section presents a novel paraffin actuated normally-open inline microfluidic valve. The fabrication of the valve requires a simple, low temperature microfabrication process making it easily integrated with other fluidic or microelectronic components. Key to this new inline valve technology is that many independently operating valves can be

fabricated on a single die permitting the implementation of complex integrated microfluidic systems on the same substrate.

Each inline microvalve uses a piston element that is microfabricated inside the capillary. The piston element encloses a sealed paraffin actuation layer. Additional paraffin reservoirs have been used on both sides of the valve structure providing hydraulic advantage to the device for increasing diaphragm deflection. When electrically heated, the sealed paraffin in the reservoir and piston element area expands deflecting the piston element thus closing the channel. The valve structure presented in this section demonstrates the feasibility of fabricating integrated microfluidic systems using the scalable paraffin actuated inline microvalve. This section presents the design, fabrication and preliminary testing of the integrated inline microvalve.

4.2.3.1 Device Structure

Figure 103 shows a three dimensional rendering of the paraffin actuated inline microvalve. The actuation layer is fabricated on the top side of the microchannel. A reduced channel region has been formed in the center of the channel. When the paraffin is heated, the sealed paraffin layer expands and the top of the channel in the reduced channel region acts as a diaphragm deflecting downwards closing the channel. Figures

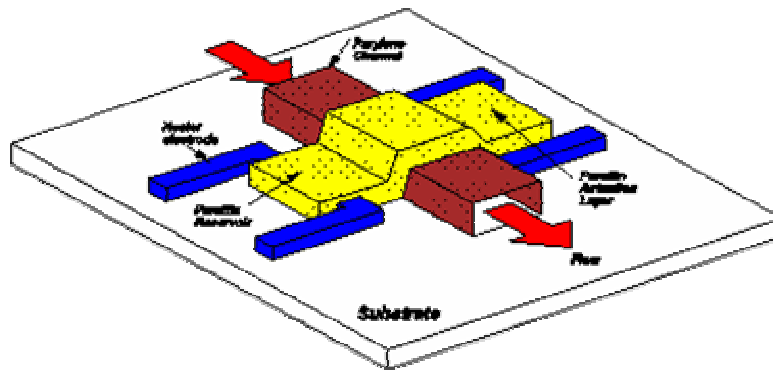


Figure 103: Three dimensional view of inline microvalve showing the paraffin actuation layer

104 (a) and (b) show the cross-section of the inline valve in the normally-open and actuated closed states, respectively. In the actuated state, the liquid (melted) paraffin, which is sealed between two parylene layers, forces the bottom parylene layer vertically downwards closing the channel. The top parylene layer serves primarily as a sealing layer for the paraffin layer. The bottom parylene layer acts as a diaphragm for the piston element in the reduced channel region. The top most device layer is the reinforcement layer preventing the top parylene layer from moving during the actuated state. To

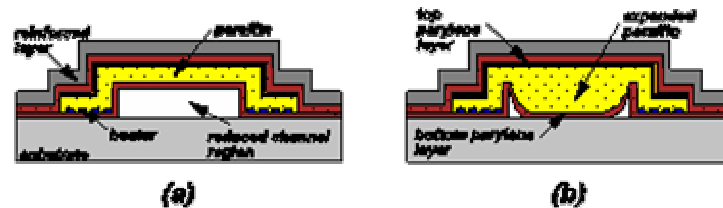


Figure 104: Cross-section of inline microvalve (a) normally-open state (b) actuated-closed state

increase the closing ability of the valve, hydraulic advantage is used with the aid of two paraffin reservoirs. When the sealed paraffin actuation layer is heated and subsequently melted, the reinforcing layer prevents the top parylene layer from moving; therefore, the paraffin *flows* towards the reduced channel region, with the aid of the *funnel* regions, seeking the path of least flow resistance. The principle of operation is identical to the operation of the hydraulic advantage device presented earlier. The flexible bottom parylene layer directly above the reduced channel region deflects downwards closing the channel to liquid flow. Figures 105 (a) and (b) show top views of the inline valve with and without the paraffin actuation layer covering the device heaters, respectively. Since

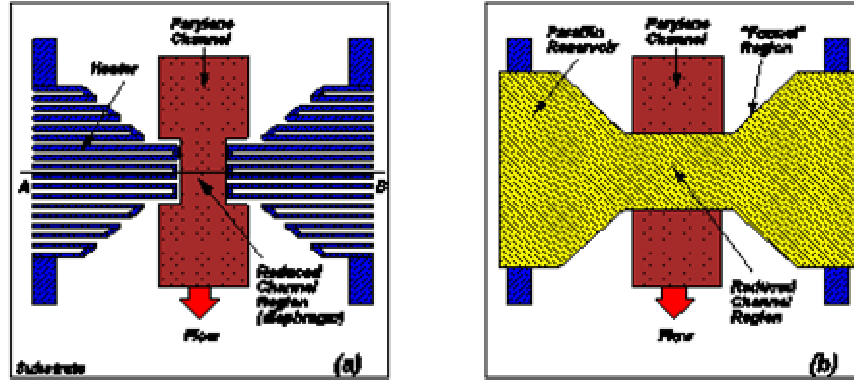


Figure 105: Top view of inline microvalve (a) without paraffin actuation layer showing the heater structure (b) with paraffin actuation layer showing the paraffin reservoirs, funnel structure and reduced channel region

the device uses hydraulic advantage, the size of the paraffin reservoirs should be chosen large enough to ensure adequate closing of the channel. For adequate diaphragm deflection, the volume of expanded paraffin V_{res} must be larger than volume V_{dia} required to fully deflect the piston element diaphragm.

The volume of the deflected membrane can be calculated by first considering the deflection of the rectangular diaphragm. Since the diaphragm is rectangular with simply supported edges, the diaphragm deflection can be expressed as [58]

$$w(x,y) = (16w_{max}) / (12\pi^6 c_1 (1 - \nu^2)) \sum_{n=1}^{\infty} \sum_{m=1}^{\infty} (\sin(n\pi x/L) \sin(m\pi y/2L)) / (nm(n^2 + m^2/4)^2), \quad (67)$$

where $c_1 = 0.11087$ and L represents the short side of rectangular diaphragm. The volume of paraffin contained in the deflected diaphragm can be calculated by integrating the diaphragm deflection expression

$$V_{dia} = \int_0^{2L} \int_0^{2L} w(x,y) dx dy. \quad (68)$$

Using $L = 50 \mu m$, and a maximum deflection distance of $w_{max} = 3 \mu m$, the paraffin volume required to deflect the diaphragm is approximately $V_{dia} = 1446 \mu m^3$. The volume of expanded paraffin in the reservoir regions assuming a paraffin thickness $h = 3 \mu m$ and expansion coefficient $m = 0.1$ is approximately $V_{res} = 43 \times 10^3 \mu m^3$. The volume of

available paraffin is nearly 30 times greater than the paraffin required to fully close the channel thus ensuring that the diaphragm can be fully deflected.

4.2.3.2 Fabrication

The entire inline microvalve is fabricated using a low temperature process ($< 110^{\circ}\text{C}$) and seven lithography steps. Figure 106 shows the simplified process flow for the inline valve. The process flow shown in Figure 106 follows cross-section A-B from Figure 105 (a).

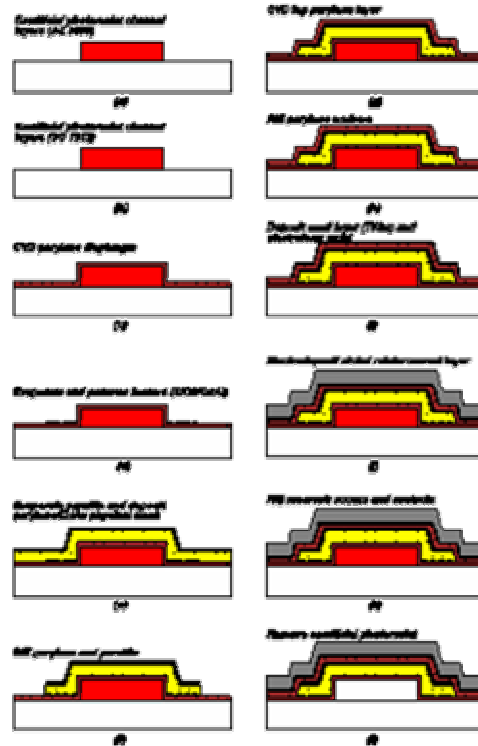


Figure 106: Simplified inline microvalve fabrication process flow

The fabrication begins by spin casting a $10 - 20 \mu\text{m}$ thick photoresist (Clariant AZ 9260) layer followed by softbake (110°C for 10 minutes on a hotplate), exposure ($5\text{mW}/\text{cm}^2$ for 400 sec.), and development (1:4 AZ400K (Clariant):DI H_2O for 5 mins.). Next, a thin photoresist layer (Microposit SC1813) is spin cast on the substrate defining the height of the reduced channel region. Typically, the reduced channel region photoresist thickness ranges between $2-5 \mu\text{m}$ depending on the desired reduced channel height. The entire substrate is then coated with the bottom parylene layer $3 \mu\text{m}$ thick. Next, $\text{SiO}_2/\text{Cr}/\text{Al}$ ($100/300/5000\text{\AA}$) layers are sputter coated on the wafer. The Cr/Al layers are then patterned and wet etched forming the actuator heaters. The SiO_2 layer is then removed in the field areas. Paraffin is then thermally evaporated and covered with the parylene/Cr/Au ($5000/500/3000\text{\AA}$) etch mask materials. The Cr/Au layers are patterned and parylene/paraffin films are removed using a $\text{CF}_4:\text{O}_2$ RIE step. The second parylene layer, $5 \mu\text{m}$ thick, is then vapor deposited and patterned. A Ti/Au ($500/5000\text{\AA}$) seed layer for the electrodeposited nickel reinforcing layer is then sputter coated on the sample. A thick photoresist electroforming mold is then spin casted and patterned. A $20 \mu\text{m}$ thick nickel reinforcement layer is then electrodeposited. After the nickel deposition

is complete, the photoresist mold is removed with acetone and the exposed Ti/Au areas are wet etched. Inlet holes in the reservoir are then etched in an O₂ plasma using a photoresist mask. Finally, the sacrificial photoresist is removed in acetone. Figure 107 shows many fabricated inline valves on a single square die. The density of the batch fabricated inline microvalves shown can be increased as the individual devices are scalable and the geometry can be optimized for functionality and performance. Figure 108 shows a fabricated inline valve after the sacrificial photoresist has been removed.

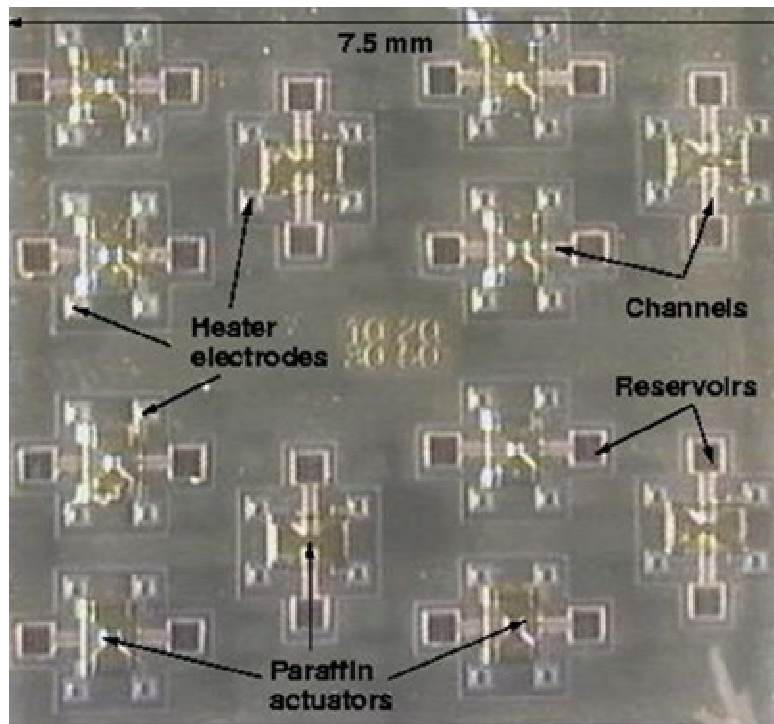


Figure 107: Microscope photograph of a 7.5 x 7.5 mm² die showing many independently operating valves

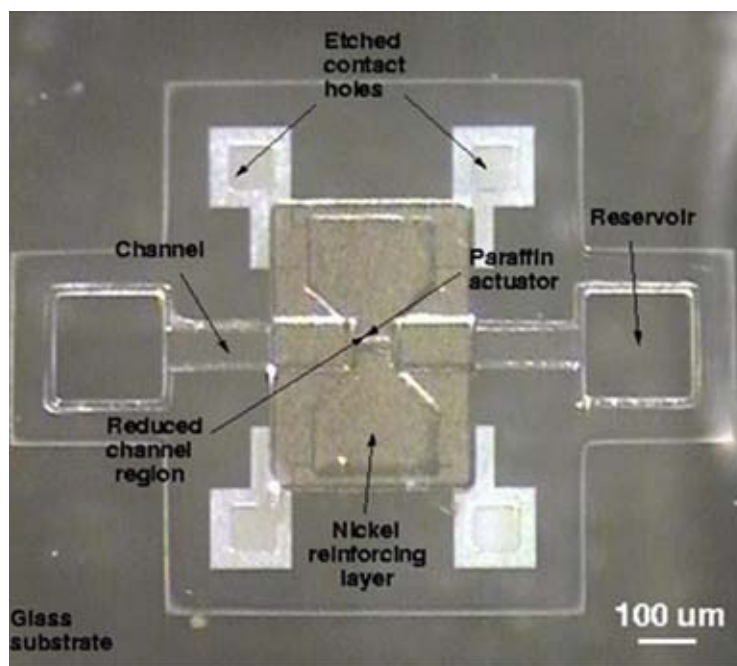


Figure 108: Microscope photograph of a single fabricated inline valve

4.2.3.3 Experiments

The performance of the valve was tested by visually measuring the presence or absence of liquid in one side of the microchannel while the opposite reservoir is filled with a test liquid. First, the channel was closed by applying a positive voltage to the heater thus actuating the paraffin actuator. One of the channel reservoirs was then filled with deionized water with a 10 mL syringe. The heater voltage was then removed opening the channel to the test liquid. Finally, the channel is closed and the liquid is isolated from the test liquid source. If the channel is closed the isolated liquid will evaporate. Since the heater structures are fabricated on parylene, which has a very low thermal conductivity, the actuation power requirements are very low, on the order of 25 mW, for a single valve. These low power requirements are important when fabricating large integrated microfluidic systems.

Liquid flow measurements

Figures 109(a), (b) and (c) show photographs from a video clip of the inline microvalve opening and closing the channel to deionized water flow. First, 3.0 volts was applied to the device heaters thus closing the channel as shown in Figure 109(a). The reservoir, not shown, was then filled with deionized water. The channel is visibly free of water indicating that the channel is sealed in the actuated state. The heater voltage was then changed to 0.0 volts opening the channel to liquid flow. Figure 109(b) shows that the channel turned dark indicating that it completely filled with water after the microvalve was opened and did not subsequently evaporate until the channel was closed again. The heater voltage was then changed back to 3.0 volts closing the channel to liquid flow. Figure 109(c) shows that the water in the channel evaporated indicating that the microvalve completely sealing the channel to liquid flow.

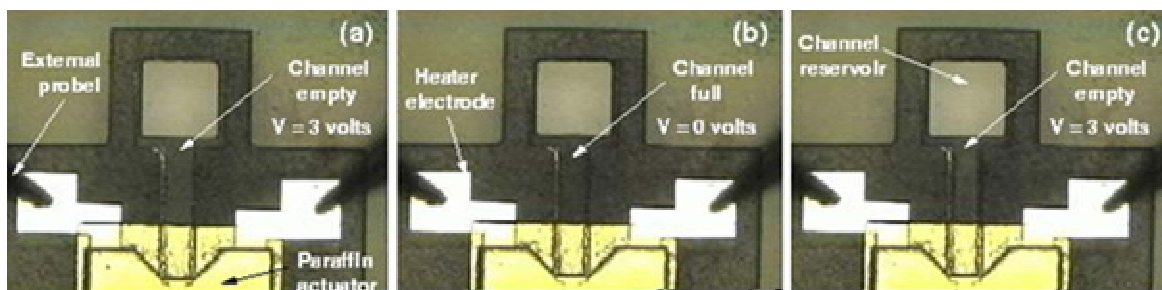


Figure 109: Microscope photographs of the inline microvalve opening and closing the capillary to deionized water flow

More comprehensive testing of the microvalve is required. A micropump can be connected to one reservoir and the test liquids subsequently forced through the channel. Uncharged microspheres added to the test liquid can be used to optically measure the flow rate of the liquid in the channel. The flow rate as a function of heater input power can then be measured.

4.3 Microfluidic Pump

Pumps are essential in microfluidic systems for fluid transport but also have other applications like mixing, cooling and pressure generation. Pumping can be achieved using different actuation mechanisms such as electrohydrodynamic, electrokinetic, mechanical displacement and bubble generation. All of these have been miniaturized and used for pumping liquids in mostly glass and silicon based microsystems. Ideally, pumps should be inexpensive, easy to fabricate and easy to integrate within a plastic microfluidic system with high flow rates and pressure generation at relatively low power. For most bioassay applications, bubble generation and local heating of the liquid are undesirable.

We have developed a wax-based actuator similar to the actuator developed by Carlen et al. that makes use of the large volumetric expansion of wax when it transitions from solid to liquid phase to generate large volume displacement that can be used to pump liquids. The volumetric expansion of PEG 8000 is significant and volume changes of up to 30% can be obtained. The fabrication technique is simple and inexpensive and these actuators can be mass fabricated on cast epoxy substrates. The actuator is used in a nozzle-diffuser arrangement in series to generate a net fluid flow. The pump uses relatively low power and there is no bubble generation because it operates at low temperatures ($< 100^{\circ}\text{C}$ at the surface of the wax patch). The device is fabricated using epoxy casting. The channel structure is cast on one substrate and the wax actuator is fabricated using a screen-printing technique on another substrate. Both the substrates are then bonded together using an adhesive bonding technique.

4.3.1 Nozzle-diffuser pumps theory

Nozzle-diffuser pumps are built by coupling a nozzle, pumping chamber and diffuser together in series. The volume of fluid in the pumping chamber is periodically varied using an oscillating pressure (actuator). The kinetic energy of the fluid (velocity) is converted to potential energy (pressure) in both the nozzle and diffuser but the efficiency of this process is much greater in the diffuser direction thus discharging more fluid through the diffuser. If Q_d is the discharge through the diffuser and Q_n the discharge through the nozzle then an increase in the chamber volume causes $|Q_d| > |Q_n|$ and a

decrease in the chamber volume causes $|Q_d| < |Q_n|$ resulting in a net pumping action, as shown in Figure 110.

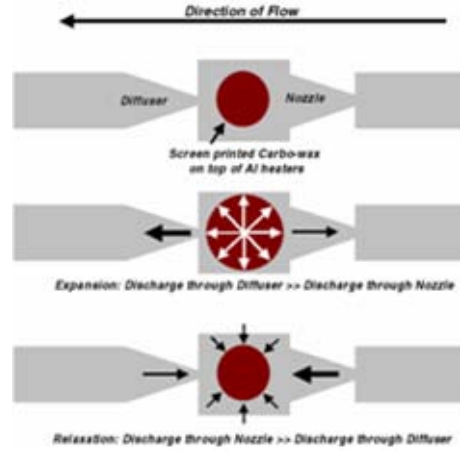


Figure 110: Principle of operation of nozzle-diffuser pumps and fluid flow with increasing and decreasing chamber volume.

The pressure differences across the diffuser and nozzle are given by

$$\Delta P_d = \rho v_d^2 \xi_d / 2 \quad (69)$$

$$\Delta P_n = \rho v_n^2 \xi_n / 2 \quad (70)$$

Where ΔP_d and ΔP_n are pressure differences across the diffuser and nozzle, respectively, ξ_d and ξ_n are the pressure loss coefficients for the diffuser and nozzle, and v_d and v_n are the average velocities at the diffuser and nozzle. If ξ_d is less than ξ_n , then pumping will occur in the direction of the diffuser. These pumps cannot generate large pressures and are suitable for low-pressure fluidic systems. The volume flow rate is given by

$$Q = 2V_f \frac{\left[\left(\xi_n / \xi_d \right)^{1/2} - 1 \right]}{\left[\left(\xi_n / \xi_d \right)^{1/2} + 1 \right]}, \quad (71)$$

where Q is the volume flow rate, V is the volume variation per cycle, and f is the pulse frequency.

4.3.2 Fabrication

The device is fabricated using plastic casting as, shown in Figure 111. The substrate with the channels, reservoirs, pumping chamber and the nozzle-diffuser geometry is made using epoxy EPOTEK 301-2 FL, see Figure 112(a), which is a clear optical grade epoxy ($> 97\%$ light transmission), with low viscosity (125 cpS at 100 rpm) and glass transition temperature $T_g = 65^\circ\text{C}$. A stamper with 50 μm tall negative replicas of the channels, chamber and nozzle-diffuser geometry is formed by etching a silicon wafer using a deep RIE process (SF_6 160 sscm, C_4F_8 80 sscm O_2 13 sscm, coil power 800W, and platen power 600W). The stamper is then vapor deposited with a 1 μm thick

parylene layer, which serves as a release layer to aid separation of the cured plastic from the stamper. The silicon stamper is sandwiched with a Teflon O-ring (2 mm thick) and flat polypropylene disc in an aluminum mold. The epoxy resin is injected into the sandwich and maintained at 80°C for 3 hours and then the cured plastic is released. Access holes for channels and electrodes are drilled using a micro drill press. A second epoxy substrate is made by casting, using EPOTEK-314, a clear, high temperature epoxy ($T_g = 150^\circ\text{C}$). This epoxy is essential because of the metal heaters and contacts. The two substrates are then bonded using an adhesive which is patterned on the surface using conventional photolithography techniques and the plastic must be able to withstand temperatures of up to 110°C. This epoxy is made using the same technique but a blank silicon wafer with a 1 μm thick parylene layer is used instead of the etched stamper. The released substrate is then vapor deposited with a 0.5 μm thick parylene layer to improve adhesion of metals to the surface. Then metal layers Cr/Al (50 nm/ 200 nm) are evaporated onto the substrate and heaters and contacts are patterned using photolithography.

The wax patches are made using a screen-printing process. The screen-printing process uses a 15 μm thick stencil screen made of aluminum with precision cut openings for wax printing. The plastic substrate (EPOTEK 314) with the patterned heaters is then mounted on the screen printer and the openings on the screen and the heaters on the substrate are aligned and the screen is locked in position. The wax used is Polyethylene Glycol, MW 8000 (PEG 8000), which is a water-soluble carbowax with a melting point of 65°C and a volumetric expansion of 30% on transition from solid to liquid. The wax is melted by heating to 80°C and then screen-printed using a teflon squeegee (2kPa pressure, 8 ft/min speed). The substrate is released and placed in an oven at 65°C for 3 minutes for the wax to re-flow and to obtain a smooth surface. The contacts for the heaters are masked using masking tape and the substrate is coated with 4 μm thick parylene C layer. Figure 112(b) shows a picture of 15 μm tall wax actuator.

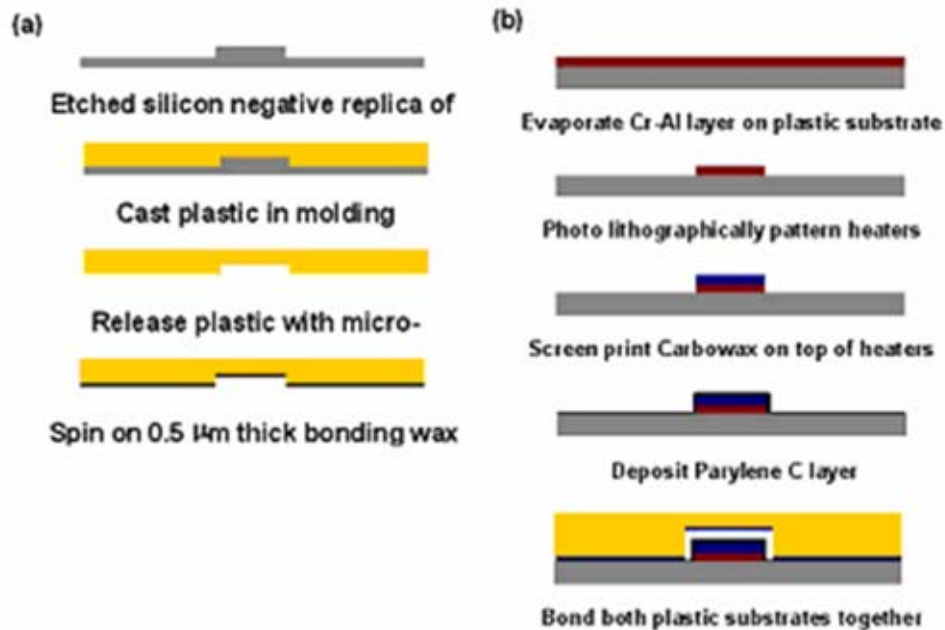


Figure 111 (a) and (b). Shown is the process flow for fabrication of the channel structure and wax actuator respectively.

The EPOTEK 301-2 FL substrate with the channels and nozzle-diffuser geometry is spin coated with a 0.5 μm thick layer of bonding wax solution (Blanchard bonding wax dissolved 1:1 by weight in acetone) and then aligned and bonded to the EPOTEK 314 substrate with the wax actuator using a laminator with the rollers at 60°C, speed of 2 ft/min and gauge of 4 mm. The access holes for the electrodes are filled with conductive epoxy and cured at room temperature for 18 hours. Figure 112(c) shows a picture of the bonded device. The pumping chamber is 500 μm in diameter with diffuser angle of 30°, and channel widths of 400 μm .

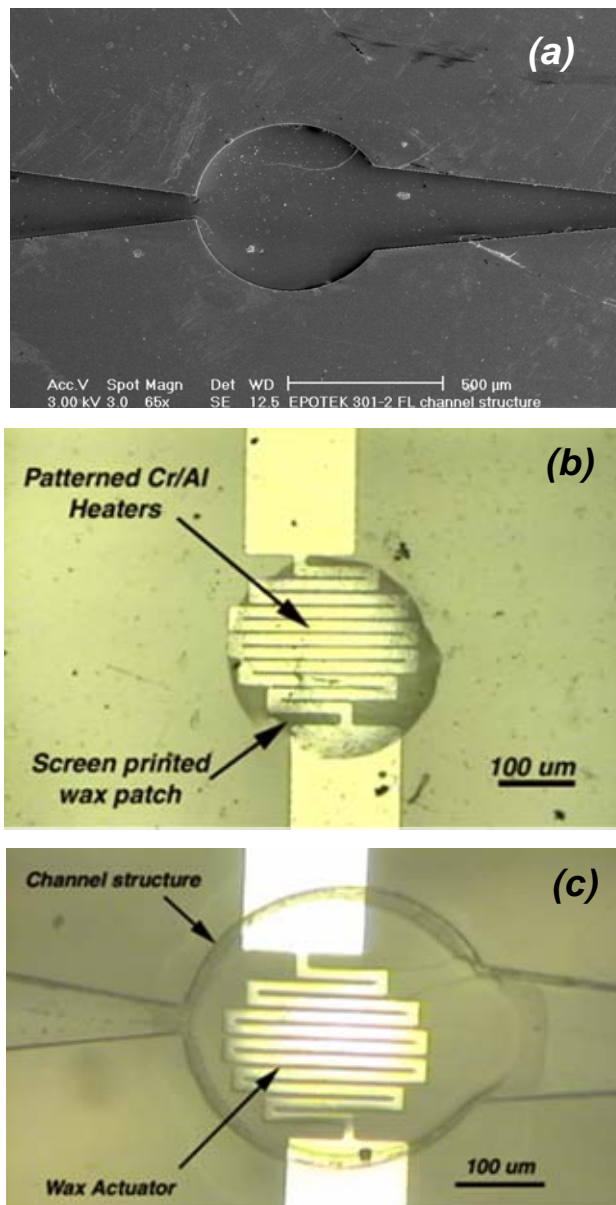


Figure 112: (a) Pictures show SEM of EPOTEK 301-2 FL substrate with chamber, channel and nozzle-diffuser geometry, (b) wax actuator on EPOTEK 314 substrate and (c) bonded nozzle-diffuser pump respectively.

4.3.3 Thermal Modeling

Actuation methods like bubble based actuation makes use of bubble generation in the liquid to create a volume change in the pumping chamber which causes a net flow in one direction. Bubble generation occurs at elevated temperatures and is not ideal for transport of biofluids, which are sensitive to high temperatures. The wax-based actuator operates at lower temperatures and the thermal modeling, which was performed to determine the heater temperature and the heat transferred to the fluid in the channels, shows that the temperature at the wax-liquid interface at the maximum operating power is less than 100°C. This is essential to avoid generation of bubbles and to prevent sample loss due to evaporation and sample damage due to high temperatures.

A one dimensional steady state heat transfer model was developed to first model the temperature of the heater with increasing power. The heater is fabricated on top of an epoxy substrate by evaporation of 200 nm of aluminum. The resistance of the fabricated heater, which is 0.01 m long, 100 µm wide was determined and found to be 80 ohms. The temperature of the heater can be determined by modeling the system using a steady state model with constant thermal properties and ignoring the losses due to radiation. By the first law of thermodynamics we know

$$E_g - E_{out} = E_{st} \quad (72)$$

where E_g , E_{out} , E_{st} are the energy generated, energy outflow and the energy stored per unit volume respectively and are given by

$$E_g = I^2 R_e' L \quad (73)$$

$$E_{out} = h(\pi D L) (T - T_\infty) \quad (74)$$

$$E_{st} = d/dt (\rho V c T) \quad (75)$$

where I is the applied current, R_e' is the electrical resistance per unit length, L is the length of the wire, D is the diameter of the wire, V is the total wire volume, T is the temperature of the wire, T_∞ is the ambient temperature, ρ is the density of aluminum and c is the specific heat capacity of aluminum. Since we assume steady state, the term E_{st} goes to zero. The equation reduces to

$$\pi D h (T - T_\infty) = I^2 R_e'. \quad (76)$$

The temperature of the heater for an aluminum wire, with the given dimensions, for different applied current was calculated and plotted in Figure 113. The maximum operating current was approximately 30 mA (5V AC).

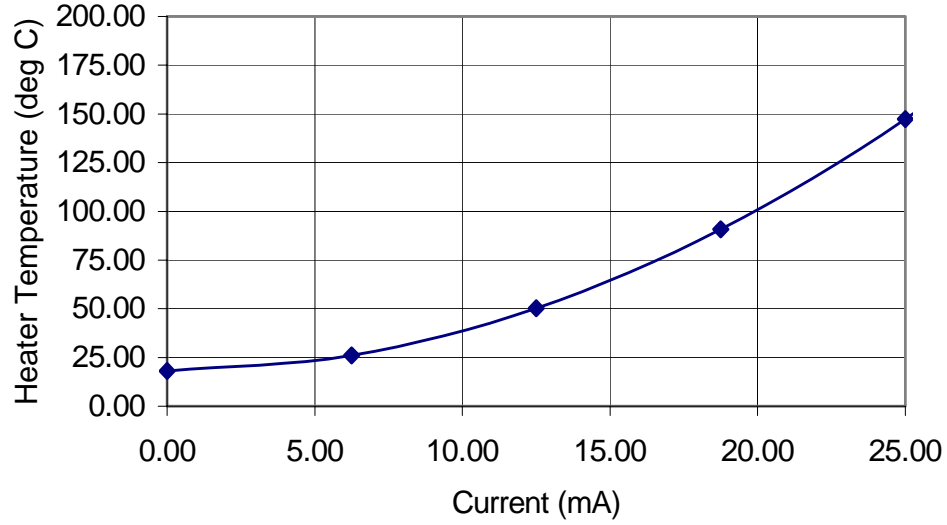


Figure 113. The graph shows the calculated change in heater temperature with increasing current

The entire actuator can also be modeled using a one dimensional steady state heat transfer model. Figure 114 shows a layer-by-layer representation of the actuator along with the thickness of each layer. The actuator that was modeled for the test devices had a 2 mm diameter and a height of only 20μm and therefore the heat transfer through the

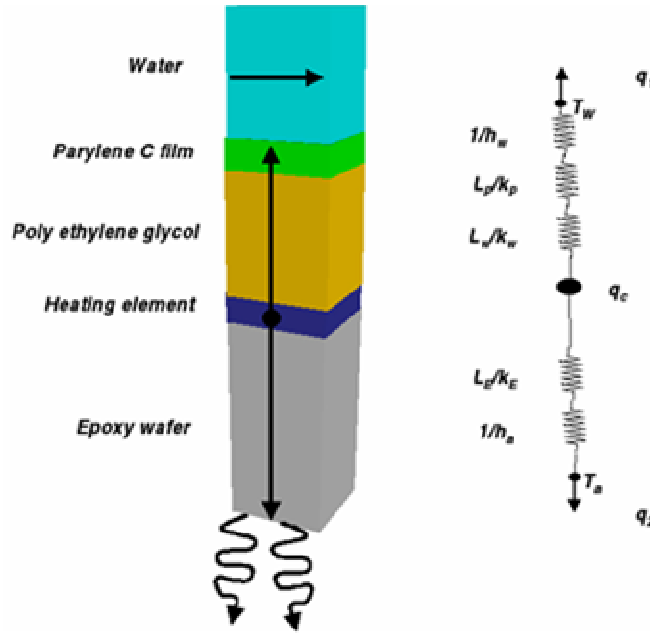


Figure 114: Layer by layer representation of the actuator.

sides is negligible. The convection heat transfer coefficient of water can be calculated using the equation

$$h = (Re)^{1/2} (Pr)^{1/2} / L \quad (77)$$

where Re and Pr are the Reynolds number and Prandlt number, respectively and L is the length traveled by the fluid. The value of h was $45 \text{ W/m}^2\text{K}$, and a convective heat transfer coefficient of air $100 \text{ W/m}^2\text{K}$ was assumed. The thermal conductivity of epoxy, PEG 8000 and parylene C are shown in Table 12. The thermal resistances of each layer are calculated and since we know the ambient temperature and the heater temperature for different applied voltages the fluid temperature T_w can be calculated.

$$q_c = q_1 + q_2, \quad (78)$$

where q_c , q_1 , and q_2 are equal to the power generated and dissipated in the upward and downward direction of the actuator equal to

$$q_1 = (T_c - T_w) / R_1 \quad (79)$$

$$q_2 = (T_c - T_\infty) / R_2 \quad (80)$$

where T_c , T_w and T_∞ are the heater, fluid and ambient temperatures, R_1 is the sum of thermal resistances in the upward direction and R_2 the sum of the thermal resistances in the downward direction. The values of T_c for different values of applied current have been previously calculated, therefore T_w can also be calculated for different values of current and the plot is shown in Figure 115. From the Figure, it can be seen that the temperature of the fluid at the interface at maximum operating current 30 mA (5V AC) is below 100°C .

Table 12: Thermal conductivity of materials used in fabricating the PEG 8000 actuator

| Material | Thermal Conductivity (W/mK) |
|----------|--------------------------------|
| PEG | 0.23 |
| epoxy | 6.92 |
| parylene | 0.86 |

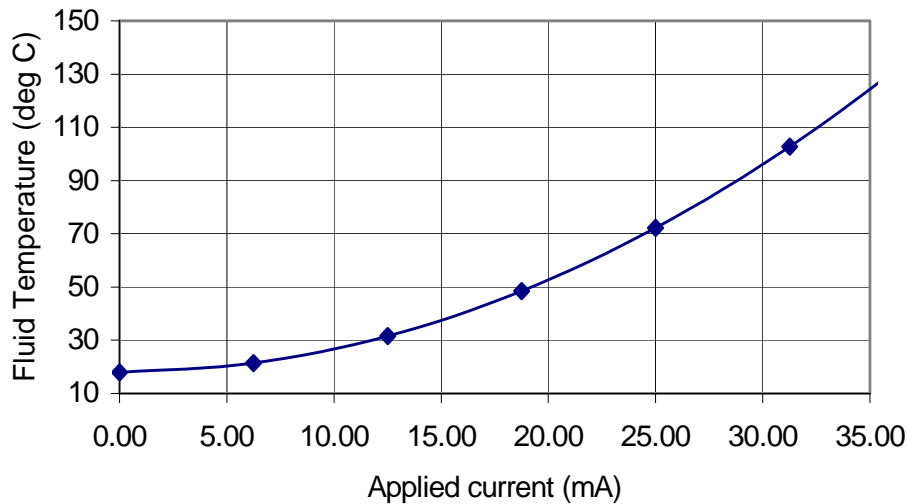


Figure 115: The graph shows the change in fluid temperature with increasing current. The pump usually operates below 30 milliamps (2.5V DC).

4.3.4 Measured Results

The surface profiles obtained due to deflection of the membrane due to expansion of wax at different applied voltages is shown in Figure 116. Voltages up to 5V were applied and a maximum deflection of 23 μm was obtained at 5V. The deflecting 4 μm parylene C membrane containing the wax fails at higher voltages due to high stress obtained when the wax expands, which results in the liquid wax escaping from the actuator.

Flow rate measurements were made using the setup shown in Figure 117(a) and the particle flow velocities were measured for different applied voltages and pulse frequencies. Volume flow rates were calculated and plotted, as shown in Figure 118. A flow rate of 70 nl/min was obtained at an applied voltage of 5V AC and a pulse frequency of 1 Hz. The wax-based actuator operates best at lower frequencies (0.5 Hz – 1.5 Hz). This is due to the slow response time of the carbowax. High frequencies result in low volumetric expansion and hence low volume displacement, because the heat generated due to the pulse is not sufficient to melt the entire wax patch.

Experiments were performed to calculate the pumping pressure generated using the nozzle-diffuser pump. The setup used is shown in Figure 117(b). The channels were filled with fluid and air was trapped in a column, which is located just past the diffuser. The pump was operated at 5V AC and the pulse frequency was varied. The pressure generated was calculated from the data obtained for height of the trapped air column. Maximum pumping pressure of 1400 Pa was obtained at a frequency of 1 Hz. Results are plotted in Figure 119.

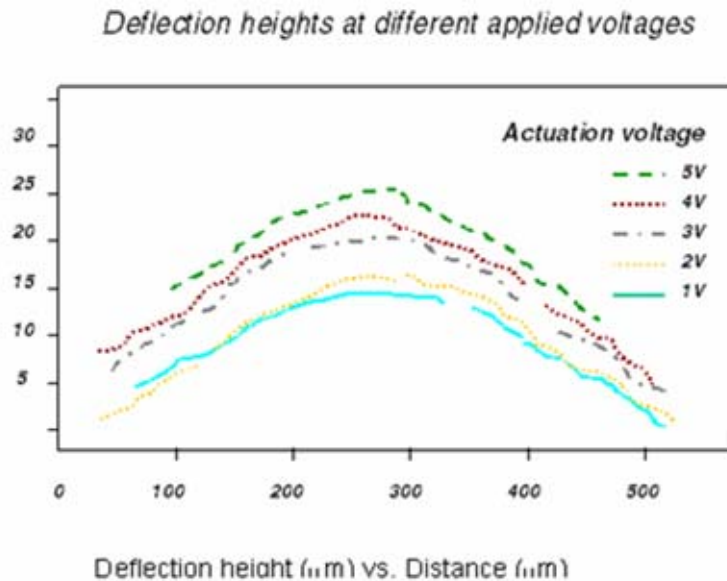


Figure 116: Optical profiles of the deflection heights of the wax actuator surface obtained at different voltages using a ZYGO optical interferometer.

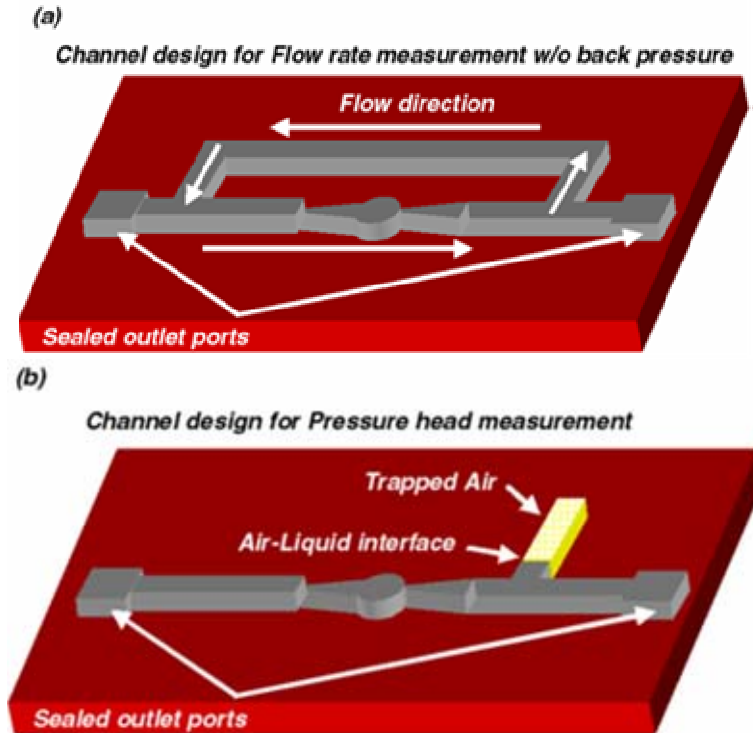


Figure 117: Channel design for calculation of (a) flow rate with zero back pressure and (b) pumping pressure.

Volume Flow Rate Vs. Frequency

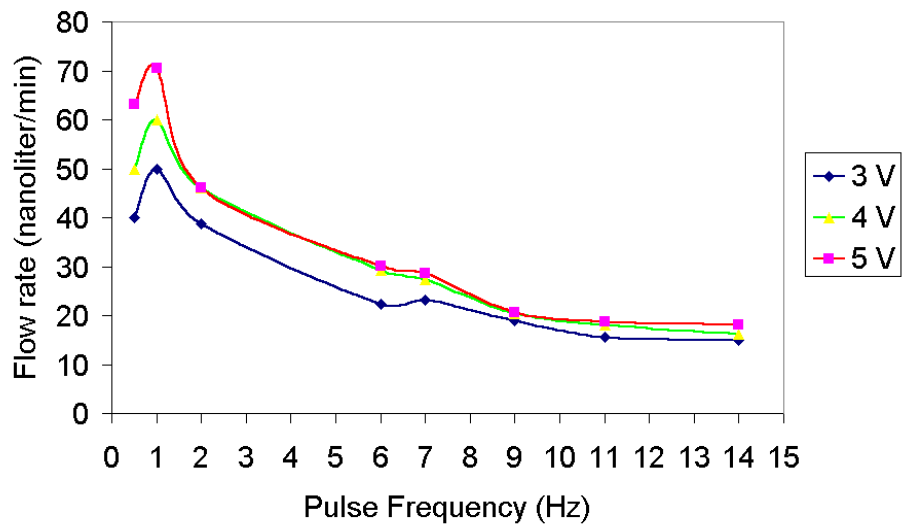


Figure 118: Volume flow rates obtained at different pulse frequencies for different applied voltages.

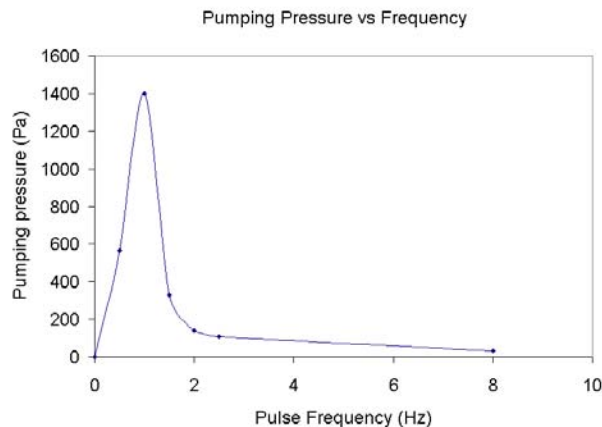


Figure 119: Pumping pressure generated at 5V, plotted for different pulse frequencies.

4.4 PCR Device

4.4.1 Device Fabrication

Materials for plastic casting are liquid monomers or pre-polymers that are stable under ambient temperature or in the absence of UV light. Once mixed with hardeners, or heated to a higher temperature, or brought under UV radiation, they start to polymerize or cross-link, becoming solids. Unlike other plastic replication techniques, casting processes can be carried out under near atmospheric pressure at relatively low temperature ranges. This makes it possible to incorporate functional elements out of various materials. The monomers or the pre-polymers are in a relatively low viscosity fluidic state during the casting process, which leads to intimate mold contact, and as a result, high-resolution micro features.

Figure 120 shows the structure of the thermal chemical reactor. The cylindrical reaction chamber (glass capillary, Laboratory Devices, Inc., with 1 mm inner diameter (ID)) is surrounded by a resistive heater coil (Scientific Instrument Services, W73). The reaction mixture temperature is sensed with a thermocouple (Omega Engineering, Inc. OD 250 μm). A thermal electric device (Melcor, 4 mm x 4 mm x 2.2 mm) is positioned at the bottom of the chamber to facilitate cooling and to assist uniform heating. The entire assembly is embedded in a transparent polymer matrix (Epotek, 301-2Fl) with the normal heating side of the TE device exposed for better heat conduction.

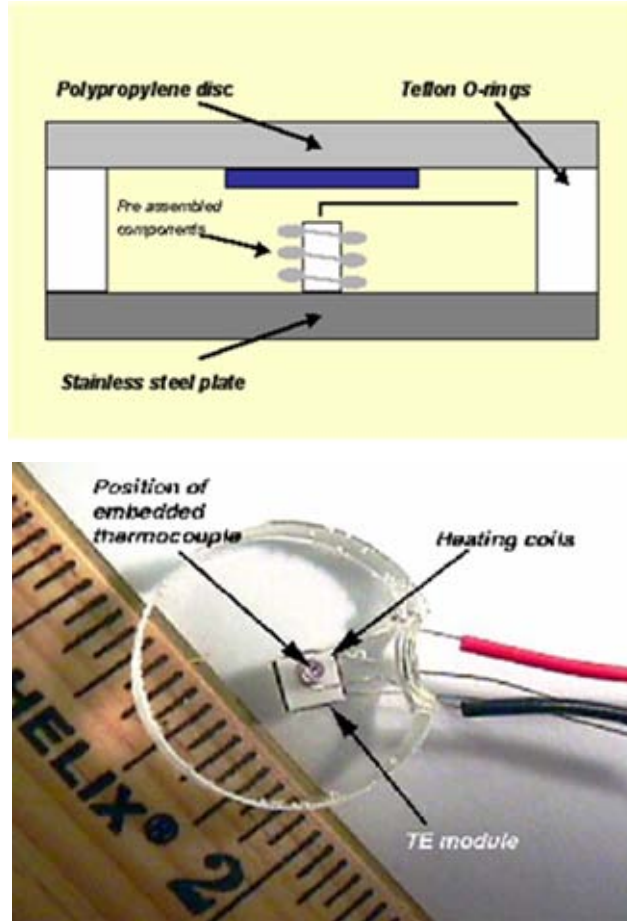


Figure 120: Device design and fabricated PCR device.

Figure 121 shows the schematics of a casting mold assembly. Device components were first pre-assembled on a release-assisting surface at one side of the metal mold. A circular Teflon O-ring with a sample injection opening was placed around the component assembly. The mold was closed by placing a second release assisting surface. After the mold assembly was tightened to avoid leakage, casting resin was injected and cured at 110°C for 50 minutes.

The fabrication scheme presented here allows achieving the 3-D nature of the structure. This would be very difficult to accomplish through other fabrication technologies that are based on surface micromachining or multilayer stacking.

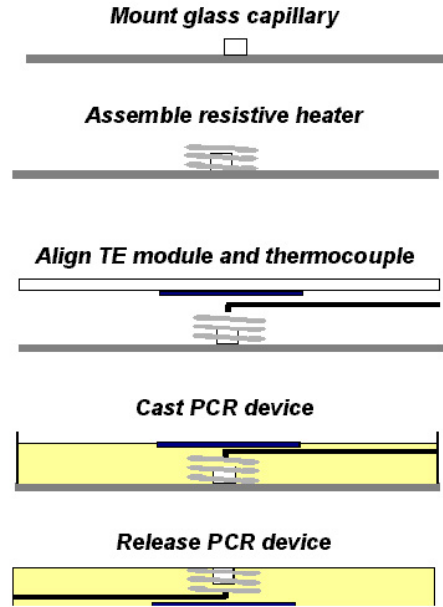


Figure 121: Process flow for fabrication of the PCR device.

4.4.2 Thermal Modelling

Modeling was carried performed understand the thermal performance of the device using the ACE+ software package from CFD Research Corporation. The computational domain includes the plastics, sample, liquid wax and air regions as in a normal testing situation, shown in Figure 122. The governing equation is the energy conservation equation in 2D asymmetric form. The boundary conditions assumed here were natural convection on the top of the cover as well as the sidewall of the device. At the bottom, the device is in contact with a thermoelectric (TE) device, and does have some heat loss. The computed steady-state temperature distribution is shown in Figure 122. The input power was varied until the maximum temperature of the sample was 94°C . At a heater power setting of approx. 0.12 W the maximum temperature inside the sample was 94°C . As seen here, the temperature in the sample is a maximum inside the mid-height of the sample. A temperature variation of about 1°C was seen over the entire sample volume.

4.4.3 Device Characterization

A controller (Physical Interface Device (PID) loop) (MOD30ML from ABB) was programmed to allow flexible automation. The temperature control point was taken from the thermocouple located at the bottom of the chamber. The output of the PID was sent to a HP power supply directly to provide heating via the coils. The TE device, when turned on, was running at both heating and cooling modes, which are controlled via an exponential relationship based on the temperature difference between the set point and measured temperatures. The controller was connected to a PC that was running a custom graphical user interface.

A two-step temperature cycle (94°C for 30 s and 70°C for 60 s) was used to evaluate the thermal performance of the device. Figure 123 (a) shows the measured

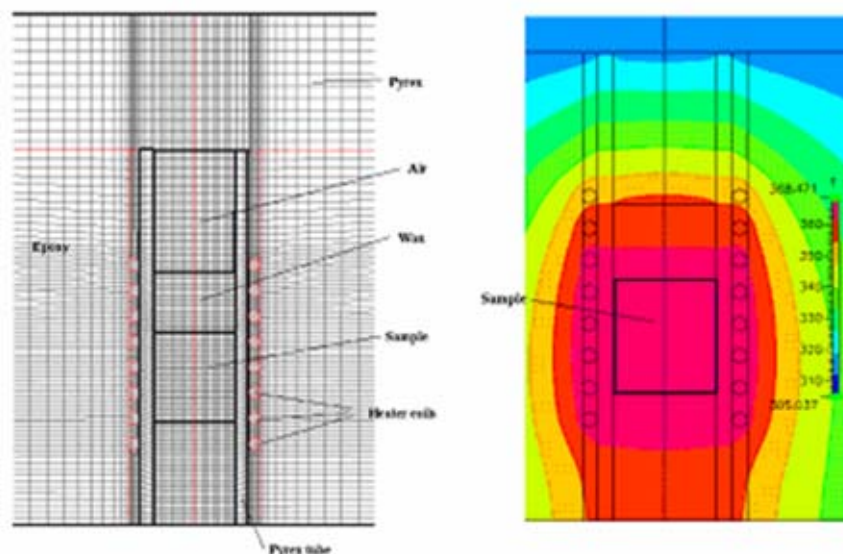


Figure 122: Meshing and Heat Distribution around the PCR chamber.

temperature when the device has active heating/cooling control, (i.e., heating coils and TE device are turned on). The heating rate is approximately 2.4°C/s while the cooling rate is around 2.0°C/s . When the device is controlled by heating coils only, (i.e., TE device turned off), the heating rate is about 1.0°C/s while the cooling rate is approximately 1.6°C/s .

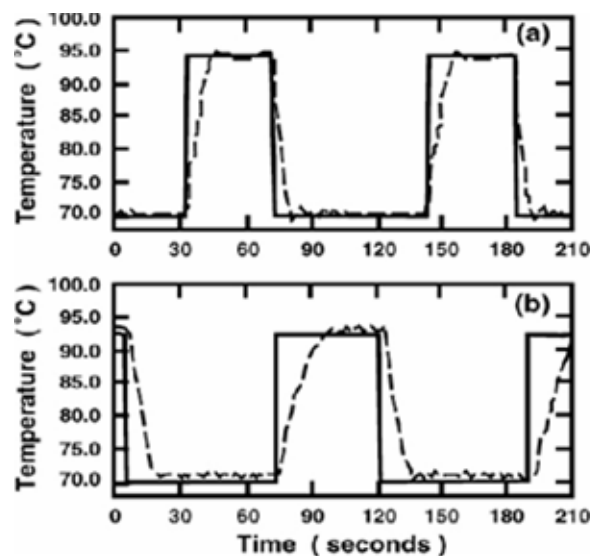


Figure 123: Profiles of heating and cooling cycles using on-chip heaters and coolers.

4.4.4 On-Chip Thermal Lysis and PCR

Escherichia coli cell lysis and the subsequent amplification of the released genomic DNA segments were carried out using the described micro-chip. Approximately two-thirds of an *E. coli* bacterial colony was collected and resuspended in 50 μL of sterile H_2O . This suspension was diluted 1:10 in a PCR reaction mixture containing 10 mM

Tris-HCl (pH 8.3), 50 mM KCl, 1.5 mM MgCl₂, 0.001% gelatin, 250 g/mL bovine serum albumin, 200μM each deoxynucleotide triphosphate, 1.0 μM each primer, and 2.5 units/100μl AmpliTaq DNA polymerase. The cell and PCR mixture, 1.5 μL, was loaded in the micro reaction chamber. Chill-out™ liquid wax was topped on the solution to prevent sample evaporation. The temperature program was initiated at 94°C for 1 min to induce cell lysis. The analyte was then cycled between 50°C for 30 sec and 72°C for 30 sec. The primer set used to amplify a 346-bp segment of the *E. coli* lamB gene was 5'-CTG ATC GAA TGG CTG CCA GGC TCC-3' and 5'-CAA CCA GAC GAT AGT TAT CAC GCA-3'. The PCR product was visualized and compared with control reaction through gel electrophoresis, shown in Figure 124.

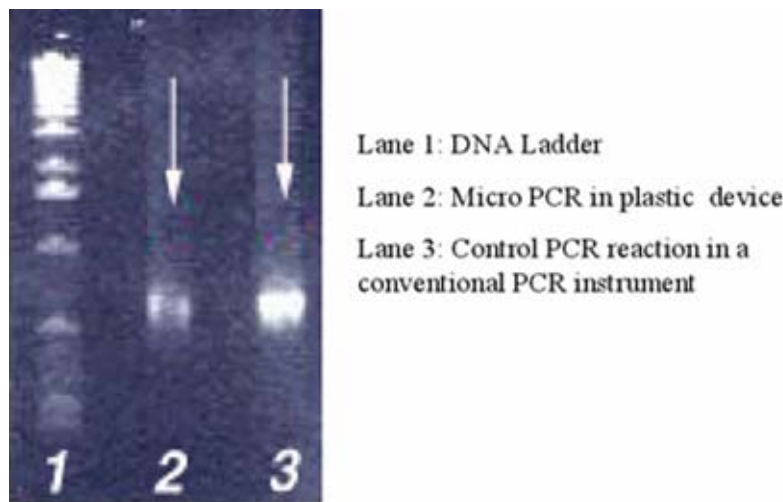


Figure 124: PCR product compared with control reaction through gel electrophoresis.

4.5 Capillary Electrophoresis Device

4.5.1 Device Fabrication

Figure 125 shows the simplified microcasting process. First, patterns for channels, reservoirs, chambers, and reactors are etched in a silicon wafer using a deep RIE system (Specialty Technology Systems), (SF₆:130 sscm, O₂:30 sscm, C₄F₈: 80 sscm, coil power: 800 Watts, and platen power: 600 Watts, 30 mins.). Next, a 1 μm-thick p-xylylene (parylene-C) layer is vapor deposited on the patterned silicon substrate [127]. This thin film serves as a release layer, which facilitates the separation between the casted material and the wafer surface. The patterned silicon substrate is then used to create a mold by joining it with a supporting plastic plate and teflon ring spacer. The mold assembly is then placed between two aluminum molds as was shown in Figure 26. The mold is then heated to 45°C for 8 hrs and filled with a low viscosity catalysed epoxy (EPOTEK 301-2, EPOTEK 301-2 FL). In order to seal channels and reservoirs, a flexible transparent film is laminated on top of the epoxy substrates.

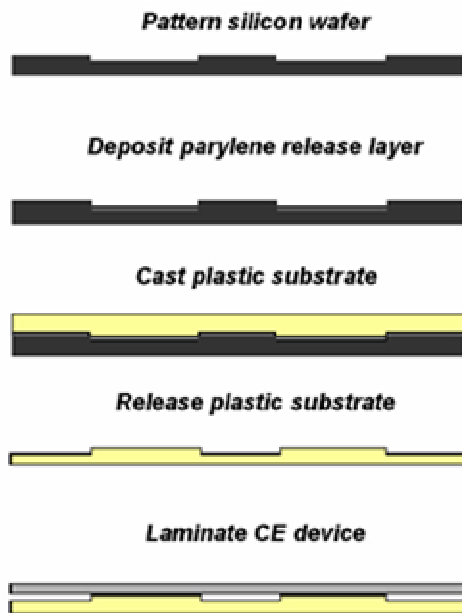


Figure 125: Process flow for fabricating the CE device.

The lamination process uses a desktop roll type laminator (Kepro Circuit Systems, Inc. BLT 121-A) and a thin mylar film (2 mil, Monokote, Top-Flite, Inc.) is used to laminate the plastic substrates. The substrate is first treated with acetone, and then the film is laminated onto the substrate by passing it between two rollers. The process is carried out at room temperature and at a feed rate of 2 ft/min. These structures show excellent permeation barrier characteristics with water permeabilities $P \ll 1.7 \mu\text{l}/\text{cm}^2/\text{day}$ at room temperature. When these capillaries are filled with sample there is no seeping present at the bond interface. The separation channel is 3 cm long and the reservoir dimensions are $5 \times 5 \text{ mm}^2$. The channels for sample introduction are 0.5 cm long. Figure 126 shows a fabricated capillary electrophoresis device.

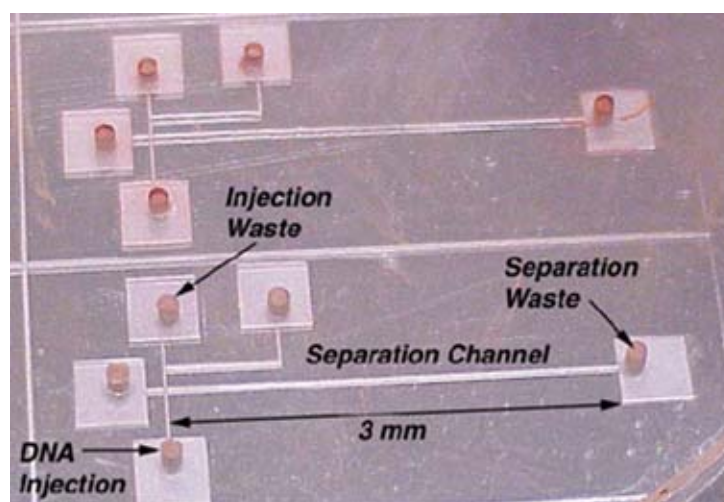


Figure 126: Fabricated CE device.

4.5.2 Separation Results (HEC)

The fabricated capillary electrophoresis devices were used to perform separations using a 0.5% (w/v) hydroxyethylcellulose (HEC) (MW 90,000-105,000) sieving matrix. Approximately 3 μ l of the electrophoresis buffer (0.2g HEC, 4 ml of 1x TBE buffer, and 36 ml of distilled, DI water) was introduced in the analyte waste reservoir using a stiff needle syringe. After the channels have filled completely due to capillary action, the other reservoirs are filled with the buffer and the analyte reservoir is filled with 0.5x TBE (1X Tris-borate EDTA). Pre-electrophoresis was done by applying 300 V/cm across the separation channel for 10 minutes and keeping the analyte and analyte waste reservoirs at a potential of 0 V. This is done to produce a concentration gradient in the HEC while increasing the concentration of HEC in the column above 0.5%. Approximately 2 μ l of a DNA sample labeled with SYBR Green I at an intercalating ratio of greater than 1:5, dye:DNA bp is loaded into the injection reservoir. Samples were then separated under an electric field of 110 V/cm in a distance of 3 cm. Figure 127 shows the DNA plug and separations obtained using the plastic capillary electrophoresis devices. The plastic has very low background fluorescence and does not interfere with the fluorescence of the DNA bands.

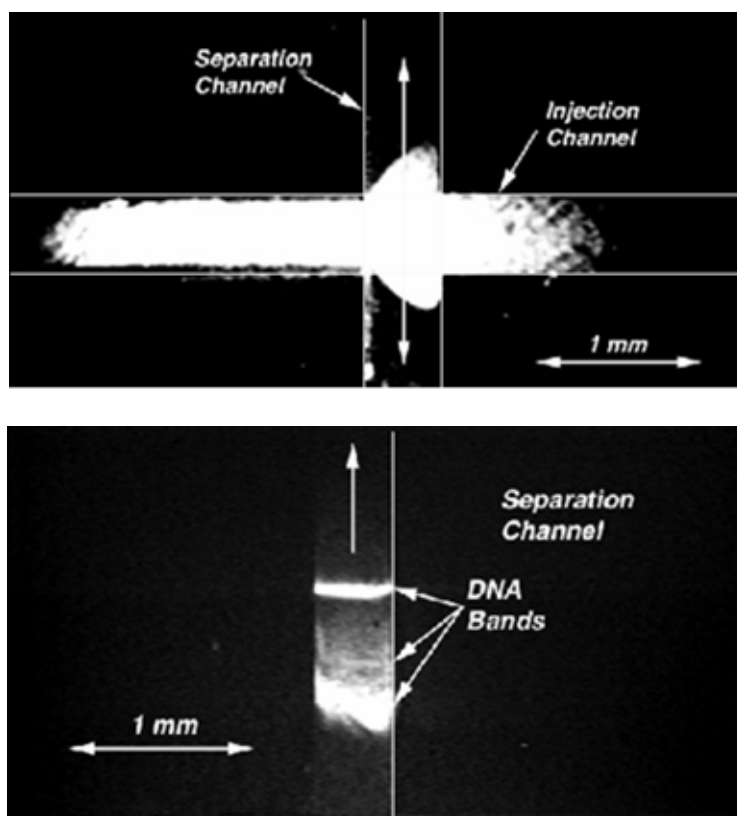


Figure 127: DNA plug and separated bands (HEC).

4.5.3 Separations results (UV gels)

Though satisfactory results were obtained and it was shown that electrophoretic separations can be done in devices made of cast epoxy, the resolution of the bands obtained needs to be improved. In order to achieve this, separation was done again using

the same devices but the sieving matrix was replaced by polyacrylamide. Controlled polymerization only in the separation channel was obtained using UV initiated cross linking, once the gel in the separation channels is polymerized the unpolymerized gel can be removed and filled with 0.5X TBE. The DNA is loaded in the injection channel and it diffuses everywhere except into the separation channel. Voltage (60 V/cm) is applied across the separation channel, and DNA slowly moves into the separation channel. Once there is a sufficient DNA plug in the separation the voltage is reduced to zero and the remaining DNA in the injection channel is removed and 0.5X TBE is added. Separation is now done at 120 V/cm with the small DNA plug captured during the initial procedure. The resolution of bands obtained using UV initiated poly acrylamide is of better quality than the HEC sieving matrix. The bands however are not very sharp and tend to diffuse, but resolution is good enough to identify 100 bp bands. The results are shown in Figure 128.

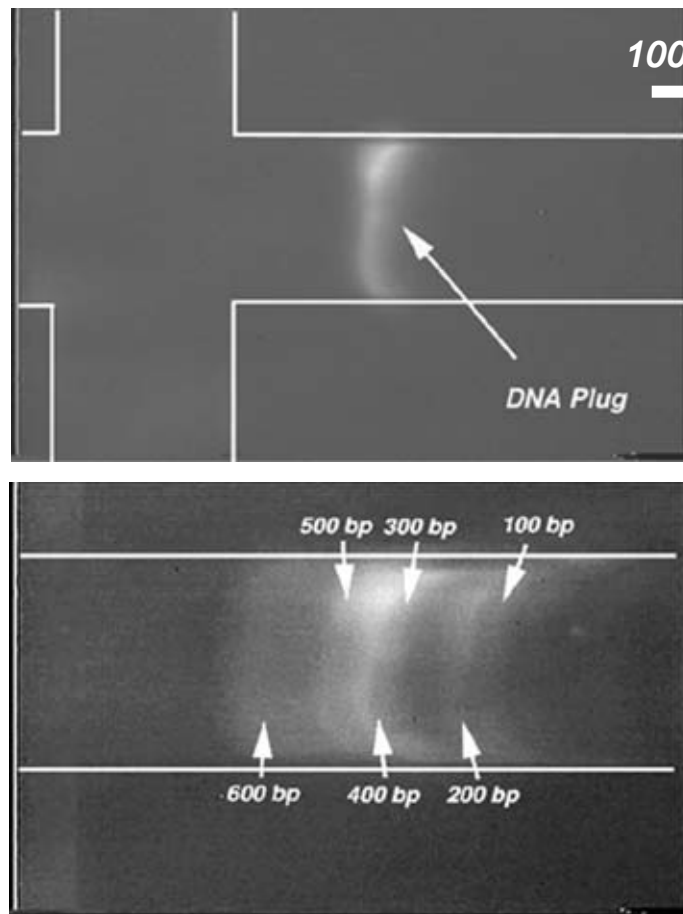


Figure 128: DNA plug and separated bands (UV gels).

4.6 Laminar Flow Patterning of Protein Doped Conductive Polymers

4.6.1 Electrode Fabrication

The devices were fabricated using the epoxy casting technique to provide a low cost but high quality platform for cell culture applications. These substrates are extremely

cheap and easy to fabricate and can be used for single assay use. The device consists of 2 substrates bonded to each other. The bottom substrate is made using EPOTEK 301-2 FL (Epoxy Technologies). This epoxy is optically clear and has no background auto fluorescence. A blank epoxy substrate is fabricated using the casting technique and a thin layer of parylene C is deposited to improve gold adhesion. A 200 nm thick layer of gold is then evaporated onto the substrate and photolithographically patterned into electrodes. Figure 129 shows a picture of the fabricated electrodes. The working electrode is 300 μm wide and has a working length (area for deposition) of 900 μm . The counter electrode is 1 mm wide and 900 μm long. The counter electrode is made significantly larger than the working electrode to aid the electro polymerization process. The substrate processing is similar to conventional photolithography techniques except that the soft bake is done for 40 minutes at 60°C, which is the T_g for this epoxy.

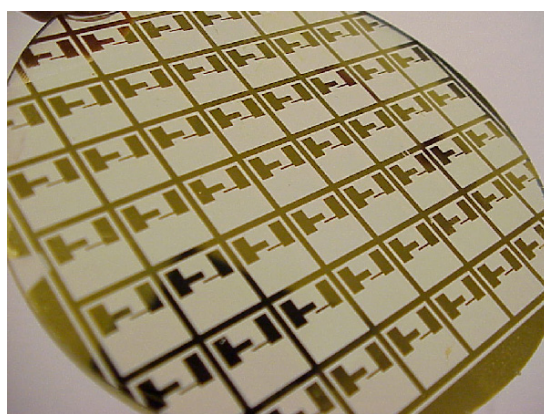


Figure 129: Fabricated electrodes

4.6.2 Channels for Laminar Flow Patterning

The channel structures are made on a separate substrate, which is also made using the epoxy casting technique. The epoxy used is EPOTEK 310 (Epoxy technologies). This epoxy is an elastomer and has a T_g below room temperature. The fabricated, shown in Figure 130, device has three inlet channels, which feed into one wider channel that enables the flow of 3 different liquids through the 3 inlet channels resulting in laminar flow of 3 streams in the main channel. Mixing of different fluids in the laminar flow regime is only due to diffusion, which is significantly small. By creating a stream of polyelectrolyte flanked on either side by an inert liquid ECD can be achieved on an area defined by the stream of polyelectrolyte thus enabling precise patterning and incorporation of proteins into PPy. The smaller channels are 300 μm wide and the large channel is 900 μm wide. The soft epoxy substrate seals reversibly to the other substrate with electrodes without the use of any adhesive resulting in a completely bonded device. Colored liquids are used to demonstrate laminar flow, shown in Figure 131.

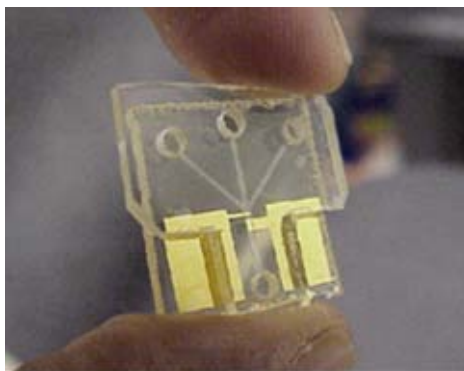


Figure 130: Fabricated device for laminar flow patterning of protein doped conductive polymers

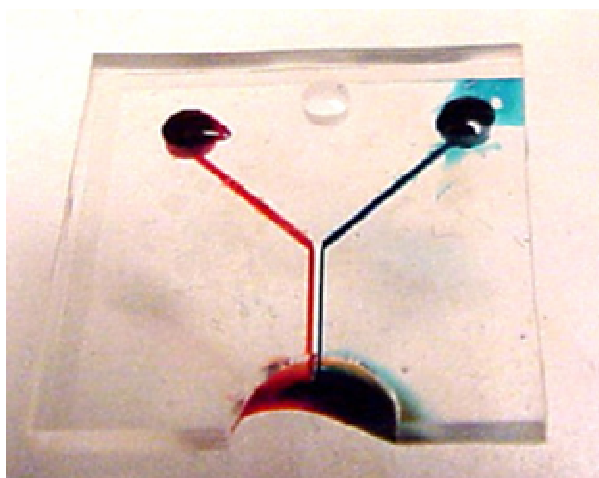


Figure 131: Laminar flow demonstration in fabricated channel structure

5.0 Conclusion

Technologies for fabricating plastic MEMS have been developed and are presented in this report. Surface micromachining of thin polymer films has led to the implementation of microactuation based on the thermal expansion of thin paraffin films, which is an attractive solution for microfluidic valve applications. Active microfluidic valves for controlling the flow of both liquid and gaseous samples have been developed and presented. First, a blocking microvalve used for valving gases has been reported. Low leak rates and roughly linear flow rate with applied voltage have been achieved. An active inline microfluidic valve has been developed for liquids in a microchannel. Finally, an active micropump has been demonstrated using the paraffin actuation technology and structure with low dead volume.

Technology for fabrication of high quality, cheap, disposable polymers has been shown to implement a variety of microanalytical systems, including a micro PCR system and CE system for amplifying and separating DNA, respectively. Demonstrations on how to integrate complexity into plastic based systems is shown using two techniques, sub-die embedding and surface micromachining. Techniques for cellular micropatterning are also shown using electrochemical deposition of conductive polymers doped with extracellular matrix proteins.

6.0 List of Publications

6.1 Theses

[1] Edwin Carlen, *Electrothermally Actuated Polymer Microvalves*, Ph.D, Thesis, University of Michigan, Department of Electrical Engineering and Computer Science, 2001.

[2] Sethu Palaniappan, *Microfabricated Compounds for Integrated Microfluidic Electroanalysis Systems*, Ph.D, Thesis, University of Michigan, Department of Electrical Engineering and Computer Science, 2002.

6.2 Refereed Journal Publications

[1] Selvaganapathy, R., Carlen, E.T. and Mastrangelo, C.H., ``Batch Fabricated Inline Microvalve," Submitted to *Sensors and Actuators, Part A*, August 2002.

[2] Carlen, E.T. and Mastrangelo, C.H., ``Paraffin Actuated Surface Micromachined Valves," *IEEE Journal of Microelectromechanical Systems*, vol. 11, no. 5, Oct. 2002.

[3] Carlen, E.T. and Mastrangelo, C.H., ``Electrothermally Activated Paraffin Microactuators," *IEEE Journal of Microelectromechanical Systems*, vol. 11, no. 3, Jun. 2002.

6.3 Conferences

[1] Selvaganapathy, R., Carlen, E.T. and Mastrangelo, C.H., ``Batch Fabricated Inline Microvalve," Submitted to *Sensors and Actuators, Part A*, August 2002.

[2] Carlen, E.T. and Mastrangelo, C.H., ``Paraffin Actuated Surface Micromachined Valves," *IEEE Journal of Microelectromechanical Systems*, vol. 11, no. 5, Oct. 2002.

[3] Carlen, E.T. and Mastrangelo, C.H., ``Electrothermally Activated Paraffin Microactuators," *IEEE Journal of Microelectromechanical Systems*, vol. 11, no. 3, Jun. 2002.

[4] Carlen, E.T. and Mastrangelo, C.H., "Simple, High Actuation Power, Thermally Activated Paraffin Microactuators," *Transducers '99*, Sendai Japan, June 7-10, 1999.

[5] Carlen, E.T. and Mastrangelo, C.H., "Paraffin Actuated Surface Micromachined Valves," *IEEE MEMS 2000*, Miyazaki Japan, pg 381-385.

[6] Yu, H., Sethu, P., Chan, T., Kroutchinina, N., Blackwell, J., Mastrangelo, C.H. and Grodzinski, P., "A Miniaturized and Integrated Plastic Chemical Reactor for Genetic Analysis," *Micro Total Analysis Systems*, 2000, Enschede, The Netherlands, pg 545-548.

[7] Sethu, P., Mastrangelo, C.H. and Grodzinski, P., "Fabrication of Genetic Analysis Microsystems using Plastic Microcasting," *2000 Solid-State Sensor and Actuator Workshop*, Hilton Head Island, SC.

[8] Sethu, P. and Mastrangelo, C.H., "Polymer Based Actuator for Nozzle-Diffuser Pumps in Plastic Microfluidic Systems" *2002 Solid-State Sensor and Actuator Workshop*, Hilton Head Island, SC.

7.0 List of Inventions

[1] E.T. Carlen, C.H. Mastrangelo, ``Thermally Activated Paraffin Microactuator and Manufacturing Method," US patent pending (University of Michigan ref. no. 1778).

[2] P. Selvaganapathy, E.T. Carlen, C.H. Mastrangelo, ``Paraffin based thermally actuated inline microvalve," US patent pending (University of Michigan ref. no. 2479).

8.0 References

- [1] C.A. Rich and K.D. Wise, "A thermopneumatically-actuated microvalve with improved thermal efficiency and integrated state sensing," Tech. Digest IEEE Solid-State Sensor and Actuator Workshop, pp.234--237, 2000.
- [2] M.J. Zdeblick, J.J. R.Anderson, B.Kline-Schoder, L.Christel, R.Miles, and W.Weber, "Thermopneumatically actuated microvalves and integrated electrofluidic circuits," Tech. Digest IEEE Solid-State Sensor and Actuator Workshop, pp.251--255, 1994.
- [3] H. Jerman, "Electrically-activated, normally-closed diaphragm valves," J. Micromechanics and Microengineering, vol.4, pp.210--216, 1994.
- [4] X.Yang, C.Grosjean, Y.-C. Tai, and C.-H. Ho, "A thermopneumatic silicone rubber membrane valve," Sensors and Actuators A, vol.64, pp.101--108, 1998.
- [5] J.K. Robertson and K.D. Wise, "An electrostatically-actuated microvalve for semiconductor gas flow control," in Solid-State Sensor and Actuator Workshop, Hilton Head, South Carolina, pp.148--151, 1996.
- [6] S.C. Terry, "A gas chromaography system fabricated on a silicon wafer using integrated circuit technology," Ph.D dissertation, Stanford University; Stanford, {CA, 1975.
- [7] S.Hannoe, I.Sugimoto, and T.Katoc, "Silicon-micromachined separation columns coated with amino acid films for an integrated on-chip gas chromatograph," Proc. of the microTAS'98 Workshop, Banff, Canada, pp.145--148, October 13-16 1998.
- [8] D.Figeys, "Towards a modular microfluidic system for proteome analysis by mass spectrometry," Proc. of the microTAS'98 Workshop, Banff, Canada, pp.457--462, October 13-16 1998.
- [9] M.A. Burns and et al., "An integrated nanoliter {DNA analysis device," Science, vol.282, pp.253--258, October 16 1998.
- [10] D.J. Harrison and et al., "Capillary electrophoresis and sample injection systems integrated on a planar glass chip," Anal. Chem., vol.64, pp.1926--1932, 1992.
- [11] A.vanden Berg and P.Bergveld, Micro Total Analysis Systems. Kluwer, Boston, MA, 1994.
- [12] A.vanden Berg, W.Olthuis, and P.Bergveld, Micro Total Analysis Systems 2000. Kluwer, Boston, MA, 2000.
- [13] C.H. Mastrangelo, M.A. Burns, and D.T. Burke, "Microfabricated devices for genetic diagnostics," Proceedings of the IEEE, vol.86, pp.1769--1787, August 1998.
- [14] Y.-C. Tai, "Check valves," Proc. Int. Conf. Micro Electromechanical Systems (MEMS 2000), pp.1364--1367, Miyazaki, Japan, January 23-27 2000.
- [15] S.Shoji and M.Esashi, "Microflow devices and systems," J. Micromech. Microeng., vol.4, pp.157--171, 1994.
- [16] P.F. Man, C.H. Mastrangelo, M.A. Burns, and D.T. Burke, "Microfabricated capillarity-driven stop valve and sample injector," Proc. Int. Conf. Micro Electromechanical Systems (MEMS'97), pp.45--50, 1997.
- [17] M.Esashi, "Integrated microflow control systems," Sensors and Actuators A, vol.A21-A23, pp.161--167, 1990.

- [18] S.Shoji and M.Esashi, "Micromachining for chemical sensors," *Chem. Sensor Tech.*, vol.1, pp.179--193, 1988.
- [19] S.Shoji, M.Esashi, and M.Matsuo, "Prototype miniature blood gas analyzer fabricated on a silicon wafer," *Sensors and Actuators*, vol.14, pp.101--107, 1988.
- [20] T.Ohnstein, T.Fukura, J.Ridley, and U.Bonne, "Micromachined silicon microvalve," *Proc. Int. Conf. Micro Electromechanical Systems (MEMS'90)*, pp.95--98, 1990.
- [21] M.A. Huff, J.R. Gilbert, and M.A. Schmidt, "Pressure characteristics of a pressure-balanced microvalve," *Transducers 93*, pp.98--101, 1993.
- [22] D.Bosch, B.Heimhofer, G.Muck, H.Seidel, U.Thumser, and W.Welser, "A silicon microvalve with combined electromagnetic/electrostatic actuation," *Sensors and Actuators*, pp.684--692, 1992.
- [23] <http://www.sma-mems.com/pneuvalve.htm>, 2001.
- [24] Z.Zhang and B.Jang, "Actuating power capacities of polymers, gels and composites for use in smart materials systems," *SPIE*, vol.2447, pp.26--34, 1995.
- [25] W.C. Tang, T.-C.H. Nguyen, and R.T. Howe, "Laterally driven polysilicon resonant microstructures," *Proc. 1989 IEEE Micro Electro Mechanical Systems Workshop (MEMS'89)*, pp.53--59, 1989.
- [26] H.Guckel, K.Fischer, and E.Stiers, "Closed loop controlled, large throw, magnetic linear microactuator with 1000 μm structural height," *Proc. 1998 IEEE Micro Electro Mechanical Systems Workshop (MEMS'98)*, pp.414--418, 1998.
- [27] P.Kruevitch, A.P. Lee, P.B. Ramsey, J.C. Trevino, J.Hamilton, and M.A. Northrup, "Thin film shape memory alloy microactuators," *J. Microelectromechanical Systems*, vol.5, no.4, pp.270--281, 1996.
- [28] W.Riethmuller, "Thermally excited silicon microstructures," *IEEE Transactions on Electron Devices*, vol.35, June 1988.
- [29] P.L. Bergstrom, J.Ji, Y.-N. Liu, M.Kavany, and K.D. Wise, "Thermally driven phase-change microactuation," *J. Microelectromechanical Systems*, vol.4, no.1, pp.10--17, 1995.
- [30] B.Z. Jang and Z.J. Zhang, "Thermally and phase transformation-induced volume change of polymers for actuator applications," *Journal of Intelligent Material Systems and Structures*, vol.5, pp.758--763, 1994.
- [31] D.Dowen, "Design and implementation of a paraffin based micropositioning actuator," *SPIE*, vol.3132, pp.127--134, 1997.
- [32] V.C. Miles, *Thermostatic control; principles and practice*. Newnes, 1965.
- [33] S.Tibbitts, "High-output paraffin linear motors: utilization in adaptive systems," *SPIE: Active and Adaptive Optical Components*, vol.1543, pp.388--426, 1991.
- [34] N.Kabei, "A thermal-expansion-type microactuator with paraffin as the expansive material (basic performance of a prototype linear actuator)," *JSME Intl. Jnl-Series C*, vol.40, p.4, 1997.
- [35] Y.Jin and B.Wunderlich, "Heat capacities of paraffins and polyethylene," *J. Phys. Chem.*, vol.95, pp.9000--9007, 1991.

- [36] S.C. Systems, "Parylene conformal coatings specifications and properties," Specialty Coating Systems Handbook, 1996.
- [37] A.Breskin, A.Buzulutskov, E.Shefer, R.Chechik, and M.Prager, "Removable organic coating for alkali-antimonide photocathodes," Nuclear Instruments and Methods in Physics Research A, vol.413, pp.275--280, 1998.
- [38] Y.K. Godovsky, Thermophysical Properties of Polymers. Springer-Verlag, 1992.
- [39] B.Wunderlich, Macromolecular Physics, Volume 3: Crystal Melting. Academic Press, 1980.
- [40] C.L. Choy, "Thermal conductivity of polymers," Polymer, vol.18, pp.984--1004, Oct 1977.
- [41] P.Zoller and D.J. Walsh, Standard Pressure Volume Temperature Data for Polymers. Technomic Publishing Company, Inc., 1995.
- [42] S.-F. Lau and B.Wunderlich, "Calculation of the heat capacity of linear macromolecules from theta temperatures and group vibrations," Journal of Thermal Analysis, vol.28, pp.59--67, 1983.
- [43] Y.V. Cheban, S.-F. Lau, and B.Wunderlich, "Analysis of the contribution of skeletal vibrations to the heat capacity of linear molecules in the solid state," Colloid & Polymer Science, vol.260, pp.9--19, 1982.
- [44] S.C. Selbrede and M.L. Zucker, "Characterization of parylene-n thin films for low-k vlsi applications," in Low-Dielectric Constant Materials III Materials Research Society Symposium Proceedings v 476, pp.219--224, 1997.
- [45] A.J. Rafanelli, "Review of coating technologies with regard to reliability of plastic encapsulated microcircuits (pems)," in American Society of Mechanical Engineers (Paper), pp.1--9, 1998.
- [46] P.F. Man, D.K. Jones, and C.H. Mastrangelo, "Microfluidic plastic capillaries on silicon substrates: A new inexpensive technology for bioanalysis chips," in Proceedings of the 1997 IEEE 10th Annual International Work shop on Micro Electro Mechanical Systems (MEMS '97), pp.311--316, 1997.
- [47] J.R. Webster and C.H. Mastrangelo, "Large-volume integrated capillary electrophoresis stage fabricated using micromachining of plastics on silicon substrates," in Proceedings of the 1997 International Conference on Solid- State Sensors and Actuators (Tranducers '97), pp.503--506, 1997.
- [48] X.Wang, Q.Lin, and Y.C. Tai, "Parylene micro check valve," in Proceedings of the IEEE Micro Electro Mechanical Systems (MEMS) 1999, pp.177--182, 1999.
- [49] C.A. Rich and K.D. Wise, "An 8-bit microflow controller using pneumatically-actuated microvalves," Proc. 1999 IEEE Micro Electro Mechanical Systems Workshop (MEMS'99), pp.130--134, January 17-21 1999.
- [50] E.T. Carlen and C.H. Mastrangelo, "Paraffin actuated surface micromachined valves," MEMS 2000, pp.1364--1367, Miyazaki, Japan, January 23-27 2000.
- [51] X.Yang, J.M. Yang, X.Q. Wang, E.Meng, Y.C. Tai, and C.M. Ho, "Micromachined membrane particle filters," in Proceedings of the IEEE Micro Electro Mechanical Systems (MEMS) 1998, pp.137--142, 1998.
- [52] R.d'Agostino, Plasma Deposition, Treatment, and Etching of Polymers. Academic Press, 1990.
- [53] G.K. Vinogradov, P.I. Nevzorov, L.S. Polak, and D.I. Slovetsky, "Kinetics and mechanisms of chemical reactions in nonequilibrium-plasma etching of silicon and silicon compounds," Vacuum, vol.32, no.9, pp.529--537, 1982.

- [54] I.C. Plumb and K.R. Ryan, "A model of the chemical processes occurring in the $\text{CF}_4\text{-O}_2$ discharges used in plasma etching," *Plasma Chem. and Plasma Processing*, vol.6, no.3, pp.205--230, 1986.
- [55] S.R. Cain, F.D. Egitto, and F.Emmi, "Relation of polymer structure to plasma etching behavior: Role of atomic fluorine," *J. Vac. Sci. Technol. A*, vol.5, pp.1578--1584, Jul/Aug 1987.
- [56] T.R. Dietrich, W.Ehrfeld, M.Lacher, M.Kramer, and B.Speit, "Fabrication technologies for microsystems utilizing photoetchable glass," *Microelectronic Engineering*, vol.20, pp.497--504, 1996.
- [57] C.H. Mastrangelo, *Thermal Applications of Microbridges*. PhD thesis, University of California, Berkeley, 1991.
- [58] A.C. Ugural, *Stresses in Plates and Shells*. McGraw-Hill, 1999.
- [59] K.W. Childs, "Heating 7.2 user's manual," Computing Applications Division, Oak Ridge National Laboratory, Feb 1993.
- [60] F.P. Incropera and D.P. DeWitt, *Introduction to Heat Transfer*. John Wiley & Sons, 1985.
- [61] J.J. Mahoney, "Heat transfer at small grashof numbers," *Proc. Roy. Soc.*, vol.A238, pp.412--423, 1957.
- [62] E.T. Carlen and C.H. Mastrangelo, "Simple, high actuation power, thermally activated paraffin microactuator," *Transducers'99*, vol.2, pp.1364--1367, Sendai, Japan, June 7-10 1999.
- [63] J.F. O'Hanlon, *A User's Guide to Vacuum Technology* John Wiley & Sons, New York, 1990.
- [64] A. Roth, *Vacuum Technology*, 3rd, upd. and enl. ed. North-Holland Pub. Co., New York, 1990.
- [65] L.Holland, W.Steckelmacher, and J.Yarwood, *Vacuum Manual*. E. & F. N. Spon, London, 1974.
- [66] S.Dushman, *Scientific Foundations of Vacuum Technique*, 2nd ed. Wiley & Sons, New York, 1962.
- [67] B.J. Williams and J.A.A. Emery, "Practical design aspects of a continuous air-to-air vacuum processing machine," *Proc. of the Fourth Intl. Vacuum Congress*, pp.753--758, 1968.
- [68] R.J. Cornish, "Flow in a pipe of rectangular cross-section," *Proc. Roy. Soc. A*, vol.120, pp.691--700, 1928.
- [69] A.S. Berman, "Free molecular transmission probabilities," *J. Appl. Phys.*, vol.10, p.3356, 1965.
- [70] "Model development: Guide to writing templates," *Analogy, Inc. Release 4.1 Manual*, Oct. 1996.
- [71] J.Robertson, *An electrostatically actuated integrated microflow controller*. PhD thesis, University of Michigan, Ann Arbor, 1996.
- [72] S.Wolf and R.N. Tauber, *Silicon Processing for VLSI Era, Vol. 1: Processing Technology*. Lattice Press, Sunset Beach, CA, 1986.
- [73] U.I.A. Note, "Basics of thermal mass flow," *Unit Instruments App. Note*, 1999.
- [74] R.M.A. Note, "Mass flow controllers," *Redwood Microsystems App. Note*, 1999.
- [75] Terry, S. C., Jermann S. H., Agnell, J. B., *IEEE Trans. Electron Devices*, 1979, ED 26, 1880-1886.

- [76] Manz, A., Graber, M., Widmer, H. M., *Sensors and Actuators*, 1990, B 1, 244-248
- [77] Bhatia SN, Balis UJ, Yarmush ML, Toner M. 1998. Probing heterotypic cell interactions: Hepatocyte function in microfabricated co-cultures. *J. Biomater. Sci. Polym. Ed.* 9(11):1137–60 RH. 1996. Biotechnology at low Reynolds numbers. *Biophys. J.* 71(6):3430–41
- [78] Bratten CDT, Cobbold PH, Cooper JM. 1998. Single-cell measurements of purine release using a micromachined electroanalytical sensor. *Anal. Chem.* 70(6):1164–70
- [79] Clark RA, Ewing AG. 1998. Experimenting in picoliter microvials. *Chem-tech* 28(2):20–25
- [80] Crofcheck CL, Grosvenor AL, Anderson KW, Lumpkin JK, Scott DL, Daunert S. 1997. Detecting biomolecules in picoliter vials using aequorin bioluminescence. *Anal. Chem.* 69(23):4768–72 microliquid handling systems. *J. Micromech. Microeng.* 4(4):227–45
- [81] Dogterom M, Yurke B. 1997. Measurement of the force-velocity relation for growing microtubules. *Science* 278(5339):856–60
- [82] Fodor SPA, Read JL, Pirrung MC, Stryer L, Lu AT, Solas D. 1991. Light-directed, spatially addressable parallel chemical synthesis. *Science* 251(4995):767–73
- [83] Holy TE, Dogterom M, Yurke B, Leibler S. 1997. Assembly and positioning of microtubule asters in microfabricated chambers. *Proc. Natl. Acad. Sci. USA* 94(12):6228–31
- [84] McConnell HM, Owicki JC, Parce JW, Miller DL, Baxter GT, et al. 1992. The cytosensor microphysiometer: biological applications of silicon technology. *Science* 257(5078):1906–12
- [85] Najafi K. 1994. Solid-state microsensors for cortical nerve recordings. *IEEE Eng. Med. Biol. Mag.* 13(3):375–87
- [86] Shoffner MA, Cheng J, Hvieh GE, Kricka LJ, Wilding P. 1996. Chip PCR. 1. Surface passivation of microfabricated silicon-glass chips for PCR. *Nucleic Acids Res.* 24(2):375–79
- [87] Stenger DA, McKenna TM, eds. 1994. *Enabling Technologies for Cultured Neural Networks*, San Diego, CA: Academic. 355 pp.
- [88] Stieglitz T, Meyer J-U. 1998. Microtechnical interfaces to neurons. In *Micro-system Technology in Chemistry and Life Science*, ed. H Becker, A Manz; *Top. Curr. Chem.* 194:131–62. Berlin: Springer-Verlag
- [89] Sutton N, Tracey MC, Johnston ID, Greenaway RS, Rampling MW. 1997. A novel instrument for studying the flow behaviour of erythrocytes through micro-channels simulating human blood capillaries. *Microvasc. Res.* 53(3): 272–81
- [90] Wang L, Beebe DJ, Williams AR, Easley KD. 1997. Electrothermal branding for embryo labeling. *IEEE Trans. Biomed. Eng.* 44(11): 1128–38
- [91] McDonald, J. C., D. C. Duffy, J. R. Anderson, D. T. Chiu, H. Wu, O. J. A. Schueller, and G. M. Whitesides, “Fabrication of Microfluidic Systems in Poly(dimethylsiloxane),” *Electrophoresis*, 21, 27 (2000).
- [92] Quake, S. R., and A. Scherer, “From Micro- to Nanofabrication with Soft Materials,” *Science*, 290, 1536 (2000).
- [93] Langer, R., “Biomaterials: Status, Challenges, and Perspectives,” *AIChE J.*, 46,1286, (2000).

- [94] Martynova, L., Locasico, L. E., Gaitan, M., Kramer, G. W., Christensen, R. G., MacCrehan, W. A., *Analytical Chemistry*, 1997, 69, 4783-4789.
- [95] Locasico, L. E., Gaitan, M. Hong, J., Eldefrawi, M., *Proc. Micro-TAS'98*, Banff, Canada, 1998, pp 367-370
- [96] Yi, F., Wu, J., Xian, D. (1993) LIGA technique for microstructure fabrication. *Weixi Jiagong Jishu Microfabrication Technology*, n 4, 1-7.
- [97] McCormick, R. M., Nelson, R. J., Alonso-Amigo, M. G., Benvegna, D. J., Hooper, H. H., *Analytical Chemistry*, 1997, 69, 2626-2630.
- [98] Becker, H, Heim, U., *Proc. MEMS'99*, Orlando, FL, 1999, pp 228-231.
- [99] Elders, J., Jansen, H. V., Elwenspoek, M., Ehrfeld, W., *Proc. MEMS'95*, 238-244.
- [100] Weber, L., Ehrfeld, W., Freimuth, H., Lacher, M., Lehr, H., Pech, B. (1996) Micromolding: A powerful tool for large-scale production of precise microstructures. *Proceedings of SPIE - The International Society for Optical Engineering*. v 2879, 156-167.
- [101] Weber, L., Ehrfeld, W., Begemann, M., Berg, U., Michel, F. (1999) Fabrication of plastic microparts on wafer level. *Proceedings of SPIE - The International Society for Optical Engineering*. v 3874, 44-52.
- [102] Benzler, T., Piottter, V., Hanemann, T., Mueller, K., Norajitra, P., Ruprecht, R., Hausselt, J. (1999) Innovations in molding technologies for microfabrication. *Proceedings of SPIE - The International Society for Optical Engineering*. v 3874, 53-60.
- [103] Becker, H., Heim, U. (1999) Silicon as a tool material for polymer hot embossing. *Proceedings of IEEE Micro Electro Mechanical Systems (MEMS)*. 228-231.
- [104] Lee, G., Chen, S., Huang, G., Lin, Y., Sung, W. (2000) Microfabricated plastic chips by hot embossing methods and their applications for DNA separation and detection. *Proceedings of SPIE - The International Society for Optical Engineering*. v 4177, 112-121.
- [105] Lin, L., Chiu, C., Bacher, W., Hecke, M. (1996) Microfabrication using silicon mold inserts and hot embossing. *Proc. of the International Symposium on Micromachines and Human Science*. 67-71.
- [106] Folch, A., Ayon, A., Hurtado, O., Schmidt, M. A., Toner, M. (1999) Molding of deep polymethyl-disiloxane microstructures for microfluidic and biological applications. *Journal of Biomechanical engineering, Transactions of ASME*. v 121, n 1, 28-34.
- [107] Jo, B. H., Van Lerberghe, L. M., Motsegood, K. M., Beebe, D. J. (2000) Three dimensional micro-channel fabrication in Polydimethylsiloxane (PDMS) elastomer", *Journal of Microelectromechanical Systems*. v 9, n 1, 76-81.
- [108] McDonald, J. C., Duffy, D. C., Anderson, J. R., Chiu, D. T., Wu, H. K., Schueller, C. J. A., Whitesides, G. M. (2000) Fabrication of microfluidic systems in polymethyl-disiloxane. *Electrophoresis*. v 21, 27-40.
- [109] Sethu, P, Yu, H., Grodzinski, P., Mastrangelo, C. H. (2000) Fabrication of genetic analysis micro-systems using plastic microcasting. *Proceedings: Solid-State Sensor and Actuator Workshop*.
- [110] Naessens, K., Van Hove, A., Coosemans, T., Verstuyft, S., Vanwassenhove, L., Van Daele, P., Baets, R. (2000) Microgroove fabrication with excimer laser ablation techniques for optical fibre array alignment purposes. *Proceedings of SPIE - The International Society for Optical Engineering*. v 4088, 327-332.

- [111] Yamasaki, K., Juodkazis, S., Watanabe, M., Matsuo, S., Kamada, K., Ohta, K., Misawa, H. (2000) Transient light-induced refractive index change made by laser microfabrication in nitroaniline-doped PMMA film. *Proceedings of SPIE - The International Society for Optical Engineering*. v 4088, 51-54.
- [112] Wang, J., Niino, H., Yabe, A. (1999) Microfabrication of fluoropolymer using conventional XeCl excimer laser by laser induced backside wet etching. *Japanese Journal of Applied Physics. Part 2: Letters*. v38, n 7, L761-L763.
- [113] Man, P. F. (2000), Monolithic structures for integrated microfluidic analysis. Final Thesis, Department of Electrical Engineering and Computer Sciences, Solid State Electronics Lab, University of Michigan, Ann Arbor.
- [114] Webster, J. R., Burke, D. T., Burns, M. A., Mastrangelo, C. H. (2000) Electrophoresis system with integrated on-chip fluorescence detection. *Proceedings of IEEE Micro Electro Mechanical Systems (MEMS)*. 306-310.
- [115] Danev, G., Spassova, E., Popova, K. (1993) Morphology of thin polyimide films. *Thin Solid films*, v 228, n 1-2, 301-303.2.12
- [116] A. T. Woolley, D. Hadley, P. Landre, A. J. deMello, R. A. Mathies, and M. A. Northrup, "Functional integration of PCR amplification and capillary electrophoresis in a microfabricated DNA analysis device," *Anal. Chem.*, vol. 68, pp. 4081-4086, 1996.
- [117] S. C. Jacobson, J. P. Cutter, C. T. Culbertson, and J. M. Ramsey, "Rapid electrophoresis and chromatographic analysis on microchips," *Micro Total Analysis Systems '98*, Banff, Canada, 1998.
- [118] M. A. Northrop, B. Bennett, D. Hadley, P. Lander, S. Leeway, J. Richards, and P. Stratton, "A miniature analytical instrument for nucleic acids based on micromachined silicon reaction chambers," *Anal. hem.*, vol. i70, p. 918922, 1998.
- [119] T. D. Boone, H. H. Hooper, and D. S. Sane, "Integrated chemical analysis on plastic micro fluidic devices," *Solid State Sensor and Actuator Workshop '98*, Hilton Head Island, South Carolina, 1998.
- [120] H. Becker and W. Dietz, "Microfluidic devices for micro-TAS applications fabricated by polymer hot embossing," *SPIE Conference '98*, Santa Clara, California, 1998.
- [121] E. Kim, Y. Xia, and G. M. Whitesides, "Polymer microstructures formed by molding in capillaries," *Nature*, vol. 376, p. 347, 1996.
- [122] R. K. Traeger, "Nonhermeticity of polymeric lid sealant," *IEEE Transactions, Parts, Hybrids and Packaging*, vol. PHP-13, pp. 147-152, 1977.
- [123] P. F. Man, C. H. Mastrangelo, M. A. Burns, and D. T. Burke, "Microfabricated capillarity-driven stop valve and sample injector," in *International Workshop on Micro Electro Mechanical Systems (MEMS 98)*, Heidelberg, Germany, pp. 45-50, 1998.
- [124] J. S. Rossier, M. A. Roberts, R. Ferrigno, and H. H. Girault, "Electrochemical detection in polymer microchannels," *Analytical Chemistry*, vol. 71, pp. 4294-4298, 1999.
- [125] A. T. Woolley, D. Hadley, P. Landre, A. J. deMello, R. A. Mathies, and M. A. Northrup, "Functional integration of PCR amplification and capillary electrophoresis in a microfabricated DNA analysis device," *Anal. Chem.*, vol. 68, pp. 4081-4086, 1996.
- [126] E. Kim, Y. Xia, and G. M. Whitesides, "Polymer microstructures formed by molding in capillaries," *Nature*, vol. 376, p. 347, 1996.

- [127] S. Palaniappan, et. al., "Fabrication of Genetic Analysis Microsystems using Plastic Microcasting", Technical Digest of the 2000 Solid- State Sensor and Actuator Workshop, Hilton Head Isl., SC, pp. 175 – 179, (2000).
- [128] Webster, J. R. "Monolithic structures for integrated capillary electrophoresis systems", Final Thesis, Department of Electrical Engineering and Computer Science, 1999, University of Michigan.
- [129] R. K. Traeger, "Nonhermeticity of polymeric lid sealant," IEEE Transactions, Parts, Hybrids and Packaging, vol. PHP-13, pp. 147–152, 1977.
- [130] C.T. Wittwer, G.C. Fillmore and D.R. Hillyard, Automated polymerase chain reaction in capillary tubes with hot air. *Nucleic Acids Res.* 17 (1989), pp. 4353-4357.
- [131] A.T. Woolley, D. Hadley, P. Landre, A.J. de Mello, R.A. Mathies and M.A. Northrup, Functional integration of PCR amplification and capillary electrophoresis in a microfabricated DNA analysis device. *Anal. Chem.* 68 (1996), pp. 4081-4086.
- [132] P. Wilding, L.J. Kricka, J. Cheng, G. Hvichia, M.A. Shoffner and P. Fortina, Integrated cell isolation and polymerase chain reaction analysis using silicon microfilter chambers. *Anal. Biochem.* 257 (1998), pp. 95-100.
- [133] A.M. Chaudhari, T.M. Woudenberg, M. Albin and K.E. Goodson, Transient liquid crystal thermometry of microfabricated PCR vessel arrays. *J. Microelectromech. Syst.* 7 (1998), pp. 345-355.
- [134] J.H. Daniel, S. Iqbal, R.B. Millington, D.F. Moore, C.R. Lowe, D.L. Leslie, M.A. Lee and M.J. Pearce, Silicon microchambers for DNA amplification. *Sens. Actuators, A* 71 (1998), pp. 81-88.
- [135] M.A. Northrup, B. Benett, D. Hadley, P. Landre, S. Lehew, J. Richards and P. Stratton, A miniature analytical instrument for nucleic acids based on micromachined silicon reaction chambers. *Anal. Chem.* 70 (1998), pp. 918-922.
- [136] T.B. Taylor, S.E. Harvey, M. Albin, L. Lebak, Y. Ning, I. Mowat, T. Schuerlein and E. Principe, Process control for optimal PCR performance in glass microstructures. *Biomedical Microdevices* 1 (1998), pp. 65-70.
- [137] L.C. Waters, S.C. Jacobson, N. Kroutchinina, J. Khandurina, R.S. Foote and J.M. Ramsey, Multiple sample PCR amplification and electrophoretic analysis on a microchip. *Anal. Chem.* 70 (1998), pp. 5172-5176.
- [138] J. Cheng, M.A. Shoffner, G.E. Hvichia, L.J. Kricka and P. Wilding, Chip PCR: 2. Investigation of different PCR amplification systems in microfabricated silicon-glass chips. *Nucleic Acids Res.* 24 (1996), pp. 380-385.
- [139] N.Y. Zhang, H.D. Tan and E.S. Yeung, Automated and integrated system for high-throughput DNA genotyping directly from blood. *Anal. Chem.* 71 (1999), pp. 1138-1145.
- [140] M.U. Kopp, A.J. de Mello and A. Manz, Chemical amplification: continuous-flow PCR on a chip. *Science* 280 (1998), pp. 1046-1048.
- [141] R.P. Oda, M.A. Strausbauch, A.F.R. Huhmer, N. Borson, S.R. Jurens, J. Craighead, P.J. Wettstein, B. Eckloff, B. Kline and J.P. Landers, Infrared-mediated thermocycling for ultrafast polymerase chain reaction amplification of DNA. *Anal. Chem.* 70 (1998), pp. 4361-4368.
- [142] I.M. Lazar, R.S. Ramsey, S.C. Jacobson, R.S. Foote and J.M. Ramsey, Novel microfabricated device for electrokinetically induced pressure flow and electrospray ionization mass spectrometry. *J Chromatogr A* 892 (2000), pp. 195-201

- [143] T. Tang, L. Yuehe, D.W. Matson, K. Taeman and R.D. Smith, Generation of multiple electrosprays using microfabricated emitter arrays for improved mass spectrometric sensitivity. *Anal Chem* 73 (2001), pp. 1658-1663.
- [144] Corso TN, Prosser SJ, Zhang S, Taheri A, Schultz GA: An automated microchip-based electrospray device for high throughput MS analysis. *Proceedings of the 48th ASMS Conference on Mass Spectrometry and Allied Topics: 2000 Jun 11-15; Long Beach, CA. [Published on CD-ROM.]*.
- [145] S. Hjerten, High-performance electrophoresis: elimination of electroendosmosis and solute adsorption. *J. Chromatogr.* 347 (1985), pp. 191-198.
- [146] M. Esashi, S. Shoji and A. Nakano, Normally closed microvalve and micropump fabricated on a silicon-wafer. *Sens. Actuators* 20 (1989), pp. 163-169.
- [147] R.C. Anderson, G.J. Bogdan, Z. Barniv, T.D. Dawes, J. Winkler and K. Roy, Microfluidic biochemical analysis system. In: (1997), pp. 477-480.
- [148] J. Behrens, A. Meckes, M. Gebhard, W. Benecke, Micropumps and -valves with electromagnetic actuation, *Proc. Micro System Technologies '96, Potsdam, Germany*, pp. 820-822.
- [149] J. Behrens, A. Meckes, M. Gebhard, W. Benecke, Electromagnetic actuation for micropumps and valves, *Proc. Actuator '96*, pp. 124-127.
- [150] C. Perego, G. Sberveglieri, A. Taroni, W. Hellmich, Chr. Bosch-v.Braunmühl, A. Krenkow, G. Müller, Silicon micromachining technology for heated gas sensor elements, *Proc. 5th Int. Conf. on Micro-, Electro-, Opto-, Mechanical Systems and Components, Potsdam, September 17-19, (VDE-Verlag: Berlin, Offenbach)*, pp. 29-37.
- [151] G. Sberveglieri, G. Faglia, S. Gropelli, P. Nelli and A. Camanzi, A new technique for growing large surface area SnO₂ thin films. *Semicond. Sci. Technol.* 5 (1990), p. 1231.
- [152] B. Ruhland, Th. Becker and G. Müller, Gas kinetic interactions of nitrous oxides with SnO₂ surfaces. *Sensors and Actuators B* 50 (1998), pp. 85-94.
- [153] A. Meckes, J. Behrens, M. Hausner, M. Gebhard, W. Benecke, Enhancement of air monitoring by combined microsensors and -actuators, *Concept and design considerations for a miniaturised gas analyser, Proc. µTAS '96, Basel, Switzerland*, pp. 126-128.
- [154] W. Benecke, A. Meckes, A modular miniaturized gas analyzer based on microsystem technologies, *Proc. ECS Microstructures and Microfabricated Systems, Montreal, Canada, V97-5*, pp. 1-11.
- [155] W. Benecke, Silicon microactuators: activation mechanisms and scaling problems. In: *Transducers '91: Sixth International Conference on Solid-State Sensors and Actuators* (1991), pp. 46-49.
- [156] F.C.M. van de Pol, H.T.G. van Lintel, M. Elwenspoek and J.H.J. Fluitman, A thermopneumatic micropump based on micro-engineering techniques. *Sensors and Actuators* 21 (1990), pp. 198-202.
- [157] S. Böhm, W. Olthius and P. Bergveld, An electrochemically actuated micropump for use in a "push-pull" microdialysis based in-vivo monitoring system. In: *Proceedings of the Transducer '99: Tenth International Conference on Solid-State Sensors and Actuators, Sendai, Japan* (1999), pp. 880-881.
- [158] W.S.N. Trimmer, K.J. Gabriel and R. Mahadevan, Silicon electrostatic motors. In: *Transactions of the '87: Fourth International Conference on Solid-State Sensors and Actuators* (1987), pp. 857-860.

- [159] B. Wagner, M. Kreutzer and W. Benecke, Linear and rotational magnetic micromotors fabricated using silicon technology. In: Proceedings of the IEEE Micro Electro Mechanical Systems, Travemünde, Germany (1992), pp. 183-189.
- [160] W.P. Robbins, D.L. Polla, T. Tamagawa and D.E. Glumac, Design of linear-motion microactuators using piezoelectric thin films. *J. Micromech. Microeng.* 1 4 (1991), pp. 247-252.
- [161] L. Que, J.-S. Park and Y.B. Gianchandani, Bent-beam electro-thermal actuators for high force applications. In: Proceedings of IEEE micro electro mechanical systems, Orlando, USA (1999), pp. 31-36.
- [162] D. Reynaerts, J. Peirs and H. Van Brussel, An implantable drug-delivery system based on shape memory alloy micro-actuation. *Sensors and Actuators A61* (1997), pp.
- [163] E. Quandt and K. Seemann, Fabrication and simulation of magnetostrictive thin-film actuators. *Sensors and Actuators A50* (1995), pp. 105-109.
- [164] Abbas A, Dufour I, Sarraute E, Allano S. Comparison of torque optimised electromagnetic and electrostatic micromotors. *J Micromech Microeng* 1995;192-95.
- [165] T. Furuhashi, T. Hirano, K.J. Gabriel and H. Fujita, Sub-micron gaps without sub-micron etching. In: Proceedings of IEEE MEMS, Nara, Japan (1991).
- [166] R. Legtenberg, F. Berenschot, M. Elwenspoek and J. Fluitman, Electrostatic curved electrode actuators. In: Proceedings of IEEE Micro Electro Mechanical Systems, Amsterdam, The Netherlands (1995), pp. 37-42.
- [167] T. Akiyama and S. Katsufusa, A new step motion of polysilicon microstructures. In: Proceedings of MEMS, Fort Lauderdale, USA (1993), pp. 272-277. 46. L. Paratte, G.-A. Racine, N.F. de Rooij and E. Bornand, A rigid ring electrostatic harmonic wobble motor with axial field. In: *Transducers '91: Sixth International Conference on Solid-State Sensors and Actuators* (1991), pp. 890-893.
- [168] M. Baltzer, Th. Kraus and E. Obermeier, A linear stepping actuator in surface micromachining technology for low voltages and large displacements. In: *Transducers '97: Ninth International Conference on Solid-State Sensors and Actuators* (1997), pp. 781-784.
- [169] M. Baltzer, Th. Krauss and E. Obermeier, A new type of a linear actuator in surface micromachining technology. In: Proceedings of the MST '96: Fifth International Conference on Micro Electro, Opto, Mech. Sys. and Comp., Potsdam, Germany (1996), pp. 591-596.
- [170] E. T. Carlen and C. H. Mastrangelo, "Simple, High Actuation Power, Thermally Activated Paraffin Microactuator", International conference on Solid-State Sensors and Actuators (*Transducers 99*), Japan, 2, 1364-1367, (1999).
- [171] E. Stemme and G. Stemme, "A Valveless Diffuser/Nozzle based Fluid Pump", *Sensors and Actuators*, A339, pp. 159-167. (1993).
- [172] Olsson, et. al., "Valve-Less Planar Pumps fabricated using thermoplastic replication", Technical Digest of the 10th annual workshop of Micro Electro Mechanical Systems, Nagoya, Japan, pp. 305 – 310, (1997).
- [173] A. Manz et al., Miniaturized total chemistry analysis systems: a novel concept for chemical sensing. *Sens. Actuators B 1* (1990), pp. 244-248.
- [174] D.J. Harrison et al., Rapid separation of fluorescein derivatives using a micromachined capillary electrophoresis system. *Anal. Chim. Acta* 283 (1993), pp. 361-366.

- [175] S.C. Jacobson et al., High speed separations on a microchip. *Anal. Chem.* 66 (1994), pp. 1114-1118.
- [176] A.T. Wooley and R.A. Mathies , Ultra-high-speed DNA fragment separations using microfabricated capillary array electrophoresis chips. *Proc. Natl. Acad. Sci. U. S. A.* 91 (1994), pp. 11348-11352.
- [177] A.T. Wooley et al., High-speed DNA genotyping using microfabricated capillary array electrophoresis chips. *Anal. Chem.* 69 (1997), pp. 2181-2186.
- [178] C.S. Effenhauser et al., High speed separation of antisense oligonucleotides on a micromachined capillary electrophoresis device. *Anal. Chem.* 66 (1994), pp. 2949-2953.
- [179] J. Khandurina et al., Integrated system for rapid PCR-based DNA analysis in microfluidic devices. *Anal. Chem.* 72 (2000), pp. 2995-3000.
- [180] A. Paulus , CE of DNA using capillaries and micromachined chips. *Am. Lab.* 30 (1998), pp. 59-62.
- [181] C.S. Effenhauser et al., Integrated chip-based CE - a review. *Electrophoresis* 18 (1997), pp. 2203-2213
- [182] S.C. Jacobson and J.M. Ramsey , Microchip electrophoresis with sample stacking. *Electrophoresis* 16 (1995), pp. 481-486.
- [183] C.S. Effenhauser , Integrated chip based microcolumn separation systems. In: A. Manz and H. Becker, Editors, *Microsystem Technology in Chemistry and Life Sciences*, Springer-Verlag (1999), pp. 51-82
- [184] Y. Liu, R.S. Foote, S.C. Jacobson, R.S. Ramsey and J.M. Ramsey , Electrophoretic separation of proteins on a microchip with noncovalent, postcolumn labeling. *Anal Chem* 72 (2000), pp. 4608-4613
- [185] L. Bousse, S. Mouradian, A. Minalla, H. Yee, K. Williams and R. Dubrow , Protein sizing on a microchip. *Anal Chem* 73 (2001), pp. 1207-1212
- [186] N. Gottschlich, S.C. Jacobson, C.T. Culbertson and J.M. Ramsey , Two-dimensional electrochromatography/capillary electrophoresis on a microchip. *Anal Chem* 73 (2001), pp. 2669-2674
- [187] R.D. Rocklin, R.S. Ramsey and J.M. Ramsey , A microfabricated fluidic device for performing two-dimensional liquid-phase separations. *Anal Chem* 72 (2000), pp. 5244-5249.
- [188] C. Ericson, J. Holm, T. Ericson and S. Hjerten , Electroosmosis- and pressure-driven chromatography in chips using continuous beds. *Anal Chem* 72 (2000), pp. 81-87
- [189] R. Shediach, S.M. Ngola, D.J. Throckmorton, D.S. Anex, T.J. Shepodd and A.K. Singh , Reversed-phase electrochromatography of amino acids and peptides using porous polymer monoliths. *J Chromatogr A* 925 (2001), pp. 251-263.
- [190] J. Xu, L.E. Locascio, M. Gaitan and C.S. Lee , Room-temperature imprinting method for plastic microchannel fabrication. *Anal Chem* 72 (2000), pp. 1930-1933.
- [191] K. Macounova, C.R. Cabrera and P. Yager , Concentration and separation of proteins in microfluidic channels on the basis of transverse IEF. *Anal Chem* 73 (2001), pp. 1627-1633.
- [192] S.B. Cheng, C.D. Skinner, J. Taylor, S. Attiya, W.E. Lee, G. Picelli and D.J. Harrison, Development of a multichannel microfluidic analysis system employing affinity capillary electrophoresis for immunoassay. *Anal Chem* 73 (2001), pp. 1472-1479.

- [193] K. Sato, M. Tokeshi, T. Odake, H. Kimura, T. Ooi, M. Nakao and T. Kitamori , Integration of an immunosorbent assay system: analysis of secretory human immunoglobulin A on polystyrene beads in a microchip. *Anal Chem* 72 (2000), pp. 1144-1147.
- [194] Dodge A, Fluri K, Verpoorte E, de Rooij NF: Electrokinetically driven microfluidic chips with surface-modified chambers for heterogeneous immunoassays. *Anal Chem* 2001, 73:3400-3409.
- [195] C. Wurzel and B. Wittmann-Liebold , New approaches for innovations in sensitive Edman sequence analysis by design of a wafer-based chip sequencer. *Exs* 88 (2000), pp. 145-157.
- [196] A. Schultz, T.N. Corso, S.J. Prosser and S. Zhang , A fully Integrated monolithic microchip electrospray device for mass spectrometry. *Anal Chem* 72 (2000), pp. 367-375.
- [197] L. Licklider, X. Wang, A. Desai, Y. Tai and T. Lee , A micromachined chip-based electrospray source for mass spectrometry. *Anal Chem* 72 (2000), pp. 367-375.
- [198] D.M. Pinto, Y. Ning and D. Figeys , An enhanced microfluidic chip coupled to an electrospray Qstar mass spectrometer for protein identification. *Electrophoresis* 21 (2000), pp. 181-190.
- [199] I.M. Lazar, R.S. Ramsey, S.C. Jacobson, R.S. Foote and J.M. Ramsey , Novel microfabricated device for electrokinetically induced pressure flow and electrospray ionization mass spectrometry. *J Chromatography A* 892 (2000), pp. 195-201.
- [200] T. Tang, L. Yuehe, D.W. Matson, K. Taeman and R.D. Smith , Generation of multiple electrosprays using microfabricated emitter arrays for improved mass spectrometric sensitivity. *Anal Chem* 73 (2001), pp. 1658-1663.
- [201] Corso TN, Prosser SJ, Zhang S, Taheri A, Schultz GA: An automated microchip-based electrospray device for high throughput MS analysis. *Proceedings of the 48th ASMS Conference on Mass Spectrometry and Allied Topics: 2000 Jun 11-15; Long Beach, CA.*
- [202] T. Wachs and J. Henion , Electrospray device for coupling microscale separations and other miniaturized devices with electrospray mass spectrometry. *Anal Chem* 73 (2001), pp. 632-638.
- [203] H. Liu, C. Felten, Q. Xue, B. Zhang, P. Jedrzejewski, B.L. Karger and F. Foret , Multichannel devices with an array of electrospray tips for high-throughput mass spectrometry. *Anal Chem* 72 (2000), pp. 3303-3310
- [204] B. Zhang, F. Foret and B.L. Karger , A microdevice with integrated liquid junction for facile peptide and protein analysis by capillary electrophoresis/electrospray mass spectrometry. *Anal Chem* 72 (2000), pp. 1015-1022.
- [205] B. Zhang, F. Foret and B.L. Karger , High-throughput microfabricated CE/ESI-MS: automated sampling from a microwell plate. *Anal Chem* 73 (2001), pp. 2675-2681
- [206] C. Felten, F. Foret, M. Minarik, W. Goetzinger and B.L. Karger , Automated high-throughput infusion ESI-MS with direct coupling to a microtiter plate. *Anal Chem* 73 (2001), pp. 1449-1454.
- [207] J. Li, J.F. Kelly, I. Chernushevich, D.J. Harrison and P. Thibault , Separation and identification of peptides from gel-isolated membrane proteins using a microfabricated device for combined capillary electrophoresis / nanoelectrospray mass spectrometry. *Anal Chem* 72 (2000), pp. 599-609.
- [208] J. Li, C. Wang, J.F. Kelly, D.J. Harrison and P. Thibault , Rapid and sensitive separation of trace level protein digests using microfabricated devices coupled to a quadrupole-time-of-flight mass spectrometer. *Electrophoresis* 21 (2000), pp. 198-210.

- [209] Y. Deng, J. Henion, J. Li, P. Thibault, C. Wang and D.J. Harrison , Chip-based capillary electrophoresis/mass spectrometry determination of carnitines in human urine. *Anal Chem* 73 (2001), pp. 639-646.
- [210] J. Wen, Y. Lin, F. Xiang, D.W. Matson, H.R. Udseth and R.D. Smith , Microfabricated isoelectric focusing device for direct electrospray ionization-mass spectrometry. *Electrophoresis* 21 (2000), pp. 191-197.
- [211] I.M. Lazar, R.S. Ramsey and J.M. Ramsey , On-chip proteolytic digestion and analysis using "wrong-way-round" electrospray time-of-flight mass spectrometry. *Anal Chem* 73 (2001), pp. 1733-1739.
- [212] J. Gao, J. Xu, L.E. Locascio and C.S. Lee , Integrated microfluidic system enabling protein digestion, peptide separation, and protein identification. *Anal Chem* 73 (2001), pp. 2648-2655
- [213] C. Wang, R. Oleschuk, F. Ouchen, J. Li, P. Thibault and D.J. Harrison , Integration of immobilized trypsin bead beds for protein digestion within a microfluidic chip incorporating capillary electrophoresis separations and an electrospray mass spectrometry interface. *Rapid Commun Mass Spectrom* 14 (2000), pp. 1377-1383
- [214] S. Ekstrom, P. Onnerfjord, J. Nilsson, M. Bengtsson, T. Laurell and G. Marko-Varga , Integrated microanalytical technology enabling rapid and automated protein identification. *Anal Chem* 72 (2000), pp. 286-293.
- [215] T. Laurell, J. Nilsson and G. Marko-Varga , Silicon microstructures for high-speed and high-sensitivity protein identifications. *J Chromatogr B Biomed Sci Appl* 752 (2001), pp. 217-232.
- [216] L. C. Waters, S. C. Jacobson, N. Kroutchinina, J. Khandurina, R. S. Foote, and J. M. Ramsey, "Microchip device for cell lysis, multiplex PCR amplification and electrophoretic sizing," *Anal. Chem.*, vol. 70, pp. 158-162, 1998.
- [217] A. T. Woolley, D. Hadley, P. Landre, A. J. deMello, R. A. Mathies, and M. A. Northrup, "Functional integration of PCR amplification and capillary electrophoresis in a Microfabricated DNA analysis device," *Anal. Chem.*, vol. 68, pp. 4081-4086, 1996.
- [218] C. H. Mastrangelo and D. T. Burke, "Integrated microfabricated devices for genetic assays," presented at Microprocesses and Nanotechnology '99, Yokohama, Japan, 1999.
- [219] H. Becker, W. Dietz, and P. Dannberg, "Microfluidic Manifolds By Polymer Hot Embossing for Micro Total Analysis System Applications," *Micro Total Analysis Systems '98*, pp. 253, 1998.
- [220] O. Larsson, O. Ohman, A. Billman, L. Lundblad, C. Lindell, and G. Palmkog, "Silicon Based Replication Technology of 3-D-Microstructures by Conventional CD-Injection Molding Techniques," *Transducers '97*, pp. 1415, 1997.
- [221] T. D. Boone, H. H. Hooper, and D. S. Soane, "Integrated Chemical Analysis on Plastic Microfluidic Devices," *Transducers '98*, pp. 87, 1998.
- [222] C. S. Effenhauser, G. J. M. Bruin, A. Paulus, and M. Ehrat, "Integrated Capillary Electrophoresis on Flexible Silicone Microdevices," *Anal. Chem.*, vol. 69, pp. 3451, 1997.
- [223] C. H. Mastrangelo, M. A. Burns and D. T. Burke, "Integrated Microfabricated Devices for Genetic Assays," invited paper, Microprocessor and Nanotechnology Conference, Yokohama Japan, pg. 58-59, July 6-8, 1999.
- [224] Brandon and Tooze "Protein Structure and Function" Garland Pub. 2000.

- [225] G. Fuhr, Examples of three-dimensional microstructures for handling and investigation of adherently growing cells and submicron particles. *Anal. Methods Instrum.* (1996), pp. 39-54 Special Issue Micro TAS '96.
- [226] G. Fuhr and S.G. Shirley, Cell handling and characterisation using micron and submicron electrode arrays. *J. Micromech. Microeng.* **5** (1995), pp. 77-85.
- [227] N.B. Standen, P.T.A. Gray and M.J. Whitaker Editors, *Microelectrode Techniques* The Company of Biologists, Cambridge (1987).
- [228] D.J. Harrison, P. Li, T. Tang and W. Lee, Manipulation of biological cells and of DNA on-chip. *Anal. Methods Instrum.* (1996), pp. 147-149 Special Issue ~~Micro~~ TAS '96.
- [229] P.E. Andersson, P.C.H. Li, R. Smith, R.J. Szarka and D.J. Harrison, Biological cell assays on an electrokinetic microchip. *Proc. Transducers '97, 1997 Int. Conf. On Solid-State Sens. Actuators*, Chicago (1997), pp. 1311-1314.
- [230] S. Hediger, A. Sayah and M.A.M. Gijs, Fabrication of a novel microsystem for the electrical characterisation of cell arrays. *Sensors and Actuators, B* **56** (1999), pp. 175-180.
- [231] D.S. Misfeldt, S.T. Hammamoto and D.R. Pitelka, Transepithelial transport in cell culture. *Proc. Natl. Acad. Sci., USA* **73** (1976), pp. 1212-1216.
- [232] L.C. Milks, M.J. Brontoli and E.B. Cramer, Epithelial permeability and the transepithelial migration of human neutrophils. *J. Cell Biol.* **96** (1983), pp. 1241-1247.
- [233] Corning Costar® product literature, Corning Costar, Acton, MA, USA, 1999.
- [234] Falcon® product literature, Becton Dickinson, Franklin Lakes, NJ, USA, 1998.
- [235] Harrison RG. 1912. The cultivation of tis-sues in extraneous media as a method of morphogenetic study. *Anat. Rec.* **6**:181–93
- [236] Weiss P. 1945. Experiments on cell and axon orientation in vitro: the role of colloidal exudates in tissue organization. *J. Exp. Zool.* **100**:353–86
- [237] Curtis ASG, Valverde M. 1964. Control of cell behavior: topological factors. *J. Natl. Cancer Inst.* **33**(1):15–26
- [238] Rovensky YA, Slavnaia IL, Vasiliev JM. 1971. Behaviour of fibroblast-like cells on grooved surfaces. *Exp. Cell Res.* **65**(1): 193–201
- [239] Furshpan EJ, MacLeish PR, O'Lague PH, Potter DD. 1976. Chemical transmission between rat sympathetic neurons and cardiac myocytes developing in microcul-trues: evidence for cholinergic, adrenergic, and dual-function neurons. *Proc. Natl. Acad. Sci. USA* **73**(11):4225–29
- [240] Grumbacher-Reinert S. 1989. Local influence of substrate molecules in determining distinctive growth patterns of identified neurons in culture. *Proc. Natl. Acad. Sci. USA* **86**:7270–74
- [241] Turner DC, Lawton J, Dollenmeier P, Ehrismann R, Chiquet M. 1983. Guidance of myogenic cell migration by oriented de-posits of fibronectin. *Dev. Biol.* **95**:497– 504
- [242] Lieberman M, Roggeveen AE, Purdy JE, Johnson EA. 1972. Synthetic strands of cardiac muscle: growth and physiological implication. *Science* **175**:909–11

- [243] Ivanova OY, Margolis LB. 1973. The use of phospholipid film for shaping cell cultures. *Nature* 242:200–1
- [244] Rovasio RA, Delougee A, Yamada KM, Timpl R, Thiery JP. 1983. Neural crest cell migration: requirements for exogenous fi-bronectin and high cell density. *J. Cell. Biol.* 96(2):462–73
- [245] Blawas AS, Reichert WM. 1998. Protein patterning. *Biomaterials* 19(7–9):595–609
- [246] Izzard CS, Lochner LR. 1976. Cell-to-substrate contacts in living fibroblasts: an interference reflexion study with an evaluation of the technique. *J. Cell Sci.* 21(1):129–59
- [247] Wehland J, Osborn M, Weber K. 1979. Cell-to-substratum contacts in living cells: a direct correlation between interference reflexion and indirect-immuno-fluorescence microscopy using antibodies against actin and alpha-actinin. *J. Cell Sci.* 37:257–73
- [248] Grinnell F. 1980. Visualization of cell-substratum adhesion plaques by antibody exclusion. *Cell Biol. Int. Rep.* 4(11):1031– 36
- [249] Ruoslahti E, Reed JC. 1994. Anchorage dependence, integrins, and apoptosis. *Cell* 77(4):477–78
- [250] Van den Berg A, Lammerink TSJ. 1998. Micro total analysis systems: microfluidic aspects, integration concept and applications. *Top. Curr. Chem.* 194:21
- [251] Dekker A, Beugeling T, Wind H, Poot A, Bantjes A, et al. 1991. Deposition of cellular fibronectin and desorption of human serum albumin during adhesion and spreading of human endothelial cells on polymers. *J. Mater. Sci. Mater. Med.* 2:227–33
- [252] Blawas AS, Reichert WM. 1998. Protein patterning. *Biomaterials* 19(7–9):595–609
- [253] Grinnell F, Feld MJ. 1981. Adsorption characteristics of plasma fibronectin in relationship to biological activity. *J. Biomed. Mater. Res.* 15:363
- [254] Iuliano DJ, Saavedra SS, Truskey GA. 1993. Effect of the conformation and orientation of adsorbed fibronectin on endothelial-cell spreading and the strength of adhesion. *J. Biomed. Mater. Res.* 27:1103
- [255] Miyamoto S, Ohashi A, Kimura J, Tobe S, Akaike T. 1993. A novel-approach for toxicity sensing using hepatocytes on a collagen-patterned plate. *Sens. Actuator B* 13(1–3):196
- [256] Corey JM, Brunette AL, Chen MS, Weyhenmeyer JA, Brewer GJ, Wheeler BC. 1997. Differentiated B104 neuroblastoma cells are a high-resolution assay for micropatterned substrates. *J. Neurosci. Methods* 75(1):91–97
- [257] Bhatia SN, Toner M, Tompkins RG, Yarmush ML. 1994. Selective adhesion of hepatocytes on patterned surfaces. *Ann. NY Acad. Sci.* 745:187–209
- [258] Tai HC, Buettner HM. 1998. Neurite outgrowth and growth cone morphology on micropatterned surfaces. *Biotechnol. Prog.* 14(3):364–70
- [259] Ratner BD. 1992. Plasma deposition for biomedical applications: a brief review. *J. Biomater. Sci. Polym. Ed.* 4(1):3–11
- [260] P, Stenger DA, et al. 1994. Rational pattern design for in-vitro cellular networks Hammarback JA, Palm SL, Furcht LT, Le-tourneau PC. 1985. Guidance of neurite outgrowth by pathways of substratum-adsorbed laminin. *J. Neurosci. Res.* 13(1– 2):213–20
- [261] Folch A, Jo B-H, Beebe D, Toner M. Microfabricated elastomeric stencils for micropatterning cell cultures. *J. Biomed. Mater. Res.* In press

- [262] Branch DW, Corey JM, Weyhenmeyer JA, Brewer GJ, Wheeler BC. 1998. Micro-stamp patterns of biomolecules for high-resolution neuronal networks. *Med. Biol. Eng. Comput.* 36(1):135–41
- [263] Jackman RJ, Duffy DC, Cherniavskaya O, Whitesides GM. 1999. Using elastomeric membranes as dry resists and for dry lift-off. *Langmuir* 15(8):2973
- [264] Kapur R, Spargo BJ, Chen MS, Calvert JM, Rudolph AS. 1996. Fabrication and selective surface modification of 3- dimensionally textured biomedical polymers from etched silicon substrates. *J. Biomed. Mater. Res.* 33(4):205–16 222(2):380
- [265] Delamarche E, Bernard A, Schmid H, Bietsch A, Michel B, Biebuyck H. 1998. Microfluidic networks for chemical patterning of substrate: design and application to bioassays. *J. Am. Chem. Soc.* 120: 500–8
- [266] Delamarche E, Bernard A, Schmid H, Michel B, Biebuyck H. 1997. Patterned delivery of immunoglobulins to surfaces using microfluidic networks. *Science* 276:779–81
- [267] Kenis PJA, Ismagilov RF, Whitesides GM. 1999. Microfabrication inside capillaries using multiphase laminar flow patterning. *Science* 285:83–85
- [268] Takayama S, McDonald JC, Ostuni E, Liang MN, Kenis JA, et al. 1999. Patterning cells and their environments using multiple laminar fluid flows in capillary networks. *Proc. Natl. Acad. Sci. USA* 96:5545–48
- [269] Schmidt CE, Shastri VR, Vacanti JP, Langer R. Stimulation of neurite outgrowth using an electrically conducting polymer. *Proc Natl Acad Sci USA* 1997;94:8948–8953.
- [270] Wallace GG. Conductive electroactive polymers: Intelligent materials systems. Lancaster, Pennsylvania: Technomic Publishing Co.; 1997.
- [271] Silk T, Hong Q, Tamm J, Compton RG. AFM studies of polypyrrole film surface morphology. I. The influence of film thickness and dopant nature. *Syn Metals* 1998;93:59–64
- [272] Wang J, Jiang M. Toward genoelectronics: Nucleic acid doped conducting polymers. *Langmuir* 2000;16:2269–2274.
- [273] Garner B, Georgevich A, Hodgson A, Liu L, Wallace GG. Poly-pyrrole– heparin composites as stimulus-responsive substrate for endothelial cell growth. *J Biomed Mater Res* 1999;44:121– 129.
- [274] Freemantle M. The endless polymer science frontier. *Chem Eng News* 2000;78:39–45.
- [275] Hodgson AJ, John MJ, Campbell T, Georgevich A, Woodhouse S, Aoki T, Ogata N, Wallace GG. Integration of biocomponents with synthetic structures - Use of conducting polymer polyelectrolyte composites. *SPIE* 1996;2716:164–176.